Modeling, Experimentation and Optimization for a Mixed Gas Joule-Thomson Cycle with Precooling for Cryosurgery

by

Harrison M. Skye

A dissertation submitted in partial fulfillment of the
requirements for the degree of:

Doctor of Philosophy
(Mechanical Engineering)

at the

UNIVERSITY OF WISCONSIN – MADISON
2011

This page was intended to be left blank.

Modeling, Experimentation, and Optimization for a Mixed Gas Joule-Thomson Cycle with Precooling for Cryosurgery

Harrison M. Skye

Under the supervision of Professors Sanford Klein and Greg Nellis
at the University of Wisconsin - Madison

Abstract

Cryosurgery is a medicinal technique for destroying undesirable tissues such as cancerous tumors using a freezing process. The cryolesion that is formed is typically on the order of tens of millimeters in diameter, and the lethal zone extends from the probe tip to the location where the tissue temperature is about 240 K. The handheld portion of the cryoprobe must be compact and powerful in order to serve as an effective surgical instrument; a system that meets these criteria is a Mixed Gas Joule-Thomson (MGJT) cycle integrated with a cryoprobe. The next generation of MGJT cycles for cryosurgery is able to provide additional cooling by using a pre-cooling stage that consists of a conventional Vapor Compression (VC) cycle. Selecting mixtures and precooling cycle parameters to meet a cryogenic cooling load in a size-limited application is a challenging design problem that must be solved through careful consideration of the thermodynamic and transport processes in the system. However, current modeling tools available in the literature for MGJT cycles largely focus on selecting mixtures based on favorable thermodynamic properties and do not include effects of pressure drop or heat transfer for the multi-phase, multicomponent mixture in the complex geometry of a helically wound recuperator/precooler. Therefore, the focus of this research project is to improve the state-of-the-art by developing an empirically-tuned mixture optimization model that includes the

transport processes in the heat exchangers. This effort is carried out through a series of modeling, experimental, and optimization studies presented in this thesis.

A thermodynamic model of the precooled MGJT cryoprobe has been developed and integrated with a genetic optimization algorithm in order to guide the selection of the optimal mixture compositions as well as other operating parameters. The model is useful for demonstrating the benefit of the precooled cycle over the single-stage system, and for investigating cycle design issues related to proper selection of precooling temperature and working fluid. A tradeoff is identified between the compactness of the cryoprobe, and the size and power requirements of the compressors and condensers.

A commercially available MGJT cryoprobe system has been disassembled and installed in a vacuum insulated dewar. The system has been modified in order to integrate a suite of measurement instrumentation that can completely characterize the performance of individual components as well as the overall system. Measurements include sufficient temperature and pressure sensors to resolve thermodynamic states, and flow meters used in the calculation of heat and work transfer rates. A thermal load is applied to the cycle using an electric heater to characterize the refrigeration performance. Temperature sensors are also integrated within the recuperator in order to capture the heat transfer performance of the two-phase, multi-component mixture as it flows through the recuperator. Test conditions were varied to achieve a range of temperatures, pressures, and thermodynamic qualities using mixtures of argon, R14 and R23. These data are used to establish empirical, but largely physics-based, models for pressure drop and heat transfer in the precooler and recuperator. The mixture optimization model was modified to include these correlations and provide for a more realistic estimate of the system

performance. Finally, this tuned system model is used to demonstrate the design process for selecting mixture compositions, tip temperature, and heat exchanger sizes to maximize cryoprobe performance.

Approved:

Professor Sanford Klein
Department of Mechanical Engineering
University of Wisconsin – Madison

Professor Greg Nellis
Department of Mechanical Engineering
University of Wisconsin - Madison

Acknowledgements

The list of people who have in some way contributed to my progression through a PhD program at Madison is truly humbling. The professors and students I've worked with on a daily basis, the engineering shop staff, the great teachers I've had along the way, the employees at American Medical Systems, family and friends, and the numerous health care professionals who've helped me keep my back healthy – all have played a vital role in this research project, my education, and my life in the past four years. This has been such a fulfilling and defining experience that will provide me opportunities for a successful and engaging career - I will always remember how your support made it possible.

I owe a special gratitude to my project advisors, Professors Sanford Klein and Greg Nellis, who have guided me through the PhD and MS degrees. Its fun to think about how we got started eight years ago working with vortex tubes; I still remember your patience in reassuring me that it's normal when the CFD simulations don't exactly match the experimental data on the first try. I have looked forward to our weekly meetings for advice about the project and the occasional sage direction for life outside engineering. Your careful critiques of my reports and papers have always significantly improved their quality and clarity, and have helped me tremendously to become a better writer. I've noticed a slow shift in your critiques of my reports from "this needs work" to "comments attached"; I hope this is an indication that you also think my writing has improved.

Through the years I've been continually awed by your dedication to research and classes you teach – we've all learned not to be surprised by email responses sent close to midnight. The prestigious awards you've received over the years are well deserved; your reputation precedes you and people clamber to fill up your classes and laboratory.

My initial interest in the thermal sciences began in Professor Klein's ME 361 Thermo class. I was amazed how your lectures elegantly combined the hard science, policy issues, and a cheerful disposition balancing cynicism and optimism about the state of the world. You have a knack for illuminating even the most complex concepts in a methodical and understandable fashion that is evidenced by your well attended classes. I always made it a point to regularly attend office hours for the four thermodynamics courses I've had with you, because every time you gave some additional insight into the course material or computational tools. Thanks for enduring my endless questions. Also, I'd like to give extra thanks for all the capabilities to the EES Macros that you added in the past few months to help with processing the experimental data. The new features eliminated many hours of tedious data manipulation and graph formatting, and have allowed us to process data nearly in real-time to help guide the direction of the experimental tests.

I've learned that the best teachers are the ones who make you work hard, and Greg is no exception. Interesting and challenging homework highlighted each week of class and your ability to pose real world design issues as engineering problems for your students to solve is astounding. Your lecture notes are always precise and thorough, and have the unique characteristic of truly being the only resource one needs to learn the material. I could always count on your extensive experimental background to help me navigate the numerous problems

in the lab that continually arose according to Murphy's Law. Thanks for your wisdom and direction, and the occasional blunt assessment that is sometimes critical to moving a project forward.

Going through a back surgery in the middle of a PhD turned out to be a difficult process. The expected two week recovery period turned into three or four months, and I relied heavily on friends and family to build up my health. Thanks to my advisors for their understanding and allowing me to work a flexible schedule until I could return to a full day. I owe the most gratitude to my wife, Naomi. You were there the day of the surgery, you were there the two subsequent weeks where I could barely get out of bed, and you were there to encourage me to move forward with physical therapy and returning to work in the following months. I don't know how you found the time or energy to hold a full time job, go to school, keep the house running, and change my socks when I couldn't reach my feet.

Naomi, I'm looking forward to the next chapter in our lives. It won't be easy moving far away from friends and family, but we will always find a way to make a home wherever we settle. Our closely awaiting role as parents is sure to bring a whole new level of adventure; I can't wait for our little peanut to pop out of the shell.

To my parents, Harry and Dorothy – I certainly would not be at this point if not for your support. You've always encouraged me and provided opportunities to excel in education, sports, and life. Despite your consuming jobs you've been closely involved with your children, traveled the world and made contributions to the community. I hope to follow the humility you carry in your impressive lives. Weston and Jenny, it's been a wonderful coincidence to have all the Skye children attending school at Madison again; I will surely miss our weekly dinner party. Finally, Grandpa George, thank you for all your kind letters and for always spicing up the party with signs and eclectic hats.

The students and other researchers in the lab make the SEL one the best places to work. I owe gratitude to the many people that helped me get my "lab legs" including Steve Meitner, Dan Hoch, Gabe Bernhardt, and Jim Maddocks. A number of undergraduate researchers have participated in my two graduate research projects; thanks to Branden Krause, Ben Cox, Greg Marsicek, Koua Moua, Joe Jaeckels, and Jake Kilbane. Special acknowledgement goes to Jeremiah Osborn who was heavily involved with both projects since 2007. To my office mates, Mike Cheadle, John Dyreby, Ryan Taylor, Kurt Englebrecht, and Steve Meitner – I've enjoyed our cozy desk arrangements and the endless debates about engineering, politics, and philosophy. Thanks to John Dyreby for always being a great friend, confidant, and party planner, not to mention for your expertise with numerical modeling and curve fitting that accelerated my data processing computations at a critical time near the end of the PhD. Kendra, I've enjoyed getting to know you and working with you on the cryoprobe project. Our difference in height has made sharing lab space and equipment comical at times; you can finally just leave the sleeves on the welding coat rolled up. Don't forget to keep me informed with all the new progress you make. Goodbye to Amanda Pertzborn, Jake Leachman, Amir Jahromi, Ty Neiss, Will Seidel, Jan Beerman, Luke Feirabend, Mike Frischmann, Scott Hackel, Scott Schuetter (you get rounded up to a member of the SEL), Kevin Myers, Matt Boyd, Jake Brenner, Pete Mumanachit, Mark Rodarte, Bill Brey, Stephanie Knauf, Bryant Mueller, Rodrigo Barraza, Dan Schick, Dan Potratz, Sonke Teichel, and Ryan Jester. Thanks to the other SEL professors who served on my

PhD committee including Franklin Miller and John Pfotenhauer, as well as Jay Martin who stepped in and offered an outside perspective.

Gratefully acknowledged financial support for this project was provided by the Wisconsin Space Grant Consortium, the UW-Madison Mechanical Engineering Department through the Alex Cowie Fellowship, the American Society of Heating, Refrigerating, and Air-Conditioning Engineers (ASHRAE) under Research Project 1472. Furthermore, the technical assistance of Mike Perkins has been invaluable to the progress of this project. Thanks for all your help in understanding the system operation, providing ideas for measurement techniques, and guiding the resolution of problems related to oil, moisture, and contamination control.

Table of Contents

List of Figures

List of Tables

List of Variables

Nomenclature

A	Area (m^2)
A_c	Corrected gas chromatograph integrator area
$A_{c,i}$	Corrected gas chromatograph integrator area
A_{uc}	Uncorrected gas chromatograph integrator area
a_i	Thermocouple voltage coefficients
a	Recuperator/precooler pressure drop and conductance correlation coefficients
b	Recuperator/precooler pressure drop and conductance correlation coefficients
c	Thermal capacitance (kJ kg^{-1} K^{-1})
$\overline{c}$	Average thermal capacitance (kJ kg^{-1} K^{-1})
cp	Constant pressure specific heat (kJ kg^{-1} K^{-1})
COP	Coefficient of Performance (refrigeration capacity divided by compressor power)
C_r	Capacity ratio between heat exchanger streams
D	Tube diameter (m)
$dist$	PRT to tube center distance (m)
$Eterm$	Exponential term used to transition between the vapor and two-phase precooler conductance correlations
e	Tube surface roughness (m)
F	Mixture constituent mole fraction from gas chromatograph
f	Friction factor
$f_{trans,vap}$	Fraction of precooler tube length in the phase-transition section assumed to contain vapor-only flow
h	Enthalpy (kJ kg^{-1})
h_f	Fin height (m)
h_{rec}	Annulus height for recuperator (m)
G	Amplifier gain
i	Electric current (A)
I	Electric current (A)
ID	Inner diameter (m)

k	Thermal conductivity (W m^{-1} K^{-1})
L	Tube length (m)
m	Fin parameter
$\dot{m}$	Mass flow (kg s^{-1})
min	minimum
MR	Mass flow ratio (1^{st} stage/2^{nd} stage)
N	Number of discrete heat exchanger sections, number of data points used for calibration
n	Number of calibration curve fitting coefficients
Nf_{rev}	Number of fins per recuperator tube helix revolution
N_{points}	Number of data points used in a curve fit
N_{turns}	Number of helical tube turns
NC	Number of component in mixture3
NTU	Number of Transfer Units in a heat exchanger
OD	Outer diameter
P	Pressure (kPa)
p	Helical tube pitch
PRT	Platinum Resistance Thermometer
$\dot{Q}$	Heat transfer or refrigeration load (W)
R	Electrical resistance (ohm or Ω)
R^2	Statistical coefficient of determination – measure of ability of curve fit to predict future outcomes
Re	Reynolds number
$Reynolds$	Reynolds number
RF	Gas chromatograph response factor used to correct mixture mole fraction readings
r	Radius (m)
rf	Radius of annular fin
T	Temperature (K)
tf	Fin thickness (m)
s	Entropy (kJ kg^{-1} K^{-1})
U	Uncertainty or sensitivity

UA	Conductance (W K^{-1})
UA/L	Conductance per length of finned tube (W K^{-1} m^{-1})
V	Voltage (V)
$\dot{V}$	Volumetric flow rate (m^3 s^{-1})
v	Specific volume (m^3 kg^{-1}), velocity (m s^{-1})
$\dot{W}$	Work (W)
wf	Recuperator tube center to PRT weighting factor
x	Thermodynamic quality, distance
$\bar{y}$	Mixture mole fraction vector

Greek symbols

Δh_T	Isothermal enthalpy difference (kJ kg^{-1})
ΔT	Temperature difference or pinch point temperature difference (K)
ε	Heat exchanger effectiveness
η	Isentropic efficiency
ρ	Density (kg m^{-3})
θ	Temperature difference from fluid

Subscripts

#	*Temperature or pressure transducer number*
i#	*PRT# for sensors embedded in G10 sheath that surrounds the recuperator*
1^{st}	First stage cycle (vapor compression cycle)
2^{nd}	Second stage (mixed gas JT cycle stage)
3^{rd}	Third order fit region of recuperator UA/L correlation
1102	National Instruments 1102 thermocouple amplifier module for SCXI chassis
40°C	Thermocouple voltage sensitivity computed at 40°C
6036	National Instruments 6036E Data Acquisition Card
a	actual fluid properties in test condition
acc	Accuracy
amb	Ambient condition
ave	Averaged property
b	Temperature difference at the base (for the thermocouple, between the fluid and the thermocouple wire feedthrough at ambient temperature)

c	Cold stream; cross section
cal	Uncertainty related to calibrating sensor error
cal,acc	Uncertainty in calibration temperature measurement related to Polyscience 9112 bath temperature sensor accuracy
cal,stab	Uncertainty in calibration temperature measurement related to Polyscience 9112 bath temperature stability
cond	Uncertainty related to conduction through sensor wires
CJC	Cold junction compensation
cold	Cold end temperature difference
comp	Compressor
d	Distal end of recuperator
elec	Electronic uncertainty
f	Finned tube
ff,rec,c,tube	Frontal flow area of recuperator cold side annulus
ff,rec,c,mf	Frontal flow area of recuperator monofilament wire
ff,rec,h	Frontal flow area inside (hot side) of recuperator tube
freeze	Freezing point
f,rev	Finned section of heat exchanger tube per helix revolution
G10	Frontal flow area of G10 sheath
h	Hot stream
helix	Finned tube helix
high	High pressure stream
hpe,i	Length of 1/8” high pressure exit tube inside the SS sheath
hpe,o	Length of 1/8” high pressure exit tube outside the SS sheath
hsheath-pc	Annulus height between precooler and SS sheath
int	Interpolation error
JT	Joule-Thomson effect – i.e. a change in fluid temperature caused by isenthalpic expansion
i	Node or heat exchanger section index
int	Interpolation table entries
lin	Linear fit region of UA/L correlation
load	Cryoprobe tip refrigeration load

low	Low pressure stream
m	Frontal flow area of recuperator mandrel
max	Maximum possible refrigeration
meas	Uncertainty related to resolution
mfi	Inner monofilament wire
mfo	Outer monofilament wire
mod	Modeled
mol,meas	Uncorrected molecular mole fraction measured from the gas chromatograph
mol, cal	Corrected molecular mole fraction from the gas chromatograph
mol%,c	Corrected molar fraction for mixture constituent measured by gas chromatograph
$N_{2,std}$	Nitrogen, at standard atmosphere and pressure conditions (25°C, 1 atm)
ohmic	Electrical ohmic dissipation
p	Proximal end of cryoprobe or recuperator, parasitic heating
parasitic	Parasitic heating
pc	Precooler
pc,2ϕ	Portion of precooler tube containing two-phase flow
pp	Pinch point
PRT	PRT slot length
rec	Recuperator
rec,c,out	Outlet of cold side of recuperator
rec,h,in	Inlet of hot side of recuperator
rec,tube	Frontal flow area of recuperator tube
rec,f	Frontal flow area of recuperator tube fins
ref	reference temperature for thermocouples (0°C)
rep	Repeatability
res	Resolution
rev	Per recuperator/precooler tube helix revolution
rms	RMS error
s	Smooth and straight section of finned heat exchanger tubing
sheath-pc	Length of annulus between precooler and SS sheath
sub	Number of numerical sub-heat exchangers representing the recuperator sections between each PRT embedded in the G10 sheath

std	Temperature computed using standard thermocouple temperature-voltage data
TC	Thermocouple
tc	recuperator tube center temperature
total	Combined from precooler/recuperator (UA,L) or $1^{st}/2^{nd}$ stage ($\dot{v}$)
tp	Triple point
trans	Precooler tube section where the 2^{nd} stage refrigerant transitions from vapor to two-phase
tube,f,pc	Length of finned precooler tube section
tube,f,pc,2ϕ	Length of finned precooler tube section containing two-phase flow
tube,f,pc,vap	Length of finned precooler tube section containing vapor phase flow
typeE	Type E thermocouple
w	Smooth and wrapped section of finned heat exchanger tubing

1 Introduction

1.1 Overview of cryosurgery and cryosurgical probes

Cryosurgery is a technique for destroying undesirable tissue such as cancers using a freezing process. Treatments include prostate and liver tumor ablation, as well as a variety of dermatological and gynecological procedures. Cryosurgery relies on some type of cryosurgical probe that is inserted into the body in order to create the necessary cryogenic temperatures; the cryoprobe tip reaches approximately 150 K and the surgery may last anywhere from a few minutes to an hour (Rubinsky 2000). These handheld surgical instruments must be compact and ergonomic to facilitate precise placement and to ensure the procedure is minimally invasive. Figure 1-1 shows the components of a particularly small cryoprobe energized by a Joule Thomson (JT) cycle, and demonstrates the level of miniaturization available with this technology.

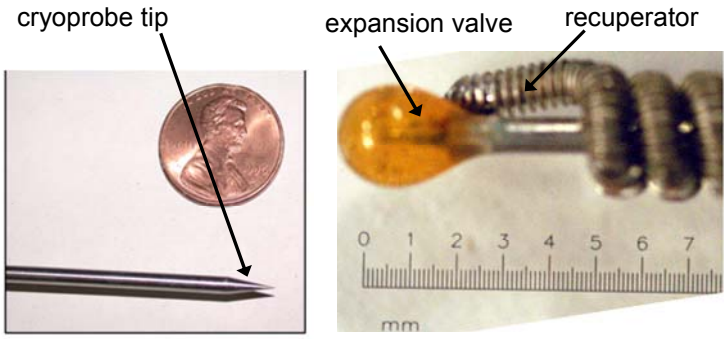

Figure 1-1: Photos of miniature cryoprobe components including the (a) tip and (b) the expansion valve and recuperator of a probe energized by a Joule-Thomson cycle.

The cryolesion that is formed has been studied by Fredrikson (2004) and is typically on the order of tens of millimeters in diameter. The lethal zone (i.e., the region in which cell death is complete) extends outward into the tissue from the cryoprobe active portion of the probe

approximately to the location where the tissue temperature is about 240 K, although this will vary by ±15 K depending on the details of the surgical procedure and location (Rubinsky 2000). The cryolesion is pear-shaped, as shown in Figure 1-2. The outline of the probe has been enhanced in the figure to clarify the boundary between the probe and the iceball. The cryosurgical procedure is inherently less invasive than other treatments as the affected tissue extends beyond the contact point of the instrument. Cryosurgery is therefore an attractive alternative for procedures where surgical resection is not possible because of the proximity of the diseased tissue to large, healthy blood vessels, which may become damaged using a more invasive technique (Zhong 2006).

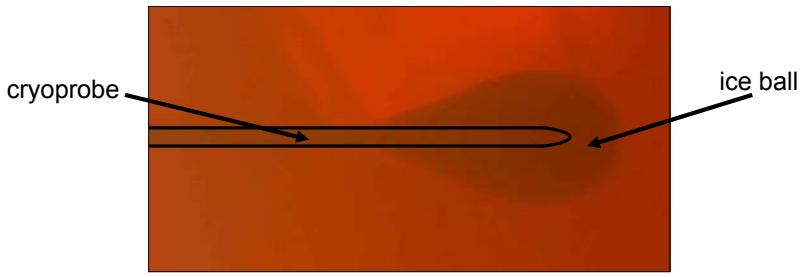

Figure 1-2: Photograph of an iceball grown in a gelatin solution using a cryoprobe (Fredrikson 2004).

Cryosurgical treatment of cancers began in the mid-nineteenth century when James Arnott (Arnott 1851) investigated the use of freezing for the treatment of cancer. Freezing tissues using a mixture of ice and various solutes had been previously used as an anesthetic, but Arnott found that freezing was also an effective treatment option for tumors in the breast and uterine cavity (Rubinsky 2000). Advances in cryogenics over the next century led to availability of various cryogens including liquid oxygen and liquid nitrogen as well as solid carbon dioxide (dry ice). However, instrumentation for medical cryogen application was limited during this time and generally capable of freezing to a depth of only a few millimeters (Rubinsky 2000).

Therefore, the use of cryogenics in medicine was primarily limited to treatment of superficial tissues in the fields of dermatology and gynecology.

Irving Cooper and Arnold Lee (Cooper 1961) invented the first cryosurgical probe that was capable of producing sizable cryolesions deep within the body. Liquid nitrogen (LN2) was pumped through thin concentric tubes; liquid nitrogen entered the probe where it was evaporated by the surgical load at the tip and then nitrogen vapor exited. Liquid nitrogen cryoprobes are still used today, however, the nitrogen vapor is not recovered which leads to ventilation issues, and the cryogen storage tanks must be periodically refilled which limits the duration of the procedure and adds other logistical complexity. Additionally, the probes and other equipment involved in transporting the liquid nitrogen to the cryoprobe must be vacuum insulated and therefore the system is bulky and difficult to precisely handle; these are undesirable properties for a piece equipment that is meant to be minimally invasive and used in a surgical setting.

The next generation of cryosurgical probes uses a pure gas (e.g., argon) in a Joule-Thomson (JT) refrigeration cycle. A high pressure (often 20 MPa or 3000 psig) gas cylinder is used to provide high pressure gas to an open-cycle JT system where the low temperature gas in the tip of the cryoprobe creates the cooling effect. The advantage of this system is that the gas entering the cryoprobe is at room temperature and therefore vacuum insulation is not required; these probes are much smaller than their liquid nitrogen counterparts. However, the pressures required by single component gas in a JT system are too large to be provided by any portable compressor and thus the need for a high pressure gas bottle. The low pressure gas leaving the open system is not recovered and therefore represents an asphyxiation hazard; the medical

facility must be equipped with an auxiliary ventilation system. The system provides a small amount of cooling per unit of gas consumed and therefore the amount of gas consumed in order to complete a procedure is large and the cylinders must be replaced frequently.

JT systems utilizing a mixture of gases, rather than a pure gas, represent a significant advance in cryosurgical probe technology. The pressure required by a Mixed Gas Joule-Thomson (MGJT) system is much lower than for a pure gas JT system (typically 1.5 MPa or 200 psi - an order of magnitude smaller than pure gas systems). Therefore it is possible to recover the low pressure mixture leaving the probe and recompress it in a small, portable compressor placed in the operating room. MGJT systems are closed systems that offer the considerable advantage of not using a consumable working fluid; this advantage reduces the hardware, floor space, logistical and ventilation requirements, and expense associated with a procedure. Brodyansky et al. (1971) showed that MGJT systems can provide substantially more cooling per unit mass than pure gas JT systems, which leads to a relatively compact and convenient device that is more appropriate for a clinical environment. Section 1.2 discusses the thermodynamics underlying the MGJT cycles and shows how this cycle can be configured for use in a cryoprobe.

The current clinical limitations on the use of cryosurgery are primarily related to the cryoprobe technology itself. For treatments that cover large regions deep within the body, current cryoprobe technology requires that multiple probes be inserted and precisely positioned in order to ensure complete cell death. Clearly, a single probe with more power in the same geometric envelope is more desirable as it is less invasive and more easily controlled. The most recent advancement in cryosurgical probe technology addresses this need by improving the

underlying thermodynamic cycle. Multi-stage Joule-Thomson cycles are used to divide the large temperature range that must be spanned (from room temperature to approximately 150 K) into two smaller temperature stages that can each be addressed using a more compact system. The result is a probe that can provide more refrigeration in the same compact configuration. A cryoprobe energized by a two-stage MGJT cycle is the focus of this project and is discussed in detail in Section 1.3.

1.2 MGJT cryoprobes and cycles

Figure 1-3 provides a schematic of a single-stage MGJT cryoprobe configuration and Figure 1-4(a) shows the primary components in the single-stage MGJT thermodynamic cycle including numbered thermodynamic states. The compressor and aftercooler deliver high pressure and approximately room temperature gas mixture to the recuperator at state 3. The high pressure mixture is cooled by the returning low pressure stream in the recuperator; this heat exchange process enables the cycle to efficiently provide cooling at low temperatures. Isenthalpic expansion across the expansion valve reduces the mixture temperature to the lowest temperature in the cycle at state 5. The biological thermal load ($\dot{Q}_{load}$) is then applied to the flow stream at the cryoprobe tip (represented in Figure 1-4(a) as the load heat exchanger); the temperature after the tip (T_6) is typically referred to as the load temperature. The low pressure mixture then flows through the recuperator and finally returns to the compressor for recovery. The working fluid in the MGJT cycles is typically a Hydrocarbon (HC) or Synthetic Refrigerant (SR) based blend, where the balance gases are noble gases such as nitrogen, krypton, or argon. As discussed in Section 1.1, the mixture enters and exits the base of the cryoprobe near room

temperature; therefore, the mixture can be transported to and from a remotely located compressor via small and flexible plastic tubing.

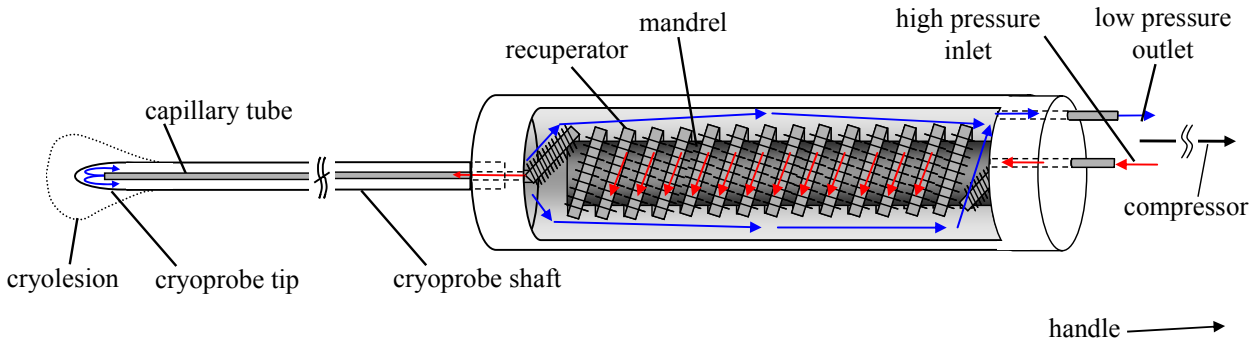

Figure 1-3: Geometric schematic of a single-stage MGJT cryoprobe showing the fluid flow, expansion valve, cryoprobe shaft, coiled fin tube recuperator wound about a mandrel, and the locations of the remote compressor (not shown) and handle (not shown).

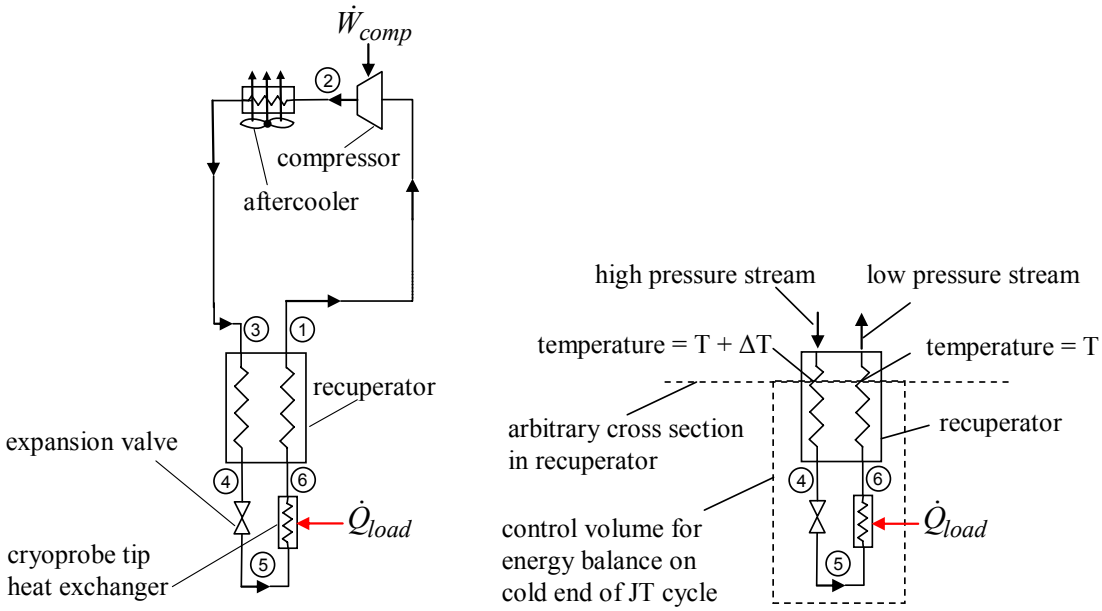

Figure 1-4: (a) Schematic of single-stage MGJT refrigeration cycle showing the locations of key components. (b) Control volume around cold end of JT cycle which passes through an arbitrary cross section in the recuperator

The refrigeration capacity of a JT cycle is fundamentally limited by the Joule-Thomson effect associated with the working fluid. The refrigeration can be computed by performing an energy balance on a control volume that encloses the cold end of the cycle; Figure 1-4 (b) shows

a control volume that passes through an arbitrary location in the recuperator and encloses the expansion valve and load head exchanger. The energy balance shows that the refrigeration load is equal to the enthalpy difference between the two streams at any-cross section in the heat exchanger:

$$\dot{Q}_{load} = \dot{m}\left[enthalpy\left(P_{low}, T, \overline{y}\right) - enthalpy\left(P_{high}, T + \Delta T, \overline{y}\right)\right] \tag{1.1}$$

where $\dot{m}$ is the mass flow rate, P_{high} and P_{low} are the suction and discharge pressures associated with the compressor (neglecting pressure loss in the recuperator), T is the temperature of the low pressure stream at the location of the control surface, ΔT is the temperature difference between the streams at the cross section, and $\overline{y}$ is a vector of the molar concentrations of each component in the gas mixture.

In the limit that the recuperator conductance is infinitely large (i.e., the recuperator is providing the maximum possible rate of stream-to-stream heat transfer), the temperatures of the fluid streams will coincide (i.e., ΔT in Equation (1.1) will approach zero) at some location in the recuperator; this location is commonly referred to as the pinch point. The maximum possible enthalpy difference between the two streams, which is equal to the maximum achievable refrigeration load per unit mass flow rate, can therefore be calculated as the minimum value of the isothermal enthalpy difference evaluated over the range of temperature that is spanned by the recuperator:

$$\frac{\dot{Q}_{load,\max}}{\dot{m}} = \min\left(\underbrace{\left[enthalpy\left(P_{low}, T, \overline{y}\right) - enthalpy\left(P_{high}, T, \overline{y}\right)\right]}_{\Delta h_T} \text{for } T = T_3 \text{ to } T_6 \right) \tag{1.2}$$

The isothermal enthalpy difference (Δh_T) is readily evaluated using a pressure-enthalpy (*P-h*) chart for the working fluid. Figure 1-5(a) shows a *P-h* chart for pure nitrogen. Also shown in Figure 1-5(a) is Δh_T evaluated for a cycle operating between 1000 and 100 kPa at several different temperatures. Notice that the 100 K isotherm passes through the vapor dome and therefore Δh_T is quite large at this temperature. However at higher temperatures such as 150 K and 200 K, nitrogen exhibits behavior that is approaching ideal-gas behavior and therefore Δh_T is very small. This behavior is typical of any working fluid: Δh_T tends to be large only near the vapor dome where real-gas effects govern fluid behavior. The recuperator must nominally span the temperature range from 290 K (warm inlet of recuperator) to 150 K (load temperature – recuperator cold inlet) for a single stage cryosurgical system. Therefore, the minimum Δh_T will occur at the warm end of the recuperator and will significantly restrict the refrigeration capacity of the cycle. The best JT cryoprobe would operate within the vapor dome of the working fluid; however, the recuperator temperature span that is required far exceeds the vapor dome of any single component working fluid.

The vapor dome associated with a mixture of gases tends to extend over a larger temperature range, corresponding to a temperature that is near the lowest boiling point of the components, to one that is near the highest boiling point of the components. The use of gas mixtures therefore significantly extends the temperature range over which Δh_T is large. Figure 1-5(b) shows a *P-h* chart for an optimized seven component mixture consisting of nitrogen, methane, ethane, propane, isobutene, isopentane, and argon. The refrigeration effect (Δh_T) is evaluated using the same pressures, 1000 kPa and 100 kPa, which were used in the nitrogen analysis above. Notice that the values of Δh_T at warmer temperatures are much larger for the

mixture because it remains in the vapor dome. The refrigeration effect for pure nitrogen and the mixture shown in Figure 1-5(a) and Figure 1-5(b), respectively, is shown in Figure 1-6 as a function of temperature; the minimum values for Δh_T for the optimized mixture and for pure nitrogen are compared. Figure 1-5 and Figure 1-6 both clearly show that over the nominal 150 K to 290 K operating temperature range, the refrigeration effect is significantly larger for the mixture than for nitrogen; in this case the mixture produces 50x greater cooling per unit mass flow. The additional refrigeration achievable with mixtures make the cycle much more practical for cryosurgery.

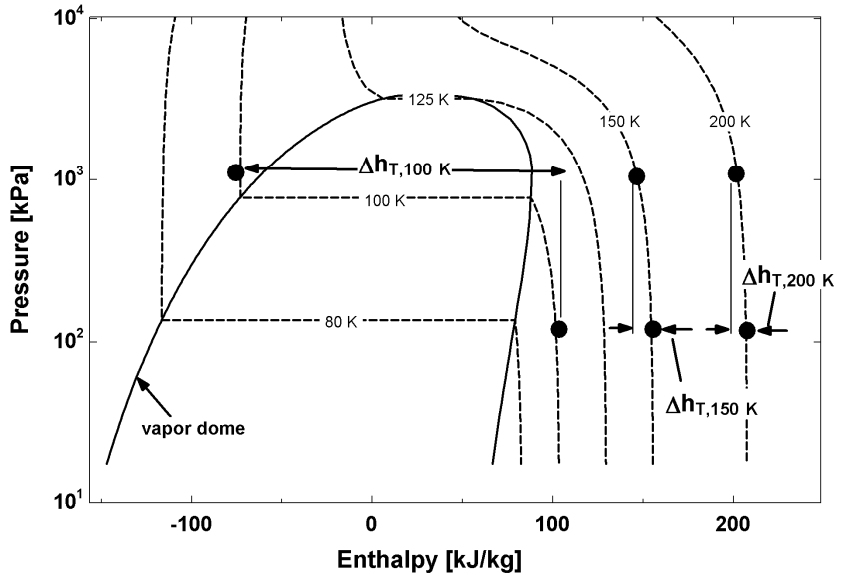

(a)

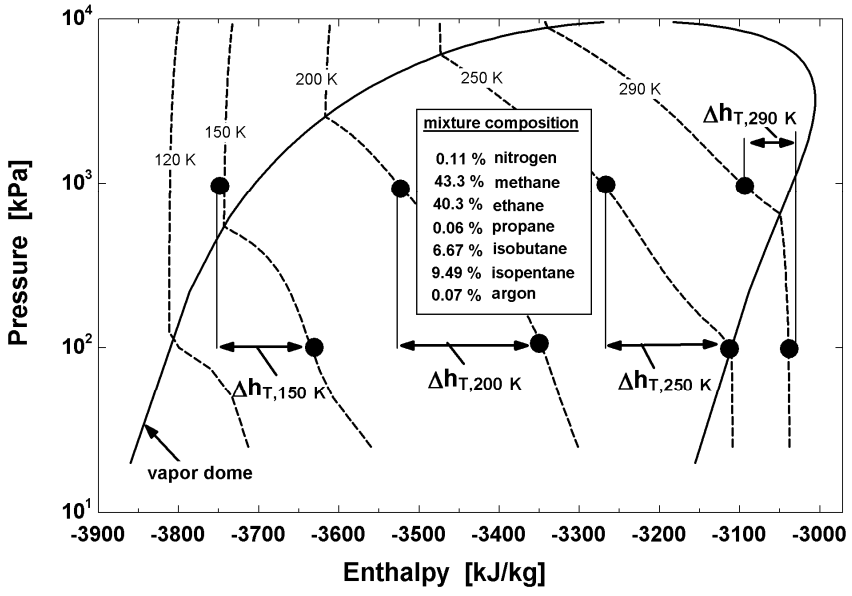

(b)

Figure 1-5: **Pressure-enthalpy chart showing the evaluation of the isothermal enthalpy difference along several isotherms for (a) a single component working fluid, nitrogen and (b) a carefully optimized gas mixture of nitrogen, methane, ethane, propane, isobutene, isopentane, and argon.**

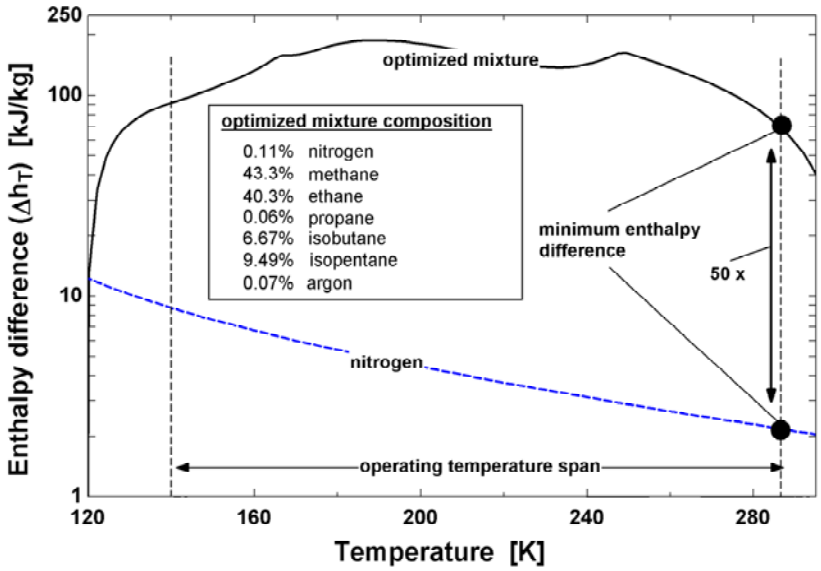

Figure 1-6: Comparison of isothermal enthalpy difference between 1000 to 100 kPa using a single component working fluid, nitrogen, and a carefully optimized mixture of nitrogen, methane, ethane, propane, isobutene, isopentane, and argon. The minimum enthalpy difference for the mixture is 50 times greater.

1.3 MGJT cryoprobe with precooling

The MGJT cycle can be configured to provide even greater refrigeration power using the same physical size of cryoprobe with the addition of a precooling stage. Figure 1-7 shows the physical integration of a conventional Vapor-Compression cycle with the MGJT cryoprobe, and Figure 1-8 provides a cycle schematic of the primary components including numbered thermodynamic states. The VC cycle denoted "1st stage" operates with a single component synthetic refrigerant and precools the high pressure gas mixture in the 2nd stage JT cycle before it enters the recuperator. The probe configuration is otherwise the same as in the single stage system where the MGJT cycle provides refrigeration ($\dot{Q}_{load}$) at the tip at the load temperature, T_7.

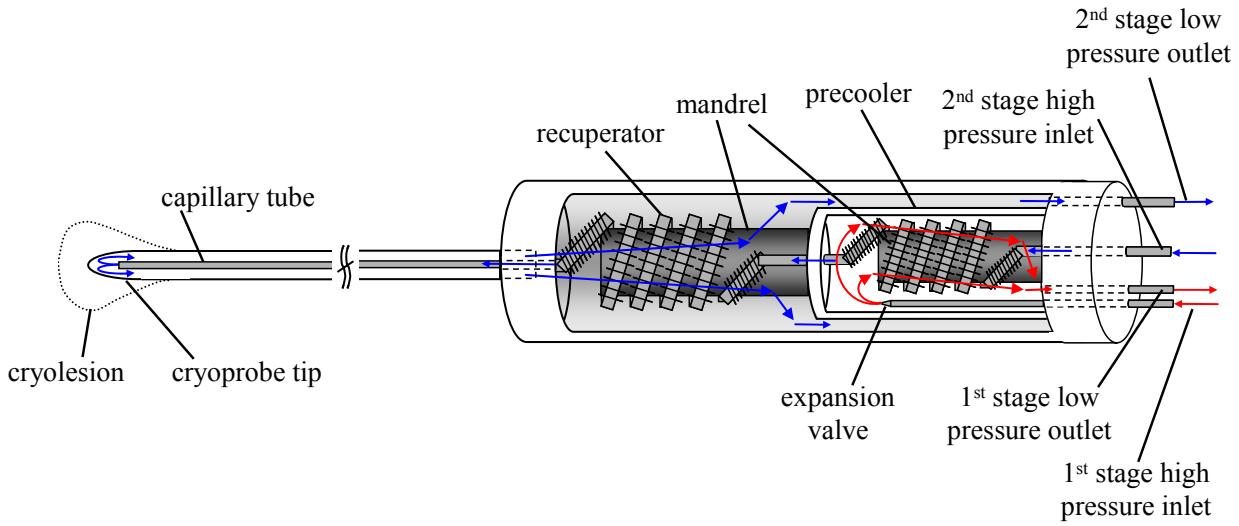

Figure 1-7: Geometric schematic of a 2 stage cryoprobe showing the fluid flow, expansion valves, cryoprobe shaft and coiled fin tube heat exchangers.

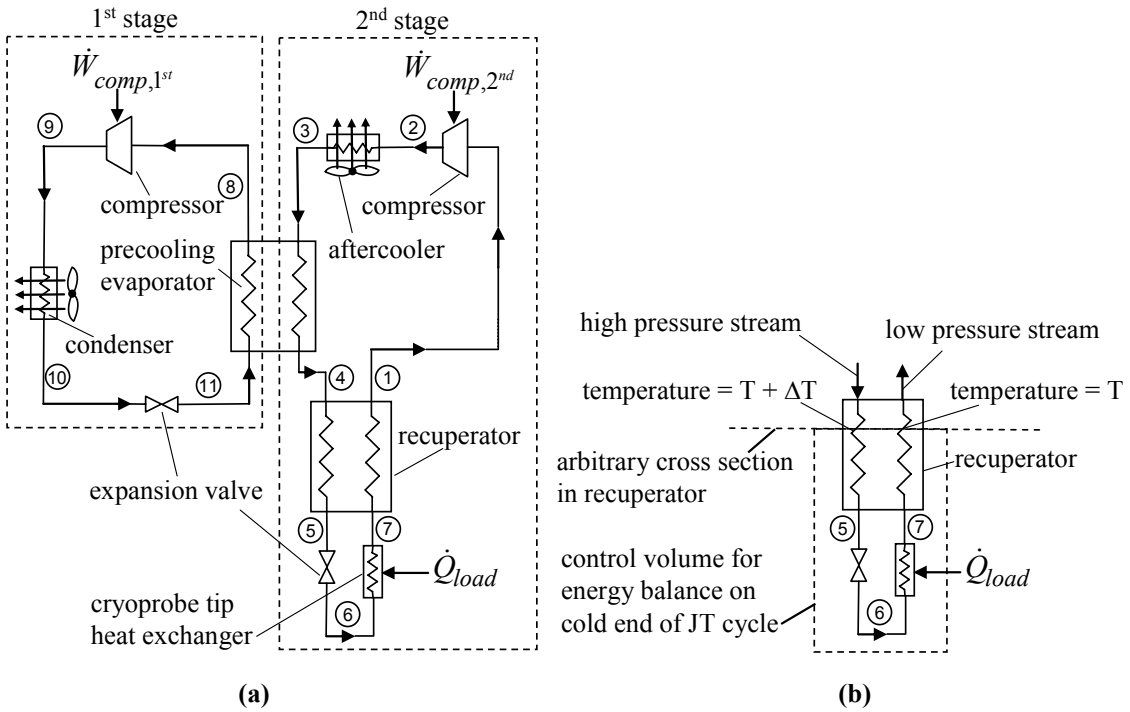

Figure 1-8: a) Schematic of two stage refrigeration cycle showing the thermodynamic states associated with each stage. b) Control volume around cold end of JT cycle which passes through an arbitrary cross section in the recuperator

The refrigeration effect for this cycle is computed using the same technique as described in Section 1.2. An energy balance on the cold end of the 2nd stage of the JT cycle that passes

through an arbitrary location in the recuperator is shown in Figure 1-8(b). The energy balance shows that the refrigeration load is equal to the enthalpy difference between the two streams at any-cross section in the heat exchanger:

$$\dot{Q}_{load} = \dot{m}_{2^{nd}} \left[enthalpy\left(P_{low,2^{nd}}, T, \bar{y}_{2^{nd}} \right) - enthalpy\left(P_{high,2^{nd}}, T + \Delta T, \bar{y}_{2^{nd}} \right) \right] \quad (1.3)$$

where $\dot{m}_{2^{nd}}$ is the mass flow rate in the 2nd stage, $P_{low,2^{nd}}$ and $P_{high,2^{nd}}$ are the suction and discharge pressures associated with the 2nd stage compressor (neglecting pressure loss in the recuperator and precooler), T is the temperature of the low pressure stream, ΔT is the temperature difference between the streams at the cross section, and $\bar{y}_{2^{nd}}$ is a vector of molar concentrations of each component in the 2nd stage fluid mixture. Again, the maximum achievable refrigeration load per unit mass flow rate is computed as the minimum value of the isothermal enthalpy difference over the range of temperature spanned by the recuperator:

$$\frac{\dot{Q}_{load,\max}}{\dot{m}_{2^{nd}}} = \min\left(\left[enthalpy\left(P_{low,2^{nd}}, T, \bar{y}_{2^{nd}} \right) - enthalpy\left(P_{high,2^{nd}}, T, \bar{y}_{2^{nd}} \right) \right] \text{for } T = T_4 \text{ to } T_7 \right) \quad (1.4)$$

The optimized mixture presented in Section 1.2 was capable of providing a substantial amount of refrigeration over a large operating temperature span. However, there is a tradeoff between the maximum cooling power that can be provided and the temperature range that must be spanned by the recuperator. For example, consider two different 7-component mixtures that could be used in the JT cycle where the load temperature is 140 K and the high and low pressures are 1000 kPa and 100 kPa. The composition of mixtures A and B have been optimized to produce the maximum JT effect over two different temperature spans but both mixtures have the same constituents: nitrogen, ethane, methane, propane, isobutane, isopentane,

and argon. The mole fractions of these constituents are listed in Table 1-1. Mixture A is the mixture presented in Section 1.2 which was optimized for a temperature span of 290 K to 140 K. Mixture B is optimized for a smaller temperature span of 238 K to 140 K, which is typical of a JT cycle with some precooling that lowers the recuperator hot inlet temperature to 238 K. Figure 1-9 shows that the maximum cooling effect (i.e., the minimum value of the isothermal enthalpy change) over the temperature span for mixture A is 73 W/(g/s), whereas the maximum cooling effect for mixture B over its temperature span is 115 W/(g/s). Therefore, by reducing the temperature range that must be spanned by the recuperator in a mixed gas JT system, it is possible to select a mixture which achieves a 60% increase in the amount of refrigeration provided at the tip of the cryoprobe.

A cryoprobe must be compact; that is, a surgically useful cryoprobe will provide a large amount of cooling while still being physically small and therefore surgically ergonomic, minimally invasive, and easy to control. Cryosurgical procedures utilizing a single probe with a high tissue freezing capacity (rather than multiple probes used to simultaneously target a tissue mass) can be carried out more quickly and planned with greater precision. In a single stage system, the recuperative heat exchanger is rigidly coupled to the shaft of the cryoprobe as shown in Figure 1-3, and therefore affects the overall cryoprobe size. In the two stage system, both the recuperative and precooling heat exchangers are coupled to the cryoprobe as shown in Figure 1-7. Figure 1-10 illustrates the locations of the two heat exchangers in relation to a photo of the precooled MGJT probe donated by American Medical Systems (AMS) in order to accomplish the research described in this project. The photo shows that the size of the handheld probe is largely determined by the size of the heat exchangers; therefore, the benefit of

precooling must be evaluated based on whether the increase in cooling power outweighs the increase in overall cryoprobe size and the additional complexity associated with the precooling heat exchanger. The size of the heat exchangers is approximately determined by their conductances and so the most appropriate figure of merit for comparing the compactness of different cycles is the ratio of refrigeration load to the total heat exchanger conductance ($\dot{Q}_{load}/UA_{total}$). The conductance of the two stage system includes the recuperator and precooler, the conductance of the single stage system only includes the recuperator.

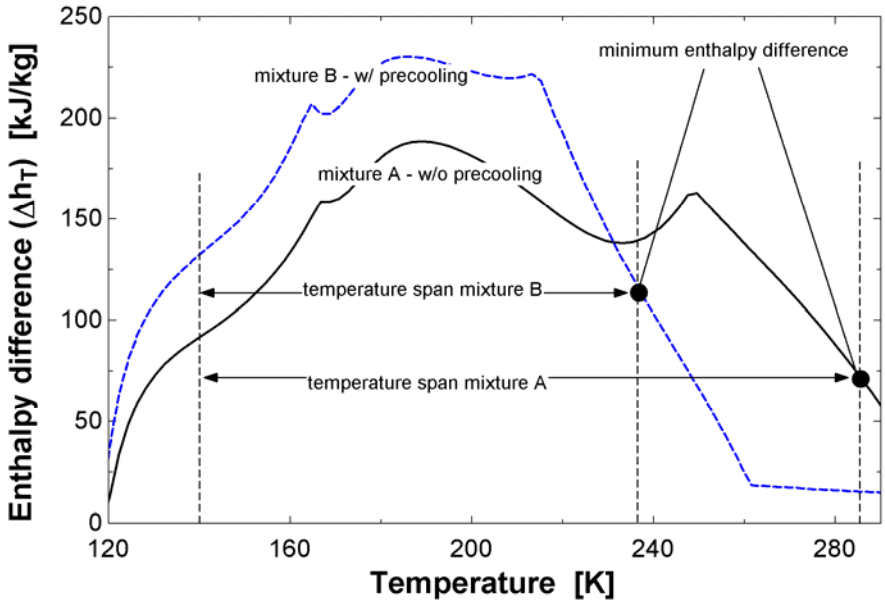

Figure 1-9: **Enthalpy difference of the high (1000 kPa) and low (100 kPa) pressure streams in the recuperator as a function of temperature for two mixtures. The mixtures are optimized to produce the largest cooling effect across two different temperature spans: Mixture A 140 K to 290 K, and Mixture B 140 K to 238 K.**

Table 1-1: Mixture operating temperatures and compositions

	Mixture A	Mixture B
Low Temp	140 K	140 K
High Temp	290 K	238 K
Nitrogen	0.11 %	0.0%
Methane	43.3 %	50.1 %
Ethane	40.3 %	39.3 %
Propane	0.06 %	1.17 %
Isobutane	6.67 %	9.38 %
Isopentane	9.49 %	0.01 %
Argon	0.07 %	0.0 %

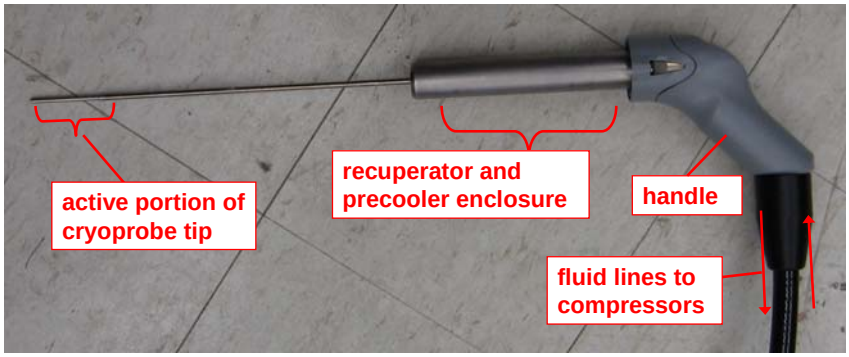

Figure 1-10: Photograph of the cryoprobe showing the locations of the precooling and recuperative heat exchangers, cryoprobe tip, and the fluid lines which couple the cryoprobe to the compressor cabinet.

A model of the precooled MGJT cycle is described in detail in a subsequent section of this document. This model is used to show that, indeed, the precooled MGJT cryoprobe achieves a substantial increase in cooling power without enlarging the cryoprobe. The increased cooling capacity comes with a penalty associated with an increase in compressor size, although, because the compressors are remotely located, an increase in their size can be tolerated (provided that the overall probe system remains portable). These and other cycle design issues are investigated in detail in Section 3.

1.4 Research objectives

The primary objective of this research is to develop an experimentally verified MGJT cryosurgical probe model that can be used to optimize mixture composition and other operating parameters. Current design methodology includes overly simplistic models such as examination of the isothermal enthalpy difference of the working fluid, as described in Section 1.2. These models neglect the impact of the operating conditions, mixture properties, and geometry on the performance of the recuperator, whose performance largely affects the overall cycle performance. The transport processes in the recuperator involve a multi-component and typically two-phase fluid flowing through a complicated geometry; such a flow is characterized by complex behavior. It is inevitable that many optimal mixtures selected by the simplistic model will perform poorly in the system because the optimization model is not capable of predicting the performance of the recuperator and/or the compressor with the selected mixture. The mixture selection process typically relies heavily on experimental tests for the specific system, a process that largely involves trial-and-error and is both costly and time-consuming.

This research seeks to improve the state of the art in modeling methodology by presenting a more complete model that captures the complicated performance of the gas mixtures in the cycle components, most notably the recuperator. These component-level models are experimentally tuned and verified; the pieces are linked together to form a complete system model capable of selecting mixtures that simultaneously address multiple design criteria such as refrigeration capacity, cryoprobe size, compressor pressure ratio, etc. This model is semi-empirical, but largely physics-based and therefore readily modified to optimize MGJT probes with varied refrigeration requirements or geometry design envelopes. Even the best models fail to predict behavior exactly, and the design process inevitably involves some experimental tests

to ensure that the system is operating at maximum performance. However, the use of a higher accuracy model will substantially reduce the number of tests required to find an optimal mixture. By establishing stricter criteria for mixture selection based on *a priori* performance predictions, many more mixtures can be eliminated from the selection pool, and the designer can more rapidly converge on a suitable composition.

The development and verification of this model involves several tasks which are outlined below:

Develop initial numerical MGJT cryoprobe model

The first task is to develop a model of the precooled MGJT cryoprobe that captures the fundamental thermodynamic and heat transfer processes in the cycle. The model described in detail in Section 3 computes all of the cycle thermodynamic states and can compute the refrigeration power for a given mixture using a few key assumptions about the operation pressures, flow rates, tip temperature, and the recuperator and precooler pinch point temperatures. Numerical models of the heat exchangers were created to accommodate the temperature variant specific heat of the mixtures; the models divide the heat exchangers into small sections over which the temperature variations are small and the effectiveness-NTU relationship can be accurately applied (Nellis 2003). The equations governing the cycle are computed using the Engineering Equation Solver (EES) (Klein 2009), which is integrated with the SUPERTRAPP or NIST4 database (Ely 1992, Klein 2008) to compute mixture properties. Mixture selection is carried out through an optimization process which utilizes a genetic algorithm developed by (Charbonneau 2007).

This model is used to investigate design issues related to the development of a minimally invasive and high capacity cryoprobe. Specifically, the model is used to select optimal mixtures that maximize the cryoprobe compactness target, $\dot{Q}_{load} / UA_{total}$. The benefit of the added precooling stage is quantified using the model by comparing the compactness of a multi-stage probe to that of a single state cryoprobe constrained to have the same physical size and operating conditions. The penalty of increased compressor size associated with the precooled system is also quantified using the model. These quantitative metrics demonstrate that the model represent a powerful design tool that enables the precise balancing of maximum refrigeration power with secondary design parameters related to compressor size and portability.

Additionally, the model was invaluable during the development of the experimental test facility; a full uncertainty analysis guided the selection of the location and precision of the measurement instrumentation. An *a priori* investigation of the cycle using the model identified salient design issues and subsequently provided direction for the experimental tests.

Design and construct the experimental test facility

The experimental test facility, described in detail in Section 4, includes a commercially available cryoprobe (energized by a precooled MGJT cycle) that has been modified to integrate measurement instrumentation. The measurements in the experiment provide, to our knowledge, an unprecedented insight into heat transfer and pressure drop performance of components operating within a compact MGJT cycle; the test facility has the added benefit of the components operating as part of cycle where the impact of individual components on overall system performance can be observed. Data collected using the facility are used for tuning and verifying the accuracy of the component and system level models presented in Chapter 6.

The modifications enable more detailed measurements than those otherwise available with the cryoprobe. For example, Figure 1-10 highlights the tip of the cryoprobe, which encloses the expansion valve and is the active section of the probe (i.e., the cold section used to form the cryolesion). The thermodynamic states at locations before and after the expansion valve, as well as at a location downstream of the refrigeration load are critical to understanding the system performance. However, the unmodified probe configuration does not allow for measurement of the temperature and pressure at these states. The modifications to the test facility enable direct measurements at these and other locations and therefore allow the resolution of the cycle thermodynamic states.

The cold components of the experimental test facility are integrated with a vacuum insulated chamber and covered with Multi-Layer radiation Insulation (MLI) to minimize parasitic heat leak. Figure 1-11 shows a schematic of the experimental test facility including the locations of the measurement instrumentation relative to the cycle as well as the vacuum test facility space. The integration of the cryoprobe with the vacuum test facility requires a significant effort. The fluid pathways, pressure taps, and electric sensor and heater wires must pass through the vacuum barrier in a manner that does not disturb the quality of the vacuum. Sensor locations were carefully selected to minimize the instrumentation within the vacuum space in order to reduce the complexity of the integration with the vacuum system. It was determined that the mass flow measurements and many of the pressure and temperature measurements could be taken outside the vacuum space without compromising the accuracy of the system characterization; this is reflected in the sensor locations shown in Figure 1-11.

Temperature and pressure measurements at various points in the system are used to identify key thermodynamics states that parallel the thermodynamic states defined using the model. Pressure measurements are denoted in the figure as with "P# where the # corresponds to the thermodynamic state. Temperature measurements including Platinum Resistance Thermometers and ThermoCouples are similarly denoted as "PRT#" and "TC#". Additional temperature measurements within the low pressure side of the recuperator denoted "PRTi" quantify the temperature profile, the pinch point temperature and location, and can be used to determine the spatially resolved conductance. Mass flow measurements are shown as $\dot{m}_{1^{st}}$ and $\dot{m}_{2^{nd}}$ for the 1st and 2nd stages and are used to calculate work and heat transfer rates. The heater used to simulate the biological thermal load is labeled by its voltage and current measurements, V_{load} and I_{load}. The figure also shows the interchangeable jewel orifice and bypass valve on the 2nd stage compressor which are used to independently regulate pressure drop and mass flow in the cycle to within the limits of the compressor capability. A bypass valve on the 1st stage compressor is used to regulate mass flow and therefore alter the cooling provided by the precooling cycle. Finally, a gas chromatograph measures the circulating mixture in the 2nd stage by sampling before the low pressure inlet of the compressor. The construction of the test facility is shown in Section 4.3 including a step-by-step procedure for the cryoprobe modification with detailed, dimensioned drawings.

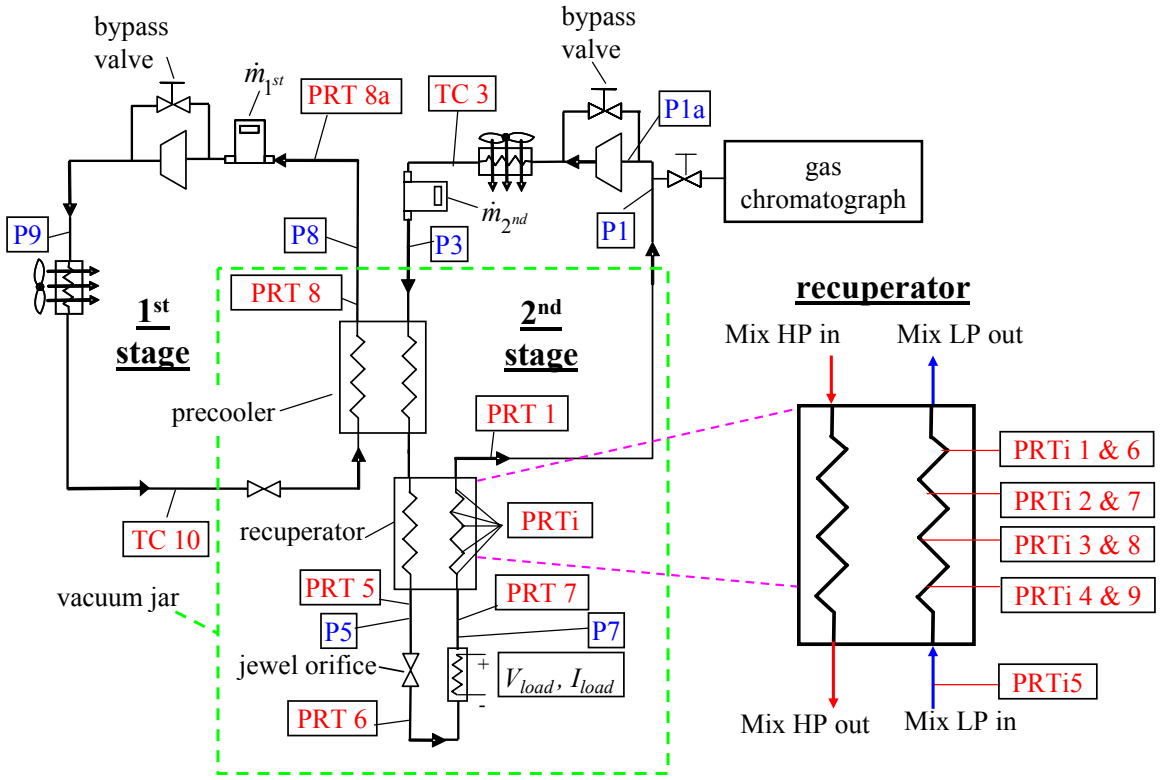

Figure 1-11: Schematic of experimental test facility including measurement instrumentation integrated with the MGJT cryoprobe system.

Experimental tests and data reduction

The first experimental tests for this project included a characterization of the cryoprobe performance in its original manufactured configuration (i.e. before any of the modifications described in Chapter 4 were carried out, and using the original proprietary mixture). These tests serve as a benchmark for the experimental test facility by providing a reference to (1) measure the refrigeration performance penalty introduced by the cryoprobe modifications, and (2) compare the refrigeration performance with the new mixtures tested in the modified cryoprobe.

The primary objectives of the experimental tests using the modified cryoprobe are to develop empirical but physics-based corrections/improvements to the model presented in Chapter 3, as well as to evaluate capabilities of this new model. This objective is achieved

using a series of experiments described in this Chapter 5, including 198 steady state operating conditions over a range of mixture compositions, pressures, temperatures and mass flows. The experimental data are used to:

1. Compare the property data from the NIST4 and REFPROP databases and show why the REFPROP are used to compute the cycle performance.
2. Compute all the thermodynamic state points relevant to cycle performance
3. Infer the performance of the overall system (i.e. refrigeration power), as well as individual components (most notably the recuperator, whose performance largely determines the refrigeration capacity of the probe).
4. Correlate the pressure drop on the high and low pressure sides of the recuperator to the flow velocities
5. Develop a model for the precooler to predict the conductance or pinch point temperature difference.
6. Create an empirical recuperator model capable of predicting the heat transfer across liquid, vapor, and two-phase flow regimes for mixtures.

Model verification and use as design tool

The predictive correlations for the cycle components are formed based on the thermodynamic analysis of the data; these correlations are validated by demonstrating the ability of the model to predict recuperator/precooler effectiveness and overall cycle refrigeration. Figure 1-12 compares the measured and predicted refrigeration capacity for the data presented in this thesis. The prediction for tests where the experimental heat input is less than 15 W is excellent – these include the tests with the pure refrigerants, and a number of tests with mixtures. The empirically tuned model predicts poor performance with mixtures that other, simpler models (isothermal enthalpy difference and pinch point models, discussed in proceeding paragraph) do not properly discount because of large pressure drop or poor heat transfer. As the heat input increases (>15 W), the agreement between the empirical model and the experiments tends to deviate as the model underpredicts the refrigeration capacity; these points unfortunately

include many of the tests that outperformed the original mixture. Differences between the experimentally measured and predicted refrigeration powers are primarily attributed to component-level modeling errors for the precooler conductance in the two-phase regime, and in the recuperator conductance in the lower quality regions (0 to 0.2). More details about these issues and suggestions for improvements are presented in Chapter 6 and 7.

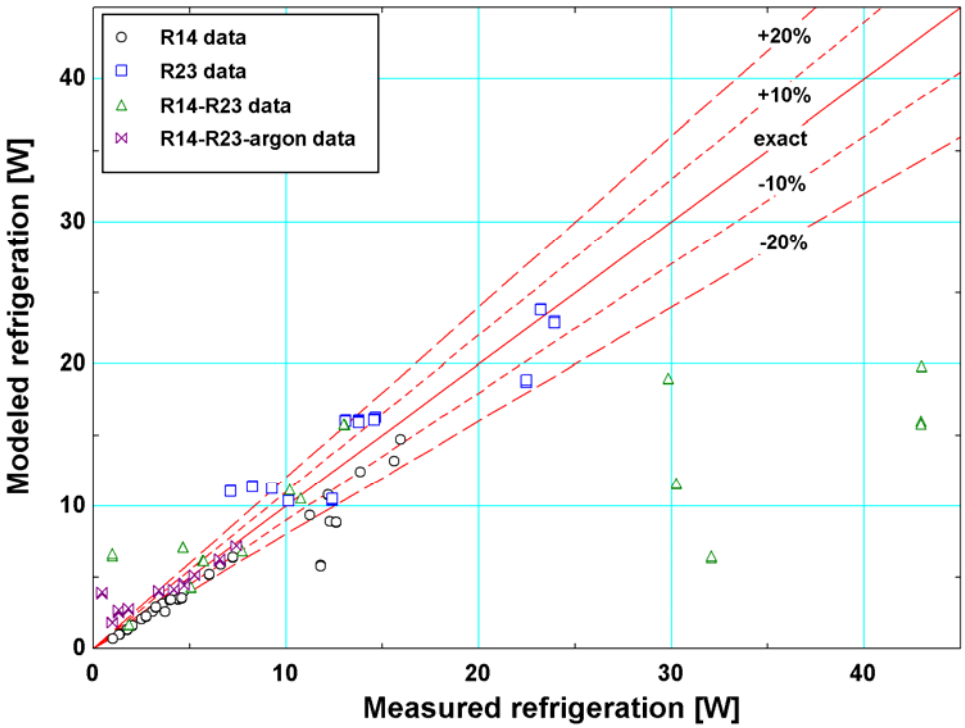

Figure 1-12: Measured refrigeration power compared to the refrigeration predicted using the empirically tuned model.

The use of the verified model as a design tool was demonstrated by identifying the optimal composition at various load temperatures for a binary mixture of R14 and R23 in 2nd stage cycle. This optimal composition is compared to those selected using two simpler models that optimize the mixture composition according to the isothermal enthalpy difference as discussed in Section 1.2 and 1.3, and the cycle $\dot{Q}_{load}/UA_{total}$ based on the component-level, pinch point model developed in Chapter 3. Figure 1-13 compares the optimal mixture compositions for the

R14-R23 binary predicted using the empirical model with (a) the isothermal enthalpy difference model and (b) the pinch point model from Chapter 3. The isothermal enthalpy difference model tends to overpredict the refrigeration power and both models yield optimal compositions that differ from the more detailed empirically tuned model by as much as 6-32%. Note that the refrigeration effect for the cycle can be significantly increased by adding constituents (optimal number is between 5-7 as reported in (Maytal 2006)), and a final design of the probe should leverage the additional refrigeration available with more components. These mixtures exhibit more complicated vapor dome structures and temperature-capacity relationships, so the differences in optimal composition related to inclusion of pressure drop and heat transfer in the empirical model are expected to become even more pronounced.

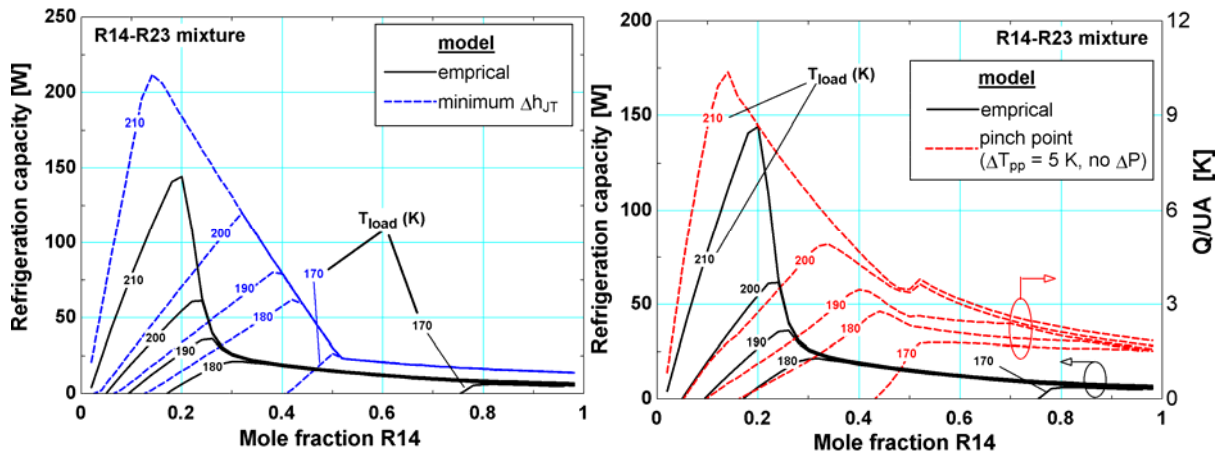

Figure 1-13: Cryoprobe refrigeration predicted by the empirically tuned model for a binary mixture as a function of mole fraction of R14. The results are compared to the (a) refrigeration predicted by the isothermal enthalpy difference model and (b) the cryoprobe compactness target (Q/UA) for the pinch point model.

Experience with the cryoprobe manufactuer has shown that the iceball size is the ultimate standard used to judge the medical effectiveness of the instrument. Developing a model to select gas mixtures that optimize the refrigeration performance of the MGJT cycle at a given

load temperature is a major component of the design process to maximize the iceball size produced by the cryosurgical probe. However, this model does not represent a complete design tool as the optimal tip temperature must still be determined. The mixture optimization model must be combined with a heat transfer analysis of the cryolesion (iceball) formation that considers: (1) the geometry of the active portion of the cryoprobe tip in contact with the tissue, (2) the thermal storage, phase change and heat transport properties of the tissue, and (3) the heat transfer from biological processes related to metabolic generation and blood perfusion (Fredrikson 2006). This heat transfer analysis establishes important design benchmarks including the optimal cryoprobe tip temperature, and the refrigeration capacity required to achieve a certain cryolesion size.

Chapter 6 illustrates the design process for a binary R23-R14 mixture that includes consideration of the iceball formation to achieve the maximum iceball size for a given probe or, a specified iceball size using the smallest possible heat exchanger. Figure 1-14(a) shows the process of selecting the proper operating point along the "best mixture locus", representing the optimal cryoprobe refrigeration available at each load temperature. The intersection of the best mixture locus and the iceball refrigeration curve represents the best operating point for a particular probe and the corresponding iceball size can be inferred from the "iceball radius" curve on the right axis (Fredrikson 2004, 2006). A more flexible design environment where the precooler/recuperator heat exchanger tube lengths could be adjusted to achieve a specified iceball size was also investigated. In the example considered in Figure 1-14(b), the specified iceball size was assumed to require 40 W of refrigeration, and the recuperator pinch point temperature and mole fraction R14 are selected to achieve the minimum tube length. The tip

temperature on the chart would be selected to match the 40 W refrigeration load point from the iceball refrigeration load curve (i.e. 192 K in Figure 1-14(a)).

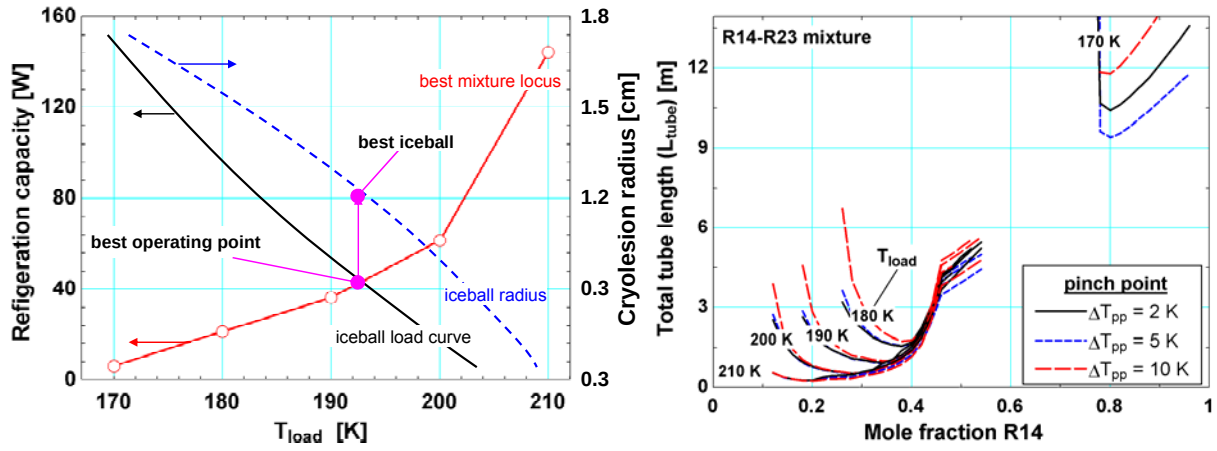

Figure 1-14: Mixture optimization considering the cryoprobe refrigeration power and the iceball formation characteristics. (a) The cryoprobe geometry is fixed and the mixture is selected to yield the largest iceball. (b) An iceball size is specified and the overall tube length to achieve the required refrigeration effect is minimized.

1.5 Outline

The purpose of the remainder of this document is to show, in detail, the process that was used to develop the experimentally tuned cryoprobe model. Chapter 0 reviews previous work available in the literature related to cryosurgical probes, and shows how this research improves the state of the art in MGJT cryoprobe modeling. While the modeling efforts and data collection are presented here specifically for a MGJT cryoprobe, the configuration is not unlike that of other cryogenic cooling applications, and so the research is also placed in the more broad context of MGJT cycle design. Chapter 3 presents the details of the mixture optimization model and summarizes the key design issues identified by the model. Chapter 4 discusses the experimental design process including the locations and purpose of the measurement instrumentation, a full uncertainty analysis to ensure adequate fidelity of the cryoprobe characterization, and detailed drawings and photographs of the experimental test facility and

modified cryoprobe. Chapter 5 discusses the design of experiments and presents the data collected in the test facility. Chapter 6 shows how the experimental data were used to empirically tune heat exchanger and overall system models, and presents an evaluation of the predictive capabilties of these models. Finally, Chapter 7 discusses conclusions and recommendations for future work on this project.

1.6 References

Arnott, J. "On the Treatment of Cancer by the Regulated Application of an Anaesthetic Temperature". London: Churchill 1851

Brodyansky, V. M.; Gresin, A. K.; Gromov, E. M.; Yagoden, V. M.; Nicolsky, V. A.; Alpheev, V. N. "The Use of Mixtures as the working Gas in Throttle Joule Thomson Cryogen Refrigerators". *Proceedings of the 13th International Congress of Refrigeration, Washington, D.C. Progress in Refrigeration Science and Technology* 1971, vol. 1, 43.

Charbonneau, P. Version 1.2 2002, PIKAIA Homepage. http://www.hao.ucar.edu/Public/models/pikaia/pikaia.html (accessed 11/3, 2007).

Cooper, I. S.; Lee, A. S. "Cryostatic Congelation: a system for producing a limited, controlled region of cooling or freezing of biologic tissues". *J Nerv. Ment. Dis.* 1961, vol. 133, 259.

Ely, J. F.; Huber, M. L. NIST Thermophysical Properties of Hydrocarbon Mixtures Database (SUPERTRAPP). 1992, 3.2.

Fredrikson, K. 2004. Optimization of Cryosurgical Probes for Cancer Treatment. M.S. thesis. Madison, WI USA: University of Wisconsin - Madison, Mechanical Engineering Dept.

Fredrikson, K.; Nellis, G.; Klein, S. A. "A Design Method for Cryosurgical Probes". *International Journal of Refrigeration* 2006, vol. 29, 700-715

Klein, S. A. EES - Engineering Equation Solver. 2009, 8.401, f-Chart Software, www.fchart.com

Klein, S.A., EES-NIST4 interface routine, f-Chart Software, www.fchart.com, 2008

Maytal, B., Nellis, G. F., Klein, S. A., Pfotenhauer, J. M.; "Elevated-pressure mixed-coolants Joule–Thomson cryocooling". *Cryogenics* 2006, 46, 55-67.

Nellis, G. F. "A heat exchanger model that includes axial conduction, parasitic heat loads, and property variations". *Cryogenics*, 2003, 43, 523-538.

Rubinsky, B. CRYOSURGERY. *Annu. Rev. Biomed.* Eng. 2000,vol. 2, 157-187.

Zhong-Shan D.; Liu, Jing., "Numerical Study of the Effects of Large Blood Vessels on Three-Dimensional Tissue Temperature Profiles During Cryosurgery", Numerical Heat Transfer, Part A: Applications, Vol 49, issue 1, pp 47-67.

2 Literature Review

2.1 Physiological and heat transfer processes during cryosurgery

Cell death during cryosurgery is caused via a number of biological processes including: (1) chemical destruction caused by high ion concentrations, (2) the cell cytoskeleton is weakened at lower temperatures and susceptible to mechanical damage caused by neighboring ice crystals and (3) restriction of vascular processes (Rubinsky 2000).

The temperature required for cell death depends on the specific structure of each organ, as well as the cooling rate and duration. Smith et al. (Smith 1974) showed cell death in rat livers below –15 °C. An in vivo study of rat livers (Popken 2000) showed that tumors would not recur in cells that reached –38 °C or lower. Rubinsky et al. (2000) and others have shown that cell death is dependant on cooling rate. Leibo et al. (1971) demonstrated that cell death as a function of cooling rate is a U-shaped function, where there is a cooling rate that corresponds to a distinct cell death minimum.

It is difficult to monitor and control the cooling rates of all cells in the cryolesion during a cryosurgical process. Therefore, it is desirable to decouple the cell death from cooling rate. If the cell temperature reaches below some critical temperature, cell death occurs regardless of cooling rate (Kim 2007). Bischof et al. (1997) demonstrated that, regardless of cooling rate, prostate cells will die below –40 °C. Therefore if the lethal zone is considered to extend from the cryoprobe to the region where the temperature is near this critical temperature, then cell death can be assumed with a high degree of confidence regardless of cooling rate. The procedure is simplified and the resulting precision of the lethal zone reduces recurrence rates. It is therefore advantageous to design cryoprobes that achieve an ice ball with a large volume of

tissue that is exposed to temperatures below the critical level. The MGJT cryoprobe mixture optimization presented in this report can be combined with the cryoprobe design process discussed in Fredrikson (2004, 2006) in order to select mixtures that maximize the region of tissue cooled to below the critical temperature.

2.2 Motivation for improved cryosurgical probe design

Freezing large tissue metastases requires a considerable effort. Multiple probes are simultaneously inserted into the body for extended periods of time; each additional probe adds complexity to the surgical process associated with positioning and monitoring the growth of the cryolesion. Extensive pre-operative planning of cryoprobe locations is also required to ensure complete metastasis destruction and often involves complex computational algorithms (Rossi 2008, for example). Additionally, cell death often is enhanced using chemical adjuvants (Rubinsky 2000), which raise the critical temperature required for cell necrosis. Based on these observations, it is clear that the refrigeration cycles underlying the current state-of-the-art cryosurgical probes are underpowered; the research presented here therefore seeks to increase the cooling capacity of the probes in order to reduce the complexity, and subsequently reduce the invasiveness of the procedure.

2.3 MGJT cycles

2.3.1 Early developments in MGJT cycles

Radebaugh (1997) presents a brief history of the early developments in MGJT cycles. The Kleemenko cycle developed in the late 1950's (Kleemenko, 1959) was one of the earliest mixed gas refrigeration cycles. This cycle uses phase separation to divide the system into several low and high temperature cooling loops, where the low pressure stream of each loop cools the high

pressure stream of the next lowest temperature loop, and the final loop provides the refrigeration lift. Fuderer and Andrija (1969), as well as Alfeev et al. (1973) are credited with early MGJT cycles involving a single cooling loop utilizing a high-efficiency recuperative heat exchanger.

2.3.2 MGJT cycle experimental studies

Over the past few decades many experimental studies have measured the overall performance of MGJT cycles in a variety of configurations using different mixture compositions. Arkhipov et al. (1998) present performance measurements for a system that is operated with several nitrogen-hydrocarbon mixtures at temperatures near 80-85 K. They additionally demonstrate that cooling at lower temperatures (65-70 K) can be achieved by adding neon to the mixture. Alexeev et al. (1996) present a theoretical and experimental investigation showing increased performance for mixtures that include higher concentrations of high boiling constituents (i.e., components that are saturated near ambient temperature at the high pressure in the cycle). Lou et al. (1998) compare the pressure drop and heat transfer performance of perforated plate and Hampson recuperative heat exchangers. Alexeev et al. (1999) discuss the 50-100% increase in cooling capacity that can be achieved through the addition of a precooling stage. In Khatri et al. (1997), the pressure drop and recuperator warm end temperature difference (which can be used to quantify the conductance) are reported for several different types of MGJT cycles operating between 70 K and 150 K using mixtures of helium, argon, nitrogen, and various hydrocarbons. Naer et al. (2002) discuss design rules for selecting refrigerants, which dictate that (1) the boiling temperature of the basic component at the pressure of the low-pressure stream should be close to the design refrigerating temperature, and (2) all the additional substances should have higher critical temperatures and Joule-

Thomson effect than the base substance. They additionally point out that the mixture composition will change due to preferential solubility of hydrocarbons in the compressor oil. Finally, the study presents performance data for a MGJT cycle with a mixture of 74.5% isobutane, 21% ethane, and 4.5% methane. Gong et al. (2000) discuss an optimization technique for mixtures used in small JT cycles integrated with cryoprobes and present data with two mixtures whose constituents were selected using the optimization model.

Unfortunately, the data in the experiments described above are of limited use for the design of MGJT cycles. Most of the studies measure only the suction and discharge pressure of the compressor, the load temperature, the refrigeration load, and the cooldown time. These measurements are relatively easy to make and are generally useful for matching coolers to appropriate applications. However, they are not sufficiently resolved and therefore do not provide the detailed information required to develop correlations for computing the pressure drop and heat transfer performance in the various cycle components. Additionally, with the exception of (Gong, 2000), the mixture compositions are not given; without the composition the thermodynamic property data required to develop empirically-based modeling strategies cannot be computed.

Several studies have directly compared a mixture optimization process with experimental data. These studies again do not publish the mixture compositions and therefore are of limited quantitative value; however, they are generally useful for understanding the limitations of some simplistic MGJT system models. Boiarski et al. (2000) compute idealized MGJT cycle performance with an optimization model and show the how the exergetic efficiency of the cycle changes with various mixtures and operating conditions. A comparative study shows adequate

prediction of the load curve of the system. An additional study by Boiarski et al (2001) compares analytic and experimental performance of single stage and multi-stage cycles (such as the one developed by Kleemenko). One of the more relevant studies to this research project is a third study by Boiarski et al. (1999). A design methodology based on ideal performance of the MGJT cycle with simple empirical corrections to the recuperator and compressor performance is discussed in detail. Experimental data are integrated with a recuperator heat transfer model that accounts for two-phase flow using a homogeneous hydrodynamic flow structure. Pressure drop in the recuperator is "selected from design experience". The authors demonstrate that the recuperator model adequately predicts the heat transfer performance over a range of mass flows. Additionally, the overall system model was shown to accurately predict load curve performance.

There is a clear lack of either theoretical or experimental studies on the performance of MGJT cycles in which the data is highly resolved and the mixture compositions are publicly available. In this project, a detailed set of experimental measurements will be recorded over a wide range of operating conditions and mixture compositions; these data will be used to tune and verify the mixture optimization model. The model and the experimental results will be published in a final thesis for this project as well as various relevant cryogenics, refrigeration, and heat transfer journals.

2.3.3 Recent MGJT Optimization models

An optimized mixture for a cryosurgical system will provide a large JT cooling effect but require a relatively small system of heat exchangers in the cryoprobe. The relationship between mixture composition and JT effect is a function of the complex mixture equation of state. Additionally, the heat exchanger size that is required depends strongly on the specific heat

capacity of the mixture, which varies substantially as a function of temperature, pressure, and mixture composition. Therefore, for the two-stage MGJT system presented in Section 1.4, it is not possible to analytically or intuitively select: (1) a 2^{nd} stage mixture, (2) a precooling temperature, and (3) recuperator and precooling evaporator pinch point temperatures for the two stage system that yield an optimum ratio of cooling power to heat exchanger size, as well as a system with a practical compressor sizes. Little (1997), Alexeev (1997), and Gong (2000) each describe methods for selecting a mixture that yield the largest cooling effect. However these optimization methods do not account for the required heat exchanger size. Keppler et al. (2004) and Maytal et al. (2006) demonstrated that a cryoprobe that uses a mixture optimized for maximum cooling (or maximum efficiency) may be more than twice the size of a cryoprobe using a mixture that is optimized for cooling per heat exchanger size. Therefore, a numerical optimization technique described in Appendix A is used to design an optimized cryosurgical probe that achieves the maximum cooling per heat exchanger size.

2.4 MGJT cycles for cryosurgical probes

This work is partially based on a model previously developed at the University of Wisconsin at Madison, which evaluated optimum gas mixtures for a single stage JT cryosurgical system (Keppler et al., 2004). This initial work has been verified and used to optimize the design of a single-stage system for cryosurgery (Fredrikson, 2006). This project utilizes the same modeling methodology but expands the approach to the two stage cycle (i.e. the MGJT cycle with precooling shown in Figure 1-8); to our knowledge, the theoretical optimization of a two stage MGJT system for cryosurgery has not previously been reported.

2.5 References

Arkhipov, V. T.; Yakuba, V. V.; Lobko M.P.; Yevdokimova O.V. "Multicomponent Gas Mixtures for J-T Cryocoolers". *Cryocoolers 10: 1998 International Cryocooler Conference* 1998, 487-495.

Alexeev, A, Quack, H., Haberstroh, Ch.; "Low Cost Mixture Joule Thomson Refrigerator", Proceedings of the 16th ICEC/ICMC Proceedings, pp 395-398, 1996.

Alexeev, A, Haberstroh, Ch., Quack, H.; "Mixed Gas J-T Cryocooler with precooling stage", Cryocoolers 10, 1999, pp 475-479

Alexeev, A.; Haberstroh, C.; Quack, H. Further Development of a Mixed Gas Joule Thomson Refrigerator. in *Advances in Cryogenic Engineering: Proceedings of the 1997 Cryogenic Engineering Conference 1997*, vol 43, 1667-1674.

Alfeev, V.N., Brodyanski, V.M., Yagodin, V.A. Nikolsky, Ivanstov, A.V., "Refrigerant for a cryogenic throttling unit, UK Patent 1,336,892 (1973).

Bischof, J. C., N. Merry and J. Hulbert. 1997. "Rectal protection during prostate cryosurgery: design and characterization of an insulating probe". *Cryobiology* 34(1): 80-92.

Boiarski, M., Khatri, A., Podcherniaev, O.; "Enhanced Refrigeration Performance of the Throttle-Cycle Coolers Operating with Mixed Refrigerants", *Advances in Cryogenic Engineering*, Vol 45, 2000, pp. 291-297

Boiarski, M., Khatri, A., Podcherniaev, O., Kovalenko, V., "Modern Trends in Designing Small-Scale Throttle-Cycle Coolers Operating with Mixed Refrigerants", Cryocoolers 11, 2001, pp. 513-521

Boiarski, M., Khatri, A., Kovalenko, V.; "Design Optimization of the Throttle-Cycle cooler with Mixed Refrigerant", Cryocoolers 10, 1999, pp. 457-465

Fredrikson, K. 2004. Optimization of Cryosurgical Probes for Cancer Treatment. M.S. thesis. Madison, WI USA: University of Wisconsin - Madison, Mechanical Engineering Dept.

Fredrikson, K.; Nellis, G.; Klein, S. A. "A Design Method for Cryosurgical Probes". *International Journal of Refrigeration* 2006, vol. 29, 700-715.

Fuderer and Andrija , Verfahren zur Tefkuhlung, German Patent 1426956 (1969).

Gong, M., Ercang, L., Zhou, Yuan, "Research on a Mixed-Refrigerant J-T Refrigerator Used for Cryosurgery", Proceedings of the Eighteenth International Cryogenic Engineering Conference (ICEC 18), Mumbai, India, 2000, pp 571 – 574.

Gong, M. Q.; Luo, E. C.; Zhou, Y.; Liang, J. T.; Zhang, L. "Optimum composition calculation for multicomponent cryogenic mixture used in Joule-Thomson refrigerators". *Advances in Cryogenic Engineering* 2000, 45, 283.

Keppler, F.; Nellis, G.; Klein, S. A. "Optimization of the Composition of a Gas Mixture in a Joule-Thomson cycle". *HVAC&R Research* 2004, vol. 10, 213-230.

Khatri, A, and Boiarski, M.; "A Throttle Cycle Cryocooler Operating with Mixed Gas Refrigerants in 70 K to 120 K Temperature range", Cryocoolers 9, 1997, pp. 515-520

Kim, C., A. P. O'Rourke, D. M. Mahvi and J. G. Webster. 2007. "Finite-element analysis of ex vivo and in vivo hepatic Cryoablation*". IEEE Trans. Biomed. Eng.* 54(7): 1177-1185.

Kleemenko, A.P., "One flow cascade cycle (in schemes of natural gas liquefaction and separation)", 10th Int'l Congress of Refrigeration (1959), Pergamon Press, London, p. 34.

Leibo, S. P.; Mazur, P. "The role of cooling rates in low-temperature preservation", *Cryobiology* 1971, 8, 447-452.

Little, W. A. 1997. *Method for Efficient Counter-Current Heat Exchange Using Optimized Mixtures*. Patent No. 5664502 .

Lou, E.C., Gong M.Q., Zhou, Y., "Experimental Investigation of a Mixed-refrigerant Joule-Thomson Cryocooler in the 70K to 100K Temperature Range", Proceedings of ICCR '98, Hangzhou, China, 1998, pp. 393-396

Maytal, B., Nellis, G. F., Klein, S. A., Pfotenhauer, J. M.; "Elevated-pressure mixed-coolants Joule–Thomson cryocooling". *Cryogenics* 2006, 46, 55-67.

Naer, V.; Rozhentsev, A. "Application of hydrocarbon mixtures in small refrigerating and cryogenic machines". *Int. J. Refrig.* 2002, 25, 836-847.

Popken, F., J. K. Seifert, R. Engelmann, P. Dutkowski, F. Nassir and T. Junginger. 2000. "Comparison of iceball diameter and temperature distribution achieved with 3-mm Accuprobe cryoprobes in porcine and human liver tissue and human colorectal liver metastases in vitro". *Cryobiology* 40(4): 302-10.

Rossi, M. R.; Tanaka, D.; Shimada, K.; Rabin, Y. "Computerized planning of cryosurgery using bubble packing: An experimental validation on a phantom material". *International Journal of Heat and Mass Transfer,* 2008, 51, 5671-5678.

Rubinsky, B. CRYOSURGERY. *Annu. Rev. Biomed. Eng.* 2000,vol. 2, 157-187.

Smith, J. J. and J. Fraser. 1974. "An estimation of tissue damage and thermal history in the cryolesion". *Cryobiology* 11(2): 139-147.

Radebaugh, R. “Advances in Cryocoolers”, *In Advances in cryocoolers;* Proceedings of 16th International Cryogenic Engineering Conference and International Cryogenic Materials Conference; Elsevier: Kitakyushu, Japan, 1997; Vol. 1, pp 33-44.

3 MGJT Cryoprobe Optimization Model

The purpose of the thermodynamic model presented here is to investigate cycle design issues; for example, the model will allow the determination of the optimal mixture compositions for the 2nd stage JT cycle as well as the appropriate amount of precooling. This work is partially based on a model previously developed at the University of Wisconsin at Madison, which evaluated optimum gas mixtures for a single stage JT cryosurgical system (Keppler et al., 2004). This initial work has been verified and used to optimize the design of a single-stage system for cryosurgery (Fredrikson 2006). This model utilizes the same methodology but expands the approach to the two stage cycle shown in Figure 3-1; to our knowledge, the theoretical optimization of a two stage MGJT system for cryosurgery has not previously been reported. Therefore, the model is used to identify the merits as well as the potential drawbacks associated with using a two stage system as compared to a single stage, mixed gas JT cycle.

The Optimization Results in Section 3.2 below demonstrates that the two-stage system offers a more compact cryoprobe over a reasonable range of precooling temperatures provided the refrigerants used in both stages are correctly optimized. Other secondary parameters that must be considered when comparing the single- and two-stage systems include the overall compressor size and power consumption, contamination control, and overall complexity and reliability of the system. The compressor requirements (power and displacement) can be precisely evaluated using the model discussed in this section; the Optimization Results section shows that the two-stage system can be implemented without a significant change in compressor size and power consumption.

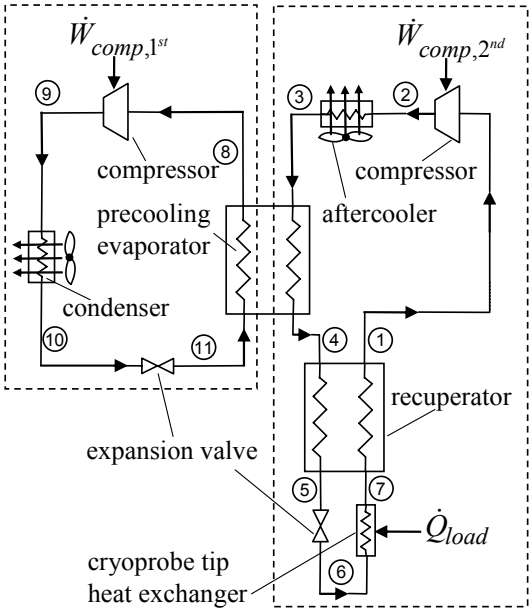

Figure 3-1: Schematic of two stage refrigeration cycle showing the thermodynamic states associated with each stage.

An optimized mixture for a cryosurgical system will provide a large JT cooling effect but require a relatively small system of heat exchangers in the cryoprobe. The relationship between mixture composition and JT effect is a function of the complex mixture equation of state. Additionally, the heat exchanger size that is required depends strongly on the specific heat capacity of the mixture, which varies substantially as a function of temperature, pressure, and mixture composition. Therefore, it is not possible to analytically or intuitively select: (1) a 2nd stage mixture, (2) precooling temperature, and (3) recuperator and precooling evaporator pinch point temperatures (also referred to as the pinch point ΔT) for the two stage system that yield an optimum ratio of cooling power and heat exchanger size, as well as a system with a practical compressor sizes. (Little 1997), (Alexeev 1997), and (Gong 2000) describe methods for selecting a mixture to yield the largest cooling effect. However these optimization methods do not account for the heat exchanger size. Keppler et al. (2004) demonstrated that a cryoprobe which uses a mixture that is optimized for maximum cooling (or maximum efficiency) may be

more than twice the size of a cryoprobe using a mixture that is optimized for cooling per heat exchanger size. Therefore, a numerical optimization technique described here is used to design an optimized cryosurgical probe that achieves the maximum cooling per heat exchanger size.

A numerical thermodynamic model of the two-stage JT system was created to evaluate: (1) the system states shown in Figure 3-1, (2) the temperature and enthalpy distribution within the heat exchangers, and (3) the overall performance of the system including refrigeration load, heat exchanger size, and compressor size. The model is integrated with a genetic optimization routine (Charbonneau 2007) in order to investigate the optimum mixture composition and precooling temperature.

3.1 Optimization model

This section presents the details of the thermodynamic model that provides the basis for the optimization of the 2nd stage mixture and precooling temperature for the two stage cryosurgical system. The working fluid for the 1st stage is a pure synthetic refrigerant and the working fluid for the second stage is a mixture of hydrocarbons and inert gases including: methane, ethane, propane, isobutene, isopentane, nitrogen and argon. A similar analysis could be performed using a synthetic refrigerant based mixture if there are flammability concerns with using a hydrocarbon based mixture. The correlations used to evaluate the mixture properties are discussed. A freezing point model is described; the freezing point model is incorporated into the optimization routine in order to provide one constraint on the optimization associated with not selecting a mixture that may freeze and clog the system. The numerical parameters that are required by the model and the optimization algorithm are investigated and appropriate

parameters are selected. Finally, the optimization algorithm that is used to select an optimal mixture for a given load temperature is presented.

3.1.1 Thermodynamic model

The two stage refrigeration cycle shown in Figure 3-1 is evaluated using a numerical modeling tool discussed in this section. The Engineering Equation Solver (EES) software (Klein 2007a) is used to solve the governing system of equations that captures the performance of the system for a particular set of operating conditions and geometry. The modeling tool is used with an optimization algorithm in order to maximize the system performance in terms of the previously discussed figure of merit (Section 1.3), the cryoprobe refrigeration load per total heat exchanger conductance ($\dot{Q}_{load}/UA_{total}$).

A variety of pure fluids or mixtures could be used in the 1st stage; the working fluids analyzed in this paper are R134a and R22. The choice of an appropriate 1st stage working fluid is partially a function of the desired precooling temperature, as discussed in the Optimization Results section. Property data for R134a and R22 are provided in EES. The 2nd stage hydrocarbon mixture property data are obtained from the NIST4 (also called SUPERTRAPP) database (Ely 1992). The numerical EES model is interfaced with the FORTRAN routines provided in the SUPERTRAPP program from the National Institute of Standards and Technology (NIST) in a separate interface routine (Klein 2007b). The interface routine was programmed in FORTRAN and validated against property calculations obtained from running the NIST4 database independently from EES. The NIST4 database program was extended to include thermodynamic property data for argon according to the procedure described in the manual (Ely 1992).

The 2nd stage aftercooler and 1st stage condenser are not explicitly modeled, rather they are assumed to be sufficiently large such that the fluid exiting the compressors is cooled to ambient temperature$\left(T_{amb}\right)$. Additionally, the 1st stage refrigerant leaving the precooling evaporator (state 8) is assumed to be saturated vapor. The pressure drop in the heat exchangers is neglected; therefore the working fluids change pressure only across the compressors and expansion valves. Operating pressures representing the high and low pressures of each cycle are defined: ($P_{high,1^{st}}, P_{low,1^{st}}, P_{high,2^{nd}}, P_{low,2^{nd}}$); these are based on pressures that can be achieved using conventional equipment. Other inputs to the model include: the 1st and 2nd stage fluid compositions ($\overline{y}_{1^{st}}$ and $\overline{y}_{2^{nd}}$, a vector of molar concentrations of each component which will be controlled, eventually, by the optimization algorithm), the ambient temperature, the load temperature(T_{load}), and the precooling and recuperative heat exchangers pinch-point temperature differences ($\Delta T_{pp,pc}$ and $\Delta T_{pp,rec}$). Note that the model is created with the flexibility to use a mixture in the 1st stage, however for this paper, only pure refrigerants are used in the 1st stage so $\overline{y}_{1^{st}}$ only has one component. A future analysis will evaluate the merit of using a mixture in the 1st stage VC cycle.

3.1.2 1st Stage Analysis.

An iterative process is required to solve the governing equations to determine the performance of the cycle. A flowchart of the iteration process used to solve both the 1st and 2nd stage governing equations is shown in Figure 3-2.

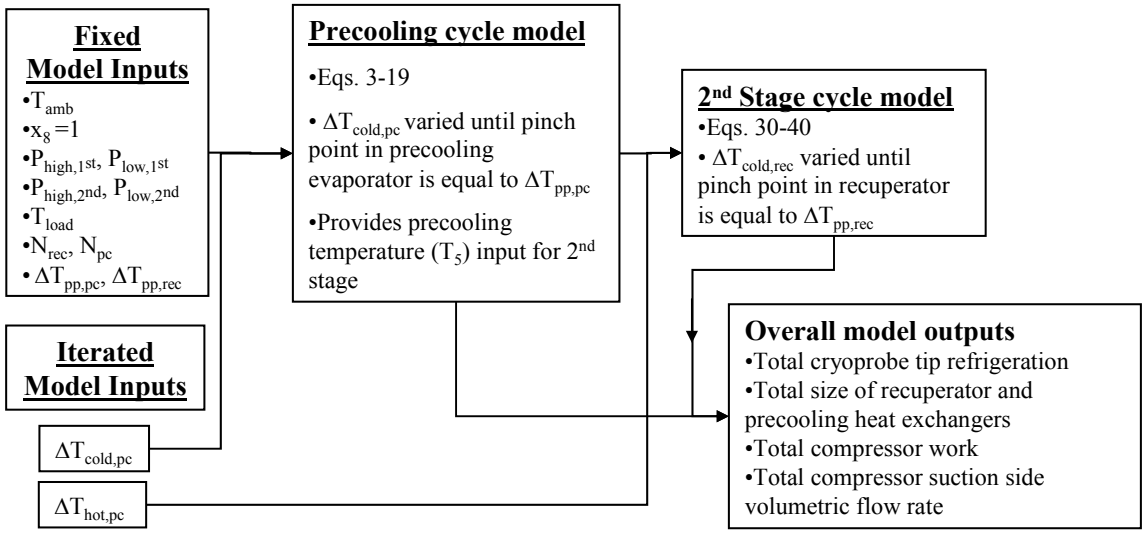

Figure 3-2: Flow chart of the iteration process used with the pinch point specifications to solve for the thermodynamic states shown in Figure 3-1 as well as the enthalpy and temperature distribution within the recuperator and precooling evaporator.

The iteration procedure begins by considering the enthalpy of the fluid entering the 1st stage expansion valve (h_{10}), which is computed according to:

$$h_{10} = enthalpy\left(T_{amb}, P_{high,1^{st}}, \overline{y}_{1^{st}}\right) \tag{3.1}$$

where *enthalpy* represents using the correlations in NIST4 or EES to evaluate the specific enthalpy at the given state. The enthalpy (h_{11}) and temperature (T_{11}) for the 1st stage fluid entering the precooling heat exchanger can be computed assuming isenthalpic expansion across the valve:

$$h_{11} = h_{10} \tag{3.2}$$

$$T_{11} = temperature\left(h_{11}, P_{low,1^{st}}, \overline{y}_{1^{st}}\right) \tag{3.3}$$

An assumed cold-end temperature difference for the precooling evaporator ($\Delta T_{cold,pc}$) is systematically varied until the specified precooling evaporator pinch-point temperature

($\Delta T_{cold,rec}$) difference is achieved, as shown in Figure 3-2. The temperature (T_4) and enthalpy (h_4) of the 2nd stage fluid leaving the precooling evaporator are calculated:

$$T_4 = T_{11} + \Delta T_{cold,pc} \tag{3.4}$$

$$h_4 = enthalpy\left(T_4, P_{high,2^{nd}}, \overline{y}_{2^{nd}}\right) \tag{3.5}$$

The 1st stage working fluid (which is analyzed here as a pure refrigerant) is assumed to exit the precooling evaporator as a saturated vapor. This assumption is reasonable for a cryoprobe optimization as the heat exchanger size is dependent on the temperature difference between the two streams; if the 1st stage refrigerant is in a superheated state in a significant portion of the precooling evaporator then the temperature difference near the warm end of the heat exchanger will be small and the required heat exchanger area would be large. Conversely, the refrigerant cannot leave the evaporator and enter the compressor with quality significantly less than one because the liquid would damage the compressor. The enthalpy (h_8) at the exit of the 1st stage side of the precooling evaporator is computed as:

$$h_8 = enthalpy\left(x_8 = 1, P_{low,1^{st}}, \overline{y}_{1^{st}}\right) \tag{3.6}$$

The enthalpy (h_3) of the 2nd stage fluid entering the precooling evaporator is calculated using:

$$h_3 = enthalpy\left(T_{amb}, P_{high,2^{nd}}, \overline{y}_{2^{nd}}\right) \tag{3.7}$$

The ratio of the mass flow rate in the 1st to the mass flow rate in the 2nd stage (MR) is defined as:

$$MR = \dot{m}_{1^{st}} \big/ \dot{m}_{2^{nd}} \tag{3.8}$$

and is computed using an energy balance on the precooling evaporator:

$$MR = \left(h_3 - h_4\right) \big/ \left(h_8 - h_{11}\right) \tag{3.9}$$

The rate of precooling heat transfer as well as all subsequent energy transfer rates are computed on a per unit of 2nd stage mass flow rate basis.

$$\dot{Q}_{pc} \big/ \dot{m}_{2^{nd}} = MR\left(h_8 - h_{11}\right) \tag{3.10}$$

The precooling heat exchanger is divided into a number (N_{pc}) of small heat exchangers, as shown in Figure 3-3(a), where each section transfers an equal fraction ($1/N_{pc}$) of the total precooling load. Dividing the heat exchanger into equal heat transfer segments rather than equal physical sizes facilitates direct computation of the enthalpy distribution in the heat exchangers and significantly increases computation speed and convergence. The first heat exchanger section is located at the hot end of the precooling evaporator and is shown in Figure 3-3(b). The enthalpy of the 1st stage working fluid leaving the precooling evaporator is equal to the enthalpy of the 1st stage fluid at the first node of the heat exchanger.

$$h_{1^{st},pc,0} = h_8 \tag{3.11}$$

The enthalpy of the mixture entering the precooling evaporator is equal to the enthalpy for the mixture at the first node of the heat exchanger.

$$h_{2nd,pc,0} = h_3 \tag{3.12}$$

The enthalpies of the hot and cold streams at the interface of each segment are computed using an energy balance.

$$h_{1^{st},pc,i} = h_{1^{st},pc,i-1} - \frac{\dot{Q}_{pc}}{\dot{m}_{2^{nd}}} \frac{1}{N_{pc}\, MR} \qquad i = 1 \ldots N_{pc} \qquad (3.13)$$

$$h_{2^{nd},pc,i} = h_{2^{nd},pc,i-1} - \frac{\dot{Q}_{pc}}{\dot{m}_{2^{nd}}} \frac{1}{N_{pc}} \qquad i = 1 \ldots N_{pc} \qquad (3.14)$$

The temperature at the inlet and exit of each side of each section (i.e. heat exchanger node index in Figure 3-3) is computed based on the enthalpy and pressure:

$$T_{1^{st},pc,i} = temperature\left(h_{1^{st},pc,i}, P_{low,1^{st}}, \overline{y}_{1^{st}}\right) \qquad i = 0 \ldots N_{pc} \qquad (3.15)$$

$$T_{2^{nd},pc,i} = temperature\left(h_{2^{nd},pc,i}, P_{high,2^{nd}}, \overline{y}_{2^{nd}}\right) \qquad i = 0 \ldots N_{pc} \qquad (3.16)$$

where *temperature* represents using the correlations in NIST4 or EES to evaluate the temperature at the given state given the specific enthalpy, pressure and stream composition. The pinch-point temperature difference is defined as the minimum temperature difference between the 1st and 2nd stage streams anywhere within the precooling heat exchanger.

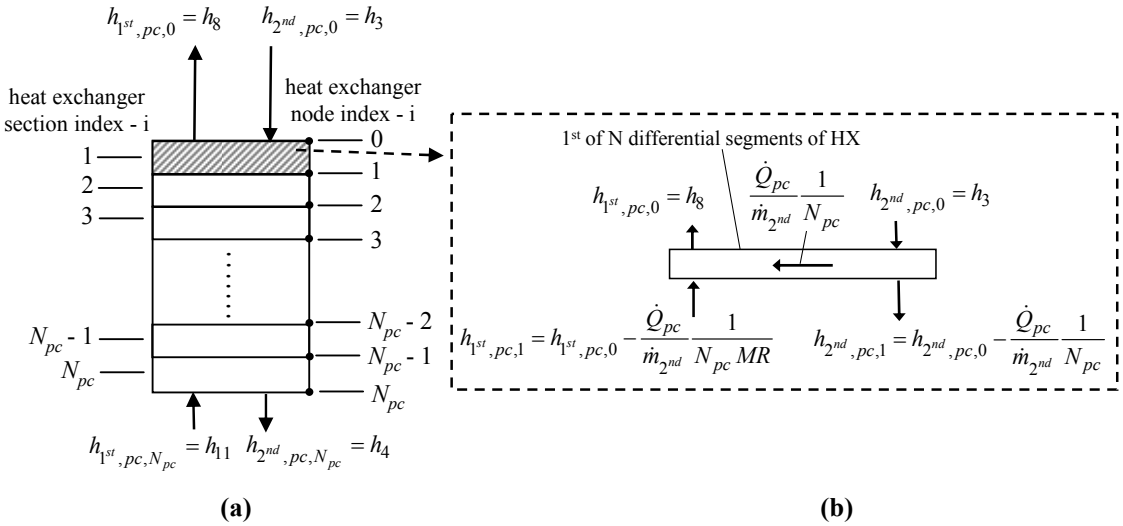

Figure 3-3: (a) Precooling heat exchanger divided into N_{pc} sections and (N_{pc} + 1) nodes. (b) First differential heat exchanger element.

$$\Delta T_{pp,pc} = \min\left(T_{2^{nd},pc,i} - T_{1^{st},pc,i}\right) \qquad i = 0 \ldots N_{pc} \tag{3.17}$$

The size of the heat exchanger is a function of the pinch-point temperature difference; a smaller pinch point temperature corresponds to a larger value of overall conductance (UA, the overall heat transfer coefficient-area product). The cryoprobe tip load is also dependent on the pinch point temperatures. As the pinch point temperature in either the recuperator or precooling evaporator decreases, the cryoprobe tip load increases. Therefore a compact cryoprobe system (where $\dot{Q}_{load}/UA_{total}$ is maximum) balances the heat exchanger size and cryoprobe load relative to the pinch point temperatures. The model uses 2 K as the pinch point temperatures for both the precooling evaporator and the recuperator.

The conductance of the precooler (UA_{pc} which is indicative of heat exchanger size) can be calculated using an effectiveness-*NTU* relationship for a counterflow heat exchanger (Incropera 2002) if the specific heat capacity of the fluids are constant throughout the heat exchanger. However, the specific heat of the mixture is very sensitive to the temperature and therefore

varies significantly within the heat exchanger. If a sufficient number of heat exchanger sections are used (i.e., if N_{pc} is large) then the specific heat capacity within each section is very nearly constant and so the effectiveness-*NTU* solution can be used to compute the conductance of each section as suggested by Nellis and Klein (2009). The total heat exchanger conductance is subsequently calculated by summing the conductances of each of the small section. The fluid specific heat within the section is reasonably represented by an average specific heat defined as:

$$\overline{c}_{1^{st},pc,i} = \frac{h_{1^{st},pc,i-1} - h_{1^{st},pc,i}}{T_{1^{st},pc,i-1} - T_{1^{st},pc,i}} \qquad i = 1 \ldots N_{pc} \tag{3.18}$$

$$\overline{c}_{2^{nd},pc,i} = \frac{h_{2^{nd},pc,i-1} - h_{2^{nd},pc,i}}{T_{2^{nd},pc,i-1} - T_{2^{nd},pc,i}} \qquad i = 1 \ldots N_{pc} \tag{3.19}$$

Note that in the case of the pure fluid evaporating in the 1st stage of the precooler, $\overline{c}_{1^{st},pc,i}$ will be infinite.

The effectiveness of each segment ($\varepsilon_{pc,i}$) is defined as the ratio of the actual heat transfer rate to the maximum possible heat transfer rate that could occur in that section. The maximum heat transfer rate in each section occurs when the outlet temperature of the minimum capacity rate stream reaches the inlet temperature of the maximum capacity rate stream.

$$\varepsilon_{pc,i} = \frac{\left(\frac{\dot{Q}_{pc}}{\dot{m}_{2^{nd}}} \frac{1}{N_{pc}} \right)}{\min\left(\overline{c}_{2^{nd},pc,i}, \overline{c}_{1^{st},pc,i} MR \right) \left(T_{1^{st},pc,i-1} - T_{2^{nd},pc,i} \right)} \quad i = 1 \ldots N_{pc} \tag{3.20}$$

Note that the capacity of the 1st stage fluid stream must be scaled by the mass flow rate ratio MR in order to compare the capacity rates of the two streams. The conductance of each section is calculated:

$$\frac{UA_{pc,i}}{\dot{m}_{2^{nd}}} = \min\left(\overline{c}_{2^{nd},pc,i}, \overline{c}_{1^{st},pc,i}\, MR\right) \frac{\ln\left(\dfrac{\varepsilon_{pc,i}-1}{\varepsilon_{pc,i}\, C_{r,pc,i}-1}\right)}{C_{r,pc,i}-1} \quad i = 1 \ldots N_{pc} \qquad (3.21)$$

where $C_{r,pc,i}$ is the capacity ratio characterizing the section:

$$C_{r,pc,i} = \frac{\min\left(\overline{c}_{2^{nd},pc,i}, \overline{c}_{1^{st},pc,i}\, MR\right)}{\max\left(\overline{c}_{2^{nd},pc,i}, \overline{c}_{1^{st},pc,i}\, MR\right)} \qquad i = 1 \ldots N_{pc} \qquad (3.22)$$

The overall conductance of the precooler per unit of 2nd stage mass flow rate is computed by summing the conductances of each of the segments.

$$\frac{UA_{pc}}{\dot{m}_{2^{nd}}} = \sum_{i=1}^{N} \frac{UA_{pc,i}}{\dot{m}_{2^{nd}}} \qquad i = 1 \ldots N_{pc} \qquad (3.23)$$

The compressor power for both stages is computed assuming an isentropic efficiency ($\eta_{comp,1^{st}}$) of 0.75. The entropy at state 8 is computed:

$$s_8 = entropy\left(h_8, P_{low,1^{st}}, \overline{y}_{1^{st}}\right) \qquad (3.24)$$

therefore the enthalpy at state 9 is:

$$h_9 = h_8 + \left(\frac{enthalpy\left(s_8, P_{high,1^{st}}, \overline{y}_{1^{st}}\right) - h_8}{\eta_{comp,1^{st}}}\right) \qquad (3.25)$$

and the compressor work transfer rate per unit of 2nd stage mass flow rate is:

$$\frac{\dot{W}_{comp,1^{st}}}{\dot{m}_{2^{nd}}} = MR\left(h_9 - h_8\right) \tag{3.26}$$

The 1st stage compressor suction side volumetric flow rate (which is proportional to compressor displacement and size) per unit of 2nd stage mass flow rate is calculated as:

$$\frac{\dot{v}_8}{\dot{m}_{2^{nd}}} = volume\left(x_8 = 1, P_{low,1^{st}}, \overline{y}_{1^{st}}\right) \cdot MR \tag{3.27}$$

3.1.3 2nd Stage Analysis.

The iterative procedure shown in Figure 3-2 is used to solve the equations governing the 2nd stage cycle; the procedure is similar to that used for the 1st stage analysis. The temperature (T_1) and enthalpy (h_1) of the 2nd stage fluid exiting the cold side of the recuperator can be calculated using the temperature (T_4) of the gas mixture leaving the precooling evaporator as well as an assumed recuperator hot-end temperature difference ($\Delta T_{hot,rec}$). The hot-end temperature difference is iteratively varied until the specified pinch point ($\Delta T_{pp,rec}$) is achieved.

$$T_1 = T_4 - \Delta T_{hot,rec} \tag{3.28}$$

$$h_1 = enthalpy\left(T_1, P_{low,2^{nd}}, \overline{y}_{2^{nd}}\right) \tag{3.29}$$

The load temperature (T_7) is specified as an input to the model so the enthalpy (h_7) can be calculated:

$$h_7 = enthalpy\left(T_7, P_{low,2^{nd}}, \overline{y}_{2^{nd}}\right) \tag{3.30}$$

The total recuperator heat transfer rate per unit of 2nd stage mass flow rate is:

$$\frac{\dot{Q}_{rec}}{\dot{m}_{2nd}} = \left(h_1 - h_7\right) \tag{3.31}$$

The recuperative heat exchanger is divided into N_{rec} sections as shown in Figure 3-4(a). The enthalpy of the low pressure mixture leaving the recuperator is equal to the enthalpy of the low pressure (cold side) mixture at the first node of the heat exchanger.

$$h_{c,0} = h_1 \tag{3.32}$$

The enthalpy of the mixture entering the recuperator is equal to the enthalpy for high pressure (hot side) stream at the first node of the heat exchanger.

$$h_{h,0} = h_4 \tag{3.33}$$

An energy balance on each of the segments yields the enthalpy of the hot and cold streams at the interface of each segment.

$$h_{c,i} = h_{c,i-1} - \frac{\dot{Q}_{rec}}{\dot{m}_{2^{nd}}} \frac{1}{N_{rec}} \qquad i = 1 \ldots N_{rec} \tag{3.34}$$

$$h_{h,i} = h_{h,i-1} - \frac{\dot{Q}_{rec}}{\dot{m}_{2^{nd}}} \frac{1}{N_{rec}} \qquad i = 1 \ldots N_{rec} \tag{3.35}$$

The temperatures at the interfaces between the sections (i.e. the node index in Figure 3-4) within the recuperator are calculated:

$$T_{c,i} = temperature\left(h_{c,i}, P_{low,2^{nd}}, \overline{y}_{2^{nd}}\right) \qquad i = 0 \ldots N_{rec} \tag{3.36}$$

$$T_{h,i} = temperature\left(h_{h,i}, P_{high,2^{nd}}, \overline{y}_{2^{nd}}\right) \qquad i = 0 \ldots N_{rec} \tag{3.37}$$

The pinch point temperature in the recuperator is calculated as

$$\Delta T_{pp,rec} = \min\left(T_{h,i} - T_{c,i}\right) \qquad i = 0 \ldots N_{rec} \tag{3.38}$$

The refrigeration load per unit of 2nd stage mass flow rate can be calculated using the enthalpy difference between the two heat exchanger sections at the warm end (as well as at any node within the heat exchanger, as the enthalpy difference in the recuperator between the hot and cold streams is constant. Losses from the jacket of the heat exchanger are neglected).

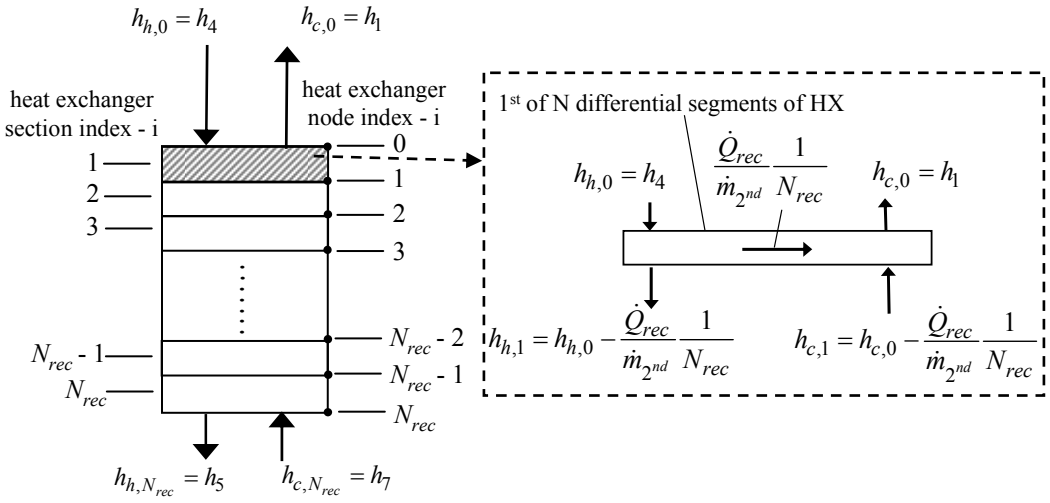

Figure 3-4: (a) Recuperative heat exchanger divided into N_{rec} sections and (N_{rec} + 1) nodes and (b) the first differential heat exchanger element.

$$\dot{Q}_{load} \big/ \dot{m}_{2^{nd}} = h_1 - h_4 \tag{3.39}$$

The enthalpy (h_6) and corresponding temperature (T_6) after the expansion valve are calculated based on the enthalpy of the mixture leaving the hot side of the recuperator ($h_{h,N_{rec}}$ which is equal to h_5) and assuming isenthalpic expansion.

$$h_6 = h_{h,N_{rec}} \tag{3.40}$$

$$T_6 = temperature\left(h_6, P_{low,2^{nd}}, \overline{y}_{2^{nd}}\right) \tag{3.41}$$

The recuperator heat exchanger overall conductance is calculated using the same method described for the precooling evaporator. The average fluid specific heat capacities in each of the recuperator heat exchanger sections for the hot and cold streams are calculated as:

$$\overline{c}_{c,i} = \frac{h_{c,i-1} - h_{c,i}}{T_{c,i-1} - T_{c,i}} \qquad i = 1 \ldots N_{rec} \tag{3.42}$$

$$\overline{c}_{h,i} = \frac{h_{h,i-1} - h_{h,i}}{T_{h,i-1} - T_{h,i}} \qquad i = 1 \ldots N_{rec} \tag{3.43}$$

The effectiveness of each heat exchanger section is evaluated as:

$$\varepsilon_{rec,i} = \frac{\left(\frac{\dot{Q}_{rec}}{\dot{m}_{2^{nd}}} \frac{1}{N_{rec}}\right)}{\min\left(\overline{c}_{h,i}, \overline{c}_{c,i}\right)\left(T_{h,i-1} - T_{c,i}\right)} \qquad i = 1 \ldots N_{rec} \tag{3.44}$$

The conductance of each heat exchanger section is calculated as:

$$\frac{UA_{rec,i}}{\dot{m}_{2^{nd}}} = \min\left(\overline{c}_{h,i}, \overline{c}_{c,i}\right) \frac{\ln\left(\frac{\varepsilon_{rec,i} - 1}{\varepsilon_{rec,i} C_{r,rec,i} - 1}\right)}{C_{r,rec,i} - 1} \qquad i = 1 \ldots N_{rec} \tag{3.45}$$

where:

$$C_{r,rec,i} = \frac{\min\left(\overline{c}_{c,i}, \overline{c}_{h,i}\right)}{\max\left(\overline{c}_{c,i}, \overline{c}_{h,i}\right)} \qquad i = 1 \ldots N_{rec} \tag{3.46}$$

The overall recuperator conductance is found by adding the conductances of the recuperator sections.

$$\frac{UA_{rec}}{\dot{m}_{2^{nd}}} = \sum_{i=1}^{N_{rec}} \frac{UA_{rec,i}}{\dot{m}_{2^{nd}}} \qquad i = 1...N_{rec} \tag{3.47}$$

The 2nd stage compressor work transfer rate per unit of 2nd stage mass flow rate is computed using a compressor isentropic efficiency ($\eta_{comp,2^{nd}}$) of 0.75.

$$s_1 = entropy\left(h_1, P_{low,1^{st}}, \overline{y}_{2^{nd}}\right) \tag{3.48}$$

$$h_2 = h_1 + \left(\frac{enthalpy\left(s_1, P_{high,1^{st}}, \overline{y}_{2^{nd}}\right) - h_1}{\eta_{comp,2^{nd}}} \right) \tag{3.49}$$

$$\frac{\dot{W}_{comp,2^{nd}}}{\dot{m}_{2^{nd}}} = \left(h_2 - h_1\right) \tag{3.50}$$

The 2nd stage compressor suction side volumetric flow rate per unit of 2nd stage mass flow rate is calculated as the specific volume at state 1.

$$\frac{\dot{v}_1}{\dot{m}_{2^{nd}}} = volume\left(T_1, P_{low,2^{nd}}, \overline{y}_{2^{nd}}\right) \tag{3.51}$$

3.1.4 Overall Thermodynamic Analysis

The overall system performance can be quantified using several figures of merit of importance to a cryosurgical probe system. From a surgical procedure standpoint, an optimal cryoprobe is small and generates a large amount of cooling power; such a probe will produce the largest possible cryolesion (i.e., frozen tissue). Larger cryolesions reduce the number of surgical sites and/or cryoprobes that are required to treat a given volume of tissue. A small cryoprobe is ergonomic, can accommodate other instrumentation given surgical site space

constraints, is less invasive, can be precisely controlled, and requires less planning. These factors contribute to reduce the overall procedure time, complication rates, and expense. Therefore the most appropriate figure of merit (Keppler et al, 2004), which is used to optimize the system, is the total cryoprobe cooling load provided per total heat exchanger conductance, which is indicative of the cryoprobe size.

$$\frac{\dot{Q}_{load}}{UA_{total}} = \frac{\dot{Q}_{load} / \dot{m}_{2^{nd}}}{UA_{rec} / \dot{m}_{2^{nd}} + UA_{pc} / \dot{m}_{2^{nd}}} \tag{3.52}$$

It is also of interest to reduce the size of the other hardware required; particularly the compressors. The compressors can be connected to the cryoprobe heat exchangers via flexible tubing and physically decoupled from the cryoprobe. Therefore, the size of the compressors is less important than the size of the cryoprobe. However, the size of the compressors largely dictates the size and weight of the cabinet that houses the compressors, 2nd stage aftercooler, and 1st stage condenser. Smaller compressors will therefore lead to a small, portable cryosurgical unit that is portable and easy to handle. The compressor suction side flow rate determines the required displaced volume and therefore, to first order, the size of the compressor. The figure of merit that captures the combined compressor size is the refrigeration load per unit of total compressor displacement:

$$\frac{\dot{Q}_{load}}{\dot{v}_{total}} = \frac{\dot{Q}_{load} / \dot{m}_{2^{nd}}}{\dot{v}_1 / \dot{m}_{2^{nd}} + \dot{v}_8 / \dot{m}_{2^{nd}}} \tag{3.53}$$

where a relatively large $\dot{Q}_{load} / \dot{v}_{total}$ will yield a system with a compact compressor cabinet.

The refrigeration load per unit of total compressor displacement is not explicitly optimized, rather, it is observed as $\dot{Q}_{load} / UA_{total}$ is optimized. This quantity provides guidance relative to the feasibility of a selected operating condition and also guides the selection of the 1st stage refrigerant.

The Coefficient of Performance (COP) of the system is observed to trend with the refrigeration load per unit of total compressor displacement; relatively large volumetric flow rates generally correspond to relatively high compressor power input. The COP is also not explicitly optimized, but is observed to ensure the optimized cryoprobe system can operate with reasonable power consumption. Although power consumption is not a primary concern in the design of a cryosurgical system, the unit should be able to operate from a standard electrical service and should not require excessively bulky power conversion electronics. The overall COP of the cycle is:

$$COP_{total} = \frac{\dot{Q}_{load} / \dot{m}_{2^{nd}}}{\dot{W}_{comp,1^{st}} / \dot{m}_{2^{nd}} + \dot{W}_{comp,2^{nd}} / \dot{m}_{2^{nd}}} \tag{3.54}$$

3.1.5 Freezing Point Model

The 2nd stage JT cycle is particularly susceptible to freezing problems; the expansion valve is a very small orifice that can easily be clogged at the point where the cycle temperature is lowest. Therefore, a freezing point model must be incorporated into the optimization routine in order to exclude mixtures that may freeze from consideration. Keppler et al. (2004) describe the use of a relatively conservative freezing point model, which computes the freezing point of the mixture as the linear mole fraction weighted average of the triple points of the respective pure components ($T_{tp,i}$):

$$T_{freeze} = \sum_{i=1}^{NC} y_i \, T_{tp,i} \tag{3.55}$$

If the temperature leaving the expansion valve is lower than the freezing point calculated using Equation (3.55), then the mixture is excluded from further consideration. The freezing point model provided by Equation (3.55) is conservative; it is likely that the phenomenon referred to as freezing point depression will act to reduce the freezing point substantially (often even below the lowest freezing point of the components that make up the mixture). Therefore, the optimization may exclude mixtures which would not have frozen but have resulted in higher efficiencies or a more compact cryoprobe. The freezing point constraint is observed to always be dominant at load temperatures below 120 K (i.e., the optimal mixture for load temperatures below 120 K identified by the procedure discussed in this paper always has a freezing point that exactly satisfies this constraint); therefore, more sophisticated methods for computing the freezing point of a mixed gas may enable substantial improvements in performance at lower temperatures.

3.1.6 Property Correlations

The thermodynamic properties of mixtures are calculated using the NIST4 mixture database. The database uses the Peng-Robinson (PR) equation of state for the vapor-liquid phase equilibrium calculations. The PR equation of state is computationally fast and reliably converges over the temperature span of the JT system evaluated in this paper. The NIST23 (or REFPRROP) database (Lemmon 2007) uses the more sophisticated Benedict-Webb-Rubin and Hemholtz-energy equations of state that likely provide more accurate property data for the mixture. However these equations of state are computationally expensive and Keppler et al.

(2004) demonstrated that the NIST23 database does not reliably converge at temperatures below 150 K and is subsequently poorly suited for use with this model.

A comparison of mixture property data between the two databases shows that they approximately agree, so the NIST4 mixture data can be used with a reasonable degree of confidence. Figure 3-5 compares the enthalpy differences (i.e., the JT effect) for mixtures at a high and low pressure (1000 kPa and 100 kPa) over a range of temperatures that is typical for a cryosurgical probe. The NIST23 database only allows mixtures with 5 or fewer components (whereas NIST4 allow for up to 20 components), so the mixtures A and B in Figure 3-5 include 5 of the 7 constituents of the mixture used in the thermodynamic model. The 5 constituents include nitrogen, methane, ethane, propane, and argon. The optimal mixtures identified in this paper primarily consist of methane and ethane, so mixtures A and B are representative of the mixtures used in the optimization routine. Figure 7 highlights the similarities and differences between the NIST4 and NIST23 databases. The property data agree very well above 180 K. Below 180 K, the data are somewhat different and over a significant temperature span (approximately 155 K to 190 K), the NIST23 database does not converge.

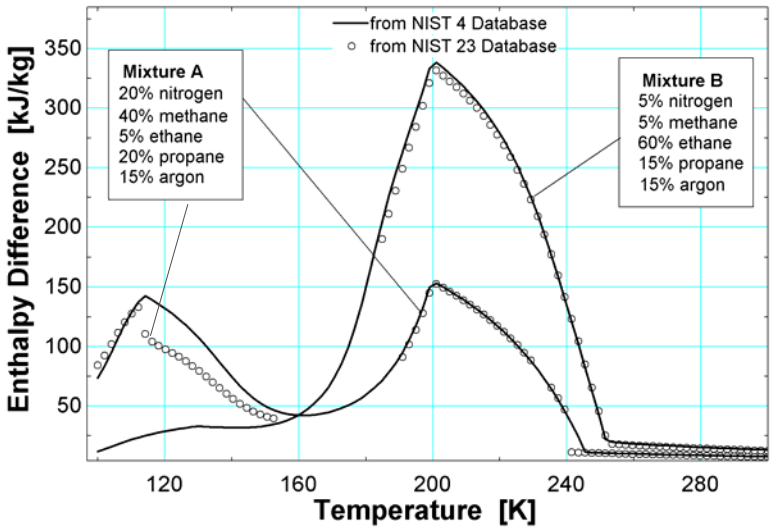

Figure 3-5: Comparison of property data computed using the NIST 4 and NIST 23 property databases. The enthalpy difference at a high (1000 kPa or 130 psig) and low (100 kPa or 0 psig) pressure stream at various temperatures are shown.

3.1.7 Numerical Parameters

The most computationally intensive process that is required by the model is the calculation and iterative adjustment of the enthalpy-temperature profile within the heat exchangers so that the model results comply with the specified pinch point temperature difference. In order to minimize this computational effort and also improve the convergence of the iteration process, a property interpolation table is created at the beginning of each computation for the mixture in the 2nd stage; the table has $N_{int,2^{nd}}$ entries and includes enthalpy as a function of temperature at regular intervals of temperature (from ambient temperature, T_3, to the load temperature, T_7) for the two operating pressures ($P_{high,2nd}$ and $P_{low,2nd}$).

The time required to carry out the computations depends primarily on the number of entries in the property table ($N_{int,2^{nd}}$) as well as the number of divisions used to model the precooler (N_{pc}) and recuperator (N_{rec}). The selection of appropriate values for these numerical parameters is a balance between modeling accuracy and computational efficiency. The figures

of merit that are used to investigate the effect of the choice of these numerical parameters is the cryoprobe refrigeration load per precooling heat exchanger conductance:

$$\frac{\dot{Q}_{load}}{UA_{pc}} = \frac{\dot{Q}_{load} \big/ \dot{m}_{2^{nd}}}{UA_{pc} \big/ \dot{m}_{2^{nd}}} \tag{3.56}$$

and the cryoprobe refrigeration load per recuperative heat exchanger conductance:

$$\frac{\dot{Q}_{load}}{UA_{rec}} = \frac{\dot{Q}_{load} \big/ \dot{m}_{2^{nd}}}{UA_{rec} \big/ \dot{m}_{2^{nd}}} \tag{3.57}$$

Figure 3-6(a) illustrates these two figures of merit as a function of $N_{int,2^{nd}}$ for a typical operating condition and illustrates that the results are relatively independent of $N_{int,2^{nd}}$ when this parameter reaches about 35; therefore 35 mixture interpolation entries are used in the model.

A similar numerical study on the effect of the choice of the number of heat exchanger divisions was performed. Figure 3-6 (b) illustrates the value of $\dot{Q}_{load} / UA_{pc}$ as a function of N_{pc} and $\dot{Q}_{load} / UA_{rec}$ as a function of N_{rec} and shows that a minimum of 15 sections are required in order for the average specific heats defined in Equations (3.19),(3.42), and (3.43) to accurately represent the specific heats in each section.

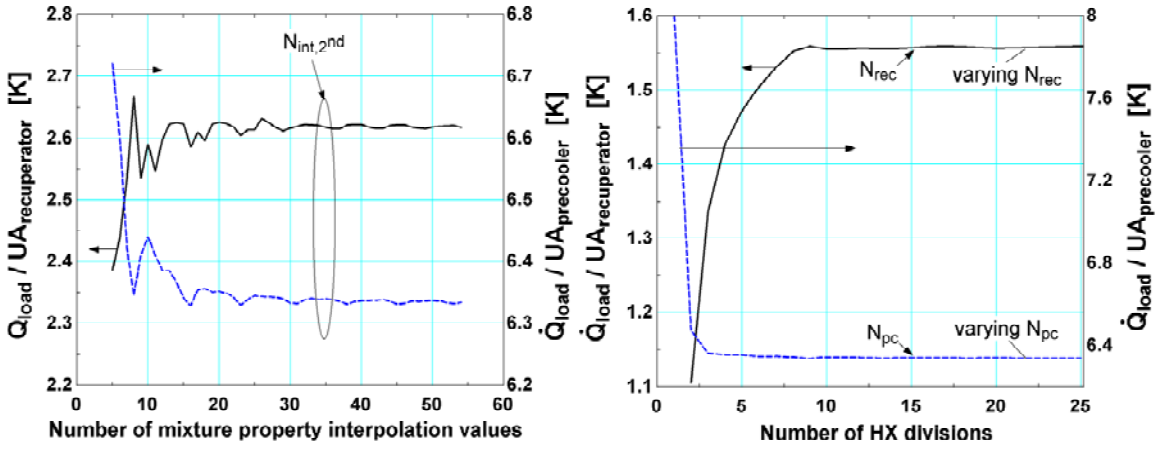

(a) **(b)**

Figure 3-6: Numerical parameter investigation. (a) The cryoprobe load per precooler and recuperator conductance as a function of the number of entries in the mixture property table, and (b) the cryoprobe load per precooler conductance as a function of the number of precooler sections and the cryoprobe load per recuperator conductance as a function of the number of recuperator sections.

3.1.8 Optimization Algorithm

The optimization process for the results presented in this paper identify the optimal mixture composition in the 2nd stage ($\bar{y}_{2^{nd}}$, the vector of compositions of each mixture component) for a particular set of operating conditions. The total cryoprobe compactness figure of merit ($\dot{Q}_{load}/UA_{total}$) calculated by the thermodynamic model varies significantly as the mixture mole fraction vector ($\bar{y}_{2^{nd}}$) changes, so it is necessary to evaluate a wide range of mole fraction combinations. It is not computationally efficient to parametrically evaluate the mole fractions for all possible $\bar{y}_{2^{nd}}$ combinations. Therefore, an optimization algorithm that is able to select the optimal mixture using significantly less computations than a parametric study is utilized here.

The optimization routine used here is the PIKAIA 1.2 (Charbonneau 2002) genetic algorithm which is implemented in EES and finds the maximum of the objective function using

an algorithm that mimics biological evolution. A detailed description and demonstration of the routine as it is used to select a best mixture is found in (Keppler et al. 2004). As shown by Keppler et al., other optimization techniques such as the direct search and variable metric strategies do not reliably converge because of the sharp discontinuities in mixture properties near phase boundaries as well as other constraints that are placed on the mixture. Note that the reliability of the genetic optimization routine comes at the expense of computation speed; the genetic algorithm should only be used when other, faster, routines (such as the direct search and variable metric methods) have failed.

The optimization routine excludes mixtures based on two practical considerations: 1) A mixture is excluded from further consideration if the temperature at the exit of the 2nd stage expansion valve is below the freezing point temperature. 2) Mixtures in a saturated or liquid state leaving the recuperator (state 1) are excluded to avoid the introduction of liquid into the 2nd stage compressor.

3.2 Optimization Results

The results of the optimization model using a pure refrigerant in the 1st stage and a hydrocarbon based mixture in the 2nd stage are presented in this section. The refrigerants used for analysis in the 1st stage include R134a and R22. The $\dot{Q}_{load}/UA_{total}$ figure of merit is optimized in order to yield the cryoprobe that provides the most cooling for a given geometric size for load temperatures spanning 100 K to 180 K. The effect of the precooling temperature (T_5) on $\dot{Q}_{load}/UA_{total}$ is studied in order to show the optimal balance of overall cryoprobe heat exchanger load between the precooler and the recuperator. The other figures of merit, including the load specific compressor power and volumetric flow rate, are not explicitly optimized but

are reported as they are important in the design of a practical system. The performance of the two stage system is normalized against the performance of a single stage system in order to show the relative benefit and penalty associated with the addition of precooling.

The $\dot{Q}_{load}/UA_{total}$ for a two stage system in which an optimal mixture has been selected for each precooling and load temperature is shown in Figure 3-7(a). As the precooling temperature is reduced, the temperature range that must be spanned by the recuperator decreases, and, as shown in Figure 1-9, the performance of the 2nd stage cycle increases considerably as evident by the improvement in the cooling that can be provided per unit of mass flow rate ($\dot{Q}_{load}/\dot{m}_{2^{nd}}$). The overall cryoprobe heat exchanger size for an optimized system remains relatively constant over the range of precooling temperatures studied here. Therefore, as the precooling temperature is reduced, $\dot{Q}_{load}/UA_{total}$ increases entirely due to the improvement in the efficiency of the 2nd stage cycle.

It is interesting to note that as the precooling temperature decreases, the total heat exchanged in the precooler and recuperator increases even though the total heat exchanger size remains essentially constant. This result can be explained with the following observations: 1) as the precooling temperature decreases, the fraction of UA_{total} that is required by the precooler increases, 2) the temperature difference between the 1st and 2nd stage streams in the precooler is relatively large because the pure refrigerant is in a constant pressure phase transition state and therefore remains at constant temperature; the temperature difference is especially large at the warm end of the precooler, and 3) the average temperature difference in the recuperator is comparatively smaller as both streams exhibit temperature glide with similar slopes. Therefore, the increase in the total heat exchange is nominally offset by the shift in the heat exchange to the

precooler, where the larger temperature difference allows for a more efficient (in the sense of being more compact, that is, requiring less conductance) heat exchange process.

Figure 3-7 (b) shows the results in Figure 3-7 (a) normalized by the cryoprobe load per heat exchanger size for a single stage system, $\left(\dot{Q}_{load}/UA_{total}\right)_{single\,stage}$. The single stage system performance is calculated using the thermodynamic model presented here while the precooling cycle is omitted, so UA_{total} represents the conductance of only the recuperator. The system performance when $\dot{Q}_{load}/UA_{total}$ is optimized is summarized in Figure 3-7. Figure 3-7 (b) shows clearly that the two stage system offers a more compact cryoprobe compared to the single stage system, and this advantage increases as the precooling temperature is reduced.

The load curve for 180 K in Figure 3-7 is somewhat of an outlier compared to the other load curves; the exact cause of the outlier is not precisely known. The majority of the heat transfer occurs in the precooler rather than the recuperator for the 180 K load curve, as opposed to the other load curves where the opposite is true. The precooler here uses a pure refrigerant and does not have a temperature glide, and therefore has a larger temperature difference throughout the heat exchanger. This tends to result in a system with a larger $\dot{Q}_{load}/UA_{total}$ because UA_{total} decreases. However, this is a complex problem, and it is possible that the increased performance at 180 K could be related to some fundamental thermodynamic property of the mixture constituents that are available to the optimizer or for some other reason entirely.

Table 3-1: Performance values at different load temperatures for an optimized single stage JT cycle using a mixture of nitrogen, methane, ethane, propane, isobutene, isopentane, and argon. The supply or high pressure (P_{high}) is 1000 kPa and the low or suction pressure (P_{low}) is 100 kPa.

T_{load}	$\frac{\dot{Q}_{load}}{\dot{m}}$	$\frac{\dot{Q}_{load}}{UA_{total}}$	COP_{total}	$\frac{\dot{Q}_{load}}{\dot{v}_{total}}$
(K)	(J/kg)	(K)	-	(J/m^3)
100	35750	0.745	0.131	48840
120	57260	1.262	0.196	71350
140	67300	1.658	0.249	89240
160	71310	2.11	0.270	96730
180	77210	3.35	0.342	12210

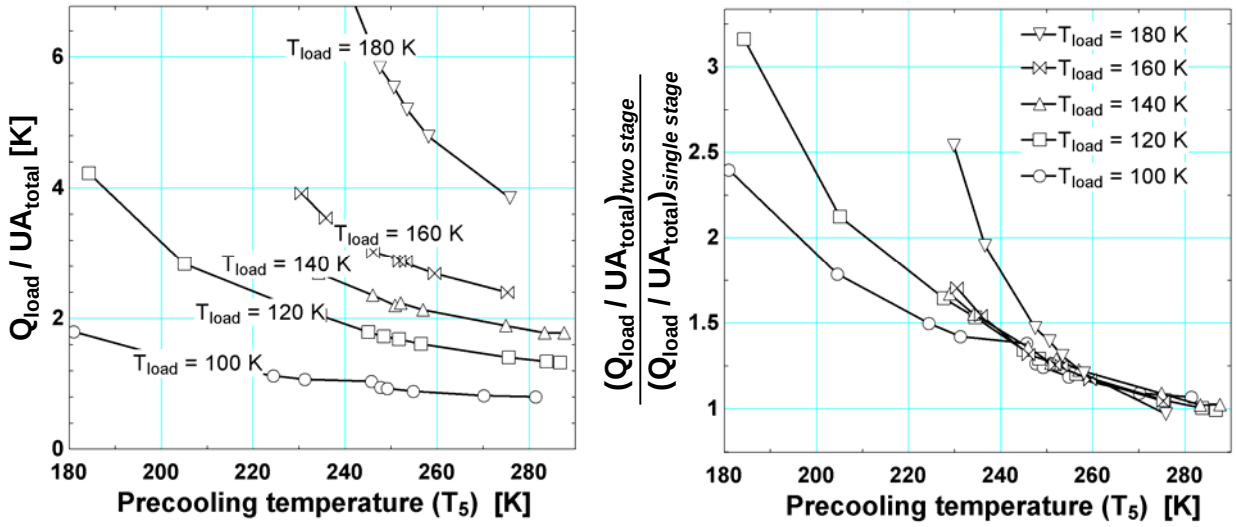

(a) **(b)**

Figure 3-7: (a) $\dot{Q}_{load}/UA_{total}$ for the two stage system over a range of precooling and load temperatures. (b) $\dot{Q}_{load}/UA_{total}$ for the two stage system normalized by the $\dot{Q}_{load}/UA_{total}$ of a single stage system.

Figure 3-7 suggests that the precooling temperature should be made as low as possible in order to achieve an optimized cryoprobe. However, other considerations related to the compressor power and size limit the range of practical precooling temperatures. Figure 3-8(a) shows the ratio of the cryoprobe refrigeration to the total volumetric flow rate at the suction to the compressors, $\dot{Q}_{load}/\dot{v}_{total}$ (which provides an indication of the size of the compressors

required). Figure 3-9(a) shows the ratio of the cryoprobe refrigeration to the power required by the compressors (COP_{total}) when R134a is used in the 1st stage. Both the size and power required by the compressors increase as the precooling temperature is reduced. The suction pressure ($P_{low,1^{st}}$) for the R134a must be significantly reduced in order to achieve the desired precooling temperature; the specific volume of the R134a at the compressor suction side increases and the compressor power and size subsequently increases. Therefore the selection of precooling temperature must balance the reduction in cryoprobe size with the increased compressor size. Similar to the trends observed in Figure 3-7 (a), the 180 K curve for both $\dot{Q}_{load}/\dot{v}_{total}$ and COP_{total} as a function of precooling temperature is somewhat of an outlier compared to the other load temperatures. Again, the exact reasons for this could not be discerned. Figure 3-8 (b) and Figure 3-9 (b) show the $\dot{Q}_{load}/\dot{v}_{total}$ and COP_{total} for the two stage system (with R134a in the 1st stage) normalized by these quantities for a single stage system (as listed in Table 3-1); the precooling temperature can be reduced to nominally 240 K before substantially increased compressor hardware is required.

Interestingly, the normalized $\dot{Q}_{load}/\dot{v}_{total}$ (Figure 3-8b) is nearly independent of load temperature; this behavior can be understood by looking at the individual terms from Equation (55). The 2nd stage compressor suction volumetric flow rate ($\dot{v}_1/\dot{m}_{2^{nd}}$) does not vary significantly with mixture composition, load temperature, and precooling temperature for the conditions considered here. The unit cryoprobe refrigeration $\dot{Q}_{load}/\dot{m}_{2^{nd}}$ does vary with load temperature (not shown in any of the figures), and the dependence is very similar for both the single-stage and two-stage systems. Therefore by normalizing the value of $\dot{Q}_{load}/\dot{v}_{total}$, the

$\dot{Q}_{load}/\dot{m}_{2^{nd}}$ terms for the single-stage and two-stage systems cancel. The remaining term in Equation (55) is the volumetric flow rate of the 1st stage compressor ($\dot{v}_1/\dot{m}_{2^{nd}}$) which is very sensitive to the precooling temperature as the precooling temperature is varied by changing the suction pressure (and therefore the 1st stage suction specific volume). Therefore, the normalized $\dot{Q}_{load}/\dot{v}_{total}$ is very sensitive to precooling temperature. The change in $\dot{Q}_{load}/\dot{v}_{total}$ therefore represents a change in the required 1st stage compressor displacement (size).

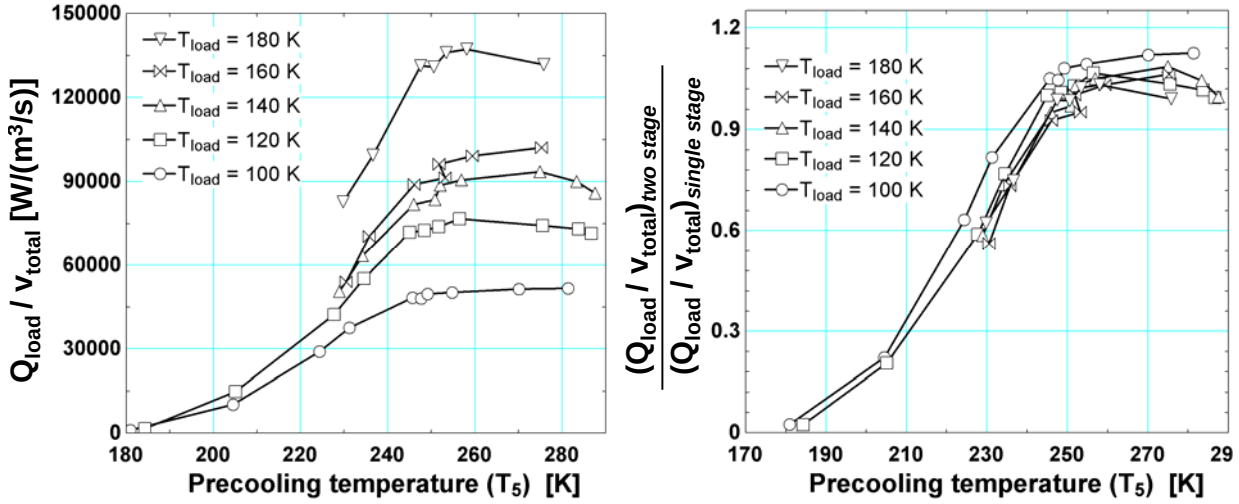

Figure 3-8: **(a) $\dot{Q}_{load}/\dot{v}_{total}$ for the two stage system over a range of precooling and load temperatures with R134a as the 1st stage working fluid (b) $\dot{Q}_{load}/\dot{v}_{total}$ for the two stage system normalized by the $\dot{Q}_{load}/\dot{v}_{total}$ of a single stage system.**

It is important to recognize that the $\dot{Q}_{load}/UA_{total}$ for the two-stage system optimized for a given precooling and load temperature (i.e., the results shown in Figure 3-7) is independent of the choice of pure 1st stage refrigerant, provided a pure fluid is used in the 1st stage; the heat exchange in the precooler occurs with the 1st stage fluid at a constant temperature and therefore could be achieved using any pure refrigerant at an appropriate suction pressure. However, the 1st stage compressor volumetric flow rate and power (i.e., the results shown in Figure 3-8 and,

Figure 3-9 respectively) are highly dependent on the choice of the 1st stage working fluid. The lowest precooling temperature that is achievable, given compressor hardware limitations, is therefore dependent on the choice of the 1st stage fluid. For example, R22 is a better choice than R134a because it is a better low-temperature refrigerant; R22 has a lower specific volume at the compressor suction state and a smaller compressor power required. Figure 3-10 compares the $\dot{Q}_{load}/\dot{v}_{total}$ and COP_{total} results for 2-stage systems using R134a and R22 with a load temperature of 140 K; note that the values of $\dot{Q}_{load}/\dot{v}_{total}$ and COP_{total} are normalized by their values for a single stage system. Figure 3-10 shows that a precooling temperature of 210 K can be achieved with R22 for the same nominal $\dot{Q}_{load}/\dot{v}_{total}$ penalty (i.e., 60% of a single stage system) associated with using the R134a with a precooling temperature of 230 K. Figure 3-7(b) shows that for a load temperature of 100 K, a precooling temperature of 210 K corresponds to a 70% increase in $\dot{Q}_{load}/UA_{total}$ (relative to a single stage configuration) rather than a 40% increase associated with a precooling temperature of 230 K. This significant increase suggests that R22 or some other low-temperature refrigerant should be used in the precooling cycle.

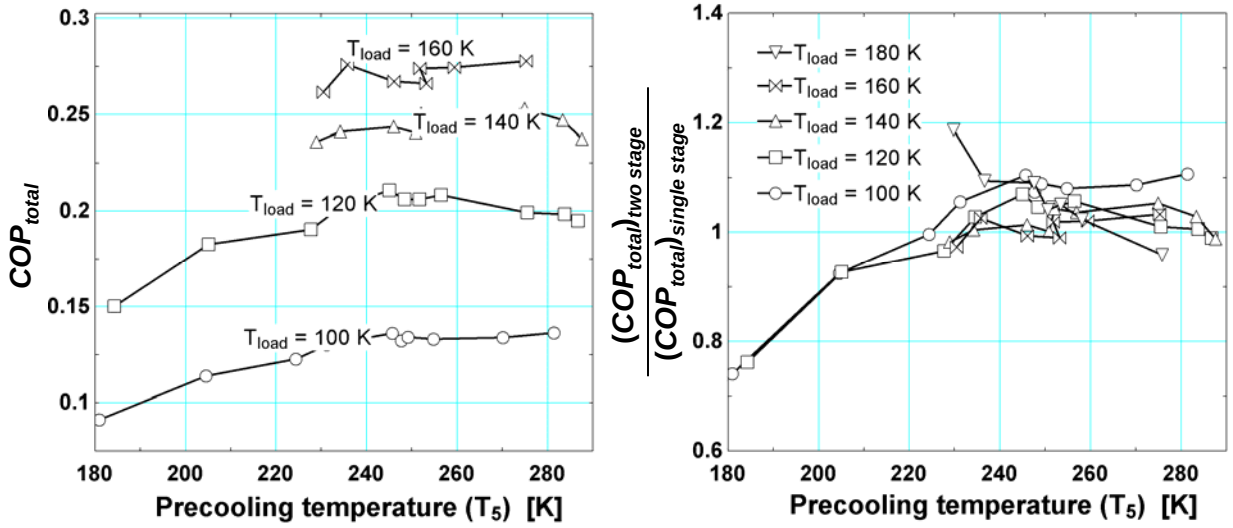

Figure 3-9: **(a) COP_{total} for the two stage system over a range of precooling and load temperatures with R134a as the 1st stage working fluid. (b) COP_{total} for the two stage system with R134a as the 1st stage working fluid normalized by the COP_{total} of a single stage system.**

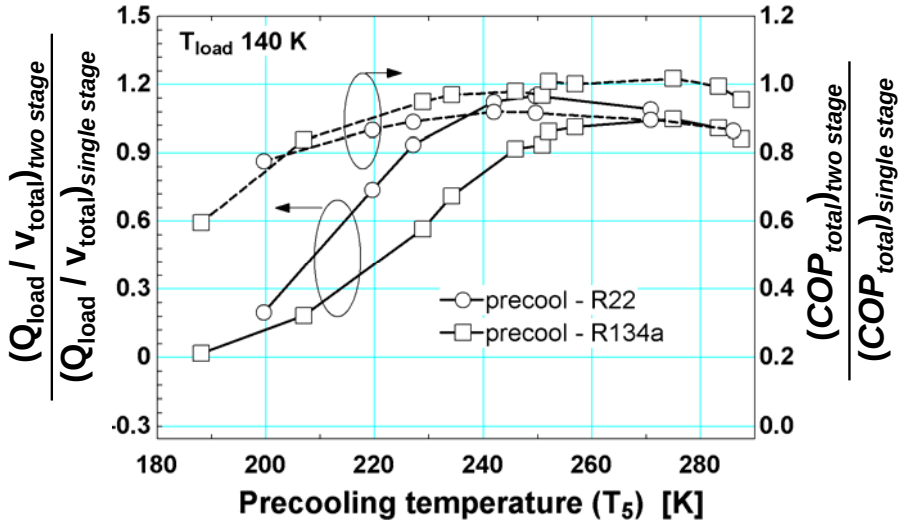

Figure 3-10: **$\dot{Q}_{load} / \dot{v}_{total}$ and COP_{total} for the two stage system with R22 and R134a as the 1st stage working fluids normalized by the respective values for a single stage system. The load temperature is 140 K.**

3.3 References

Alexeev, A.; Haberstroh, C.; Quack, H. Further Development of a Mixed Gas Joule Thomson Refrigerator. in *Advances in Cryogenic Engineering: Proceedings of the 1997 Cryogenic Engineering Conference 1997*, vol 43, 1667-1674.

Arnott, J. On the Treatment of Cancer by the Regulated Application of an Anaesthetic Temperature. *London: Churchill* 1851.

Brodyansky, V. M.; Gresin, A. K.; Gromov, E. M.; Yagoden, V. M.; Nicolsky, V. A.; Alpheev, V. N. The Use of Mixtures as the working Gas in Throttle Joule Thomson Cryogen Refrigerators. *Proceedings of the 13th International Congress of Refrigeration, Washington, D.C. Progress in Refrigeration Science and Technology* 1971, vol. 1, 43.

Charbonneau, P. Version 1.2 2002, PIKAIA Homepage. http://www.hao.ucar.edu/Public/models/pikaia/pikaia.html (accessed 11/3, 2007).

Cooper, I. S.; Lee, A. S. Cryostatic Congelation: a system for producing a limited, controlled region of cooling or freezing of biologic tissues. *J Nerv. Ment. Dis.* 1961, vol. 133, 259.

Ely, J. F.; Huber, M. L. NIST Thermophysical Properties of Hydrocarbon Mixtures Database (SUPERTRAPP). 1992*, 3.2*.

Fredrikson, K. 2004. Optimization of Cryosurgical Probes for Cancer Treatment. M.S. thesis. Madison, WI USA: University of Wisconsin - Madison, Mechanical Engineering Dept.

Fredrikson, K.; Nellis, G.; Klein, S. A. A Design Method for Cryosurgical Probes. *International Journal of Refrigeration* 2006, vol. 29, 700-715.

Gong, M. Q.; Luo, E. C.; Zhou, Y.; Liang, J. T.; Zhang, L. Optimum composition calculation for multicomponent cryogenic mixture used in Joule-Thomson refrigerators. *Advances in Cryogenic Engineering* 2000, 45, 283.

Incropera, F. P.; DeWitt, D. P. *Fundamentals of Heat and Mass Transfer, Fourth Edition;* John Wiley & Sons: New York, 2002

Keppler, F.; Nellis, G.; Klein, S. A. Optimization of the Composition of a Gas Mixture in a Joule-Thomson cycle. *HVAC&R Research* 2004, vol. 10, 213-230.

Klein, S. A. EES - Engineering Equation Solver. 2007*, 7.982*, f-Chart Software, www.fchart.com

Klein, S.A., EES-NIST4 interface routine, f-Chart Software, www.fchart.com, 2008

Lemmon, E. W.; Huber, M. L.; McLinden, M. O. NIST Reference Fluid Thermodynamic and Transport Properties - REFPROP. 2007*, 8.0*.

Little, W. A. Method for efficient counter-current heat exchange using optimized mixtures. U.S. Patent No. 5,664,502, 1997.

Pettit, J. Numerical Modeling and Experimental Testing of a Mixed Gas Joule-Thomson Cryocooler, pp. 42-56.

Nellis, G. and Klein, S., *Heat Transfer*, Cambridge University Press, 2009 ISBN 9780521881074.

Rubinsky, B. CRYOSURGERY. *Annu. Rev. Biomed. Eng.* 2000,vol. 2, 157-187.

Zhong-Shan D.; Liu, J. Numerical study of the effects of large blood vessels on three-dimensional tissue temperature profiles during cryosurgery. *Numerical Heat Transfer, Part A (Applications)* 2006, vol. 49, 47-67.

4 Design and Construction of the Experimental Test Facility

This section describes the purpose, location, and integration of the experimental sensors that are used to measure the characteristics of the cryoprobe system. An uncertainty analysis was used to guide the selection of the sensors in order to ensure that the various cryoprobe performance metrics are captured with adequate fidelity. The system was significantly modified to include the measurement instrumentation; this modification process is shown in detail in order to clarify physical locations of the measurements as well as to provide a step-by-step guide so that these experiments could be replicated in another research facility.

4.1 Experimental measurements

Figure 4-1 shows a schematic of the measurement instrumentation integrated with the cryoprobe system. Temperature and pressure measurements at various points in the system are used to identify thermodynamic states. Pressure measurements are shown with "P#" where the "#" corresponds to the numbered thermodynamic state convention defined in the model and shown in Figure 1-8. The temperatures are measured with ThermoCouples and Platinum Resistance Thermometers and are denoted as "TC#" and "PRT#", respectively. Additional PRTs, shown as "PRT_i", measure the temperatures at various points within the low pressure stream of the recuperator; these measurements are used to determine the location of the pinch point in the recuperator and to compute the spatially resolved recuperator conductance. The mass flows of the 1^{st} and 2^{nd} stages are measured using calorimetric flow meters; the output of these flow meters must be adjusted based on the specific heat of the refrigerants. These mass flow measurements are used to calculate heat and work transfer rates. A fin fan heat exchanger (not shown) warms the 1^{st} stage refrigerant exiting the precooler to protect the mass flow meter

from extreme cold, where PRT8a and P8 are used to infer the density and specific heat required to correct the flow meter reading for R410a. The pressure at the 2nd stage compressor suction port is measured and labeled "P1a", and is used to measure the pressure drop in the return line after P1. A heater attached to the cryoprobe tip simulates the biological thermal load; the power dissipation is calculated using voltage and current measurements (V_{load} and I_{load}). An interchangeable jewel orifice and a bypass valve on the 2nd stage compressor are used in order to allow independent regulation of the pressure drop and mass flow rate, within some range dictated by the compressor performance. A bypass valve on the 1st stage compressor is used to regulate the mass flow and therefore the cooling provided by the precooling cycle. The cold components of the experiment are housed in a vacuum insulated chamber and covered with radiation insulation (MLI) to minimize the parasitic heat into the system. Finally, a gas chromatograph measures the circulating mixture in the 2nd stage by sampling before the low pressure inlet of the compressor.

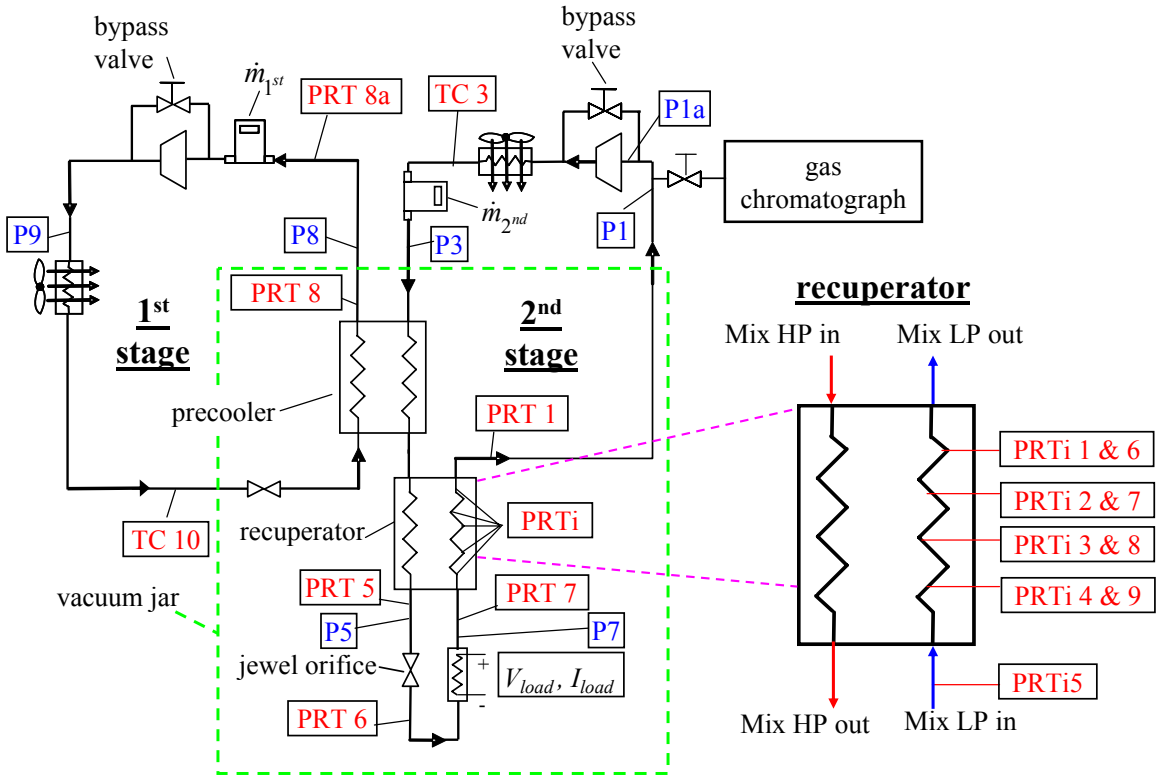

Figure 4-1: Schematic of experimental test facility including measurement instrumentation integrated with the MGJT cryoprobe system.

4.2 Uncertainty Analysis and Sensor Selection

An uncertainty analysis was performed for the cryoprobe system in order to guide the selection of measurement instrumentation. The relative uncertainties of the precooling, recuperative, and combined heat exchanger conductances as well as the cryoprobe compactness target (UA_{pc}, UA_{rec}, UA_{total}, and $\dot{Q}_{load}/UA_{total}$, respectively) were computed to determine the relative sensitivity of these calculated quantities to each of the measurements that are required for the calculation. Nominal uncertainty values that represent the expected accuracy of readily available and cost effective instrumentation were used in the calculation. The analysis was performed at several operating temperatures and loads, as well as for both hydrocarbon (HC) and synthetic refrigerant (SR) based gas mixtures. The calculations were carried out using the uncertainty propagation feature of the EES software. Table 4-1 and Table 4-2 show the

contribution of each of the measurements to heat exchanger conductance and cryoprobe compactness uncertainty for a nominal operating condition for both the HC and SR mixtures.

The analysis shows that the heat exchanger sizes and compactness target can be measured to within 10% or better. Table 4-1 shows that the HC parameters are most sensitive to the 2nd stage mass flow rate measurement ($\dot{m}_{2^{nd}}$), 2nd stage high and low pressure measurements ($P_{h,2^{nd}}$ and $P_{l,2^{nd}}$), as well as the 1st stage low pressure measurement ($P_{l,1^{st}}$). Table 4-2 shows that the SR parameters are most sensitive to the measurements of the krypton fraction, $P_{h,2^{nd}}$, $P_{l,1^{st}}$.

Table 4-3 shows a list of the purchased measurement instrumentation that will characterize the system performance. The table lists the measurement locations, as shown in Figure 4-1, the manufacturer, part #'s, the actual uncertainties, and uncertainty values used in the uncertainty analysis. All of the selected sensors meet or exceed the accuracy values used in the uncertainty analysis, so the cryoprobe performance will be captured with a high degree of precision. Note that not all of the measurements shown in Figure 4-1 and Table 4-3 are required to compute the quantities that are included for the uncertainty analysis. These additional measurements are included for completeness.

Table 4-1: Cryoprobe compactness uncertainty calculations for a nominal operating condition with a hydrocarbon gas mix.

Calculated parameters				
Parameter	Precooler conductance (UA_{pc})	Recuperator conductance (UA_{rec})	Total conductance (UA_{total})	Cryoprobe compactness ($\dot{Q}_{load} / UA_{total}$)
Value and uncertainty	5.06 ± 7.9% [W/K]	19.69 ±6.2 % [W/K]	24.7 ± 6.2% [W/K]	0.61 ± 7.2% [K]

Measurements and their contribution to above calculated parameter uncertainty						
Measurement	**Nominal Value**	**Measurement Uncertainty**	**Contribution to UA_{pc} uncertainty**	**Contribution to UA_{rec} uncertainty**	**Contribution to UA_{total} uncertainty**	**Contribution to $\dot{Q}_{load} / UA_{total}$ uncertainty**
fraction nitrogen	0.1%	4% relative	0%	0%	0%	0%
fraction methane	41.4%	4% relative	0%	3%	2%	1.5%
fraction ethane	46%	4% relative	8%	2%	3%	2.5%
fraction propane	1.7%	4% relative	0%	0%	0%	0%
fraction isobutane	9.5%	4% relative	4.5%	0%	0%	0%
fraction isopentane	0.7%	4% relative	0%	0%	0%	0%
fraction argon	0.5%	4% relative	0%	0%	0%	0%
1st stage mass flow ($\dot{m}_{1^{st}}$)	0.001 kg/s	5% relative	0%	0%	0%	0%
2nd stage mass flow ($\dot{m}_{2^{nd}}$)	0.0015 kg/s	5% relative	15%	48%	46.5%	36%
1st stage high pressure ($P_{h,1^{st}}$)	1400 kPa	5% relative	0%	0%	0%	0%
2nd stage high pressure ($P_{h,2^{nd}}$)	1400 kPa	5% relative	31%	23%	28.5%	22%
1st stage low pressure ($P_{l,1^{st}}$)	200 kPa	5% relative	20%	0%	1%	0.5%
2nd stage low pressure ($P_{l,2^{nd}}$)	100 kPa	5% relative	0%	15%	11.5%	9%
Cryoprobe load ($\dot{Q}_{load}$)	30 W	4% relative	6.5%	1%	2%	23%
Recuperator cold exit temperature (T_1)	210 K	1 K	10.5%	0.5%	0%	0%
Ambient Temperature (T_{amb})	290 K	1 K	4%	0%	0%	0%
Load temperature (T_{load})	140 K	1 K	0%	8%	6%	4.5%

Table 4-2: Cryoprobe compactness uncertainty calculations for a nominal operating condition with a synthetic refrigerant gas mix.

Calculated parameters				
Parameter	Precooler conductance (UA_{pc})	Recuperator conductance (UA_{rec})	Total conductance (UA_{total})	Cryoprobe compactness ($\dot{Q}_{load} / UA_{total}$)
Value and uncertainty	3.8 ± 10.5% [W/K]	9.13 ± 9.3% [W/K]	12.93 ± 7% [W/K]	2.32 ± 7%[K]

Measurements and their contribution to above calculated parameter uncertainty						
Measurement	**Nominal Value**	**Measurement Uncertainty**	**Contribution to UA_{pc} uncertainty**	**Contribution to UA_{rec} uncertainty**	**Contribution to UA_{total} uncertainty**	**Contribution to $\dot{Q}_{load} / UA_{total}$ uncertainty**
fraction R116	0.5%	4% relative	0%	0%	0%	0%
fraction Krypton	46.2%	4% relative	19.5%	57%	25%	25.5%
fraction R14	5.2%	4% relative	1%	0.5%	0%	0%
fraction R23	13.9%	4% relative	1.5%	1%	0%	0%
fraction R32	17.8%	4% relative	0%	0.5%	0.5%	0.5%
fraction Argon	2.88%	4% relative	0.2%	0%	0%	0%
fraction R125	13.4%	4% relative	0.1%	0.2%	0%	0%
1st stage mass flow ($\dot{m}_{1^{st}}$)	0.001 kg/s	5% relative	0%	0%	0%	0%
2nd stage mass flow ($\dot{m}_{2^{nd}}$)	0.0015 kg/s	5% relative	2.3%	8.5%	11%	11%
1st stage high pressure ($P_{h,1^{st}}$)	1400 kPa	5% relative	0%	0%	0%	0%
2nd stage high pressure ($P_{h,2^{nd}}$)	1400 kPa	5% relative	34%	16%	38%	38.5%
1st stage low pressure ($P_{l,1^{st}}$)	200 kPa	5% relative	32.5%	0%	6%	6%
2nd stage low pressure ($P_{l,2^{nd}}$)	100 kPa	5% relative	0%	9%	7.5%	7.5%
Cryoprobe load ($\dot{Q}_{load}$)	30 W	4% relative	6.5%	4%	8.5%	7%
Recuperator cold exit temperature (T_1)	210 K	1 K	2%	0%	0%	0%
Ambient Temperature (T_{amb})	290 K	1 K	0%	0%	0%	0%
Load temperature (T_{load})	140 K	1 K	0%	3%	3%	3%

Table 4-3: List of temperature, pressure, and mass flow sensors used in the experimental test facility

Measurement	Label on Figure 4-1	Manufacturer	Part #	Actual precision	Uncertainty analysis precision
Temperature – PRT	PRT 1,5,6,7,8,8a, 11	Lakeshore	PRT-111	0.5 K (calibrated in situ)	1 K
Temperature – PRT	$PRT_{rec,i}$	Lakeshore	PRT-111	0.5 K (calibrated in situ)	1 K
Temperature - thermocouple	TC 3,8,10	Lakeshore	9006-004	~1 K in 290-400 K range	1 K
Mixture high pressure ($P_{h,2^{nd}}$)	P3	Setra	206-500G	0.65 psi, plus drift = 3 psi total	10 psi
Mixture high pressure ($P_{h,2^{nd}}$)	P5	Setra	206-500G	0.65 psi, plus drift = 3 psi total	10 psi
Mixture low pressure ($P_{l,2^{nd}}$)	P7	Setra	206-100G	0.15 psi, plus drift = 1.5 total	0.7 psi
Mixture low pressure ($P_{l,2^{nd}}$)	P1	Setra	206-100G	0.15 psi, plus drift 1.5 total	0.7 psi
Pure fluid high pressure ($P_{h,1^{st}}$)	P5	Setra	206-500G	0.65 psi, plus drift =3 psi total	10 psi
Pure fluid low pressure ($P_{l,1^{st}}$)	P7	Setra	206-100G	0.15 psi, plus drift = 1.5 total	1.4 psi
1st stage mass flow ($\dot{m}_{1^{st}}$)	$\dot{m}_{1^{st}}$	Omega	FMA1742-EPDM	3% F.S. = 0.03*100 stdL/min = 3 stdL/min	5% relative
2nd stage mass flow ($\dot{m}_{2^{nd}}$)	$\dot{m}_{2^{nd}}$	Omega	FMA1741ST-EPDM	3% F.S. = 0.03*80 stdL/min = 2.4 stdL/min	5% relative
Cryoprobe load ($\dot{Q}_{load}$)	$\dot{Q}_{load}$	--	--	0.00001 W	4% relative
Heater voltage (V_{load})	V_{load}	--	--	0.005 V	
Heater current (I_{load})	I_{load}	--	--	0.002 A	
Mixture composition ($y_{2^{nd}}$)		Air Liquide		3% absolute	

4.3 Test Facility construction

4.3.1 Integration of MGJT cryoprobe with vacuum test facility

Figure 4-2 shows the graphical solid model of the experimental components that are enclosed within the vacuum chamber. The specific components used in the construction of the facility are listed in Table 4-15 at the end of Section 4.3 and are referred to by a component number that corresponds to their location in this table.

The vacuum chamber is 30" long and 8" in diameter (#1), the cryoprobe and related plumbing are suspended from the vacuum chamber lid (#2). The figure shows the physical locations of the pressure and temperature sensors (which are inserted directly into the fluid stream) that are depicted in Figure 4-1. The jewel orifice and Nichrome wire heater (#10) are also shown. The figure shows the various vacuum pass-throughs that connect vacuum space to the external environment. There are several tubes and wires that connect the cold and warm components of the test facility; these are constructed with a minimal amount of material in order to minimize parasitic conduction. The small diameter, thin wall (1/8" OD, 0.015" wall) stainless steel pressure tap tubes connect to the pressure sensors located outside the vacuum chamber. The 1st and 2nd stage high and low pressure fluid stream connections to the compressors are shown. Figure 4-3 shows a photograph of the components of the test facility that are enclosed in the vacuum chamber. The figure shows the vacuum lid, the fluid tubes that pass through the vacuum lid, the support for the cryoprobe, the pressure tap tubes, the cryoprobe sheath enclosing the precooling and recuperative heat exchangers, the in-stream PRTs, the Nichrome wire heater, and the jewel orifice location.

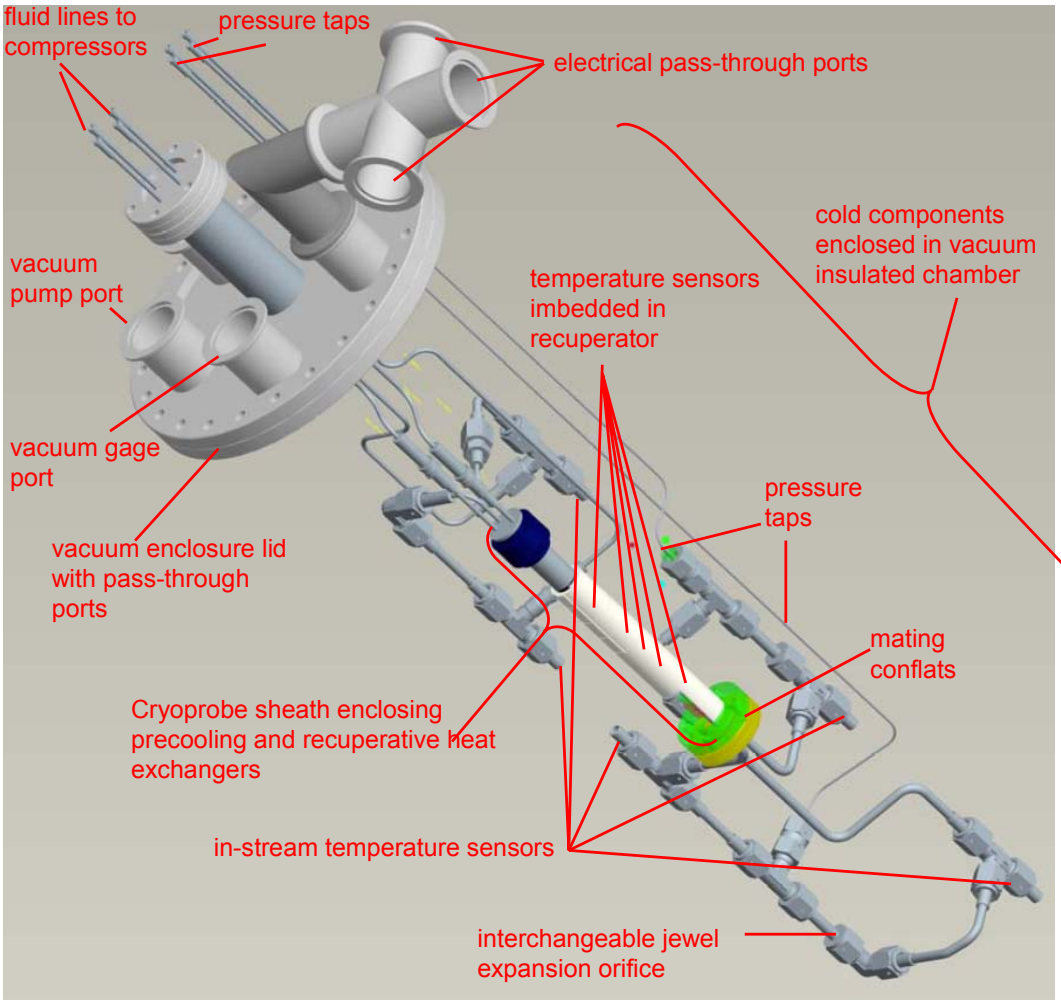

Figure 4-2: Graphical model of the cold components of experiment enclosed in the 30” long 8” diameter evacuated enclosure.

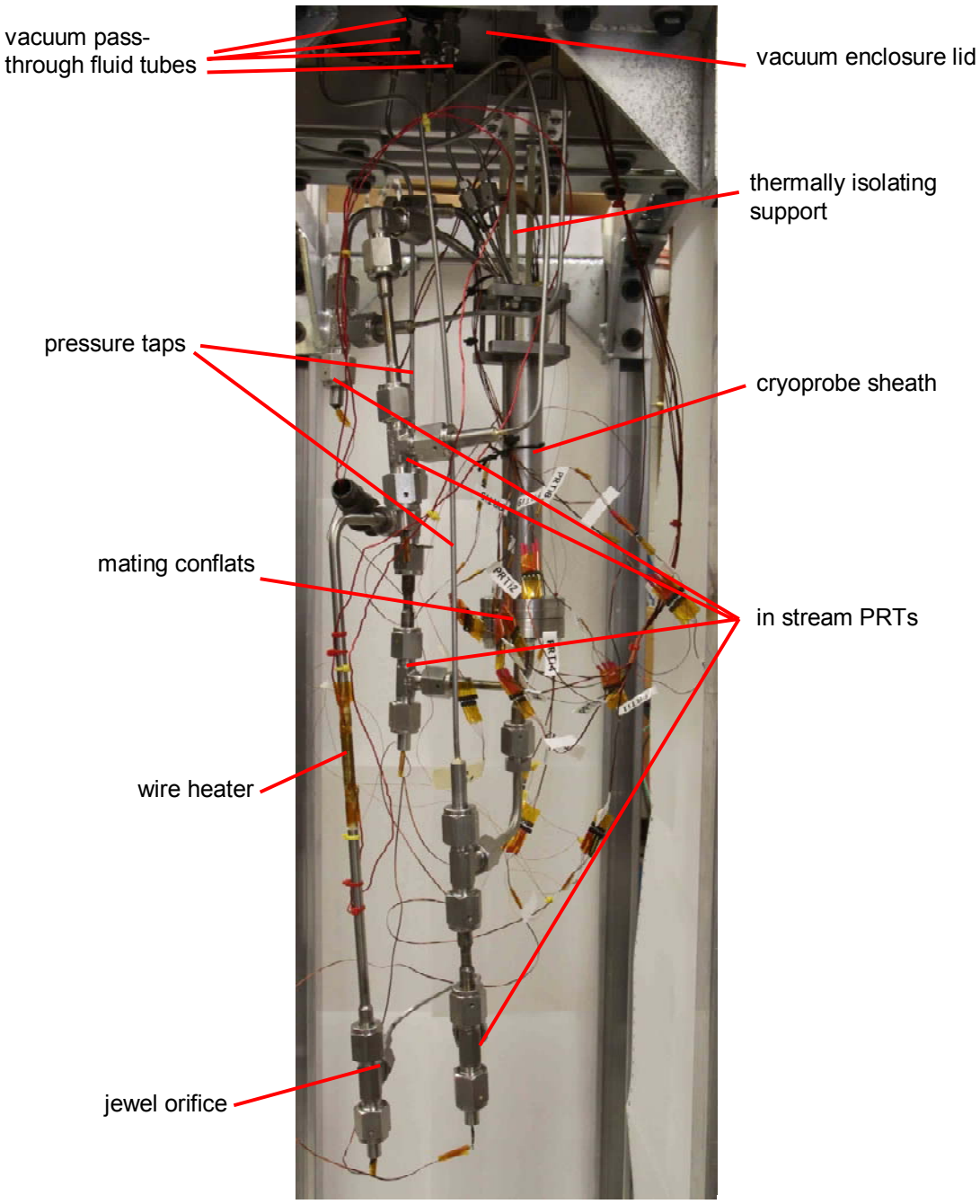

Figure 4-3: Photograph of the cold components of the experimental test facility enclosed in the vacuum chamber.

Figure 4-4 shows a graphical solid model of the instrumentation outside the vacuum chamber including most of the measurements shown in Figure 4-1. The figure also shows the secondary hardware required to operate the test facility, including the vacuum chamber support

frame, the fluid tube connections to the flexible tubes which circulate the refrigerant between the compressors and the test facility, a burst disc (#5) to protect the cryoprobe sheath from overpressure, and ports on the vacuum chamber used to integrate the vacuum pump and vacuum gauges. Figure 4-5 shows a photograph of the components outside the vacuum chamber where most of the components from Figure 4-4 can be seen.

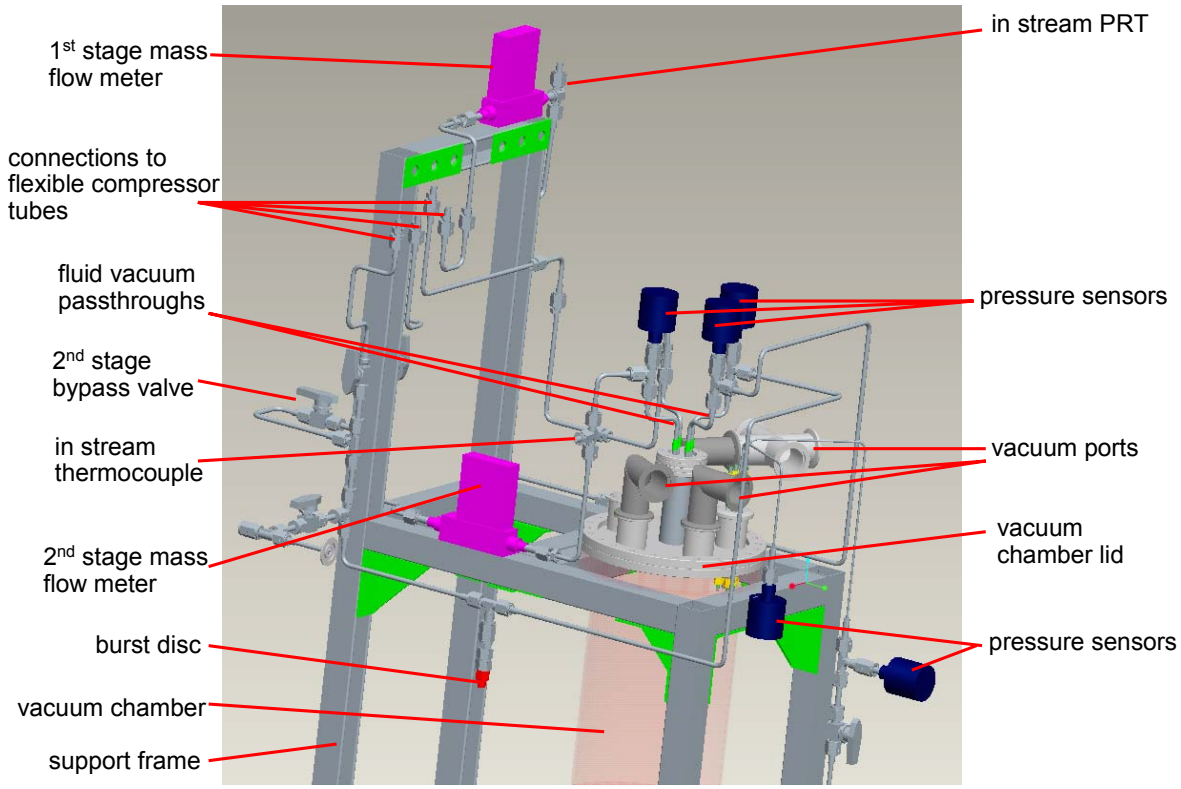

Figure 4-4: Graphical model of the instrumentation and cycle components outside the vacuum chamber.

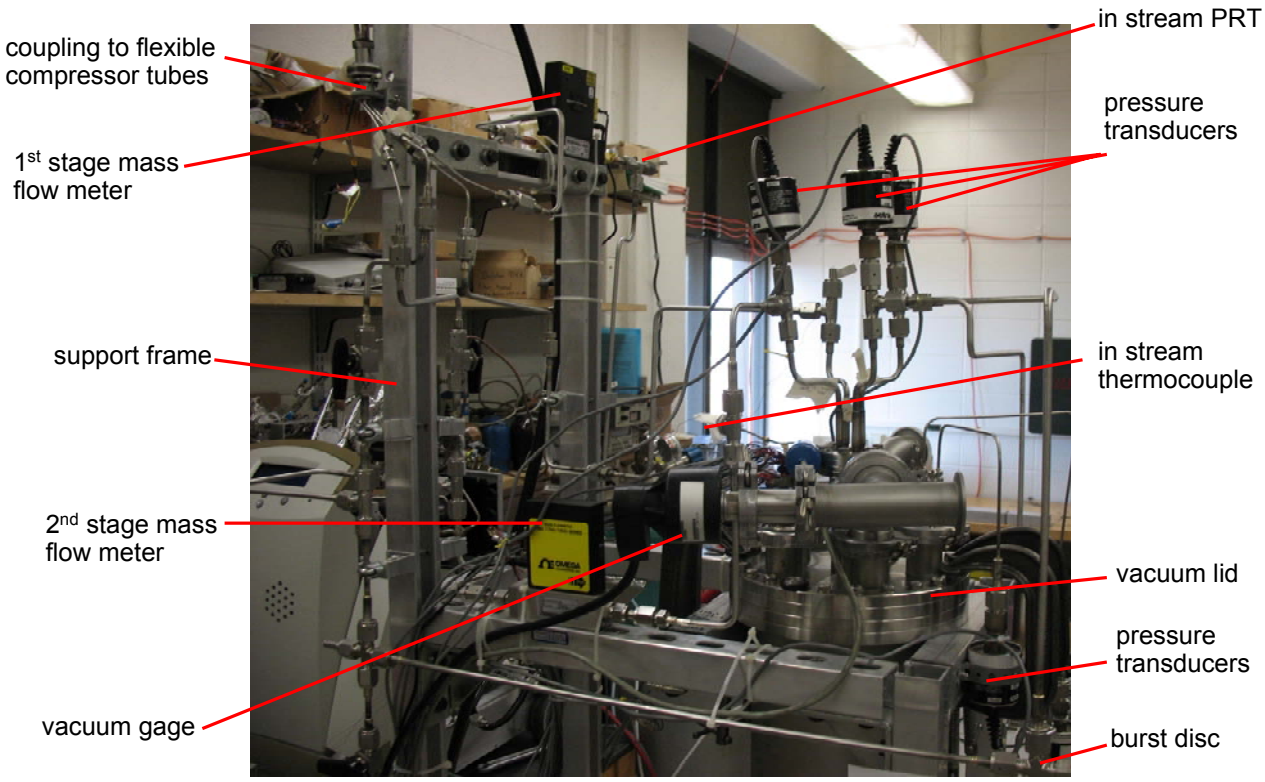

Figure 4-5: Photograph of the instrumentation and cycle components outside the vacuum chamber.

4.3.2 Cryoprobe modifications

Several modifications were made to the commercial cryoprobe in order to incorporate the measurement instrumentation. As discussed in Section 1.4, the mixture expands at the end of a capillary tube in the active portion of the cryoprobe tip shown in Figure 4-6. This small section of the probe encloses the mixture at three critical thermodynamic states: before the expansion valve, after the expansion valve, and after the thermal load is applied (corresponding to states 5, 6 and 7 in Figure 4-1, respectively). It is important to separately and accurately measure these states to understand the cycle; however, these temperatures and pressures in the flow stream cannot be measured using the as-built hardware configuration due to the space limitations at the tip of the probe. The hardware has been modified in order to separate these state points into three distinct locations where the temperature and pressure can be directly and precisely

measured. The modified cryoprobe also incorporates embedded temperature measurements on the low pressure side of the recuperator; these correspond to the "PRTi" measurements in Figure 1-11.

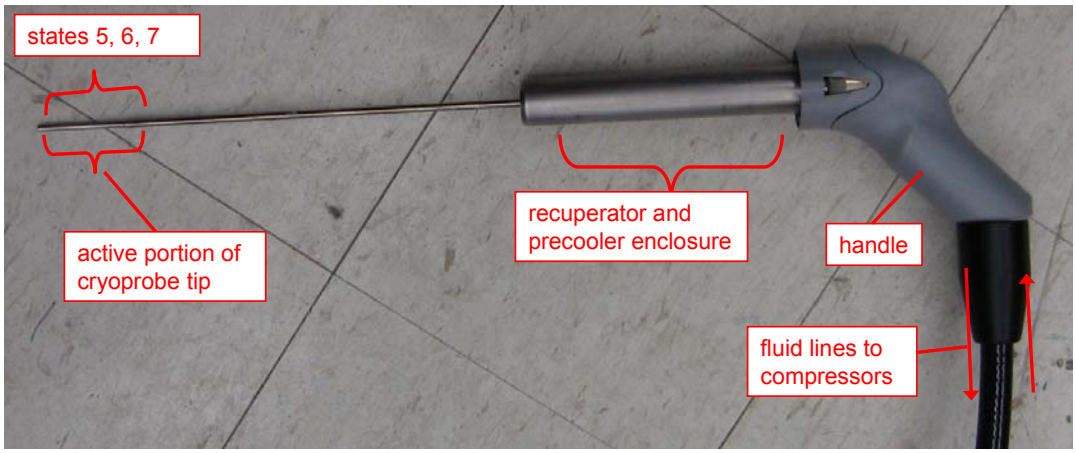

Figure 4-6: Photograph of the cryoprobe highlighting the locations corresponding to thermodynamic states 5,6, and 7 in Figure 4-1, which cannot be directly measured using the original probe configuration.

Figure 4-7(a) shows the cryoprobe after the handle and fluid lines connecting the probe to the compressors (shown in Figure 4-6) have been removed. The precooling and recuperative heat exchangers are enclosed in a double-walled stainless steel evacuated sheath, as shown in Figure 4-7(a). This vacuum sheath was removed by separating the welded joint between the warm flange and the tube manifold shown in Figure 4-7(a) and (b). The vacuum sheath is shown separated from the precooler and recuperator assembly in Figure 4-8.

The 1st and 2nd stage working fluid high and low pressure stainless steel tubes are shown in Figure 4-7(a); these tubes connect with the flexible lines to the compressors with a coupling shown in Figure 4-7(a) and (c). The flexible lines cannot be integrated with the vacuum system. Therefore the stainless working fluid tubes were cut as shown in Figure 4-7(a) and fitted with

VCR glands as shown in Figure 4-9. The VCR glands connect to tubes which that pass through the vacuum lid shown at the top left of Figure 4-2.

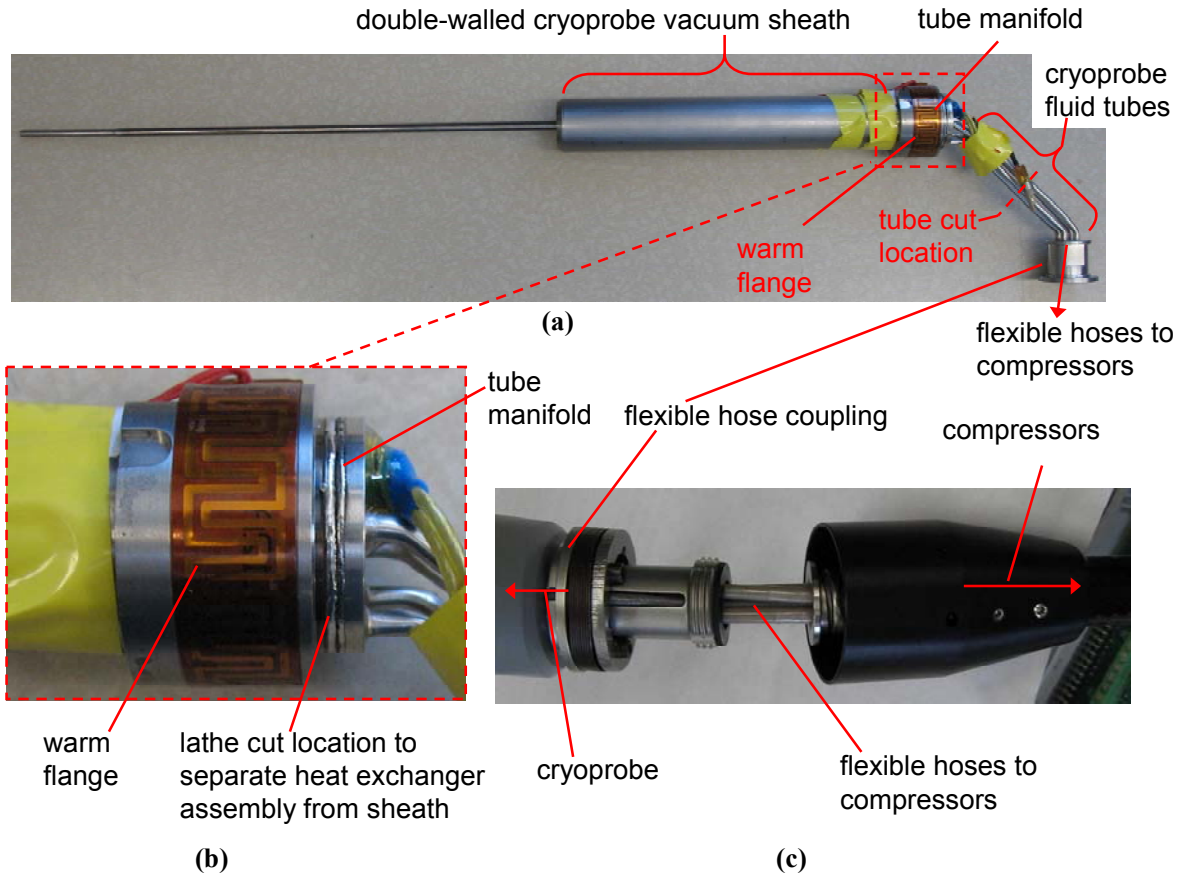

Figure 4-7: **(a) Cryoprobe with the evacuated cryoprobe sheath still attached and the flexible to the compressors hoses disconnected. (b) A close-up view of the back of the cryoprobe focusing on the warm flange and the location of the cut which separates the heat exchanger mandrel from the cryoprobe sheath. (c) Connection between the cryoprobe and the flexible lines to the compressors. The flexible hose coupling depicted in (a) is highlighted.**

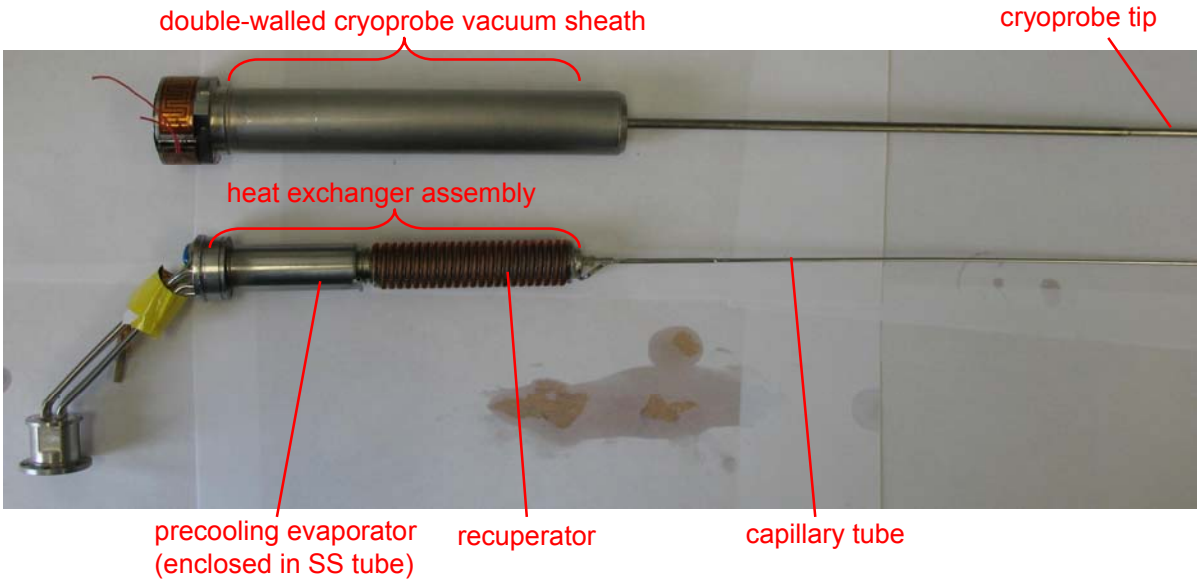

Figure 4-8: Picture of the cryoprobe double-walled vacuum sheath separated from the rest of the cryoprobe. The precooling and recuperative heat exchangers wound about a stainless steel mandrel as well as the 2nd stage capillary tube are shown.

The new cryoprobe sheath shown in Figure 4-9 was fabricated using a 1" OD stainless steel tube (#5) with thin walls (0.020") in order to limit axial conduction. A new warm flange piece, shown in Figure 4-7(a), was provided by AMS and was welded onto one end of the tube. A 2 1/8" rotatable conflat (#6) was welded onto the other end. The conflat attached to the sheath mates with another 2 1/8" conflat connected to the high pressure exit and low pressure return (corresponding to states 5 and 7 in Figure 4-1). The mating conflats are also shown in the geometric model in Figure 4-2. The tubing connected to the mating 2 1/8" conflat connects to the portion of test section that includes the jewel orifice and the Nichrome wire load heater.

A thermally isolating support shown in Figure 4-9 suspends the probe from the vacuum lid, as shown in Figure 4-3. The "warm flange clamp" holds the cryoprobe sheath and the precooler/recuperator section together; the joint is sealed with an EPDM o-ring (#7) that was selected based on its chemical compatibility with the hydrocarbon and synthetic refrigerants (according to the DuPont, Air Liquide, Advanced Specialty Gas, Advanced Fluid Connectors,

and efunda references provided at the end of this section). Figure 4-9 also shows the VCR glands soldered to the working fluid tubes that interface with the vacuum pass-through tubes. Finally, the capillary tube shown in Figure 4-8 was removed as the pressure drop will be achieved using the jewel orifice. A 1/8" stainless steel tube was soldered (using 95/5 solder) onto the end of the high pressure recuperator tube in place of the capillary tube. The tube is shown in Figure 4-9 labeled "mixture high pressure pass-through tube" and passes through the 2 1/8" mating conflats on the new cryoprobe sheath.

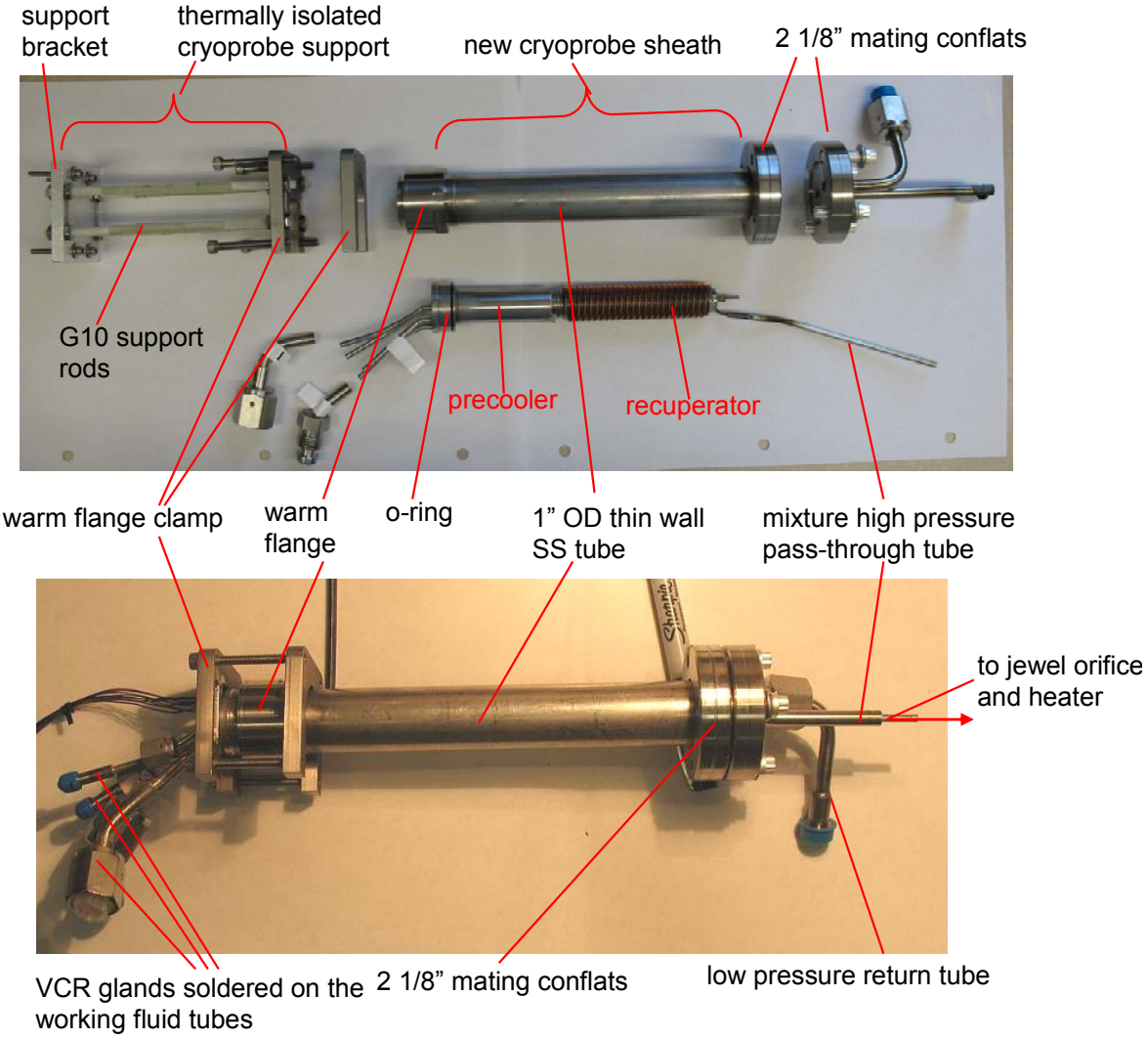

Figure 4-9: (Top) Expanded assembly view of new cryoprobe sheath assembly and thermally isolating cryoprobe support. (Bottom) Partially assembled new cryoprobe sheath. Note that photo includes the high pressure mixture tube which passes through the 2 1/8" conflat, but the tube is not shown passing through the conflat.

The commercial cryoprobe system uses a G10 sheath to fill the gap between the tips of the recuperator fins and the inside diameter of the double walled vacuum sheath. The G10 sheath piece forces the low pressure gas mixture to flow in close contact with the recuperator fins. Figure 4-10 shows the old G10 sheath over the recuperator.

A new G10-CR (cryogenic-grade G10, selected for its low thermal conductivity to minimize axial conduction) sheath (#8) shown in Figure 4-11 was fabricated to accommodate the ID of the new cryoprobe sheath and the OD of the recuperator fins. Additionally, the new G10 sheath was machined so that eight PRT sensors could be embedded at four axial locations along the recuperator (each location has a pair of diametrically opposed sensors). The sensors extend inward to the ID of the G10 sheath and therefore directly measure the fluid temperature. The sheath also has a hole near the end in order to accommodate the lead wires associated with a 9th PRT sensor that is attached to the outside of the "mixture high pressure pass-through tube" (Figure 4-10) and measures the temperature of the low pressure mixture before it enters the recuperator. Figure 4-11 also shows the circumferential and axial grooves cut in the G10 sheath for the PRT wires; the grooves are sufficiently deep so that the wires do not protrude past the OD of the G10 sheath, which is necessary as the G10 sheath and new stainless steel cryoprobe sheath are assembled with a very small clearance.

Figure 4-12 shows the G10 sheath where the PRTs and wires are embedded in the sheath. The PRT wires are wrapped once around the circumference of the sheath near the sensor to provide thermal sinking. The PRT wires are covered in small diameter (0.042") flexible shrink wrap (#9) for electrical isolation, as shown in Figure 4-13. The figure also shows the varnish (#14) used on the PRT leads at the base of the PRT in order to ensure that the wires remain electrically separated. The PRTs and wires were first glued in place using a 30-second epoxy and then covered in Stycast epoxy, as shown in Figure 4-14, in order to achieve a more permanent bond. The epoxy completely fills the grooves in order to minimize the clearance between the OD of the G10 sheath and the ID of the outer stainless steel sheath; this ensures the

mixture flows through the recuperator finned passages rather than between the G10 and outer sheath (which would reduce the effectiveness of the recuperator as the fluid not in contact with the fins does not provide cooling to the high pressure stream). A nylon rod was inserted into the G10 sheath during the epoxy process to ensure the epoxy did not drip inwards and compromise the assembly of the recuperator and the G10 sheath. Figure 4-14 also highlights the attachment of the 9th PRT to the "mixture high pressure pass-through tube" as well as a spring made from a 1/16" stainless steel tube that holds the G10 sheath in place.

Figure 4-10: Picture of cryoprobe showing the old G10 sheath covering the recuperator.

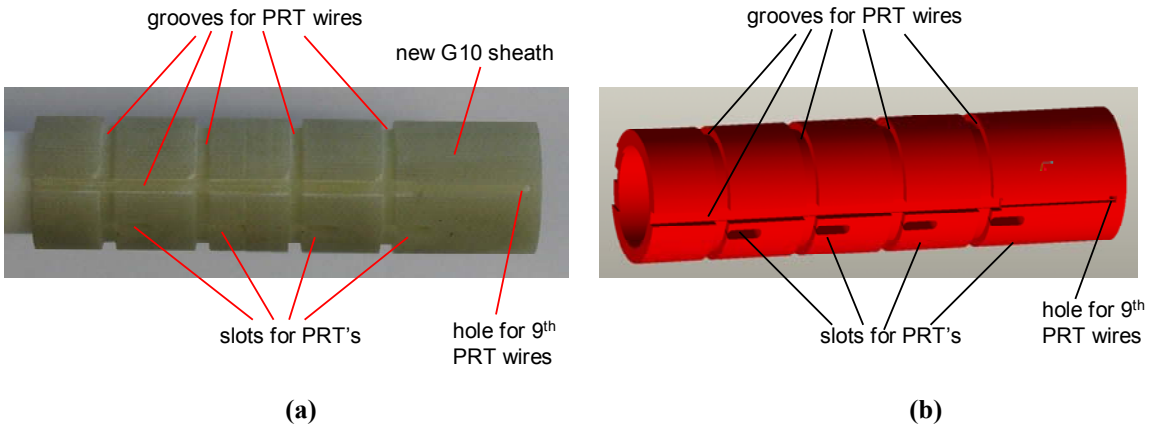

Figure 4-11: Actual (a) and modeled (b) new recuperator G10 sheath showing the slots for the PRTs which extend into the inner diameter to ensure good thermal contact between the fluid and the PRTs. The grooves for the PRT wires are also shown.

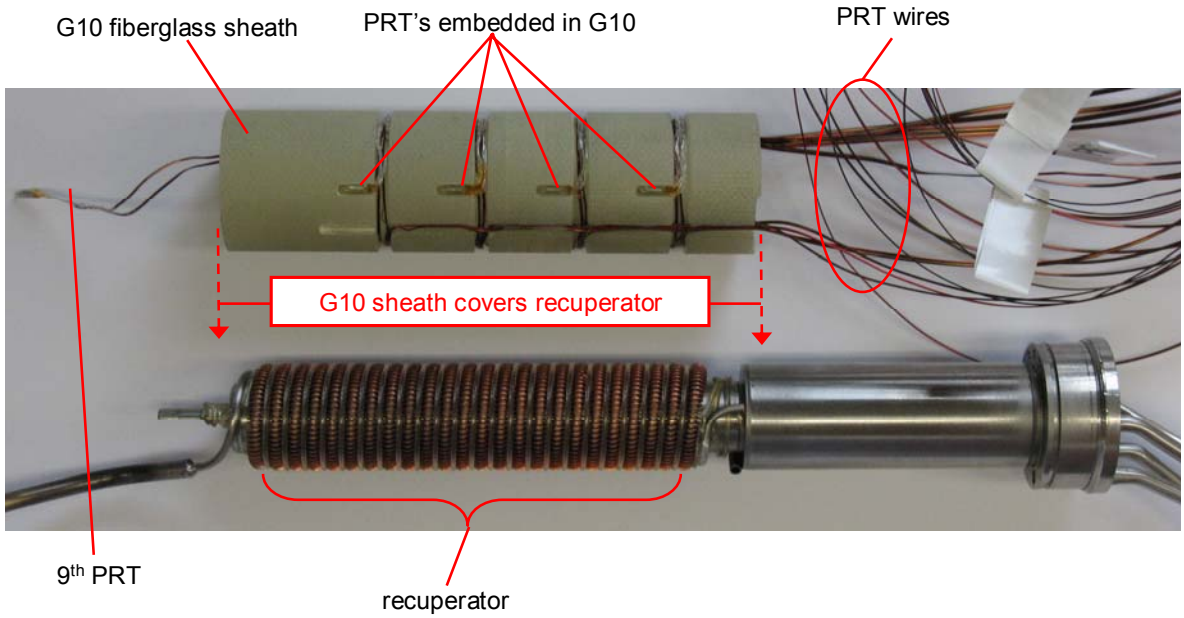

Figure 4-12: New recuperator G10 sheath with embedded PRTs and associated electrical wires. The PRT wires are wrapped once around the G10 sheath to provide thermal sinking.

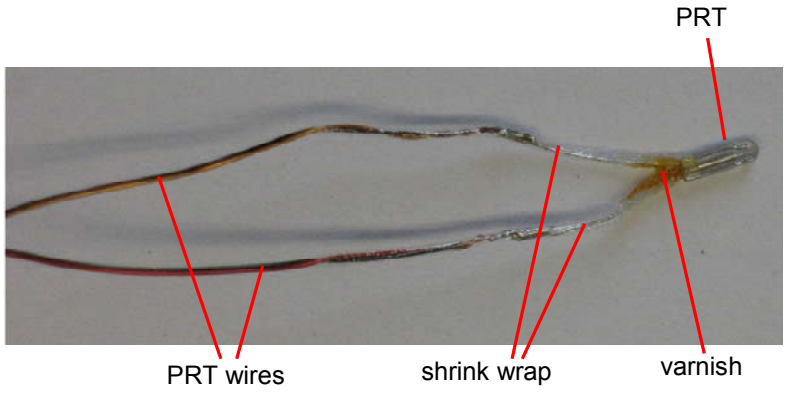

Figure 4-13: Picture of PRT showing the shrink wrap and varnish used for electrical isolation.

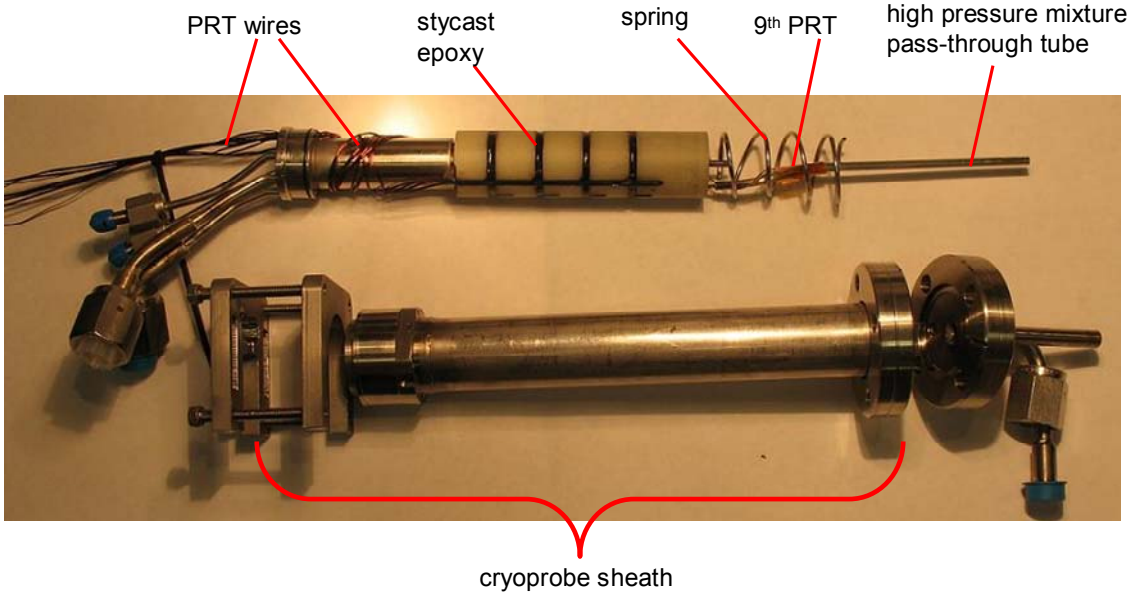

Figure 4-14: Cryoprobe assembly showing the Stycast epoxy covering the PRTs and PRT wires in the G10 sheath. The 9th PRT is shown attached to the high pressure mixture pass-through tube. Finally, the spring that holds the G10 sheath in place is shown.

Figure 4-15 shows the four small holes (0.060") drilled into the back end of the heat exchanger mandrel for the PRT wires to pass-through; these wire feed-throughs were sealed using Stycast epoxy. The figure also shows the EPDM O-ring that makes a seal with the cryoprobe sheath.

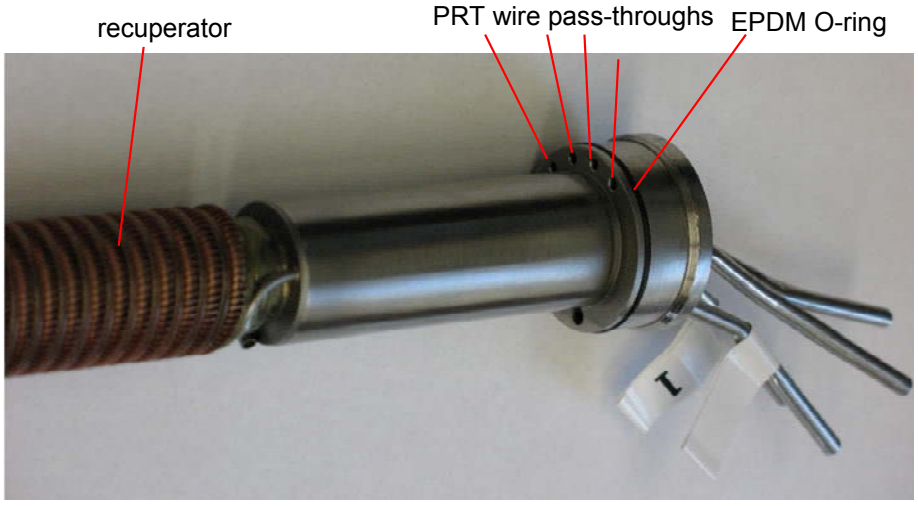

Figure 4-15: Photo of the cryoprobe heat exchanger mandrel with electrical pass-through holes and an EPDM O-ring which provides a seal with the cryoprobe sheath.

4.3.3 Cryoprobe sheath indium O-ring

The EPDM o-ring shown in Figure 4-14 and Figure 4-15 operated near the minimum recommended temperature for the material (Parker O-ring handbook), which resulted in a small refrigerant leak. Even minimal leaks can spoil the quality of the vacuum in the dewar, and in this case the vacuum level repeatedly rose above $1*10^{-3}$ torr (an order of magnitude above the maximum $1*10^{-4}$ level required to eliminate thermal parastics related to conduction and convection). This leak was addressed using an indium seal that reinforces the o-ring joint and maintains a leak-free connection even at cryogenic temperatures. Figure 4-16 shows the integration of the indium clamp and the cryoprobe sheath o-ring joint. A thin wire of indium is placed in the grove where the cryoprobe sheath meets the tube manifold at the back of the probe, the indium wire is sandwiched between the clamp and the manifold to create the seal. The clamp consists of two “c” pieces machined from stainless steel, where the inner diameter of the circle formed by the adjoined c’s is 0.002” larger than the OD of the groove where the cryoprobe sheath and tube manifold connect. The joint was leak tested, while cold, using a

helium leak detector. A spray of liquid/vapor helium was directed at the joint to cool it to approximately 173 K (which is substantially lower than the lowest expected temperature at the joint during the experimental tests – 240 K), no leaks were detected at this temperature and no futher problems were encountered at the joint during the experimental tests.

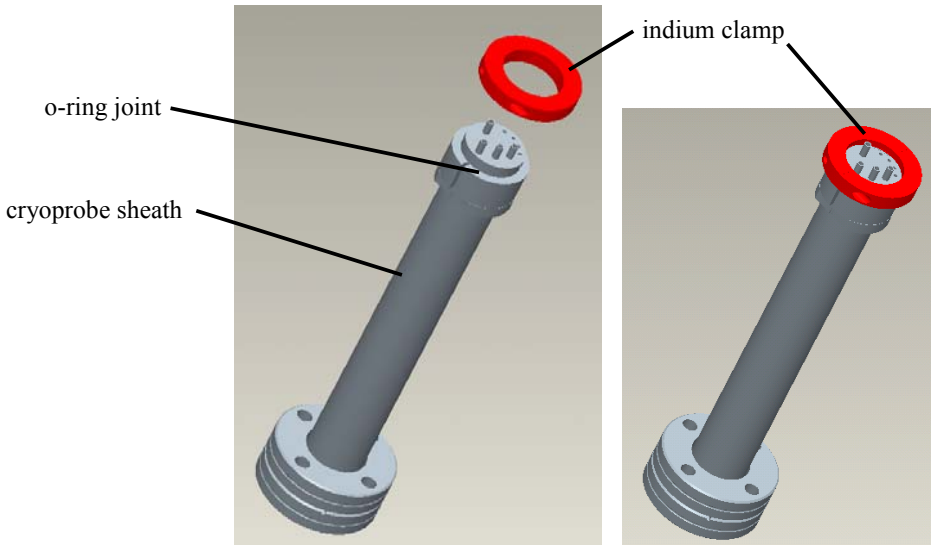

Figure 4-16: Schematic of the indium seal reinforcement of the cryoprobe sheath o-ring joint

4.3.4 Cryoprobe Geometry Analysis

A detailed 3D CAD model of the cryoprobe heat exchanger sheath assembly (which represents the assembly shown in Figure 4-9) was created to guide the test facility construction process, as well as to perform the geometric analyses required to understand the flow passage features that are critical to developing a pressure drop and heat transfer model of the recuperator. The components of the cryoprobe CAD model are shown in an expanded and assembled view Figure 4-17; the color scheme established in the figure is used consistently throughout this section to distinguish the components. The innermost component of the assembly is the precooler/mandrel (magenta), where the precooler is at the proximal (warm) end and the recuperator tube is wrapped in a helix around the mandrel at the distal (cold) end. The

recuperator tube is further divided into finned (red) and smooth (green) sections. Two monofilament wires (cyan) are wrapped about the mandrel to partially fill the interstices formed in the low pressure return path between the successive coils of the recuperator tube (detailed view in Figure 4-23). This configuration is analogous to a staggered tube array, and results in higher pressure drop and correspondingly higher heat transfer rate. The G10 sheath (blue) embedded with PRTs (green) slides over the recuperator, and is aligned on the mandrel by a slot machined in the G10 that mates with the alignment spacer (yellow) soldered on the end of the precooler. A 1/8" tube (purple) soldered to the end of the recuperator passes through the mating conflats and is welded on the distal end to a ¼" tube; the high pressure fluid exiting this tube flows to the jewel orifice, the Nichrome wire heater, and finally returns to the inside of the recuperator sheath assembly via the low pressure return tube (purple). As shown both in Figure 4-17 and Figure 4-9 the warm flange (orange), 1" SS sheath (transparent yellow) and mating conflats (orange, green) slide over the precooler and recuperator and comprise the outer shell of the low pressure return annulus for the JT cycle.

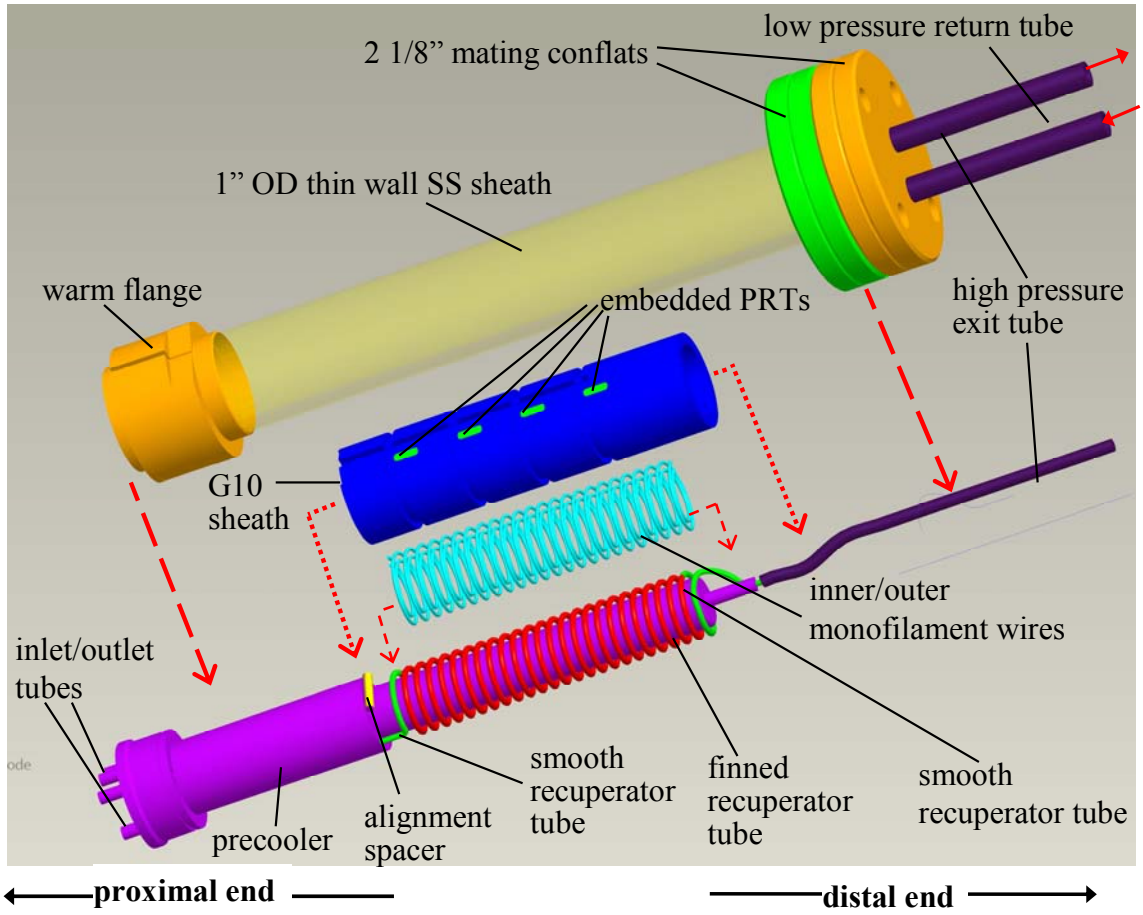

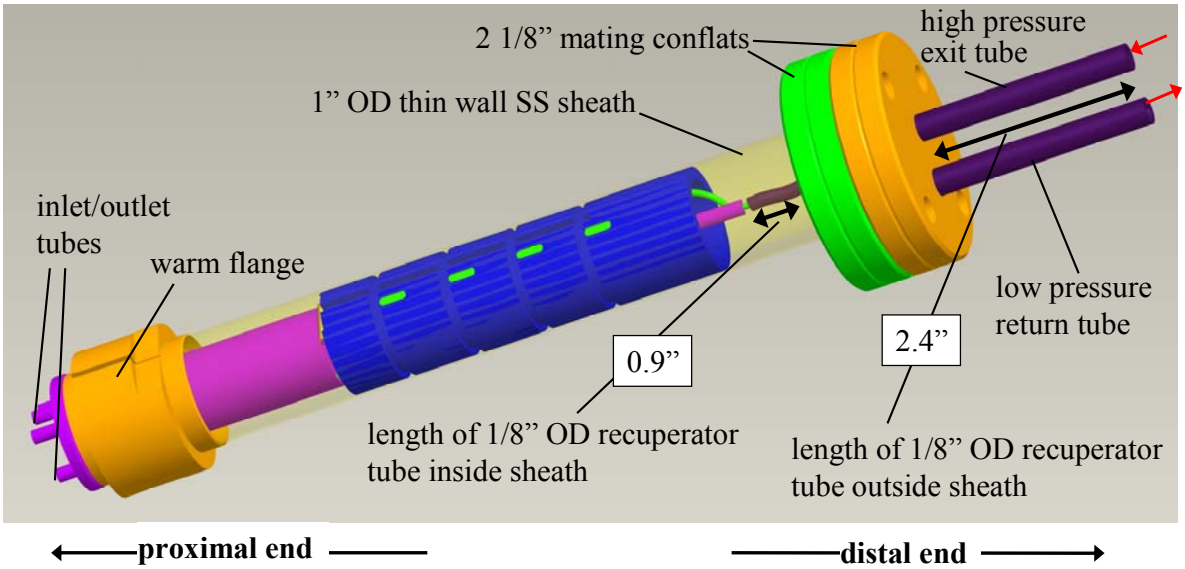

Figure 4-17: CAD geometric model of new cryoprobe sheath (Top) Expanded assembly view (Bottom) sheath assembled.

Figure 4-18 shows a cross section of the assembled cryoprobe components; the cross section passes through the axis of the recuperator and the center of the PRTs. Component labels correspond to those shown in Figure 4-17. The flow paths for the JT cycle are highlighted, including the high pressure fluid inside the recuperator tube and the low pressure stream. The low pressure stream returns first through the annulus between the G10 sheath and the mandrel and continues between the precooler outer shell and the outer 1" SS thin wall sheath before exiting the outlet tubes (magenta). The bottom section of Figure 4-18 shows the locations of the PRTs embedded in the G10 as well as key dimensions for the heat exchanger assembly.

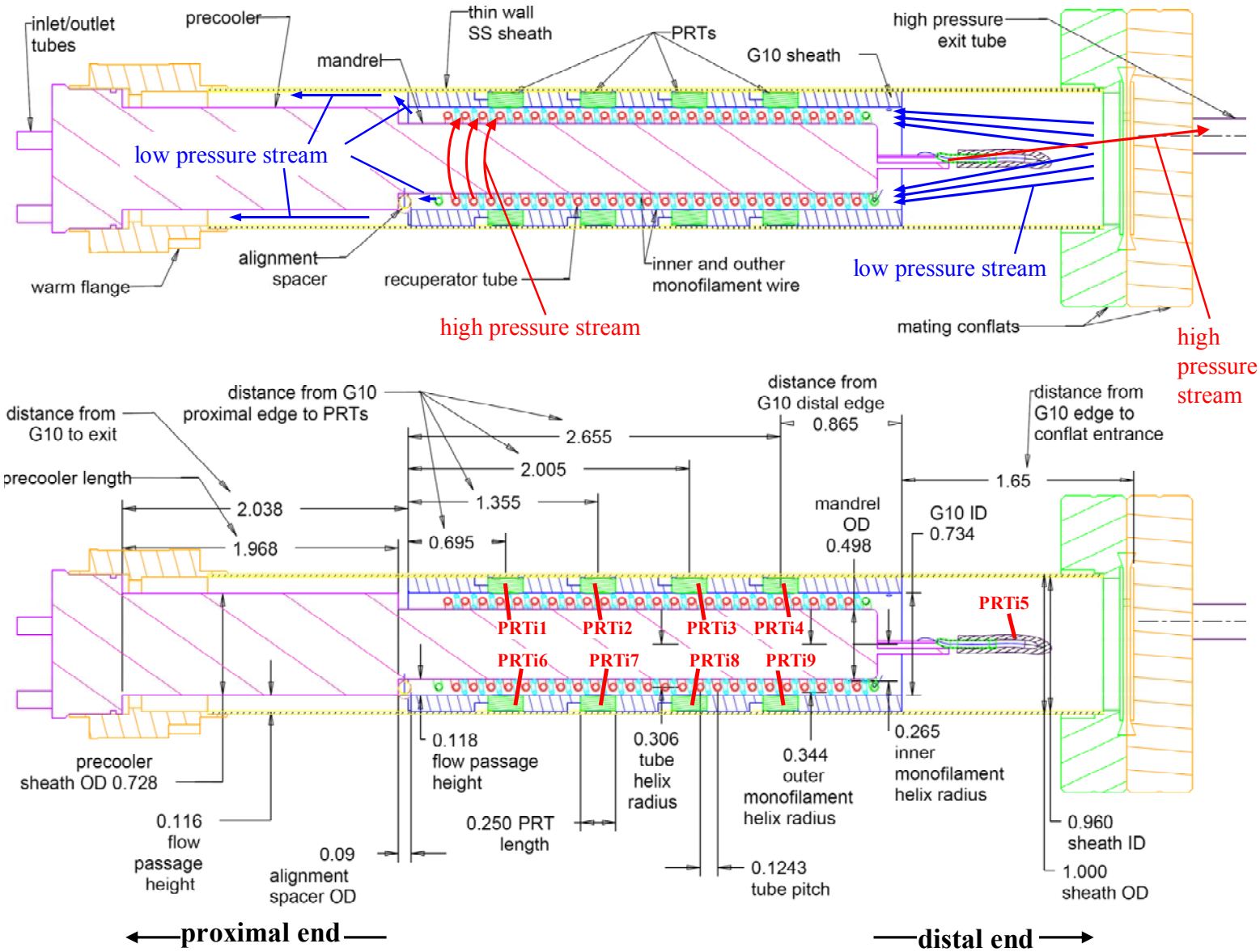

Figure 4-18: Cross section view of the cryoprobe sheath assembly showing (top) component labels and (bottom) geometric measurements.

In order to completely define the recuperator geometry, it is important to establish the orientation angles of the various recuperator tube features (i.e. finned/smooth, wrapped/straight) as well as the PRTs. These angles in turn are used to compute locations of the PRTs relative to the distance along the recuperator helix. Figure 4-19 establishes a plane of reference for these angles; the plane passes through the center of the recuperator and vertically relative to the inlet/outlet tubes. As shown in Figure 1-3, the 0° line is oriented at the top when the inlet/outlet tubes are facing downward.

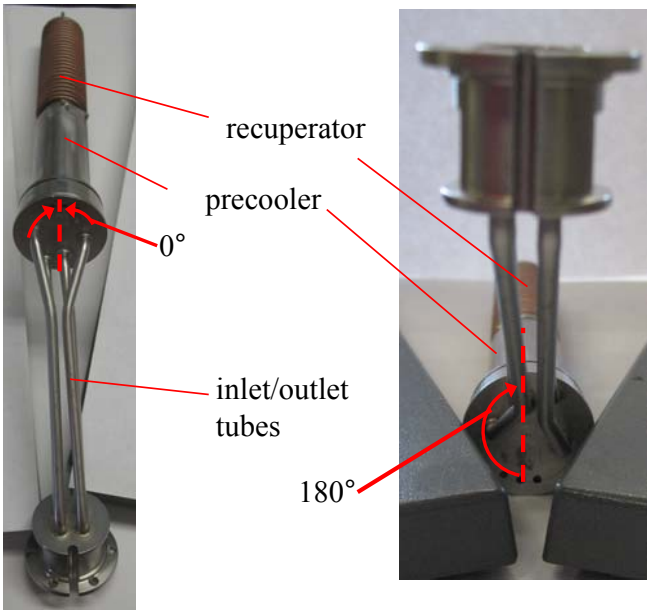

Figure 4-19: Pictures showing the orientation of the angle reference plane relative to the recuperator and inlet/outlet tubes.

Most of the stainless steel recuperator tube is clad with radial copper fins; however, the proximal and distal ends are smooth as shown in Figure 4-20. The smooth sections are further divided into straight and wrapped sections, which have different heat transfer characteristics. Figure 4-21 and Figure 4-22 show the angles of the smooth/finned tube transitions; these angles are used to compute the length of the finned tube ($L_{rec,tot}$) as well as the smooth tube sections

($L_{rec,d,s}$, $L_{rec,d,w}$, $L_{rec,p,s}$, and $L_{rec,p,w}$). These and other cryoprobe heat exchanger assembly dimensions are summarized in Table 4-6. The helical lengths of the wrapped sections of tube are computed according to:

$$L_{helix} = N_{turns}\, 2\pi\sqrt{r_{helix}{}^2 + \left(p/2\pi\right)^2} \tag{4.1}$$

where N_{turns} is the number of revolutions, r_{helix} is the helical radius, and p is the tube pitch between each successive coil. For example, the finned tube has 23.9 turns, a helix radius of 7.77 mm (0.306 in.), and a pitch of 3.15 mm (0.124 in.) resulting in an overall length of 1.171 m (46.1 in.).

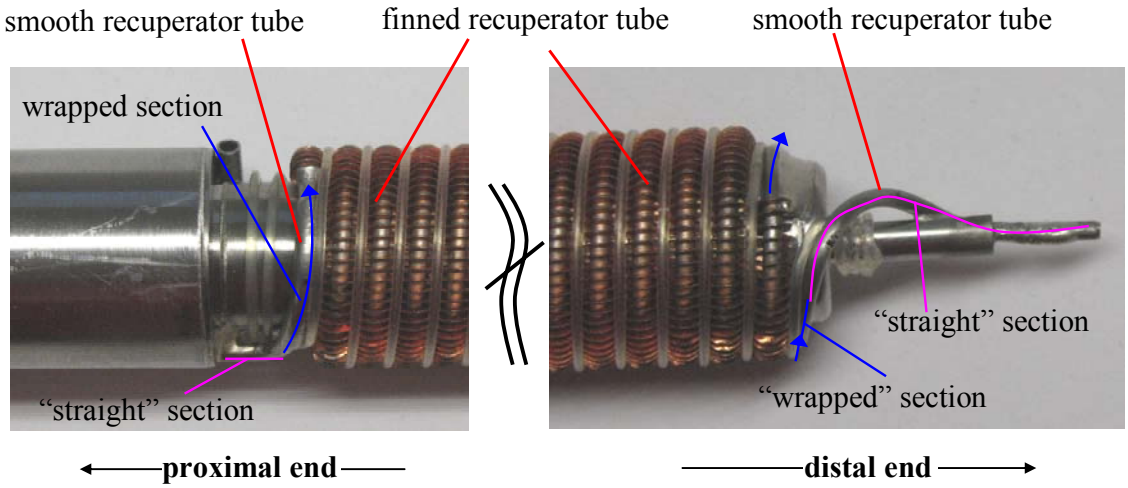

Figure 4-20: Photo of the recuperator tube showing the transition between the finned/smooth sections of the recuperator tube, as well as the wrapped/straight sections of the tube.

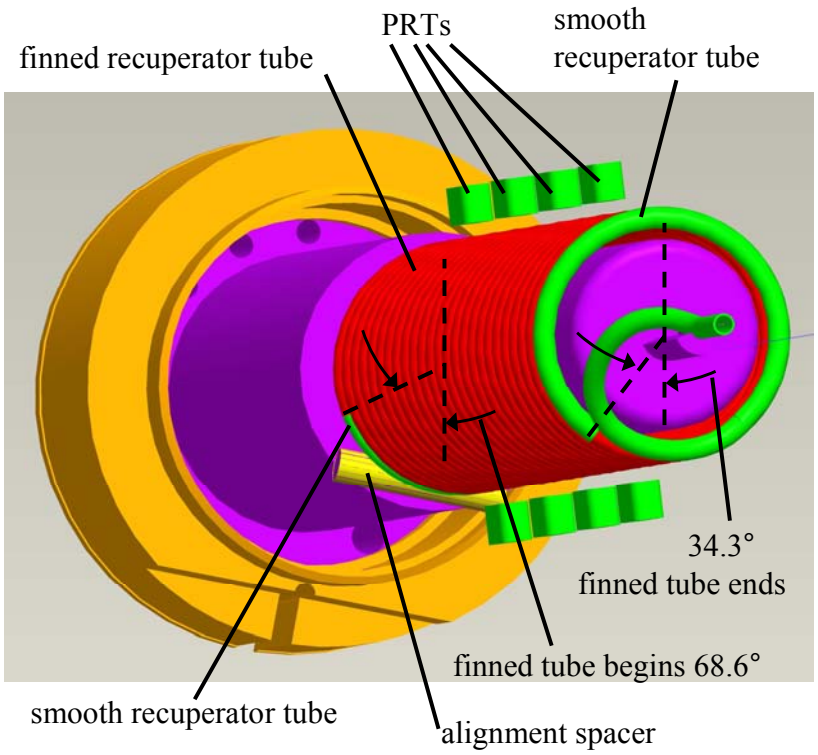

Figure 4-21: CAD drawing showing the angle alignment for the beginning and end of finned tube section of the recuperator. The G10 sheath is hidden to highlight the PRT locations.

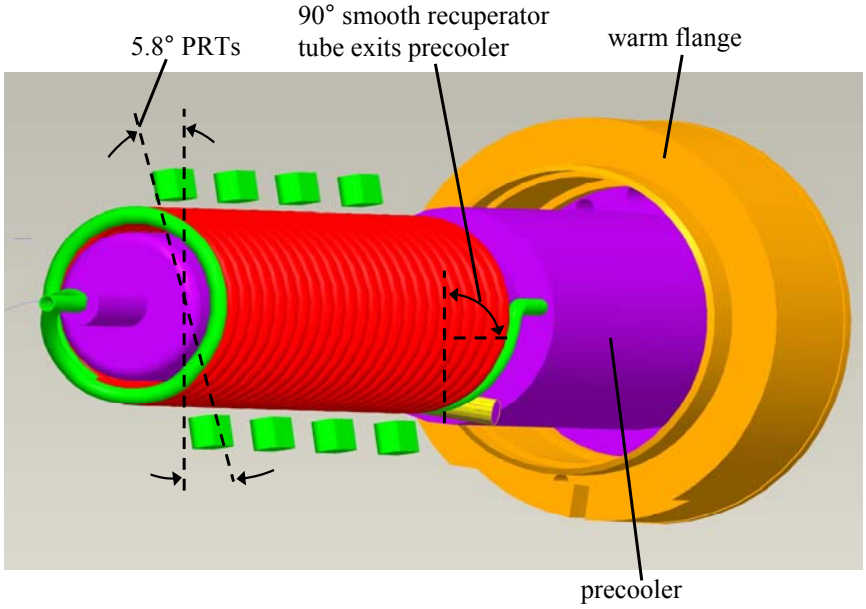

Figure 4-22: CAD drawing showing angle alignment for the PRTs and the beginning of the proximal smooth tube. The G10 sheath is hidden to highlight the PRT locations.

The eight embedded PRTs are epoxied in diametrically opposed 6.35 mm (0.25 in.) long by 2.03 mm (0.08 in.) wide slots that are machined completely through the wall of the G10 sheath. Each slot lies approximately over three tube coils, and subsequently each temperature measurement represents a weighted average of the low pressure fluid flowing over these three tubes. The weighted averages can be computed using the spatial relations of the tubes and the PRTs measured in the CAD model. Figure 4-23 focuses on the recuperator section from Figure 4-18 and shows the distances (projected along the axis of the recuperator) between each of PRT centerlines and the nearest three recuperator tubes; these dimensions are summarized in Table 4-4. Dimensions shown on left and right side of the PRT indicate whether the nearest tube is located proximally or distally, respectively, of the PRT. A magnified view of the low pressure return path is also shown to highlight the staggered flow path formed by the recuperator tube and monofilament wires.

Weighting factors are constructed from the tube-to-PRT measurements to determine the relative contribution to the measured temperature from the fluid over each of the tubes. A linear interpolation is used to determine the factor for the i^{th} distance (i.e. 1st, 2nd ,or 3rd distance for each PRT listed Table 4-4:

$$wf_{\#,i} = \sum_{j=1}^{3} dist_{\#,j} \Bigg/ \sum_{k=1}^{3}\sum_{m=1}^{3} dist_{\#,m} \qquad m \neq k, j \neq i \tag{4.2}$$

where $dist_{\#,j}$ and $dist_{\#,m}$ are the PRT-to-tube distances from Table 4-4 (# is the PRTi# and j and m index through the three distances for each PRT). For example the weighting factor for the 1st distal tube for PRTi2 is:

$$wf_{2,1d} = \frac{0.079 + 0.169}{(0.045 + 0.169) + (0.079 + 0.169) + (0.079 + 0.045)} = 0.423 \qquad (4.3)$$

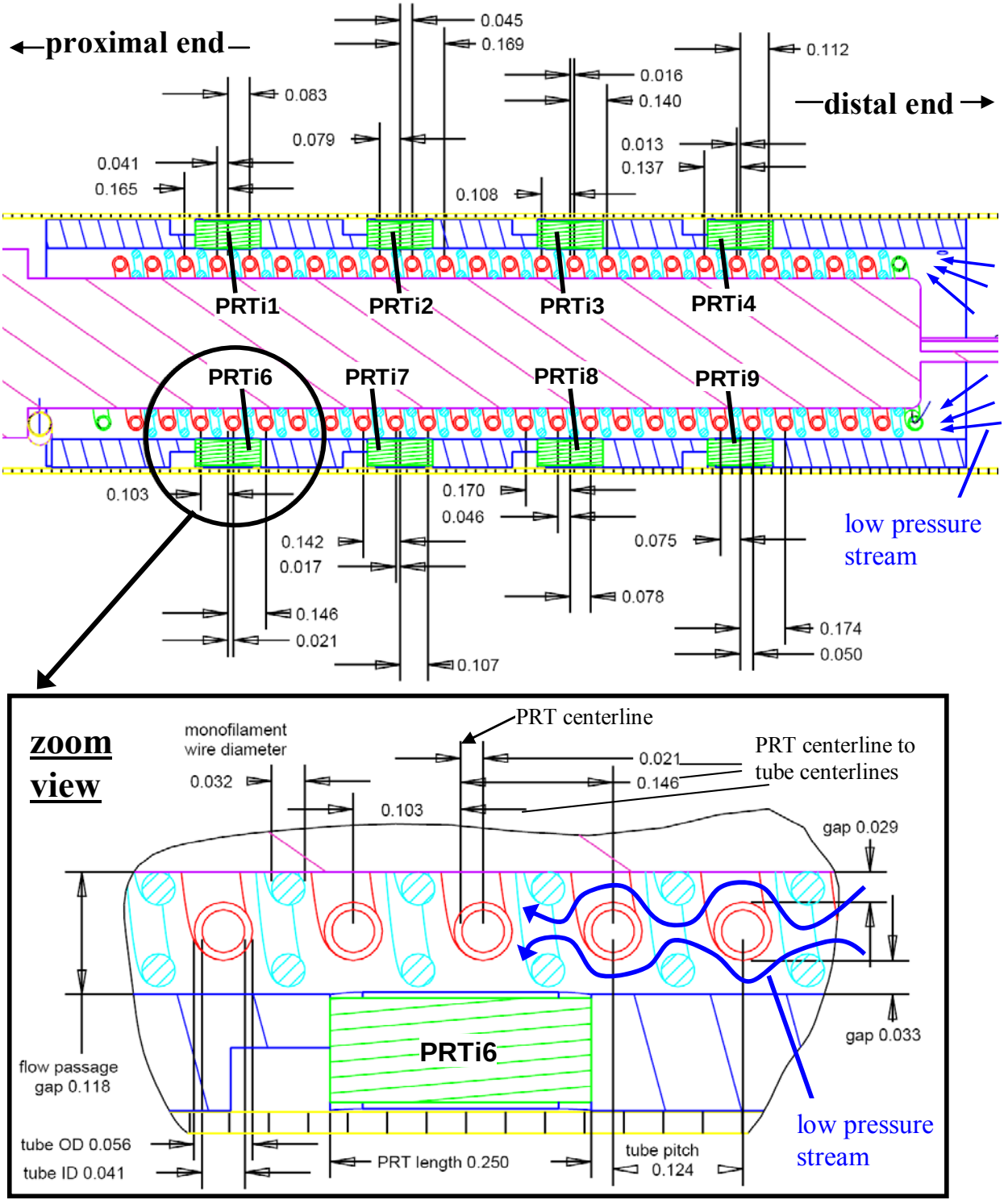

Figure 4-23: Detailed view of the recuperator and embedded PRTs showing the (top) distances from the nearest tube centers to the PRT centerlines and (bottom) magnified view of the low pressure annulus.

Table 4-4: Distances from PRT centerlines to the nearest recuperator tube centers (distance projected along the recuperator axis). The weighting factors corresponding to each measurement computed using a linear interpolation are also shown.

	Distance from PRT to nearest recuperator tube centers [in]				*Weighting factor*			
	2nd proximal	**1st proximal**	**1st distal**	**2nd distal**	**2nd proximal**	**1st proximal**	**1st distal**	**2nd distal**
PRTi1	0.165	0.041	0.083	--	0.215	0.429	0.356	--
PRTi2	--	0.079	0.045	0.169	--	0.365	0.423	0.212
PRTi3	--	0.108	0.016	0.140	--	0.296	0.470	0.235
PRTi4	0.137	0.013	0.112	--	0.239	0.475	0.286	--
PRTi6	--	0.103	0.146	0.021	0.309	0.230	0.461	--
PRTi7	--	0.142	0.017	0.107	--	0.233	0.468	0.299
PRTi8	0.170	0.046	0.078	--	0.211	0.422	0.367	--
PRTi9	--	0.075	0.050	0.174	--	0.375	0.416	0.209

Typically, heat transfer models of Hampson-style recuperators (Fredrikson 2004, 2006, and Pettit 2006) compute the temperature profile as a function of distance along the tube helix. Subsequently, the tube centers used in the preceding weighting factor calculation are related here to the length along the recuperator tube. Figure 4-24 shows the relative angular orientations of the finned/smooth recuperator tube sections to illustrate the calculation of the distance along the recuperator to each of the pertinent tube centers. To reach the 1st tube center included in the weighting factor of PRTi1, the high pressure fluid travels (from the precooler exit) through: (1) the proximal straight and proximal smooth sections, (2) three full revolutions of finned tube, and (3) and an additional 105.6° (105.6/360 = 0.29 revolution). An additional 0.5 revolution brings the fluid to the 1st tube center corresponding to PRTi6. The remaining tube centers for PRTi1-PRTi4 and PRTi6-9 are offset from these first two locations, respectively by integer number of revolutions (one revolution advances the finned tube by $L_{rec,f,rev}$ = 1.927", as computed using Eq. (4.1). Table 4-5 summarizes the distance along recuperator measurements for each of the tube centers listed in Table 4-4. The table additionally shows the distance along the recuperator to PRTi5, which is mounted on the outside of the 1/8" recuperator tube about an inch after the solder joint with the straight, smooth distal recuperator tube section as shown in Figure 4-25.

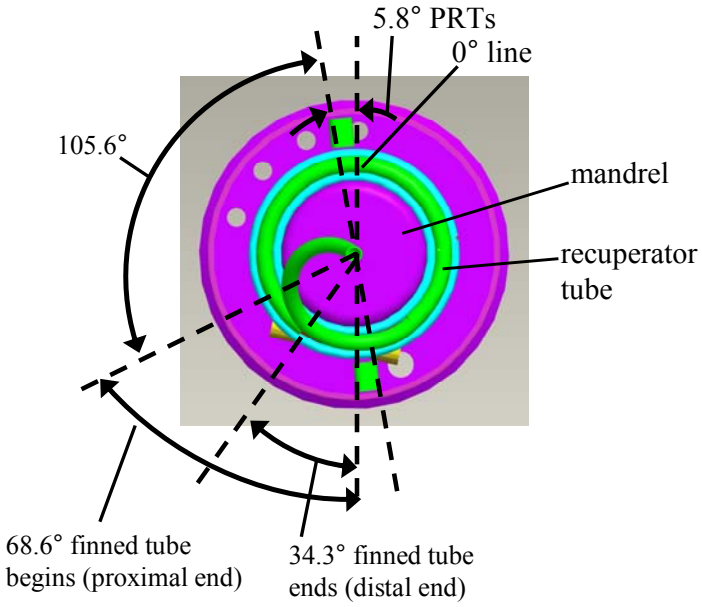

Figure 4-24: Frontal view of the mandrel and recuperator showing the relative angles of the finned tube start/end and the embedded PRTs.

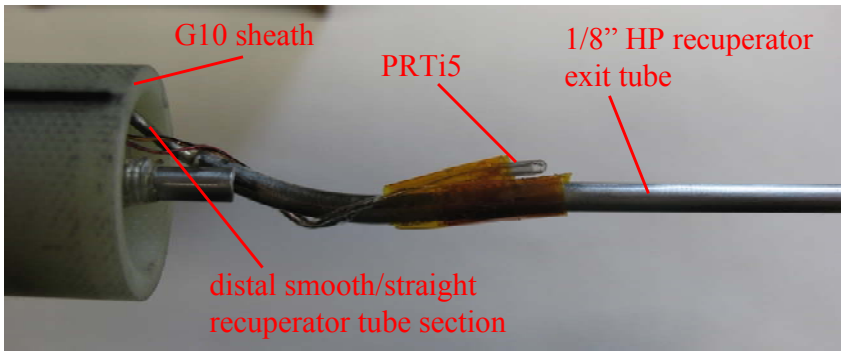

Figure 4-25: Picture showing the location of PRTi5 on the outside of the 1/8" recuperator tube.

Table 4-5: Summary of distances along recuperator to the tube centers nearest the PRTs

	Distance along recuperator after precooler			
	2nd proximal	**1st proximal**	**1st distal**	**2nd distal**
PRTi1	$L_{rec,p,s} + L_{rec,p,w} + 2.3*L_{rec,f,rev}$	$L_{rec,p,s} + L_{rec,p,w} + 3.3*L_{rec,f,rev}$	$L_{rec,p,s} + L_{rec,p,w} + 4.3*L_{rec,f,rev}$	--
PRTi2	--	$L_{rec,p,s} + L_{rec,p,w} + 8.3*L_{rec,f,rev}$	$L_{rec,p,s} + L_{rec,p,w} + 9.3*L_{rec,f,rev}$	$L_{rec,p,s} + L_{rec,p,w} + 10.3*L_{rec,f,rev}$
PRTi3	--	$L_{rec,p,s} + L_{rec,p,w} + 13.3*L_{rec,f,rev}$	$L_{rec,p,s} + L_{rec,p,w} + 14.3*L_{rec,f,rev}$	$L_{rec,p,s} + L_{rec,p,w} + 15.3*L_{rec,f,rev}$
PRTi4	$L_{rec,p,s} + L_{rec,p,w} + 18.3*L_{rec,f,rev}$	$L_{rec,p,s} + L_{rec,p,w} + 19.3*L_{rec,f,rev}$	$L_{rec,p,s} + L_{rec,p,w} + 20.3*L_{rec,f,rev}$	--
PRTi6	$L_{rec,p,s} + L_{rec,p,w} + 2.8*L_{rec,f,rev}$	$L_{rec,p,s} + L_{rec,p,w} + 3.8*L_{rec,f,rev}$	$L_{rec,p,s} + L_{rec,p,w} + 4.8*L_{rec,f,rev}$	--
PRTi7	--	$L_{rec,p,s} + L_{rec,p,w} + 7.8*L_{rec,f,rev}$	$L_{rec,p,s} + L_{rec,p,w} + 8.8*L_{rec,f,rev}$	$L_{rec,p,s} + L_{rec,p,w} + 9.8*L_{rec,f,rev}$
PRTi8	$L_{rec,p,s} + L_{rec,p,w} + 12.8*L_{rec,f,rev}$	$L_{rec,p,s} + L_{rec,p,w} + 13.8*L_{rec,f,rev}$	$L_{rec,p,s} + L_{rec,p,w} + 14.8*L_{rec,f,rev}$	--
PRTi9	--	$L_{rec,p,s} + L_{rec,p,w} + 18.8*L_{rec,f,rev}$	$L_{rec,p,s} + L_{rec,p,w} + 19.8*L_{rec,f,rev}$	$L_{rec,p,s} + L_{rec,p,w} + 20.8*L_{rec,f,rev}$
PRTi5	$L_{rec,p,s} + L_{rec,p,w} + 23.9*L_{rec,f,rev} + L_{rec,d,s} + L_{rec,d,s}$			

The geometric analysis in this section allows a modeled temperature profile to be compared to the measured temperatures using the weighting factors from Table 4-4 and the recuperator lengths in Table 4-5. A heat transfer model that captures the detailed recuperator geometry is beyond the scope of this thesis, but a comparison method is presented here for future analysis of the cryoprobe system. The modeled PRTi# values can be computed according to:

$$PRTi\#_{\text{mod}} = \sum_{i=1}^{3} T_{tc,\#,i}\, wf_{\#,i} \tag{4.4}$$

where $T_{tc,\#,i}$ is the computed tube center temperature for PRTi# at the i^{th} tube (1^{st}/2^{nd} distal/proximal relative to PRTi#). For example, the modeled temperature for PRTi2 would be computed as:

$$PRTi2_{\text{mod}} = T_{tc,2,1p}\, wf_{2,1p} + T_{tc,2,1d}\, wf_{2,1d} + T_{tc,2,2d}\, wf_{2,2d} \tag{4.5}$$

4.3.4.1 Frontal flow area

Heat transfer models typically include Reynolds number or mass flux terms that incorporate the frontal flow area. The two sections for frontal flow area in the recuperator low pressure return annulus are shown in Figure 4-26. The frontal flow area for the recuperator tube section is computed according to:

$$A_{ff,rec,c,tube} = A_{G10,i} - \left(A_m + A_{rec,tube} + A_{rec,f} \right) \tag{4.6}$$

where the cross sectional areas for the inside of the G10 sheath ($A_{G10,i}$), the mandrel (A_m), the recuperator tube ($A_{rec,tube}$) and the recuperator fins ($A_{rec,f}$) are computed using:

$$A_{G10,i} = \pi r_{G10,i}^2 \tag{4.7}$$

$$A_m = \pi r_m^2 \tag{4.8}$$

$$A_{rec,tube} = OD_{rec}\left(2\pi r_{rec,helix}\right) \tag{4.9}$$

$$A_{rec,f} = 2\left(tf_{rec}\, h_f\right) Nf_{rev} \tag{4.10}$$

where $r_{G10,i}$ is the inner radius of the G10 sheath, r_m is the radius of the recuperator mandrel, OD_{rec} is the outer diameter of the recuperator tube, $r_{rec,helix}$ is the recuperator tube helix radius ,tf_{rec} is the recuperator fin thickness, h_f is the height of the fins above the tube, and Nf_{rev} is the number of fins per revolution.

Similarly the frontal flow area in the monofilament wire section is computed as:

$$A_{ff,rec,c,mf} = A_{G10,i} - \left(A_m + A_{mfo} + A_{mfi}\right) \tag{4.11}$$

where the outer and inner monofilament wire cross sectional areas (A_{mfo}, A_{mfi}) are computed as:

$$A_{mfo} = d_{mf}\left(2\,\pi\, r_{mfo,hlx}\right) \tag{4.12}$$

$$A_{mfi} = d_{mf}\left(2\,\pi\, r_{mfi,hlx}\right) \tag{4.13}$$

where d_{mf} is the monofilament wire diameter and $r_{mfo,hlx}$ and $r_{mfi,hlx}$ are respectively the outer and inner monofilament wire helix radii.

Finally, the cross sectional area for the inside of the recuperator tube is computed as:

$$A_{ff,rec,h} = \pi\left(ID_{rec}/2\right)^2 \tag{4.14}$$

where ID_{rec} is the inner diameter of the recuperator tube. The frontal flow path dimensions and areas are summarized in Table 4-6.

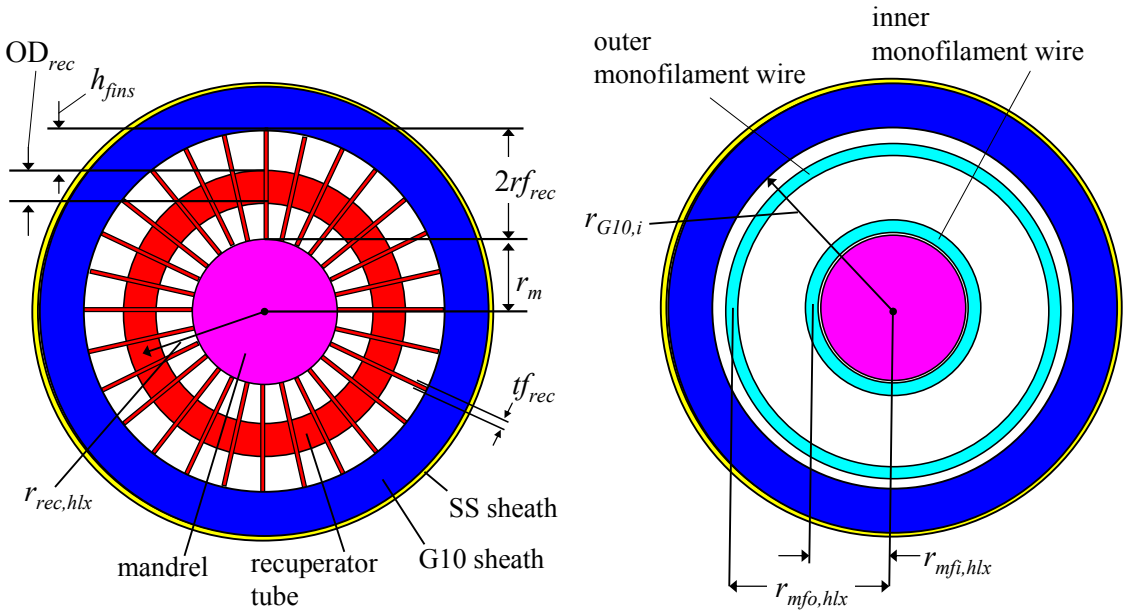

Figure 4-26: Frontal flow area for the recuperator low pressure side at the (a) the recuperator tube and (b) the monofilament wire

Table 4-6: Summary of important cryoprobe heat exchanger assembly dimensions.

Measurement description	Nomenclature	Value	Units
Frontal flow area in the low pressure (cold) side of the recuperator at the monofilament wires	$A_{ff,rec,c,mf}$	$6.833*10^{-5}$	m^2
Frontal flow area in the low pressure (cold) side of the recuperator at the tubes	$A_{ff,rec,c,tube}$	$6.136*10^{-5}$	m^2
Flow area inside the recuperator tube	$A_{ff,rec,h}$	$8.518*10^{-7}$	m^2
Cross section area inside G10 inner radius	$A_{G10,i}$	$2.73*10^{-4}$	m^2
Cross section area of recuperator mandrel	A_m	$1.257*10^{-4}$	m^2
Cross section area of inner monofilament wire	A_{mfi}	$3.438*10^{-5}$	m^2
Cross section area of outer monofilament wire	A_{mfo}	$4.462*10^{-5}$	m^2
Cross section area of recuperator fins	$A_{rec,f}$	$1.65*10^{-5}$	m^2
Cross section area around of recuperator tube	$A_{rec,tube}$	$6.946*10^{-5}$	m^2
Monofilament wire diameter	d_{mf}	0.032	in
Recuperator tube fin height	h_f	0.029	in
Annulus height for recuperator	h_{rec}	0.118	in
Annulus height between precooler and SS sheath	$h_{sheath-pc}$	0.116	in
ID of 1/8” HP exit recuperator tube	ID_{hpe}	0.055	in
Precooler un/finned tube ID	ID_{pc}	0.041	in
Recuperator un/finned tube ID	ID_{rec}	0.041	in
SS sheath ID	ID_{sheath}	0.96	in
Length of 1/8” HP exit tube inside SS sheath	$L_{hpe,i}$	0.9	in
Length of 1/8” HP exit tube outside SS sheath	$L_{hpe,o}$	2.4	in
Finned length of precooler tube (wrapped)	$L_{pc,f}$	21.7	in
Unfinned length of precooler tube (straight)	$L_{pc,s}$	0.5	in
PRT slot length	L_{PRT}	0.25	in
Distal smooth recuperator tube length (straight)	$L_{rec,d,s}$	1.2	in
Distal smooth recuperator tube length (wrapped)	$L_{rec,d,w}$	1.53	in
Proximal smooth recuperator tube length (straight)	$L_{rec,p,s}$	0.33	in
Proximal smooth recuperator tube length (wrapped)	$L_{rec,p,w}$	0.64	in
Length of a single recuperator tube revolution	$L_{rec,f,rev}$	1.927	in
Total length of finned recuperator tube (wrapped)	$L_{rec,tot}$	46.1	in
Length of annulus between precooler and SS sheath	$L_{sheath-pc}$	1.968	in
Number of fins per revolution (recuperator tube)	Nf_{rev}	63	--
Precooler un/finned tube OD	OD_{pc}	0.056	in
Recuperator un/finned tube OD	OD_{rec}	0.056	in
Recuperator tube pitch	p_{rec}	0.124	in
G10 sheath inner radius	$r_{G10,i}$	0.367	in
Mandrel radius	r_m	0.249	in
Outer monofilament wire helix radius	$r_{mfo,hlx}$	0.344	in
Inner monofilament wire helix radius	$r_{mfi,hlx}$	0.265	in
Recuperator tube helix radius	$r_{rec,hlx}$	0.306	in
Fin radius	rf_{rec}	0.057	in
Recuperator fin thickness	tf_{rec}	0.007	in

4.3.5 Oil Separator and Filter/Drier System for the JT cycle (2nd stage)

It is critical to control the oil flow, moisture, and particulate contamination in the JT cycle to prevent flow stream obstruction. The jewel orifice, which is at the coldest point in the system, is particularly susceptible to a buildup of frozen material that can completely close the small diameter opening (0.01 inch to 0.02 inch). Larger flow passages can be affected as well. For example, during some of the early experimental tests for this project, circulating oil and moisture condensed in the precooler and recuperator tubes (0.045 inch ID) causing partial and complete obstruction. An oil management system and a filter/drier system were incorporated to ensure that only clean, dry gas mixture circulates to the cold components in the cycle. The system shown in Figure 4-27 and described in the proceeding paragraphs has been implemented and has provided hundreds of hours of clog-free operation.

The oil and moisture management system shown in Figure 4-27 builds upon the manufacturer's original contamination control system which featured a single coalescing oil separator and a solenoid valve. The solenoid valve was opened periodically in order to allow the separated oil to return to the compressor. A filter and drier was also installed on the suction side of the compressor (i.e. the system shown in Figure 4-27 without the 2nd oil separator or the replaceable core filter/drier). During a surgery, the solenoid valve briefly (i.e., for 5 seconds) opens at the beginning of each freeze cycle (i.e., every 20 minutes) causing the high pressure gas to bypass the cryoprobe plumbing through the valve; during the bypass, the gas carries the separated oil back to the compressor. This configuration was not compatible with the cryoprobe system that has been modified in order to create the experimental test facility. The modifications added significant thermal mass to the cryoprobe and therefore the system requires uninterrupted flow for 60-120 minutes to reach steady state. Furthermore, a typical test matrix

may include a range of test conditions that require substantial time to achieve. Activation of the solenoid only once, at the beginning of testing, was not sufficient to carry the oil accumulated in the separator back to the compressor. Therefore, a solenoid valve control system was designed and installed that is independent of the manufacturer's control electronics, allowing for independent control of the solenoid valves. Additionally, a second oil separator (item #15 in Table 4-15) and solenoid valve were added in series with the first separator as an extra precaution against oil reaching the cold components. At intervals specified in the LabVIEW DAQ, the first and second valve open sequentially, each for four seconds, with a four second delay between the openings.

Even with the oil properly managed by the separators and solenoid valves, flow obstructions persisted in the jewel orifice. The compressors had been exposed to atmosphere during the modifications, and the highly hydroscopic compressor POE oil quickly absorbs moisture from the ambient air. This water circulates with the gas and collects and freezes in the orifice. Therefore, an oversized replaceable core filter/drier with 42 in^3 of desiccant (item #12 in Table 4-15) was added between the compressor and the cryoprobe plumbing in order to capture any moisture in the flow stream.

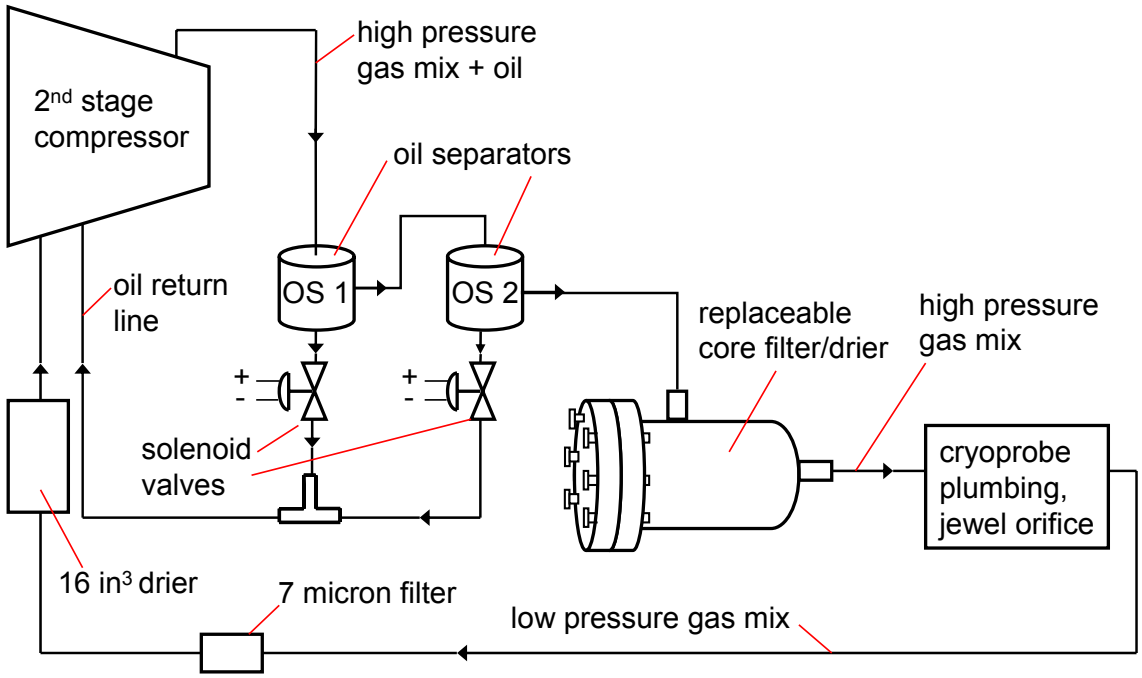

Figure 4-27: Oil separation and filter/drier system for the 2nd stage JT cycle. The solenoid valves for oil return are controlled by relays connected to the LabVIEW DAQ system.

4.3.6 Vacuum system and radiation insulation

The cold components of the cryoprobe system are enclosed in a vacuum chamber that is evacuated to less than 1×10^{-4} Torr (which effectively eliminates conduction and convection parasitic heat leak in the vacuum space) using a turbomolecular pump. In addition, the cold components are enclosed in multiple layers of radiation MultiLayer Insulation (MLI) to significantly reduce the parasitic radiation load from ambient. The MLI consists of a thin Mylar substrate coated with aluminum which provides a reflective surface (emissivity ≈ 0.05) and therefore a high radiation resistance. Dacron netting is placed between each layer to prevent conduction through the layers.

The number of MLI layers is chosen to balance the parasitic heat leak with the complexity of installation. The radiative parasitic heat leak must be reduced to a level that is small relative to the refrigeration provided by the cryoprobe. However, the number of layers should not be

excessive in order to reduce the installation time, as well as the time required to remove and replace the insulation (which will be done repeatedly to change the jewel orifice size). The radiation heat leak is estimated (Incropera & DeWitt, p 678) based on the geometry of the cryoprobe plumbing, the number of MLI layers, and the vacuum enclosure temperature (which is at ambient temperature). The heat leak calculation includes the radiation resistances between: the vacuum enclosure and the MLI, the layers of MLI, and the inner MLI layer and cold the cryoprobe fittings. The cold components are all assumed to be at a nominal load temperature of 170 K and the vacuum enclosure is assumed to be at 300 K. Many of the components would be somewhat warmer than the load (~200-250 K) so the computation represents a conservative estimate for the radiation. The radiation heat leak is shown as a function of number of MLI layers in Figure 4-28; seven layers of MLI were selected for reasons discussed below.

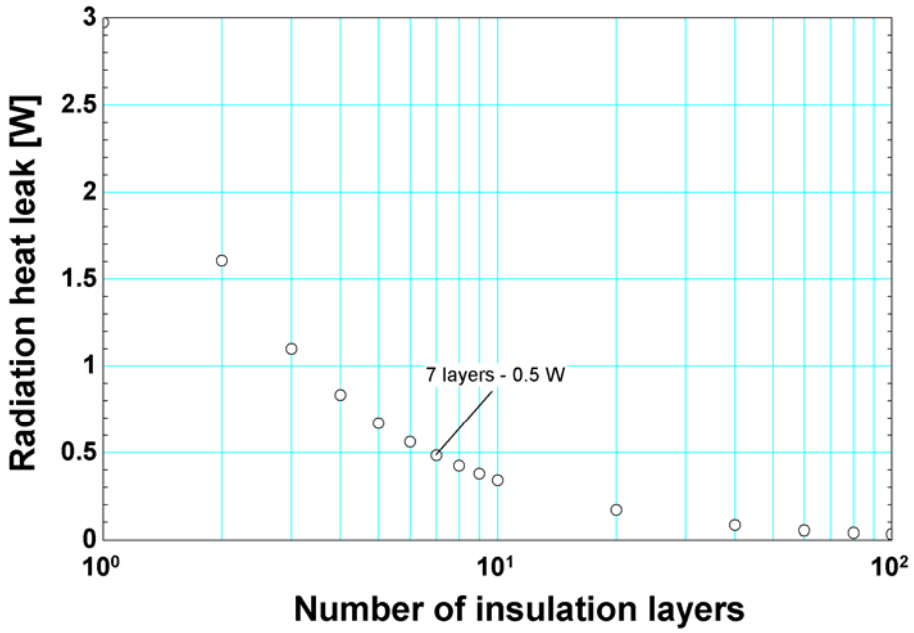

Figure 4-28: Calculated radiation heat leak as a function of number of MLI layers.

The radiation heat leak is compared to the baseline load curve (i.e. the load curve performance of cryoprobe before the modifications) to determine if the load significantly

changes the refrigeration performance. The unmodified cryoprobe was only cold at the tip, which has a very small surface area, so the radiation heat leak during these tests is considered negligible compared to the leak with the modified cryoprobe. Therefore, the parasitic heat leak in Figure 4-28 represents an additional load on the cryoprobe. The additional load is debited from the refrigeration power, so for a given tip temperature the cryoprobe will be able to accept less heat load from the Nichrome wire heater ($\dot{Q}_{load}$, computed by the voltage and current measurements V_{load} and I_{load} indicated on Figure 4-1). Figure 4-32 compares the baseline load curve and the load curve with 0.5 W of parasitic load, which corresponds to the modified cryoprobe with seven layers of MLI. The load curve shifts only slightly when compared to the range of operating temperatures and applied heat load ($\dot{Q}_{load}$) from the unmodified cryoprobe. Therefore, the use of seven layers of MLI achieves the balance of minimizing the effect of the radiative heat leak and the complexity of the installation.

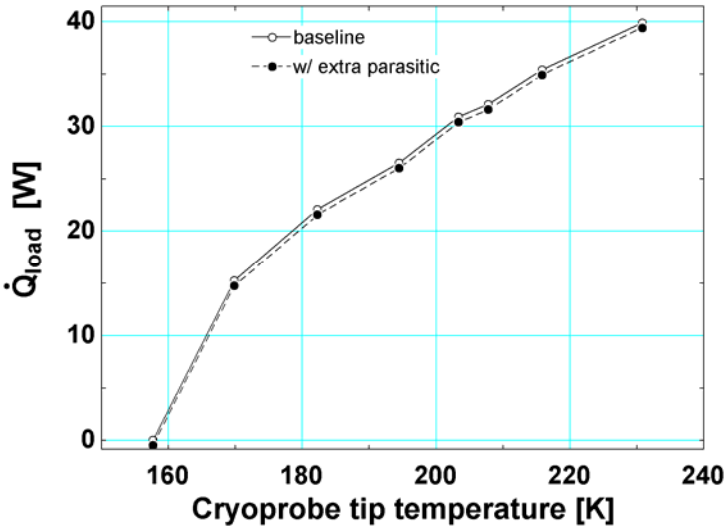

Figure 4-29: Comparison of applied heat load vs. tip temperature for the original cryoprobe and the modified cryoprobe with seven layers of MLI insulation

The locations of the MLI layers were chosen such that each successive layer attaches to plumbing that is at the same approximate temperature as the MLI. The temperatures of the layers are readily computed using the radiation resistance network described in (Incropera & DeWitt, 2002) the layer temperatures are shown in Figure 4-30. The locations of the MLI layers relative to the cryoprobe plumbing inside the vacuum chamber are shown in Figure 4-31.

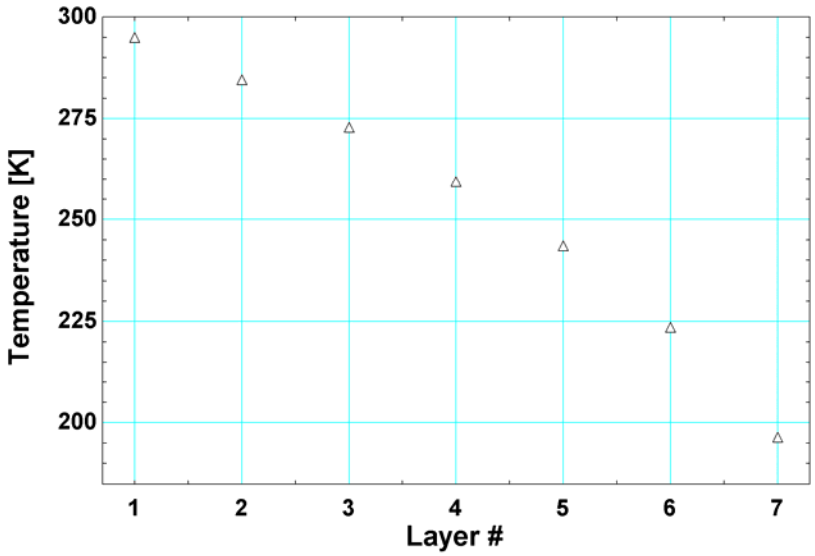

Figure 4-30: Temperatures of each of the seven layers of MLI radiation using a cold temperature of 170 K and an ambient temperature of 300 K.

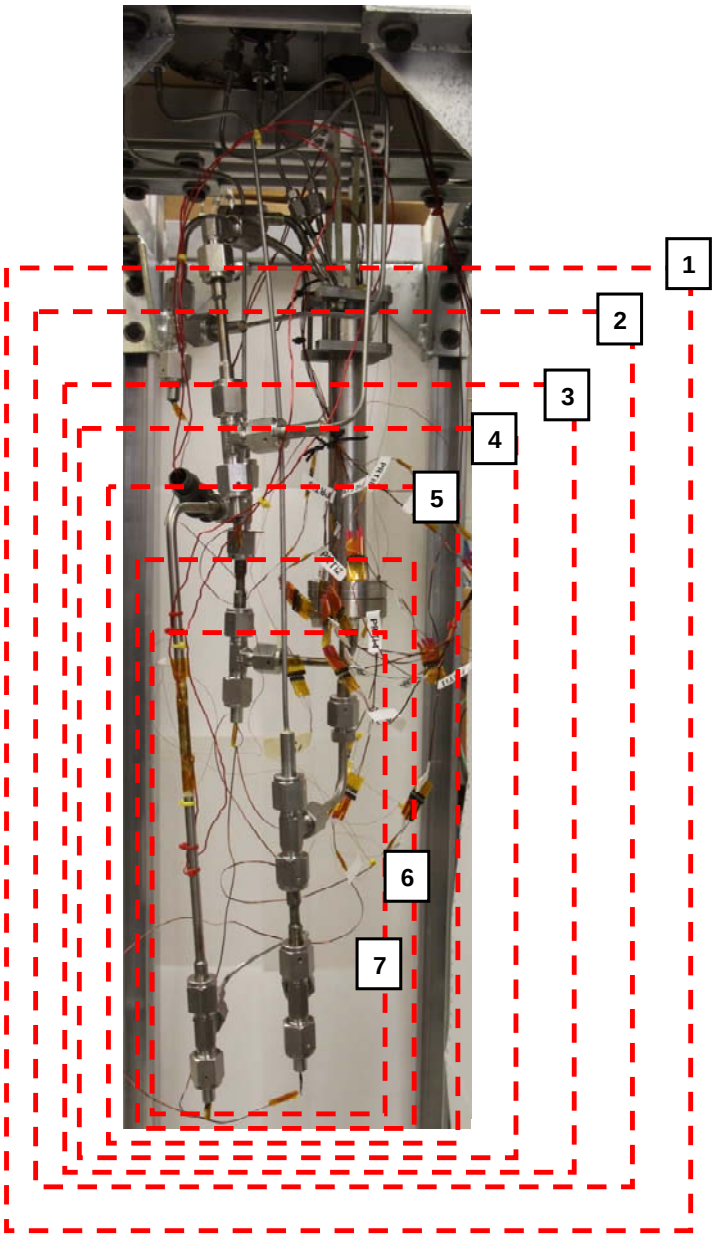

Figure 4-31: Approximate locations of MLI layers relative to the cryoprobe plumbing inside the vacuum chamber.

The parasitic heat leak into the system was quantified to ensure the leak does not significantly alter the performance of the cryoprobe. The major sources of heat leak, in order from largest to smallest, are: radiation, fluid vacuum pass-through tubes, pressure tap tubes, load

heater current wires, G10 thermally isolating cryoprobe support rods, and the PRT sensor wires. Note that these elements are shown in Figure 4-3 and Figure 4-9.

4.3.7 Parasitic Heat Leak

The estimated radiation heat load with the seven layers of MLI insulation was computed as 0.5 W as shown in Figure 4-28. The conductive heat leak through the various elements which span from room temperature to the cold components of the experiment are computed according to Fourier's law as:

$$\dot{Q}_p = \frac{k\,A\,\Delta T}{L} \tag{4.15}$$

Where $\dot{Q}$ is the parasitic heat, k is the average thermal conductivity, A is the cross sectional area, ΔT is the temperature difference driving the conduction, and L is the length of the element. The ambient temperature for these calculations is assumed to be 300 K. Table 4-7 lists the geometry, conductivity (computed at the average temperature of the element), and the total conductive heat leak introduced into the experiment through the various elements.

The final source of parasitic heat leak considered here is the ohmic heating in the load heater current wires. This is a parasitic because the heater power is measured by considering only the ohmic heating of the heater itself. The ohmic heating in the lead wires becomes an additional load that is applied partially at the load heater shown in Figure 4-1, as well as along the length of the cryoprobe plumbing system where the lead wires are wrapped to provide thermal sinking. The ohmic heating in the lead wires is computed as:

$$\dot{Q}_{ohmic} = i^2 R \tag{4.16}$$

where i is the current and R is the resistance of the current lead. The 36" long and 0.9 mm diameter copper leads have a combined resistance of 0.0206 Ω and the current ranges 0-1 A during the tests. Using a nominal test current of 0.58 A, the ohmic heating in the two leads is computed as 0.014 W.

Table 4-8 summarizes the parasitic heat leak from radiation, conduction, and ohmic dissipation; the total heat leak is computed at 0.78 W and the radiation is the dominant source of this parasitic. Figure 4-32 compares the baseline load curve with the unmodified probe to the load curve with 0.78 W of parasitic load on the modified probe. Notice that the effect of the parasitic load is to shift the load curve very slightly relative to the unmodified cryoprobe.

Table 4-7: Summary of parameters used to compute parasitic conductive heat leak in the experiment.

Element	Material	Average conductivity [W/m-K]	OD [in]	ID [in]	Temperature difference	Length [in]	Number of elements	Total conductive heat leak [W]
fluid vacuum pass-through tubes	stainless steel	18.9	0.125	0.095	300 – 240 K	6	4	0.1
pressure tap tubes	stainless steel	18.3	0.125	0.095	300 – 170 K	10	2	0.063
load heater current wires	copper	384.4	0.0354	--	300 – 200 K	36	2	0.053
G10 support rods	G10-CR	0.56	0.19	--	300 – 240 K	4	4	0.024
PRT wires	phosphor bronze	40	0.00795 (32 gauge)	--	300 – 170 K	24	64 (14 sensors x 4 wires/sensor)	0.0153

Table 4-8: Summary of the parasitic heat leak into the experiment

Heat source	Magnitude
radiation	0.5 W
conduction	0.26 W
ohmic dissipation	0.014 W
Total	**0.78 W**

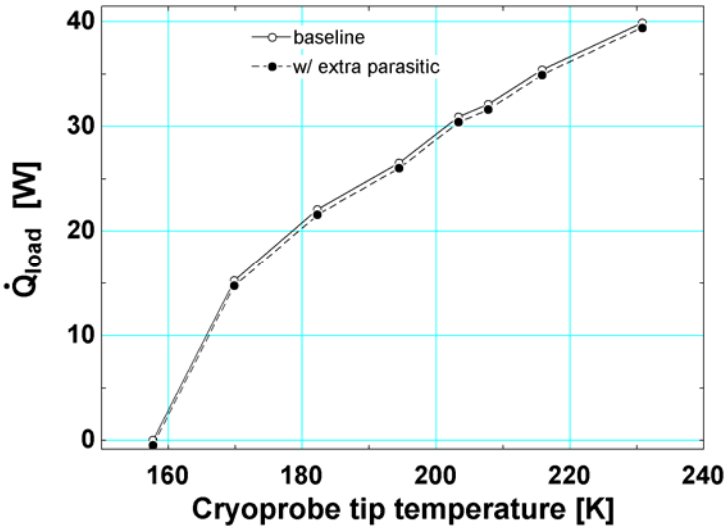

Figure 4-32: Comparison of applied heat load vs. tip temperature for the original cryoprobe and the modified cryoprobe with seven layers of MLI insulation.

4.3.8 Jewel orifice

The jewel expansion orifice (#13) shown in the cycle schematic in Figure 4-1 is integrated in the flow stream by mounting it in a ¼" stainless steel VCR gasket that is held between two VCR glands. Figure 4-33 shows a schematic and photo of the jewel mounted in the gasket using Stycast 2850 FT Black epoxy. The jewel rests on a 1/16" diameter, 0.012" deep counterbore in the gasket over a smaller diameter through-hole (0.035"). The jewel itself has an outer diameter of 0.06" and a thickness of 0.010". The orifice ID is selected to establish the desired flow rate for the specific test, but the ID nominally ranges 0.010" to 0.020". Note that the gasket was fixtured for machining by mounting it to a piece of aluminum using superglue.

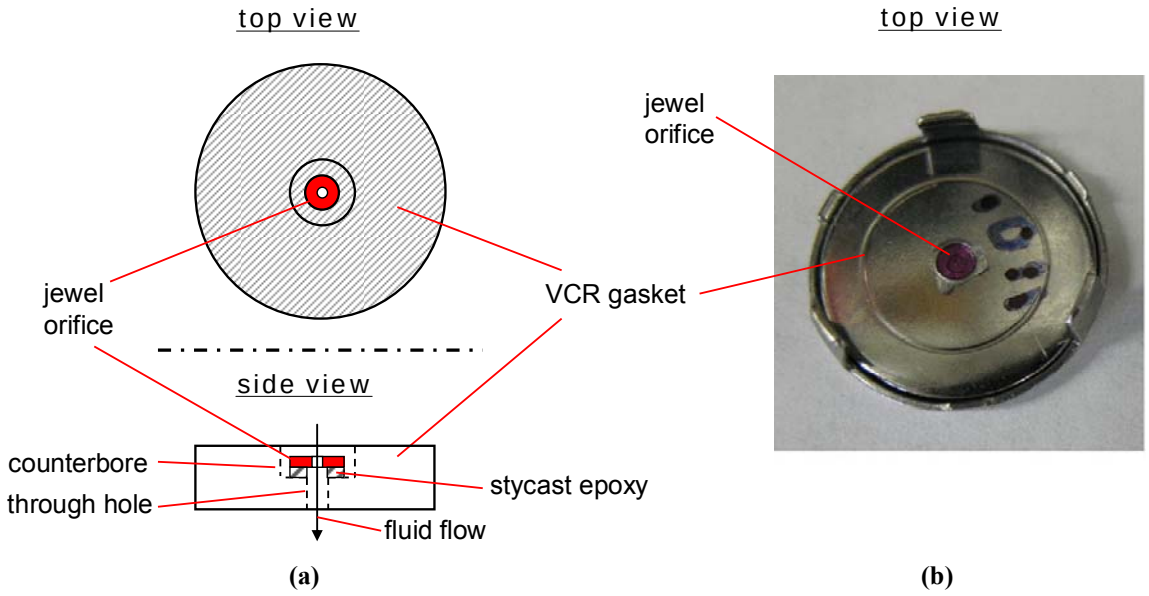

Figure 4-33: (a) Schematic and (b) photograph of the jewel orifice mounted in a ¼" stainless steel VCR gasket.

4.3.9 Nichrome wire heater

The Nichrome wire heater shown wrapped around a ¼" SS tube is Figure 4-3 is electrically connected using a 4-wire configuration and energized using a Lakeshore 332 temperature controller, as shown in Figure 4-34. The circuit elements are configured to (1) restrict the differential voltage measured by the DAQ system to 10 V, and (2) minimize the absolute voltage measured by the DAQ system (i.e. restrict the absolute voltage, relative to the DAQ system ground, at *each* of the two terminals that make up the differential measurement) in order to conform to the DAQ hardware maximum voltage specifications.

The power dissipation into the wire is calculated as the product of the current and the voltage drop, measured directly across the heater. The maximum test voltage (~50 V) is too large to be directly read by the DAQ system and therefore is scaled by a voltage divider before being measured. The overall voltage divider resistance is much larger than the heater resistance, and therefore the current, which is measured by the voltage drop across a small shunt resistor, is

assumed to pass entirely through the heater for purposes of calculating the heater power dissipation. Finally, a relay is connected in series with the heater circuit in order to protect the experiment; the relay ensures that current can only flow to the heater while the low temperature compressor is running (note that the heater is attached to the low temperature fluid circuit). The heater is thermally isolated as it is inside the vacuum enclosure and will be covered in radiation shielding. Therefore, if the system is not providing refrigeration and the heater is on, the heater can become extremely hot and damage the facility. The relay protects the test facility against this possible scenario.

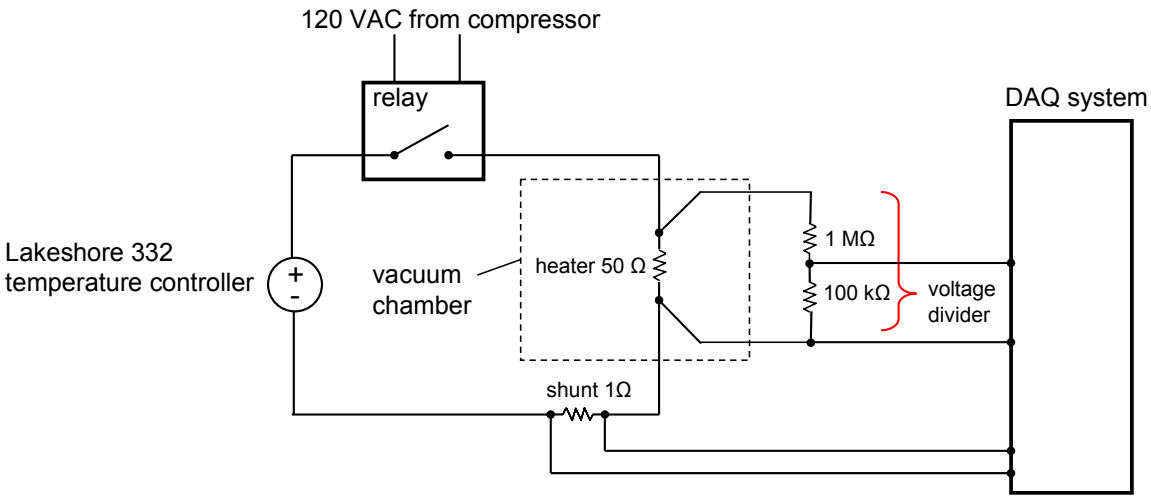

Figure 4-34: Electrical schematic of the Nichrome wire heater circuit

The voltage and current measurements provided to the DAQ system from the voltage divider and shunt resistor were calibrated *in situ* using an HP 34401A multimeter. The DAQ calibration was verified against the HP 34401A multimeter and reproduced the multimeter voltage and current measurements to within 0.005 V and 0.00015 A, respectively, over the voltage range used in these experiments. The calibration error is an order of magnitude larger than the uncertainty in the HP 34401A multimeter itself, so the calibration error alone is used in the computation of the dissipated heater power uncertainty. The maximum uncertainty in heater

power over the calibration range (0-55 W) is slightly less than 0.01 W; the heat input is expected to vary from 1 to 30 W during the experiments so the accuracy is ±1% or better.

4.3.10 In-stream PRT construction

The temperature sensors indicated in Figure 4-1 are mounted in the flow stream in order to directly measure the fluid temperature. Figure 4-35 and Figure 4-36 show how each PRT is integrated into a ¼" VCR gland that connects to a VCR tee to achieve a flexible and reliable construction. The PRT is supported and located in the center of the stream by a 0.024 inch diameter stainless steel spring wire; this arrangement minimizes contact with the wall in order to eliminate measurement errors that may result from a temperature difference between the wall and the fluid stream. Further thermal isolation from the wall is achieved by wrapping the PRT in two layers of Kapton tape. The support wire and PRT wires are epoxied into a VCR gland that is connected to the straight section of the tee, where the PRT extends nearly to the opening at the opposite end of the straight section. It is important for the PRT to be in this location in order to ensure that the PRT has good thermal contact with the flow stream (which is indicated by "flow direction" in Figure 4-36). It is possible for conductive heating in the PRT wires to introduce measurement errors in the PRT sensor; therefore, the PRT wires are wrapped around the support wire in the flow stream and again around the tube located outside the flow stream (not shown) in order to provide thermal sinking.

Both the PRT wires and the support wire pass through a 1/8 inch stainless steel tube that is brazed into the ¼ inch VCR gland. Stycast 2850 FT Black epoxy was used to seal the wire passageway (which extends from the gland side of the VCR gland to the end of the 1/8 inch stainless steel tube, as shown in Figure 4-36). Special attention to the epoxy joint is critical as it

represents the weakest bond in the assembly. Also, the differential thermal contraction between the epoxy and the stainless steel can cause "cold leaks" (i.e., a leak that opens/enlarges only when the system is cold, which can be particularly difficult to diagnose). The possible leak pathways include the interface between the PRT wires and the epoxy as well as the interface between the epoxy and stainless steel components (the VCR gland and 1/8 inch tube). The construction in Figure 4-36 and Figure 4-35 addresses these two leak paths and represents the final of three iterations that occurred during this project in order to achieve a reliable design. The wire leak path is addressed by separating the PRT wires from each other at the point where they pass through the VCR gland and 1/8 inch stainless steel tube. The 4 PRT wires are initially connected to one another by a Polyimide coating. Separating the PRT wires prevents air bubbles from forming in the epoxy around wires. The second type of leak occurs when the epoxy *inside* the stainless steel components shrinks more than the surrounding metal. The epoxy on the outside of the 1/8 inch tube solves this problem because the reliability of the joint is actually enhanced by the differential contraction; the epoxy on the outside of the 1/8 inch tube will tighten around the tube surface (Ekin 2007, p. 171).

A mold for the epoxy on the outside of the 1/8 inch tube is formed using small diameter shrink wrap where the bottom of the mold is shaped by heating the shrink tube only at the base of the 1/8 inch tube. A second epoxy mold is formed at the gland end of the VCR gland using additional shrink wrap. The epoxy is poured and set with the VCR gland end facing down so that the second mold prevents epoxy from draining out the bottom or onto the gland sealing surface. Two sizes of shrink wrap are used in the second mold, as shown in the bottom picture in Figure 4-36; a larger size fits snugly into the opening of the VCR gland, and a smaller size

that shrinks down to form a tight seal with the support and PRT wires. The inside of the larger size shrinks over the outside of the smaller size in order to create a continuous surface for the mold. After the epoxy is poured, the wires are moved up and down in order to help remove air and completely fill both molds and the inside of the VCR gland. During the first 1 to 1.5 hours of the curing process, epoxy may drip around the outside of the larger shrink tube in the 2nd mold; this excess epoxy must be removed (before curing) to ensure that the gasket will still fit on the VCR gland.

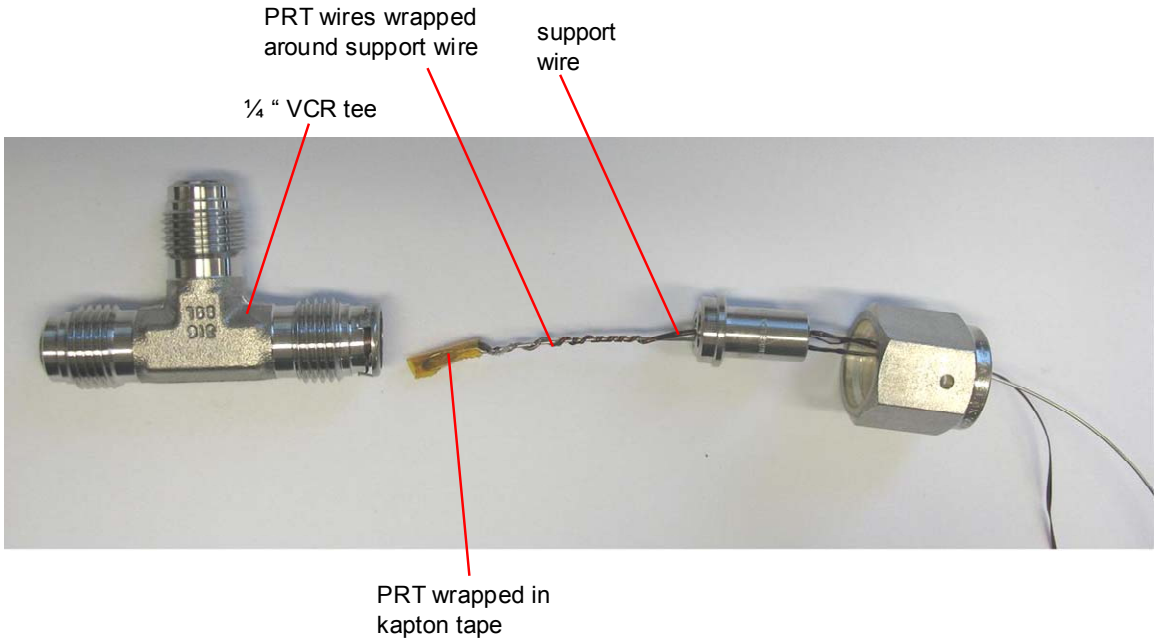

Figure 4-35: Photograph showing the PRT integrated with the ¼" VCR tee. Thermal isolation from the tee wall is achieved by wrapping the PRT in Kapton tape and using the support wire to hold the PRT in the center of the stream. The PRT wires are wrapped around the support wire to provide a thermal sink.

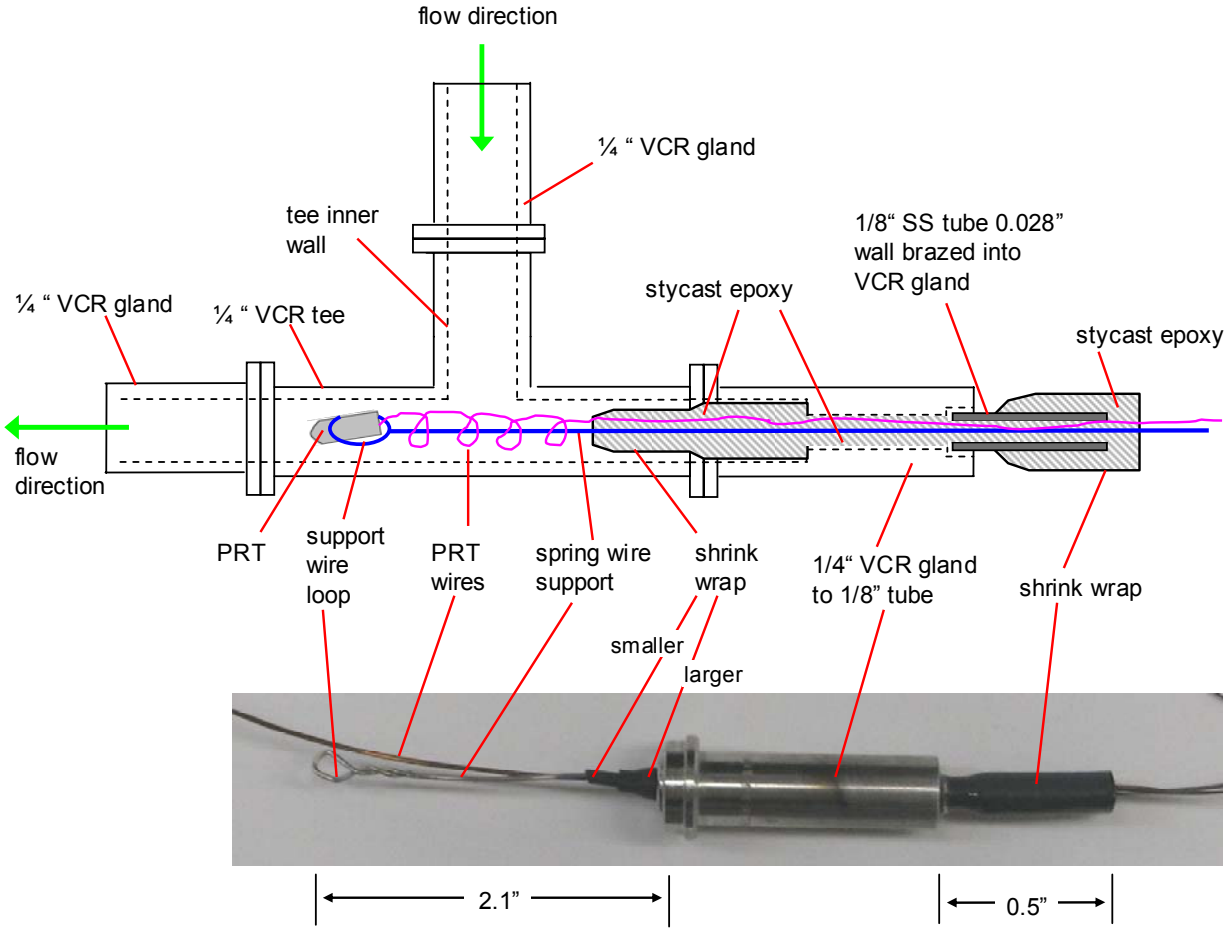

Figure 4-36: (Top) detailed schematic of the in-stream PRT construction and (bottom) picture of the VCR gland that serves as the wire feedthrough for the PRT.

4.3.11 PRT Sensor Calibration

The 14 PRTs (5 in-stream PRTs shown in Figure 4-1, as well as the 9 PRTs installed within the recuperator referred to as PRT_i) were calibrated *in-situ* using a 2-point linear correction. Liquid nitrogen was used for the first calibration point at approximately 77 K, and a constant temperature bath held at 2°C was used for the second calibration point. A linear correction factor was determined for each PRT and applied to the standard IEC 751 PRT (Lakeshore technical downloads) resistance-temperature scale. PRTs calibrated using a similar 2-point correction are available from Lakeshore Cryotronics (Lakeshore) with an accuracy of

±0.25 K, so it is reasonable to assume that the PRTs have an accuracy of ±0.5 K over the calibration temperature range (77-275 K).

4.3.12 Thermocouple Measurement Uncertainty

4.3.12.1 Data Acquisition System

The temperature sensed by the thermocouples is measured using a National Instruments (NI) Data Acquisition (DAQ) system, shown in Figure 4-37. The components in the DAQ system as well as the constant temperature water circulator used to calibrate the thermocouples are listed in Table 4-9, including the references that specify the accuracy of each component. Table 4-10 shows the hardware accuracy specifications for the temperature measurement range discussed here. Type E thermocouples are used to measure near ambient (20-40°C) cryoprobe system temperatures at locations that are outside the vacuum chamber. The thermocouple leads connect directly to a SCXI-1303 terminal block integrated with a Cold-Junction Compensation (CJC) system. The thermocouple voltages are small (~1-50 mV) so a SCXI-1102 thermocouple amplifier magnifies the voltages to a range that can be accurately measured by the 6036E DAQ card. The DAQ card uses an Analog-to-Digital Converter (ADC) to convert the amplified analog voltage signal into a digital signal that can be recorded by the computer (in LabVIEW).

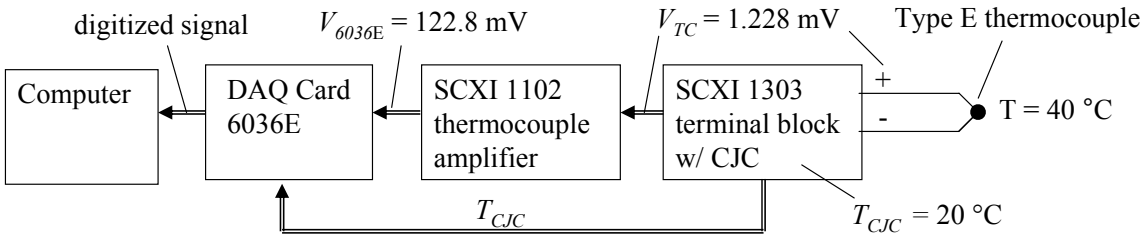

Figure 4-37: DAQ system used to record thermocouple temperature measurements.

Table 4-9: Thermocouple measurement and calibration instrumentation.

Instrument	Reference
Type E thermocouple	http://www.omega.com/temperature/Z/pdf/z206.pdf
SCXI 1303 terminal block with CJC	http://www.ni.com/pdf/manuals/321923b.pdf
SCXI 1102 thermocouple amplifier	http://www.ni.com/pdf/products/us/4scxisc278_ETC_196.pdf
6036E DAQ Card	http://www.ni.com/pdf/products/us/4daqsc205-207_229_238-243.pdf
Polyscience 9112 calibration water bath	http://www.polyscience.com/lab/9100.html

Table 4-10: Thermocouple measurement and calibration instrumentation specifications

Measurement specifications	Symbol	Value
Thermocouple voltage	V_{TC}	1.288 mV @ T = 40 ºC and T_{CJC} = 20 ºC
Thermocouple voltage sensitivity	$\partial V_{TC}/\partial T$	0.063 mV/ºC, @ 40C
NI SCXI 1303 CJC accuracy, (ºC)	$U_{cjc,acc}$	0.5 ºC
NI SCXI 1303 CJC repeatability, (ºC)	$U_{cjc,rep}$	0.2 ºC
NI SCXI 1102 accuracy in ±100 mV range,	$\Delta V_{TC,1}$	0.0321 mV@ 1.192 mV input
% of reading		0.015
offset		0.025 mV
noise(with 100 pt avg)		0.005 mV
Drift (ignore for ambient 15-35 ºC) [1]		--
NI 6036E electronic accuracy in ±0.5 V range,	$\Delta V_{6036E,elec}$	0.227 mV @ 119.2 mV input
% of reading		0.0591
offset		0.15 mV
noise (with 100 pt avg)		0.007 mV
Drift (ignore for ambient 15-35 ºC)[1]		--
NI 6036E resolution in ±0.5 V range	$\Delta V_{6036E,meas}$	0.01 mV
Polyscience 9112 temperature accuracy	$\Delta T_{cal,acc}$	0.25 ºC
Polyscience 9112 temperature stability	$\Delta T_{cal,stab}$	0.01 ºC

[1] "Specifications and accuracy" article from: http://www.ni.com/support/calibrat/accuracy.htm

The thermocouple voltage at the 1303 terminals (shown as V_{TC} in Figure 4-37) actually only represents the temperature difference between the thermocouple bead (T) and the 1303 terminals (which is measured as T_{CJC} as shown in Figure 4-37) so V_{TC} is computed as:

$$V_{TC} = V_{typeE}\left(T - T_{CJC}\right) \tag{4.17}$$

where $V_{typeE}(\Delta T)$ represents the voltage generated by a type-E thermocouple operating between the two temperatures. The standard Voltage-Temperature (VT) relationship is reported as the voltage that would be produced by a thermocouple with a bead temperature T and with the lead temperatures at the voltage measurement location at T_{ref}, which is taken to be 0°C.

$$V = \sum_{i=0}^{n} a_i \left(T - T_{ref}\right)^i \tag{4.18}$$

where the eleven empirical coefficients (a_0-a_{10}) for the 0-1000°C range are listed in Table 4-11. The voltage values are also often tabulated as shown in the thermocouple reference in Table 4-9.

Table 4-11: Type-E thermocouple voltage-temperature relationship fitting coefficients.

coefficient	value	coefficient	value
a_0	0	a_6	-0.191974955040 x10^{-15}
a_1	0.586655087100 x10^{-1}	a_7	-0.125366004970 x10^{-17}
a_2	0.450322755820 x10^{-4}	a_8	0.214892175690 x10^{-20}
a_3	0.289084072120 x10^{-7}	a_9	-0.143880417820 x10^{-23}
a_4	-0.330568966520 x10^{-9}	a_{10}	0.359608994810 x10^{-27}
a_5	0.650244032700 x10^{-12}		
Adapted from: http://srdata.nist.gov/its90/main/			

Following the form of Eq. (4.18) where the voltage is a function of (T-T_{ref}), Eq. (4.17) can be re-written as:

$$V_{TC} = V_{typeE}\left(T - T_{ref}\right) - V_{typeE}\left(T_{CJC} - T_{ref}\right) \tag{4.19}$$

Figure 4-37 shows T and T_{CJC} and the various system voltages for a nominal operating condition where T = 40°C and T_{CJC} = 20°C, which correspond to $V_{typeE}(T\text{-}T_{ref})$, $V_{typeE}(T_{CJC}\text{-}T_{ref})$ and V_{TC} of 2.420 mV, 1.192 mV and 1.228 mV, respectively. The SCXI-1102 amplifies the

1.228 mV signal by 100x, so the voltage measured by the 6036E is nominally 122.8 mV. It is important to establish these approximate voltage values at each location in the DAQ system as the electronic accuracy of each component depends on the voltage range of the applied signal.

In order to quantify the absolute temperature of the thermocouple, the temperature measurement must be corrected for the temperature of the 1303. The CJC measures the temperature of the 1303 and transmits the temperature signal to the 6036E DAQ card as shown in Figure 4-37. The temperature correction is subsequently performed in software according to:

$$T = \left(T - T_{CJC}\right) + T_{CJC} \tag{4.20}$$

By inverting the VT relationship in Eq. (4.18) and substituting it into Eq.(4.20), the temperature is computed in software as:

$$T = T_{typeE}\left(V_{TC}\right) + T_{CJC} \tag{4.21}$$

4.3.12.2 Uncertainty Computation

The uncertainty in the thermocouple temperature measurement can be broken down into three categories: inherent sensor uncertainty, instrumentation uncertainty, and system-level uncertainty. The inherent sensor uncertainty is related to the ability of the thermocouple to produce a voltage, which, when converted to a temperature using a VT relationship, accurately represents the actual sensed temperature. This uncertainty does not include the accuracy of the electronic measurement system, or any uncertainty associated with physically mounting the thermocouple in the flow stream (such as heat transfer through the sensor wires). The instrumentation uncertainty reflects the ability of the electronic DAQ system to accurately measure the small voltage produced by the thermocouple. Finally, the system-level uncertainty

represents the effect of physically integrating the sensor with the flow stream. This includes the heat leak through sensor wires and the physical mounting system used to install the sensor in the flow stream (as opposed to against the wall, which is likely at a different temperature than the flow stream). The thermocouples are physically mounted in the center of the flow stream; therefore for this analysis the only the heat leak system-level error is considered. Further information about computing system level errors for temperature measurements can be found in (Taylor, 2009)

The inherent sensor uncertainty can be further divided into the uncertainty related to (1) the sensor calibration compared to a standard temperature scale such as the ITS-90 temperature scale, (2) the interpolation uncertainty related to the fitting function used to implement the calibration data, and (3) the reproducibility of the measurement. The sensor calibration was performed using a Polyscience 9112 constant temperature circulator (i.e., a water bath) that has an accuracy of 0.25°C; note that the temperature stability in the bath is small (0.01°C) compared to the circulator temperature sensor accuracy and is neglected in the calibration uncertainty (i.e. $U_{cal} = \pm 0.25°C$)

The thermocouples were calibrated at three temperatures, 2°C and 20°C and 60°C, the calibration points were used to develop a linear correction factor to the standard VT relationship. The correction factor is defined as:

$$\Delta T_{cal} = a + b\,T_{std} \tag{4.22}$$

where a and b are fitting coefficients and T_{std} is the temperature computed using Eq. (4.18) the standard VT relationship. Figure 4-38 shows the three calibration points and the curve fit for one of the thermocouples, the fitting coefficients a and b are -6.86287°C and 0.0093644,

respectively. The RMS error for the curve fit was computed using the curve fit function in EES and is shown on the graph as 0.0848°C. The interpolation error (U_{int}) for the calibration is subsequently computed as:

$$U_{int} = \pm\sqrt{\frac{N}{N-n}\left(\Delta T_{rms}\right)^2} \tag{4.23}$$

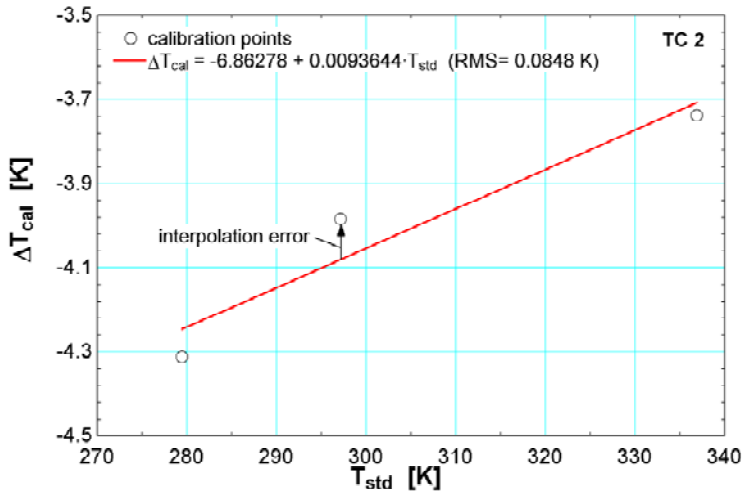

Figure 4-38: Calibration points, curve fit, and curve fit RMS error for one of the type-E thermocouples

where N is the number of data points in the calibration (three), n is the number of fitting coefficients (two), and ΔT_{rms} is the RMS error of the curve fit discussed above. The interpolation uncertainty for this particular thermocouple was computed as U_{int} = ±0.1469°C. The repeatability for the thermocouple measurement is not known and is not included in this uncertainty analysis.

The instrumentation accuracy is broken into three categories including: (1) the cold junction compensation, (2) the electronic (i.e. absolute) accuracy of the DAQ, and (3) the resolution of the DAQ system. Eq. (4.21) shows that the uncertainty in the temperature

measurement associated with the CJC is simply the uncertainty in the CJC temperature. Therefore:

$$U_{CJC} = \Delta T_{CJC} \tag{4.24}$$

The uncertainty of the CJC is comprised of two independent parameters, sensor accuracy ($\Delta T_{CJC,acc}$ = ±0.5°C) and repeatability ($\Delta T_{CJC,rep}$ = ±0.2°C). The CJC temperature uncertainty is therefore computed as:

$$\Delta T_{CJC} = \sqrt{\Delta T_{CJC,acc}{}^2 + \Delta T_{CJC,rep}{}^2} \tag{4.25}$$

where ΔT_{CJC} and U_{CJC} are calculated as ±0.54 °C.

The electronic accuracy represents the ability of instrumentation amplifiers in the SCXI-1102 and DAQ-6036E to sense and reproduce the voltage signal that is eventually converted to a digital signal by the ADC. The electronic accuracy of V_{TC} is subdivided into the uncertainty associated with the 1102, and with the 6036E. The electronic accuracy for the 1102 is computed according to the parameters given in the NI datasheet as:

$$\Delta V_{TC,1102,elec} = \left(input\ voltage \cdot \%\, of\, reading\right)/100 + offset + noise + drift \tag{4.26}$$

Using the nominal V_{TC} value for the *input voltage* (1.228 mV) computed in Eq. (4.19) and the hardware parameters listed in Table 4-10, $\Delta V_{TC,1102,elec}$ is computed as ±0.0302 mV.

The voltage measurement by the 6036E further impacts the accuracy of the V_{TC} measurement. The amplified voltage from the 1102 is measured with an electronic accuracy of:

$$\Delta V_{6036E,elec} = \left(input\ voltage \cdot \%\, of\, reading\right)/100 + offset + noise + drift \tag{4.27}$$

where the *input voltage* is 122.8 mV for the nominal 40°C temperature measurement, and so the $\Delta V_{6036E,elec}$ computed using the parameters in Table 4-10 is ±0.230 mV. The uncertainty in V_{TC} as a result of the inaccuracy of the 6036E measurement subsequently is:

$$\Delta V_{TC,6036E,elec} = \Delta V_{6036E,elec} \frac{\partial V_{1102}}{\partial V_{6036E}} \tag{4.28}$$

The change in voltage of the 1102 with respect to the 6036E voltage is the inverse of the 1102 gain (G), so Eq. (4.28) becomes:

$$\Delta V_{TC,6036E,elec} = \Delta V_{6036E,elec} \frac{1}{G} \tag{4.29}$$

where G = 100 so $\Delta V_{TC,6036E,elec}$ is ±0.00300 mV. The overall electronic uncertainty of the V_{TC} measurement is:

$$\Delta V_{TC,elec} = \sqrt{\Delta V_{TC,1102,elec}{}^2 + \Delta V_{TC,6036E,elec}{}^2} \tag{4.30}$$

and is ±0.0303 mV for the example presented here. The electronic temperature uncertainty can be computed by scaling the result from (4.30) by the inverse of the thermocouple voltage sensitivity at 40°C:

$$U_{elec} = \frac{\Delta V_{TC,elec}}{\partial V_{TC}/\partial T\big|_{40°C}} \tag{4.31}$$

where $\partial V_{TC}/\partial T\big|_{40°C}$ = 0.063 mV/°C so U_{elec} = ±0.48°C.

The final instrumentation uncertainty is related to the resolution of the ADC on the 6036E DAQ card. The resolution of the 6036E with 100 averaged points is:

$$\Delta V_{6036E,res} = \pm 0.01 mV \tag{4.32}$$

The temperature uncertainty is subsequently computed using the 1102 gain and the thermocouple voltage sensitivity according to:

$$U_{res} = \frac{\Delta V_{6036E,res}}{G \left. \partial V_{TC} / \partial T \right|_{40°C}} \tag{4.33}$$

and is as ±0.00159°C in this example.

The system-level error here is a bias error caused by the heat leak from axial conduction in the TC wires. The thermocouple bead is warmer than the ambient surroundings; therefore in this case, the thermocouple temperature measurement will be artificially offset below lower than the fluid temperature. The magnitude of the offset is computed using an extended surface analysis on the TC wires.

The wires are approximately 2" long and have a diameter of 0.0063". Furthermore, the type-E thermocouple wires are Chromel (90% Chromium, 10% Nickel) and Constantan, with thermal conductivities of approximately 19 W/m-K and 21 W/m-K, respectively (omega.com). The gas mixture is near room temperature at the thermocouple measurement locations and will be in a vapor state, a conservative estimate for the forced convection of a gas *h* was selected as 10 W/m-K (Incropera & Dewitt, p 8). The Biot# of the bead is very small (<0.001), so it is reasonable to assume that TC wire temperature at the base of the bead are the same as the bead temperature.

The temperature distribution within the wires is computing using the relationship developed for a very long fin (Incropera & DeWitt, P. 133):

$$\theta/\theta_b = e^{-mx} \tag{4.34}$$

where θ is the temperature difference between the wire and the fluid, θ_b is the temperature difference between the fluid and the TC wire feed-through at ambient temperature (i.e. T_{fluid} - T_{amb} = 20°C in this example), x is the distance from the wire feed-through towards the bead, and m is the fin parameter computed according to:

$$m^2 = \frac{h\,P}{k\,A_c} \tag{4.35}$$

where P is the perimeter of the wire, k is the conductivity of the wire, and A_c is the cross section area of the wire. The thermal conductivity is taken as the average of the conductivities of Chromel and Constantan (20 W/m-K). The temperature difference between the fluid and the wires (θ) at the bead is then computed for x = 2" using Eqs. (4.34) and (4.35) as 0.068°C and is the temperature offset uncertainty due to axial conduction, U_{cond}.

The total TC temperature measurement uncertainty is computed by summing the randomly distributed uncertainties in quadrature, and adding the bias uncertainty from U_{cond} :

$$U_T = \sqrt{U_{cal}^2 + U_{\text{int}}^2 + U_{CJC}^2 + U_{elec}^2 + U_{meas}^2} + U_{cond} \tag{4.36}$$

Table 4-12 summarizes the temperature uncertainty from each of the sources as well as the total uncertainty which is computed as ±0.77°C.

Table 4-12: Summary of the uncertainties in for the type-E thermocouple at 40°C

Sensor Uncertainty	Symbol	Value (C)
Calibration uncertainty	U_{cal}	±0.25
Interpolation uncertainty	U_{int}	±0.1469
Cold Junction Compensation (CJC)	U_{CJC}	±0.54
Electronic accuracy	U_{elec}	±0.48
Resolution	U_{meas}	±0.00159
Axial conduction	U_{cond}	-0.068
Total uncertainty	$\boldsymbol{U_T}$	**±0.78-0.068**

4.3.13 Mass flow meters

The mass flows in both cycles are measured using the calorimetric flow meters listed in Table 4-3. In principle, these meters measure the thermal capacitance rate of the flow stream; a small amount of heat is applied to the fluid and the meter detects the temperature rise across the heated section. The meters are calibrated by the manufacturer for pure nitrogen at standard conditions and therefore the measurements must be corrected for the specific heat of the actual fluid in the meter. The stream capacitance measured in units of capacitance of standard nitrogen is $\dot{m}_{N_2,std}\, cp_{N_2,std}$, and the equivalent capacitance of the actual flow stream is computed as:

$$\dot{m}_a\, cp_a = \dot{m}_{N_2,std}\, cp_{N_2,std} \tag{4.37}$$

where $\dot{m}_{N_2,std}$ and $cp_{N_2,std}$ are the mass flow and specific heat of nitrogen at standard conditions and $\dot{m}_a$ and cp_a are the mass flow and specific heat of the actual fluid at the test conditions. The signal from the meter is provided in terms of a standard volumetric flow rate of nitrogen ($\dot{V}_{N_2,std}$, in standard liters of nitrogen per minute) and must be scaled by the density at standard

conditions in order to get $\dot{m}_{N_2,std}$. The mass flow of the actual fluid is subsequently computed as:

$$\dot{m}_a = \dot{V}_{N_2,std}\, \rho_{N_2,std} \frac{cp_{N_2,std}}{cp_a} \tag{4.38}$$

where $\rho_{N_2,std}$ is the density of nitrogen at standard conditions. Note that values for $cp_{N_2,std}$ and $\rho_{N_2,std}$ used in the original manufacturers' calibration must be used in Eq. (4.38) rather than values computed using another source. The $cp_{N_2,std}$ and $\rho_{N_2,std}$ values in the original calibration are 0.2485 Cal/g-K and 1.25 g/L, respectively.

4.3.14 Gas Chromatograph

The composition of the mixture circulating in the JT cycle (2nd stage) must be measured for each steady state operating point it can change dramatically from the charged composition. The primary causes of composition shift are differential mixture constituent absorption in the compressor oil and condensation in the cold sections (Gong 2002 & 2007). Measurement of the circulating composition is critical for the thermodynamic analysis that considers the fluid applied in a cycle.

An HP 5890 Series II Gas Chromatograph (GC) with Thermal Conductivity Detection (TCD) mixture analysis was configured to measure gas samples directly from the experiment. The mixture is sampled on the low pressure side before the suction side of the compressor but before the bypass valve. A heater wrapped around a tube before the sample line ensures that the mixture entered the sample line as a gas phase to avoid sampling one phase of two-phase mixture. The TCD detectors were calibrated for the mixture constituents against a calibrated

sample (certified to ±1% by NIST traceable standard from Air Liquide) of 9.1% Argon, 40.9% R14, and 50.0% R23. Calibration factors for the constituents were computed by comparing the measured and calibrated mole fractions for seven tests of the calibrated mixture, carried out on two different days. The *uncorrected* measured mole fractions are computed using the relative integrated areas of the each of the constituents. Table 4-13 summarizes the results from these calibration tests.

Table 4-13: Calibrated and measured mole fractions for GC calibration mixture. The response factors for each constituent used to compute the corrected composition are shown.

	Argon	**R14**	**R23**
Calibrated mole fraction ($F_{mol,cal}$)	9.1%	40.9%	50.0%
Measured, uncorrected mole fraction - average of 7 tests ($F_{mol,uc}$)	6.55%	0.4223	0.5121
Response Factor (RF)	1.389	0.968	0.976

The *corrected* mixture percentages are then computed using a Response Factor (RF) analysis (Perry, 1981), which begins with computing the RF values:

$$RF = F_{mol,cal} \big/ F_{mol,uc} \tag{4.39}$$

where $F_{mol,cal}$ is the calibrated constituent mole fraction, and $F_{mol,meas}$ is the uncorrected mole fraction. The areas associated with the TCD signal integration for each constituent is corrected by the RF value:

$$A_c = A_{uc}\, RF \tag{4.40}$$

where A_c is the corrected area and A_{uc} is the uncorrected area. The corrected mole fraction of each constituent is subsequently computed according to:

$$F_{mol\%,c} = \frac{A_c}{\sum_{i=1}^{\#components} A_{c,i}} \tag{4.41}$$

where $A_{c,i}$ is the corrected area of each of the constituents. Values from an example RF correction are presented in Table 4-14.

Table 4-14: Example of corrected mole fraction values from a gas chromatograph mixture analysis.

	Argon	R14	R23
Uncorrected Area	253825	1654161	1413187
Corrected Area	352650.365	1602156.662	1379764.954
Corrected Mole Fraction	0.106	0.480	0.414

4.3.15 Bypass valves

The compressor plumbing has been modified to accommodate the bypass valves shown in Figure 4-1. The bypass valve on the 2nd stage is used in tandem with the interchangeable jewel orifice in order to independently regulate the pressure ratio and mass flow applied to the cycle. The bypass valve on the 1st stage is used to regulate the mass flow and therefore precooling provided by the cycle. Figure 4-39 shows the bypass valve connections that integrate with the compressor plumbing.

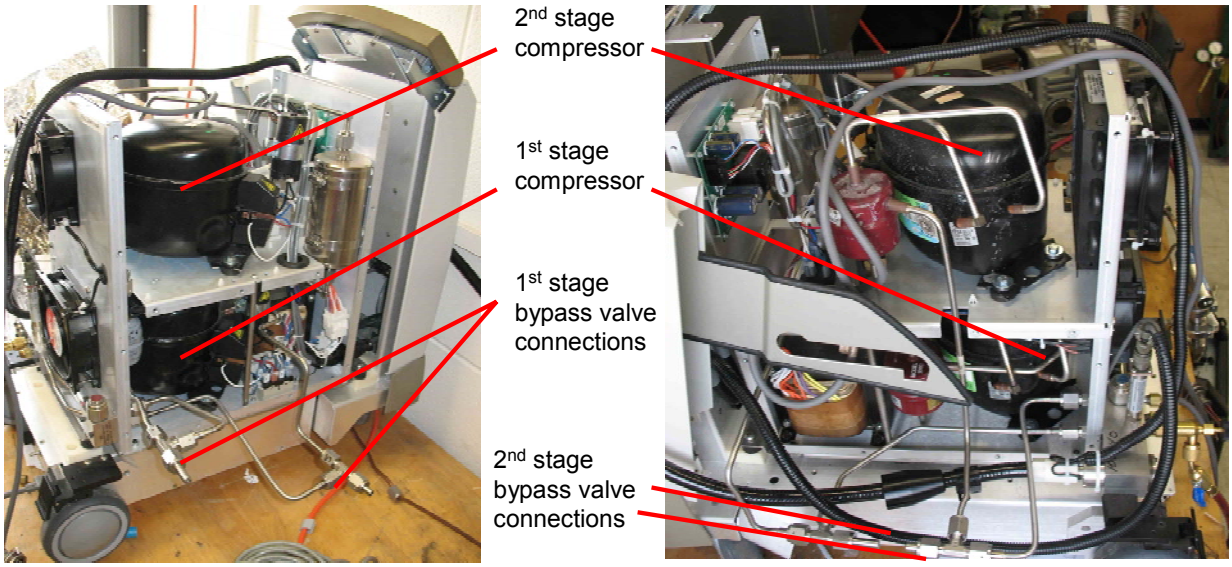

Figure 4-39: Picture of 1st and 2nd stage compressors with modifications to accommodate a bypass valve (bypass valve not shown).

4.3.16 Data Acquisition System

The experimental data are recorded using an available National Instruments (NI) Data Acquisition (DAQ) system integrated with a computer. A program was written in LabVIEW to record the temperatures, pressures, mass flows, and heater voltage and current; these data are recorded to a spreadsheet every four seconds. The program includes a digital filter to remove noise content in the 10-2000 Hz bandwidth, the majority of the noise has been recorded as 60 Hz (and several harmonics) 120 V electrical supply line EMF. The filter reduces the temperature signal noise approximately from 1 K to 0.05 K.

Table 4-15: List of equipment used in the cryoprobe test facility

#	Description	Function	Supplier	Part #
1	15" long x 8" diam. conflat flange nipples	Vacuum chamber	Norcal	2N-800N-RT
2	10" conflat flange	Vacuum chamber lid	Norcal	1000-000RT
3	Glass-metal bonded electrical pass-through	Electrical pass-through's	Detoronics	DTIH-20-41PN
4	KF-40 vacuum cap	Electrical pass-through vacuum flange	Norcal	NW-40B
5	500 psig burst disc (in low pressure stream on 2nd stage)	Protect cryoprobe sheath from overpressure	McMaster	4412T11
5	1" OD, 0.020" wall, 321 stainless tube	Cryoprobe sheath	McMaster	6622K152
6	2 1/8" rotatable conflat	Cryoprobe sheath flange	Norcal	212-100RT
7	EPDM O-ring 0.937" x 0.036"	Seals back of cryoprobe sheath	All Seals	--
8	G10-CR (cryogenics grade) tube 0.957" OD x 0.837 ID	Recuperator G10 sheath for PRTs	Accurate Plastics	--
9	Miniature electrical shrink wrap (recommend 0.042" to 0.070" to accommodate PRT wires and solder joint)	Electrical isolation for PRTs in G10 sheath	Advanced Polymers	042025CST
10	Nichrome heater wire	Apply thermal load	Lakeshore	WNC-32-100
11	PRT hookup wire - Quad ML	PRT electrical hookup wire	Lakeshore	QT-36
12	Replaceable core filter/drier	Remove moisture and other contaminants	Sporlan/Parker	C-R424-G with RCW-42 core
13	Ruby straight hole jewel orifice	Expansion valve for JT cycle	Bird Precision	22081
14	GE insulating varnish and adhesive	electrical isolation for PRT leads	Lakeshore	VGE-7031
15	Coalescing oil separator	remove oil from gas stream	Temprite	320

4.4 References

Advanced Fluid Connectors website: http://www.advancedfluidconnectors.com/files/aeroquip_fluid_compatibility_info.pdf

Advanced Specialty Gas Equipment: http://www.asge-online.com/pdf/GasCompatibilityTable.pdf

Air Liquide materials compatibility database: http://encyclopedia.airliquide.com/help.asp

"DuPont Suva 407C (R-407C) and DuPont Suva 410A (R-410A) Properties, Uses, Storage, and Handling" document. Available from the DuPont Website at: http://refrigerants.dupont.com/Suva/en_US/pdf/h65905.pdf or http://refrigerants.dupont.com/Suva/en_US/products/suva410a.html

Ekin, J.W Experimental Techniques for Low-Temperature Measurements, Oxford University Press, 2007.

Engineering Fundamentals or "efunda" website: http://www.efunda.com/designstandards/oring/oring_chemical.cfm?SM=none&SC=Freon%2012#mat

Fredrikson, K. 2004. Optimization of Cryosurgical Probes for Cancer Treatment. M.S. thesis. Madison, WI USA: University of Wisconsin - Madison, Mechanical Engineering Dept.

Fredrikson, K.; Nellis, G.; Klein, S. A. A Design Method for Cryosurgical Probes. *International Journal of Refrigeration* 2006, vol. 29, 700-715.

Gong, M.Q.; Wu, J.F.; Qi, Y.F.; Hu, G.; and Zhou, Y. "Research on the Change of Mixture Compositions in Mixed-Refrigerant Joule-Thomson Cryocoolers". Advances in Cryogenic Engineering, Vol 47, 2002.

Gong, M.; Zhou, W.; and Wu, J. "Composition Shift due to Different Solubility in Lubricant Oil for Multicomponent Mixtures", Cryocoolers 14, 2007.

Gong, M.; Deng, Z.; Wu, J.; "Composition Shift of a Mixed-Gas Joule-Thomson Refrigerator Driven by an Oil-Free Compressor", Cryocoolers 14, 2007.

Incropera, F. P.; DeWitt, D. P. *Fundamentals of Heat and Mass Transfer, Fourth Edition;* John Wiley & Sons: New York, 2002, p. 768.

Lakeshore Cryotronics website: http://lakeshore.com/

Lakeshore Cryotronics website, Platinum Resistor Thermometer (PRT) technical downloads: http://www.lakeshore.com/pdf_files/sensors/Manuals/F038-00-00.pdf

Omega.com, thermocouple thermal conductivity: http://www.omega.com/temperature/Z/pdf/z016.pdf

Perry, John, "Introduction to Analytical Chromatography", Pub. Marcel Dekker, New York, New York, 1981, p. 344, Table 14.4.

Parker O-ring Handbook, http://www.parker.com/literature/ORD%205700%20Parker_O-Ring_Handbook.pdf, accessed 04/02/2011

Taylor, R. 2009. "Optimal Pulse-Tube Design Using Computational Fluid Dynamics", PhD Thesis, Madison, WI, USA: University of Wisconsin – Madison, Mechanical Engineering Dept.

5 Experimental Data

The first experimental tests for this project included a characterization of the cryoprobe performance in its original manufactured configuration (i.e. before any of the modifications described in Chapter 4 were carried out, and using the original proprietary mixture). These tests serve as a benchmark for the experimental test facility by providing a reference to (1) measure the refrigeration performance penalty introduced by the cryoprobe modifications, and (2) compare with the refrigeration performance obtained with new mixtures tested in the modified cryoprobe.

The primary objectives of the experimental tests using the modified cryoprobe are to develop empirical but physics-based corrections/improvements to the model presented in Chapter 3, as well as to demonstrate the predictive capabilities of this new model. This objective is achieved using a series of experiments described in this chapter, including 198 steady state operating points obtained over a range of mixture compositions, pressures, temperatures and mass flows. Experimental data are used to infer the performance of the overall system (i.e. refrigeration power), as well as individual components (most notably the recuperator). The data are used to develop predictive correlations in Chapter 6.

5.1 Unmodified cryoprobe performance

The compact construction of the unmodified AMS cryoprobe (Figure 4-6) provides for limited measurement of component performance as discussed in Section 4.3.2. Available measurements include the temperature on the outside of the tip, and pressure measurements at the inlet of the 2nd stage compressor and outlet of the 1st stage compressor. Therefore, only a relatively basic load curve test was performed, in which a known heating rate is applied to the

cryoprobe tip and the tip temperature is measured ($\dot{Q}_{load}$ and T_7, respectively). The experiment was carried out in a simple experimental vacuum chamber, where only the probe tip penetrated into the vacuum space. The other cryoprobe components are either near room temperature, or insulated by the double-walled insulating vacuum sheath described in Section 4.3.2. The heat load was applied using a Nichrome wire wrapped around the cryoprobe tip and the temperature was measured using a PRT that was calibrated in-situ to ±0.5 K using a two-point calibration which is used to develop a linear correction to the standard PRT curve. The chamber was evacuated and the cold components were wrapped with MLI to minimize parasitic heat leak.

Figure 5-1 shows the measured load curve, with a no load temperature of about 160 K and 26 W at 197 K. The refrigeration performance of the new mixtures tested in the modified cryoprobe are compared with the baseline load curve in Section 5.4.1.

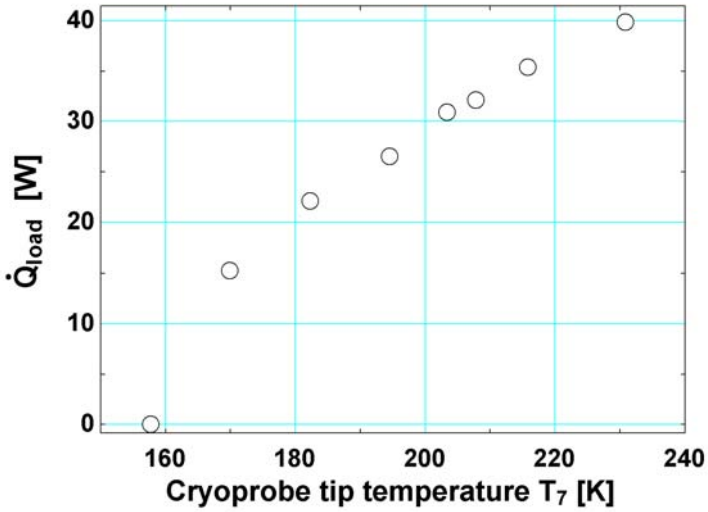

Figure 5-1: Baseline experimental load curve for the unmodified commercial cryoprobe system

5.2 Design of experiments for modified cryoprobe

The test facility was constructed using a flexible configuration that allows for precise control over the operating conditions of the system. Controllable parameters include the bypass valve setting, jewel orifice size, tip heater input, 2nd stage mixture composition, 1st stage working fluid, and charge pressures. With such a highly flexible test facility, it is important to establish bounds of the test matrix that envelope operating conditions that are relevant to forming the empirical model. The specific operating conditions for the modified cryoprobe test facility were selected in order to: (1) approximate conditions for a typical cryosurgical system, (2) verify the mixture property data computed by the NIST4 and REFPROP at cryogenic temperatures, and (3) map the performance of components whose behavior cannot be accurately predicted *a priori* (notably the precooler and recuperator). The performance maps must encompass a range of flow conditions that cause a significant variation in the operating condition of the component in order to allow the development of broadly applicable empirical models. The following Section, 5.2.1, describes the flow parameters that are relevant to the

precooler and recuperator heat transfer performance, and is used as the primary guide for selecting experimental variable ranges shown in Section 5.2.2

5.2.1 Heat transfer in the precooler/recuperator

The precooling and recuperative heat exchanger conductances are functions of the convective heat transfer coefficients on both the warm and cold sides of the heat exchangers, as well as the conductive resistance in the tube walls and fins. The convective heat transfer coefficients are complicated by the presence of two-phase flow, as well as the intricate flow passages associated with a Giaque-Hampson style heat exchanger, as shown in Figure 1-7. The conductance calculation may be further complicated by the diffusion mass transfer that is caused by the concentration gradients that occur during condensing or boiling of mixtures; diffusion results in an "effective" temperature difference driving heat transfer between the streams that is smaller than the bulk fluid temperature difference (Timmerhaus & Flynn, 1989). Correlations for pressure drop and heat transfer coefficients for two phase flow of a *single* component working fluid in a simple geometry (e.g., a tube) are scarce and provide at best 25% uncertainty (Timmerhaus & Flynn, 1989). The added complexity of a multi-component, two phase flow over a complex geometry at cryogenic temperature prohibits reasonably accurate, *a priori* estimations of the heat exchanger conductance. The model of the cryoprobe system therefore relies heavily on experimental measurements for computation of the heat exchanger conductance.

The heat exchanger conductance is highly dependent on the temperature, pressure, fluid velocities and thermodynamic quality profiles within the heat exchangers. These parameters are expected to vary with cryoprobe thermal load, cryoprobe orientation, amount of precooling,

working fluid flow rates, and mixture composition. The effects that these variables have on the heat exchanger conductance are measured and, based on these measurements, incorporated into the model in a manner that provides adequate fidelity without being overly complicated. The measured conductance as a function of these parameters is, itself, likely to be of substantial value to the community working with mixed gas refrigeration system. Despite the daunting complexity of the heat exchange process in the cryoprobe, a few simplifications can be made to illuminate the primary variables that are expected to govern the performance.

Precooling Heat Exchanger

Consideration of the precooler is simplified by three major assumptions about the working fluid: (1) the 1st stage fluid will be saturated and therefore exist at nearly constant temperature throughout the precooler, (2) the thermal resistance associated with the 1st stage pure refrigerant boiling in the precooling evaporator is negligibly small, and (3) the gas mixture is generally superheated throughout the precooler. The implications of these assumptions are discussed below.

1. The 1st stage pure refrigerant is saturated in the precooler; assuming the pressure drop is insignificant, the temperature will remain constant.
2. The pure refrigerant precooling the gas mixture boils throughout the precooler and therefore has significantly enhanced heat transfer (Kandlikar et al., 1999). The heat transfer coefficient will be large, especially when compared to the gaseous flow of the high pressure mixture (i.e., the working fluid for the 2nd stage JT cycle) in the precooler. Therefore, the convective heat transfer resistance on the pure refrigerant side can be neglected when considering the heat transfer in the precooler.

3. The majority of the optimal mixtures selected using the model in Chapter 3 are superheated, or mostly superheated in the temperature span of the precooler (nominally 290 K to 240 K). In this case, the gas mixture behaves much like a pure gas and heat transfer can be accurately described using the Dittus-Boelter and Seidler-Tate correlations, as shown by Nellis et al. (2005). Heat transfer coefficients with a fixed mass flow were calculated for the gas phase of several different mixtures over a temperature range of 240 K to 290 K; the heat transfer coefficients were generally insensitive to the mixture composition and temperature, with variances on the order of 10-15%.

With these three observations, the heat transfer within the precooler is reasonably understood. The gas mixture exchanges heat with constant temperature, saturated fluid through the combined resistances of the pure fluid boiling convection (which is negligibly small), the tube/fin conduction (which does not change substantially), and gas mixture convection which is well defined using the Dittus-Boelter and Seidler-Tate convection correlations). The temperature of the gas mixture exiting the precooler will be about the same regardless of mixture composition, and will be most sensitive to the saturation temperature of the 1st stage fluid in the precooler.

Recuperative Heat Exchanger

The simplifications applied to the precooler do not apply in the recuperator. The model developed in Chapter 3 showed that the high and low temperature sides of the recuperator both typically experience two phase flow throughout most of the heat exchanger for an optimized mixture. The two-phase local heat transfer coefficient and pressure drop governing the

performance within the recuperator are functions of the void fraction and flow distribution, i.e. flow regime, (Timmerhaus & Flynn, 1989 and Hughes et al., 2004); therefore, experimental variables that may affect the flow distribution and void fraction in the recuperator are selected. Void fraction and flow distribution are in turn largely a function of thermodynamic quality and mass flux. Thermodynamic quality is sensitive to cryoprobe load (which affects tip and recuperator temperatures), high and low side pressure, and mixture composition. Mass flux will depend on the high and low side pressures, which are controlled with the bypass valve and jewel orifice.

The variance of the recuperator performance will also give some indication of the heat transfer mechanisms at intermediate locations within the recuperator. The shell side (low pressure) flow is often the dominant thermal resistance for helically wound heat exchangers (Timmerhaus & Schoenhals, 1974) because most of the fluid on the shell side is in a gas phase, which has low conductivity. Also, the shell side has a larger hydraulic diameter than the tube side (in order to minimize pressure drop) and therefore the fluid is not as well mixed. Understanding the heat transfer mechanisms can assist in the proper selection of a two-phase heat transfer model. The shell side fluid evaporation is the focus of the discussion here.

Two phase flow heat transfer with evaporation is governed by nucleate boiling, convective motion, or a combination of the two. Wambsganss et al. (1993) have shown that heat transfer for two phase flow in small channels (such as those in the Hampson-Giaque heat exchanger) is often dominated by nucleate boiling, and is therefore independent of mass flux and quality. Flow in larger channels is typically convection-dominated with nucleate boiling suppressed, and it is a strong function of quality and mass flow (Wambsganss, 1993). Nellis et al. (2005)

reported heat transfer coefficient measurements in a small diameter tube for mixtures at cryogenic temperature under test conditions that are similar to those in the cryoprobe. Their results contradict the findings of Wambsganss et al. (1993) in that the measured heat transfer coefficients for mixtures in small tubes varied significantly with mass flux and quality and subsequently are at least partially governed by convective flow. Therefore, it was uncertain which of the heat transfer mechanisms (convection or nucleate boiling) best describe flow in the particular cryoprobe recuperator studied here.

In the tests presented here the recuperator conductance relation as a function of quality was shown to not vary significantly with mass flux as shown in Figure 5-22, which indicates that nucleate boiling is the dominant heat transfer mechanism.

Summary

In summary, the heat transfer in the precooler is relatively well understood. Therefore, mapping the two-phase flow in the recuperator is the focus of the heat transfer measurements. The two phase flow heat transfer and pressure drop are largely affected by the quality and mass flux and therefore experimental conditions are chosen to achieve the maximum range of these two parameters. Thermodynamic quality is sensitive to cryoprobe load (which affects tip and recuperator temperatures), high and low side pressure, and mixture composition. Mass flux depends on the high and low side pressure, which are controlled with the bypass valve setting and jewel orifice (0.0175” diameter for all the tests here) as well as the absolute pressures on the high and low side. Identification of convection or nucleate boiling dominated heat transfer was possible using these same parameter ranges, and could be used to select more detailed

phenomenological models (that would predict the performance without the need for extensive empirical tuning) in future studies.

5.2.2 Test matrix

The data collected using the experimental test facility are divided into four different sets based on the 2nd stage mixture compositions as shown in Table 5-1. Sets 1 and 2 include tests with pure synthetic refrigerants (R14 and R23), where the R23 data were collected with the precooling cycle deactivated. These tests were used for system debugging and test facility verification. For example, the data are used to show the agreement between the measured and predicted Joule-Thomson effect across the jewel orifice in the 2nd stage. Verification in this manner can be carried out with higher confidence using pure components whose property data are well defined (as opposed to mixtures, whose properties must be predicted using complex mixing rules that introduce a larger uncertainty).

A bottle of precisely formed mixture of argon, R14 and R23 was used to charge the system for the third set of tests. These tests were used to demonstrate the composition shift of the circulating mixture in the cycle, and also provided initial data where the recuperator operated in the two phase regime. However, this mixture yielded relatively high thermodynamic quality (above 0.8) in the recuperator and therefore, the 4th set of mixture compositions eliminated the argon and increased the R23 in order to force the recuperator to operate over a larger range of quality (from saturated liquid to saturated vapor). The majority of the two-phase heat transfer and pressure drop data used to develop the empirical correlations developed in Chapter 6 are taken from this 4th set.

Table 5-1: Summary of test parameters for the collected data

	Set 1	Set 2	Set 3	Set 4
2nd stage				
Mole fraction argon	--	--	10-15%	--
Mole fraction R14	100%	--	55-65%	20-50%
Mole fraction R23	--	100%	25-35%	50-80%
High Pressure	185-350 psig	240-350 psig	190-255 psig	160-290 psig
Low Pressure	10-40 psig	11-25 psig	10-25 psig	14-100 psig
Tip temperature (T_7)	163-255 K	240-292 K	170-215 K	175-260 K
Tip thermal load ($\dot{Q}_{load}$)	0.5-17.5 W	7-24 W	0.5-7.5 W	0.3-43 W
Mass flow ($\dot{m}_{2nd}$)	0.8 -1.6 g/s	0.65-0.9 g/s	0.8-1.0 g/s	0.7-1.7 g/s
1st stage				
Working fluid	R410a	N/A	R410a	R410a
Evaporator temperature	237-240 K	N/A	240-242 K	235-242 K
mass flow ($\dot{m}_{1st}$)	1.4-2 g/s	N/A	2-2.2g/s	1.2-1.4 g/s

5.3 Summary of data processing procedure

This section presents an overview of the methodology used to compute the important cycle operating parameters including thermodynamic states, mass flows, refrigeration load, and heat exchanger conductances and pressure drop from the experimental measurements. A more detailed discussion will be presented in the MS Thesis of a UW-Madison graduate student, Kendra Passow, who is currently working on the project. The thermal analysis used to process the experimental data is similar to the one presented in the modeling section of this thesis (Chapter 3); energy balances are applied to compute thermodynamic states that could not be measured, and numerical heat exchanger modeling techniques are used to accommodate the highly temperature dependant specific heat of the mixture (so that the effectiveness-NTU

relation can be applied to compute conductances of each subsection). Nevertheless, nuances between the methods merit a full discussion including the detailed modeling equations – readers are directed to Passow's thesis for these equations.

The data are recorded when the system achieves steady state, an operating condition established by minimal fluctuations of the computed recuperator conductance; the recuperator is thermally massive compared to the other components and therefore is the final component to achieve steady operation. Table 5-2 sows a sample of the measurements taken for a steady state operating point, as well as computation of various performance metrics accomplished using both the NIST4(Ely 1992) and REFPROP (Lemmon 2007) databases. A full listing of the measured and computed variables for all data points is available as an electronic appendix to this thesis, as well as on the UW Madison Solar Energy Lab website: (http://sel.me.wisc.edu/ publications-theses.shtml).

Table 5-2: Summary of experimental measurements and some computed performance metrics for a sample test.

Measured Quantities

1st stage

Description	Value	Unit
working fluid	R410a	--
PRT 8	241.9	K
PRT 8a	294.2	K
TC 10	294.4	K
P8	20.59	psig
P9	351.6	psig
$\dot{m}_{1^{st}}$	91.84	stdL N_2/min

2nd stage

Description	Value	Unit
mix component 1	argon	--
mix mole fraction 1	14.6%	--
mix component 2	R14	--
mix mole fraction 2	59.6%	--
mix component 3	R23	--
mix mole fraction 3	25.8%	--
PRT 1	239.7	K
TC 3	295.6	K
PRT 5	194.4	K
PRT 6	172.5	K
PRT 7	173.6	K
PRTi1	227.7	K
PRTi2	219.3	K
PRTi3	210.8	K
PRTi4	193.1	K
PRTi5	177.8	K
PRTi6	221.8	K
PRTi7	211.3	K
PRTi8	208.3	K
PRTi9	192.9	K
P1	21.5	psig
P1a	13.3	psig
P3	211.1	psig
P5	139.2	psig
P7	28.5	psig
$\dot{m}_{2^{nd}}$	30.2	stdL N_2/min
V_{load}	10.88	V
I_{load}	0.1673	A

Measured Quantities (cont.)

Other

Description	Value	Unit
vacuum pressure	2×10^{-4}	torr
ambient pressure	739.4	mmHg
ambient temperature	296.4	K

Computed Quantities

1st stage

Description	Value	Unit
$\dot{m}_{1^{st}}$	2.32	g/s
UA_{pc}	2.67	W/K
h_8	108	kJ/kg
h_{10}	93.6	kJ/kg

2nd stage

$\dot{m}_{2^{nd}}$	0.895	g/s
$\dot{Q}_{load}$	1.82	W
T_4	234.5	K
h_1 (REFPROP)	364.2	kJ/kg
h_3 (REFPROP)	394.9	kJ/kg
h_4 (REFPROP)	357.5	kJ/kg
h_5 (REFPROP)	277	kJ/kg
h_6 (REFPROP)	280.7	kJ/kg
h_7 (REFPROP)	283.7	kJ/kg
$\dot{Q}_{parasitic}$	4.465	W
$UA_{rec,0}$	4.652	W/K
$UA_{rec,1}$	1.779	W/K
$UA_{rec,2}$	0.8867	W/K
$UA_{rec,3}$	1.118	W/K
$UA_{rec,4}$	1.669	W/K
$UA_{rec,5}$	0.5902	W/K
$UA_{rec,total}$	10.7	W/K

5.3.1 Computing thermodynamic states

Figure 5-2 compares the experimental measurements discussed in detail in Chapter 4, with all of the thermodynamic states that are computed to capture cycle performance. The most important parameter associated with the 1st stage affecting the overall refrigeration performance is the evaporation temperature of the 1st stage working fluid (R410a, for the tests presented here) in the precooler. The pressure drop of the R410a in the precooler is neglected, so the R410 is assumed to boil at a nearly constant temperature (i.e the temperature at state 8 represents the temperature of the R410a throughout the precooling heat exchanger). An estimation of the pressure drop could be inferred from the recuperator cold side pressure drop data presented in Section 5.4.7, as the heat exchanger geometry is very similar. The precooler and recuperator are both annular counterflow heat exchangers constructed using finned tubing helically wound about a mandrel. The recuperator pressure drop model could be normalized by finned tube length (46.1 inches) and applied to the precooler finned tube section (21.7 inches). Such an analysis is beyond the scope of this thesis

The temperature at state 8 does not significantly change throughout the experiments (~236-241 K), and therefore the discussion here primarily focuses on the 2nd stage performance. The states can be divided into those obtained using three different methods depending on the measurement instrumentation available at the particular location.

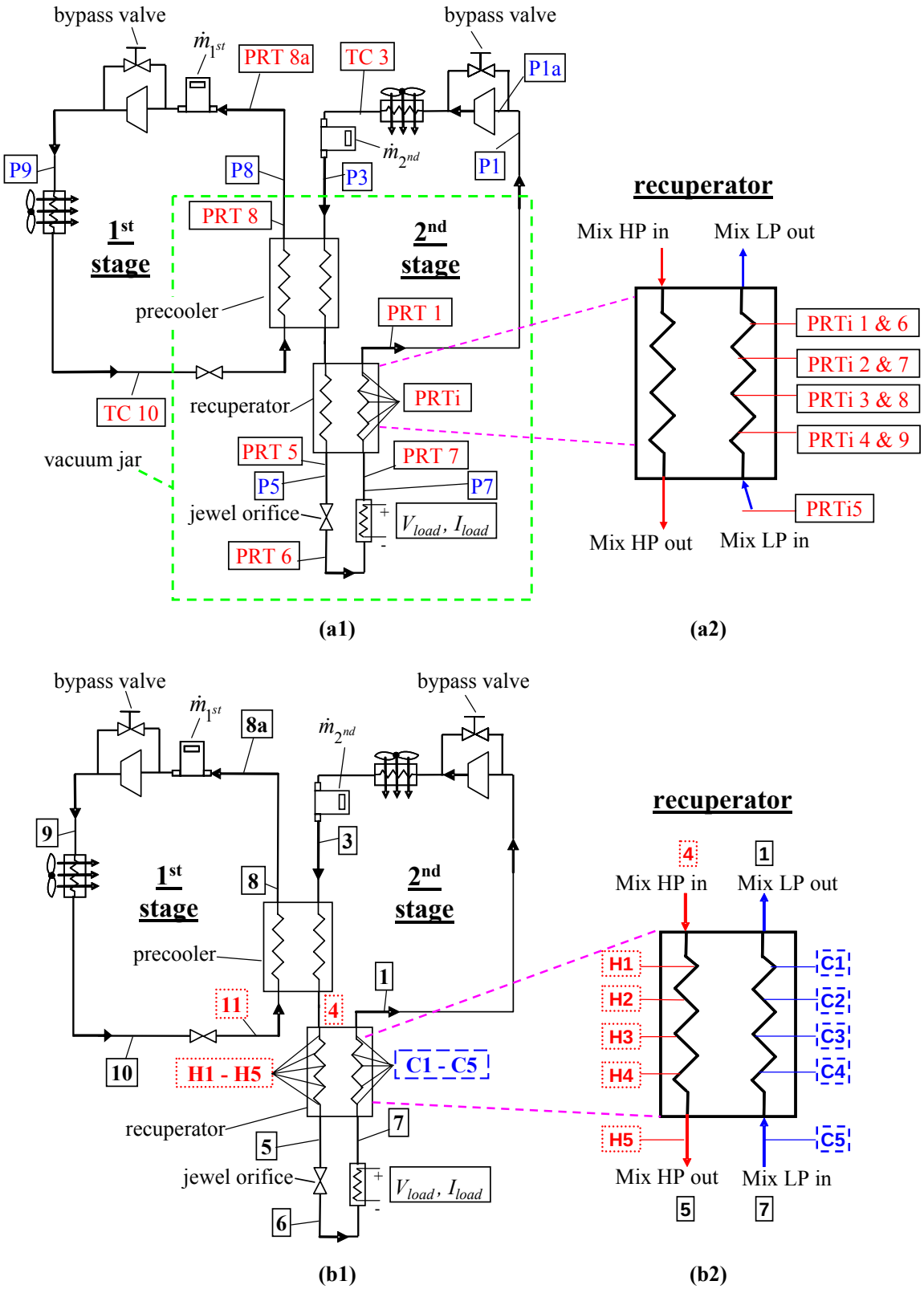

Figure 5-2: **Cycle schematics comparing the measurements (a1,a2) and the computed thermodynamic states (b1,b2).**

Method 1

Direct measurements of both temperature and pressure are recorded at states 1,3,5,6,7,8, 8a, and 10; these locations are indicated by solid black boxes in Figure 5-2(b1). Note that the pressure drops between points 6 and 7, 9 and 10, and 8 and 8a are neglected as the tubing is large here relative to other restrictions in the system. Figure 5-3 shows the directly measured 2nd stage states (1,3,5,6,7), as well as the states computed using the other two methods (described in the proceeding paragraphs), on a pressure-enthalpy (*P*-*h*) diagram for a nominal test case. Temperature and pressure measurements completely define the 2nd stage states when a mixture is used, regardless of thermodynamic quality, as mixtures exhibit temperature glide in the vapor dome. Temperature glides do not occur in the 1st stage cycle which uses a R410a (an azeotropic blend that evaporates at a nearly constant temperature for a given pressure) for the tests presented here. Therefore, the temperature and pressure measurements are not necessarily sufficient to determine the enthalpy at location 8, which may lie within the vapor dome (indeed, the R410a exited the precooler at state 8 well inside the vapor dome and a substantial amount of a latent cooling had to be removed from the stream in a fin-fan heat exchanger installed between the exit of the vacuum chamber and 1st stage mass flow meter in order to protect the mass flow meter from extreme cold). However, as discussed in the "Method 3" paragraph, the enthalpy at state 8 can be inferred from an energy balance on the precooler.

Method 2

The 2nd method is used determine the thermodynamic state at locations where direct temperature measurements are available but pressure measurements are not. These states (C1-C5) include the low pressure side of the recuperator and are indicated in Figure 5-2(b1) with

blue dashed boxes, and in Figure 5-3 with blue triangles. The temperature at each axial location is averaged between each pair of diametrically opposed PRT measurements (shown in Figure 4-11 and Figure 4-18). The pressure at these states is computed by applying a linear pressure drop (i.e. the pressure drop is assumed to be equal between each of the temperature sensor locations within the recuperator) between the pressure measurements at states 7 and 1.

Method 3

Thermodynamic states where neither pressure nor temperature is measured are computed using energy balances and assumptions about the pressure drop. These states include the high pressure side of the recuperator (H1-H5, and 4) and are displayed in Figure 5-2(b1) with red dotted boxes and in Figure 5-3 with red squares. Pressure at state 4 is estimated to lie halfway between states 3 and 5 (where pressure is measured). This relatively crude estimation is justified by examining the lengths and flow regimes in the precooler and recuperator. Table 4-6 shows that the finned tube length (carrying the high pressure mixture in the 2^{nd} stage from state 3 to 5) in the recuperator and precooler are 1.171 m (46.1 in.) and 0.551 m (21.7 in.), respectively. The mixture is mostly vapor in the precooler, whereas the recuperator exhibited two-phase flow for many of the tests. The higher densities of the colder fluid in the recuperator results in lower velocities, and subsequently, lower frictional pressure drop per length of tube. Therefore, while the finned tube in the recuperator accounts for $^{2}/_{3}$ of the length between state 3 and 5, it was estimated that only ½ of the pressure drop occurs in the recuperator. The heat transfer analysis of the recuperator showed that the conductance values computed from the data can be very sensitive to the pressure assumed at state 4; part of the ongoing work includes developing a model to provide a better estimate of the pressure at this state.

The enthalpy at state 4 is computed using an energy balance involving states 1, 5, and 7, and the temperature can be computed using the estimated pressure. The enthalpies of the intermediate recuperator hot-side locations (H1-H5) are computed using an energy balance for the sections of the recuperator between the temperature sensors in the low pressure stream. A linear pressure drop is applied between states 4 and 5, similar to the method used on the recuperator cold side. The pressures and enthalpies completely define the states so the temperatures are readily computed using the mixture database (REFRPOP, for the data presented in Figure 5-3, Figure 5-4, and Figure 5-7). The recuperator temperature profile for the same nominal test case presented in Figure 5-3 is shown in Figure 5-4.

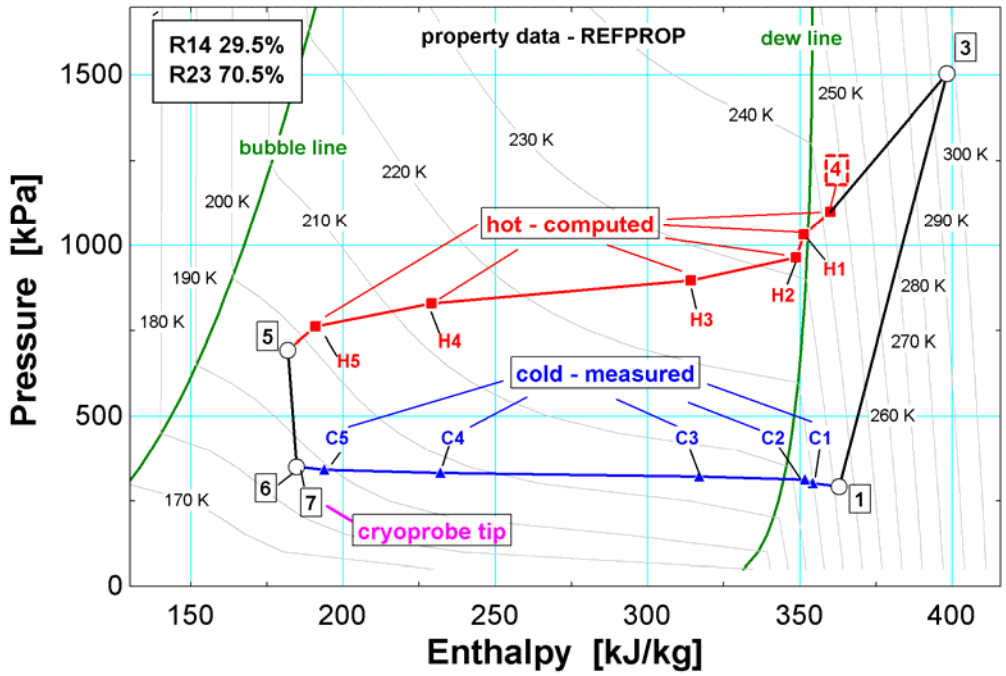

Figure 5-3: Nominal 2nd stage state points overlaid on a P-h diagram for the mixture where the #'s correspond to the thermodynamic state points indicated in Figure 5-2 (b1).

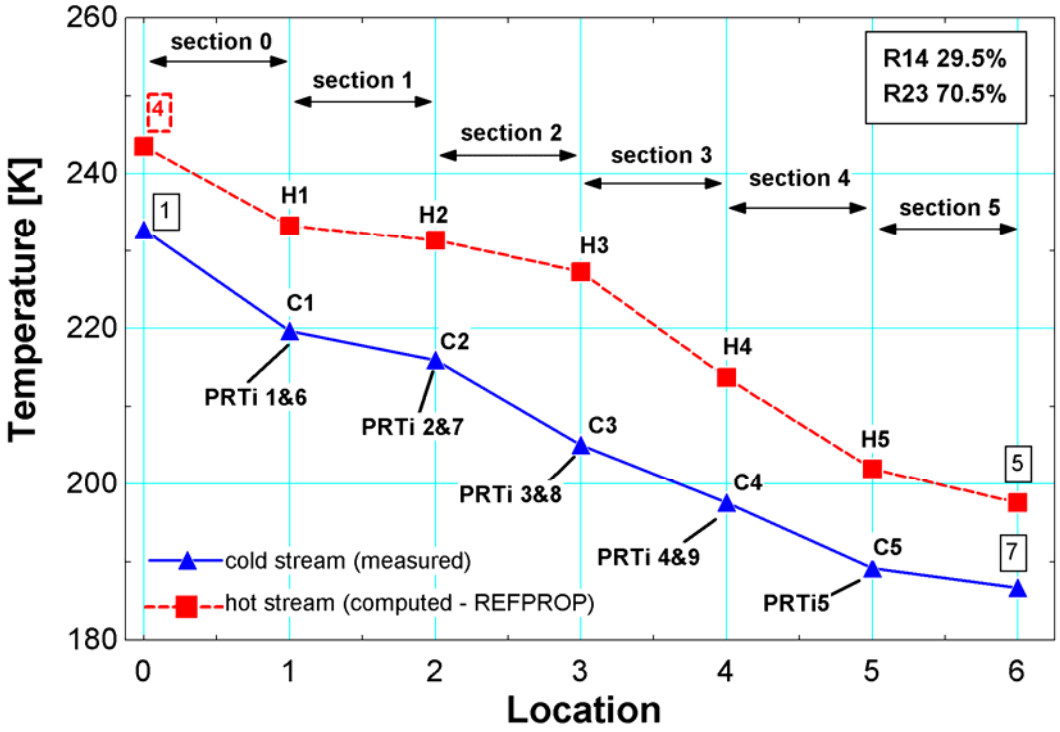

Figure 5-4: Measured and computed temperature profile in the recuperator. The section numbers and thermodynamic state locations are indicated using the same nomenclature from Figure 5-2.

The R410a was typically a subcooled liquid at state 10 so the enthalpy could be computed from the temperature and pressure measurements. Assuming isenthalpic expansion to state 11 and negligible pressure drop through the shell side of the precooler, the thermodynamic state for location 11 could be computed. An energy balance on the precooler using states 3, 4 and 11, as well as the cycle mass flows could be used to identify the enthalpy at state 8.

5.3.2 Precooling and recuperative heat exchanger conductances

The 2nd stage thermodynamic states and temperature profiles established in the previous section are used to compute the precooler and recuperator conductances. Similar to the method described in Chapter 3, discrete models divide the heat exchangers into sections with small temperature changes over which specific heat of the mixture is nearly constant and the effectiveness-NTU relationship can be accurately applied.

Figure 5-5 shows how the discrete model divides the precooler into N_{pc} sections (about 15, based on a numerical sensitivity analysis similar to the one showed in Figure 3-6), each exchanging an equal amount of heat. The overall energy exchange is computed according to:

$$\dot{Q}_{pc} = \dot{m}_{2nd}\left(h_3 - h_4\right) \tag{5.1}$$

where h_3 and h_4 are the enthalpies at state 3 and 4 in the 2nd stage, and $\dot{m}_{2^{nd}}$ is the 2nd stage mass flow. The intermediate 2nd stage enthalpies at each node are computed using an energy balance on each of the sections:

$$h_{2^{nd},pc,i} = h_{2nd,pc,i-1} - \frac{\dot{Q}_{pc}}{\dot{m}_{2^{nd}}}\frac{1}{N_{pc}} \qquad i = 1 \ldots N_{pc} \tag{5.2}$$

where i is the node index and $h_{2nd,pc,i}$ is the enthalpy of the mixture in the 2nd stage at each section. The model also assumes a linear pressure drop on the 2nd stage side so that the pressure drop is equal in each of the sections:

$$P_{2^{nd},pc,i} = P_3 - \frac{\left(P_3 - P_4\right)}{N_{pc}}\left(i\right) \qquad i = 1 \ldots N_{pc} \tag{5.3}$$

where $P_{2nd,pc,i}$ is the pressure in the 2nd stage at each section and P_3 and P_4 are the pressures at states 3 and 4. Nodal temperatures can then be computed using the mixture property data relations in NIST4 or REFPROP:

$$T_{2^{nd},pc,i} = temperature\left(P_{2^{nd},pc,i}, h_{2^{nd},pc,i}\right) \tag{5.4}$$

Finally, the temperature of the 1st stage refrigerant is assumed to be constant in the precooler so the nodal temperatures are:

$$T_{1^{st},pc,i} = T_8 \tag{5.5}$$

Using the 1st stage temperatures, as well as the 2nd stage temperatures and enthalpies, the effectiveness-NTU equations (shown for the model in Section 3.1.2) are applied to compute the conductance of each section. The overall precooler conductance (UA_{pc}) is then represented by the sum of the conductances in each section.

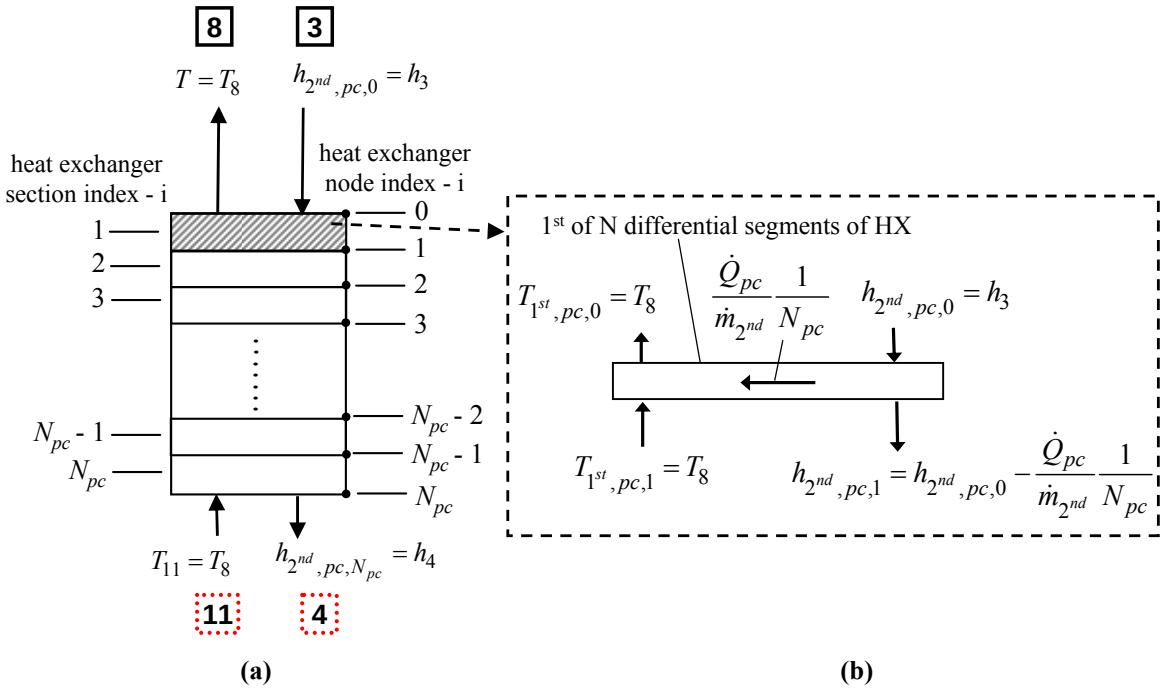

Figure 5-5: (a) Precooling heat exchanger divided into N_{pc} sections and (N_{pc} + 1) nodes. (b) First differential heat exchanger element.

The temperature measurements within the low pressure stream of the recuperator allow for more resolved conductance measurements than those in the precooler. Figure 5-6(a) shows the recuperator divided into 6 sections (labeled sec 0-5) between the 7 measurement locations defined in Section 5.3.1 (1,C1-C5, & 7 in the cold stream and 4, H1-H5 & 5 in the hot stream). The conductance in each section is computed using a discrete model that further subdivides the sections into a number of subsections (N_{sub} = 10, based on a numerical sensitivity analysis

similar to the one showed in Figure 3-6) that each exchange an equal portion of the energy transferred in each section. The effectiveness-NTU equations are applied in each subsection, where the computed conductances are summed to find the conductance of each section. Figure 5-7 shows an example of the recuperator conductance as a function of section computed using the nominal temperature profile reported in Figure 5-4. Sections 0-4 are comprised of finned tube sections, and section 5 represents a short unfinned section between PRTi5 and PRT 7. Additionally, section 5 intercepts any radiation parasitic introduced by the relatively large conflat at the cold end of the cryoprobe sheath. Therefore only sections 0-4 can be expected to perform in a similar fashion. For this particular profile, sections 4 and 3 exhibit large conductance values, while sections 0-2 have comparatively small conductance values. Sections 3 and 4 have high heat transfer because the mixture is in a two-phase state, while sections 0-2 are near dryout (with a quality above 0.9) or in a vapor state. A more detailed discussion of the conductance variation with quality can be found in Section 5.4.8.

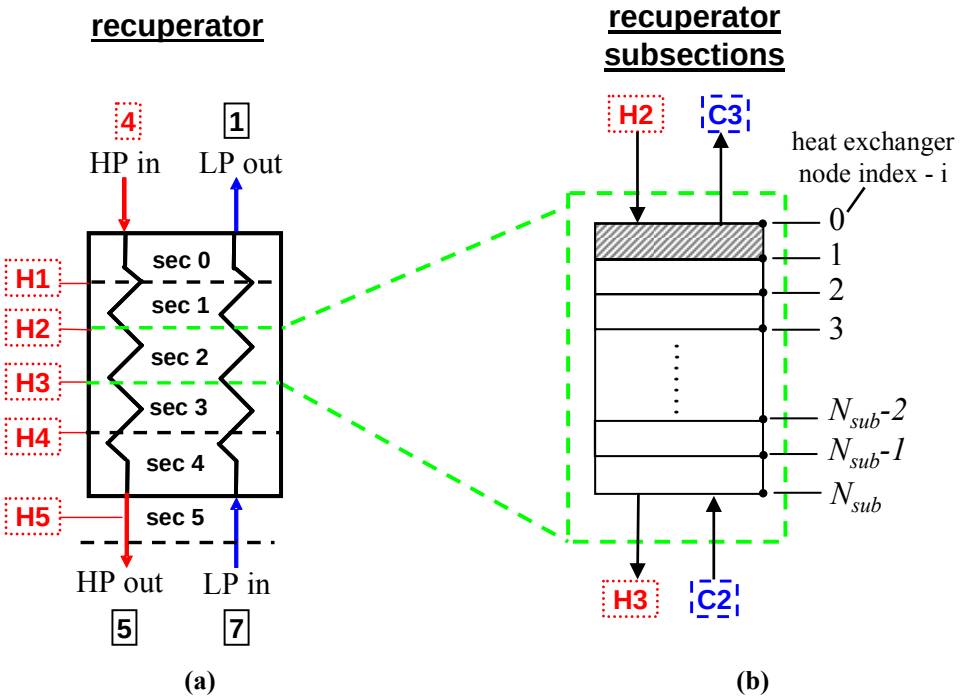

Figure 5-6: **(a) Recuperative heat exchanger showing the 6 sections between the PRT measurements. (b) Recuperator section further subdivided into N_{sub} sections.**

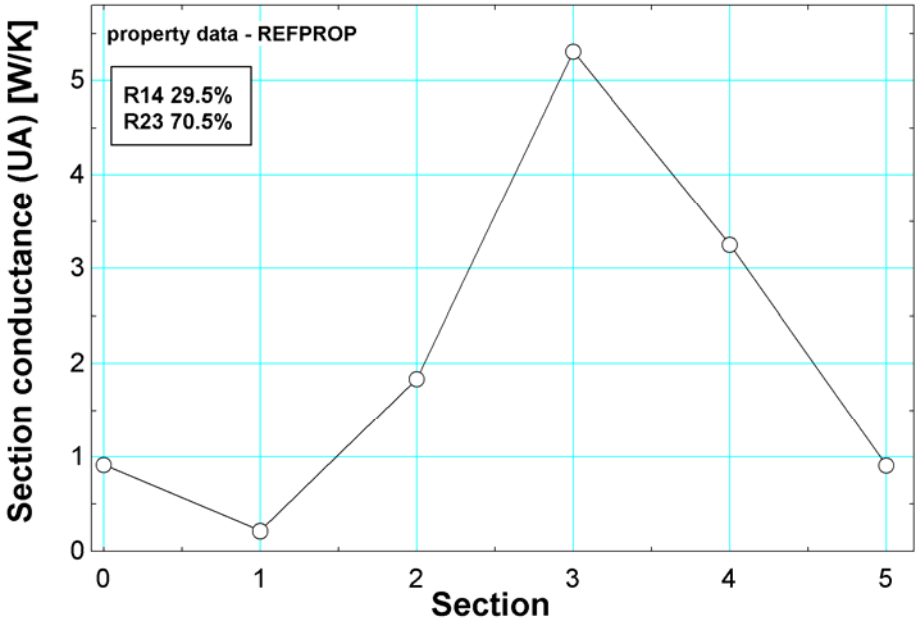

Figure 5-7: **Nominal conductance distribution in the recuperator computed using the temperature profile in Figure 5-4.**

5.4 Experimental results

5.4.1 Load curves

The load curve for the cycle represents the simplest, and yet most relevant metric of overall system performance. Combined with the overall surface area of the active portion of the cryoprobe tip, the refrigeration power at a given temperature determines the size of the iceball produced by the probe (and thus the surgical effectiveness of the instrument). Optimization of the refrigeration power and load temperature for a given cryoprobe tip geometry are discussed in detail in Fredrikson (2004) and Fredrikson (2006). Figure 5-8 shows the load curves for the four sets of working fluids shown Table 5-1 that were tested in the JT cycle of the modified cryoprobe experimental facility. Note that the composition of the mixtures is unique for each of the points indicated on the graph. The load curve obtained using the original mixture is also shown to compare the relative performance of the new mixtures.

The pure refrigerants, R14 and R23, were each tested at three high and low pressure values. Each set of pressure values produced a distinct load curve that is indicated by a solid line drawn through the points in Figure 5-8. As expected, the load curve performance is relatively poor using the pure refrigerants compared to some of the better mixtures. The R14-R23-Argon mixtures underperformed (i.e., provided less refrigeration at a given temperature) the original mixture and even some of the pure R14 tests. Finally, the binary R14-R23 mixtures spanned the largest range of load curve points as a wide range of concentrations were tested. Several of the R14-R23 mixtures significantly outperformed the original mixture in the 195-205 K region. A model that can select these high-performing mixtures *a priori* represents a valuable

design tool; the predictive capability of the empirically tuned mixture optimization model developed for this project is demonstrated in Chapter 6.

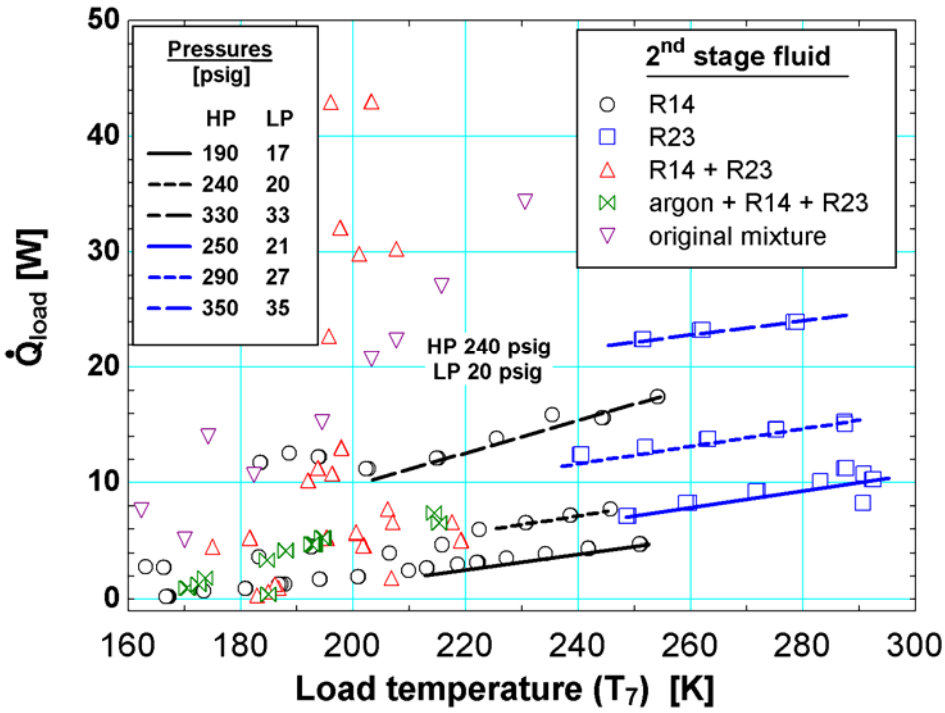

Figure 5-8: Load curves for four sets of mixture compositions tested in the modified cryoprobe compared with the load curve of the unmodified probe charged with the manufacturers' original proprietary mixture.

5.4.2 Circulating mixture composition shift

The composition of the circulating mixture can differ significantly from the charged composition. Individual mixture components are preferentially absorbed into the compressor oil and differentially pool by condensation based on their individual boiling points; the individual components are effectively removed from circulation by these mechanisms at different rates. Eventually, a new steady state circulating composition is achieved that is in thermodynamic equilibrium with the concentrations of the components asymmetrically collected at various points in the system. This new circulating composition represents the fluid applied to the cycle and is the proper mixture to use for the cycle analysis. Therefore, the composition of the

circulating mixture is measured using a Gas Chromatograph (GC) for each of the steady state data points.

Figure 5-9 shows the composition shift during system testing for a pre-made three component mixture (9.1% Argon, 40.9% R14, and 50.0% R23) used to charge the system from a high pressure bottle. The bottle composition is labeled on the graph, and the points immediately to the left represent the mixture composition after the system was charged and the components absorbed into the oil at room temperature for several days. The R23 absorbs significantly in the oil, reducing its concentration from 50% to 40%, whereas the R14 concentration increases by 9% and the argon concentration by 1%. The normal boiling points of the constituents are 87 K for argon, 145 K for R14, and 191 K for R23. As a result, when the system becomes cold the R23 condenses out of circulation and the composition becomes even more rich in R14 and argon. The data here highlight the need to measure the circulating composition, as the mole fractions changed by as much as 20% during the tests relative to the pre-made mixture used to charge the system.

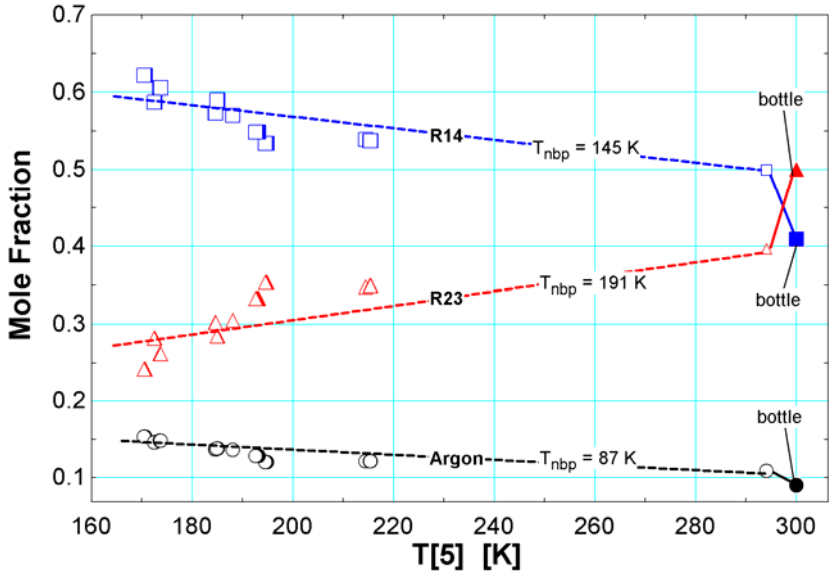

Figure 5-9: **Circulating composition shift vs T_5 for a charged mixture of 9.1% Argon, 40.9% R14, and 50.0% R23. The points immediately to the left of the "bottle" points represent the composition after the mixture has absorbed into the compressor oil at room temperature for several days.**

5.4.3 Joule Thomson effect

A critical requirement of the optimization model is the ability to compute the thermodynamic properties of the multi-component mixtures at cryogenic temperatures. The precise measurements presented here are ideal for evaluating the capability of the computed property data to predict thermodynamic phenomena occurring the cycle. Specifically, the isenthalpic expansion process across the jewel orifice in the MGJT cycle (from state 5 to state 6 in Figure 5-2) can be characterized by the Joule-Thomson effect temperature change (ΔT_{JT}). Comparisons of the predicted and measured ΔT_{JT} for the four sets of 2nd stage working fluid are presented in Figure 5-10. Temperatures at states 5 and 6 are measured with an uncertainty of 0.5 K, so the experimental uncertainty for ΔT_{JT} is 0.71 K. The predicted values are computed using both the NIST4 and REFPROP databases; given the measurements of pressure before and

after the orifice, and the upstream temperature (P5, P7, and PRT 5 in Figure 5-2(a), respectively), the database computes the downstream temperature and the predicted ΔT_{JT}.

Figure 5-10 shows that the measured and predicted values agree quite well, to within 10% for much of the data presented here. A distinct region of deviation occurs on the right edge of the vapor dome (i.e., the dew point line) for the R14, R23, and Argon+R14+R23 tests. Note that REFPROP provides a slightly better prediction near the vapor dome for the Argon+R14+R23 mixture. The REFPROP database provides a significantly better prediction for the R14+R23 data in Figure 5-10(c). These mixtures cover a wider range of thermodynamic quality, including regions that cross the bubble point line below 200 K. The NIST4 database predicts a bubble point line at higher temperatures that REFPROP, as shown in Figure 5-11, so the isenthalpic expansion is often predicted to occur with in the subcooled liquid region using NIST4 but within the vapor dome with REFRPOP. As a result, the JT effect predicted with NIST4 is often near zero (note the vertical isotherms in the subcooled region of the *P*-*h* diagram in Figure 5-3: the isenthalpic expansion produces no temperature change). The REFPROP data provide a much better estimate of the JT effect in these regions and therefore also better predicts the location of the bubble line. The superior prediction of the vapor dome was a key factor in the decision to use REFPROP to process the experimental conductance results.

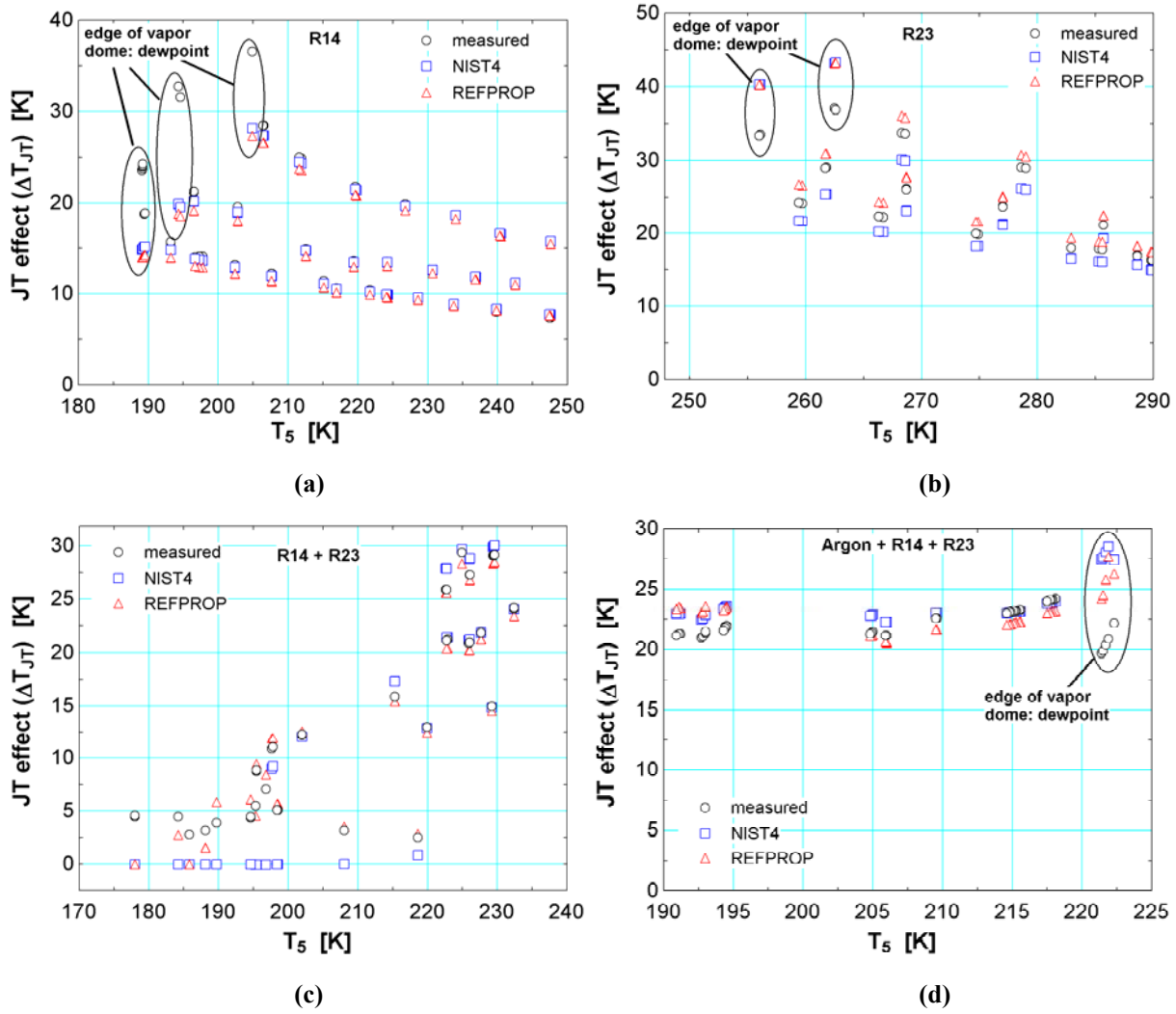

Figure 5-10: Measured and predicted JT effect temperature changed across the orifice in the 2nd stage for (a) R14, (b) R23, (c) R14+R23 mixtures, and (d) Argon+R14+R23 mixtures. The right edge of the vapor dome (dew point line) is highlighted in the figures.

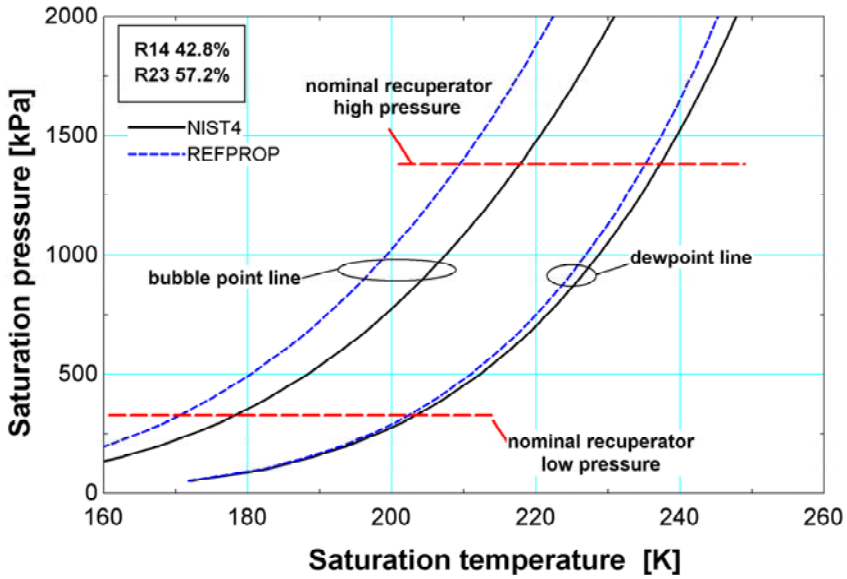

Figure 5-11: Comparison of the prediction of the dewpoint and bubble point using NIST4 and REFPROP. Nominal values for the high and low pressures in the recuperator are shown.

5.4.4 2nd Stage mass flow

The mass flow rate in the 2nd stage for the mixture was computed using the reading from the calorimetric flow meter corrected for the specific heat of the mixture as shown in Eq. (4.38). Figure 5-12 compares the mass flow readings computed using property data from the NIST4 and REFPROP databases. The mass flow measurement occurs at state 3, which is at high pressure, ambient temperature, and therefore in a vapor state for all the data presented here. Specific heat values computed using REFPROP and NIST4 are very similar in the vapor state, so the two values of mass flow for each test point agree well (within experimental error) for most of the data presented here.

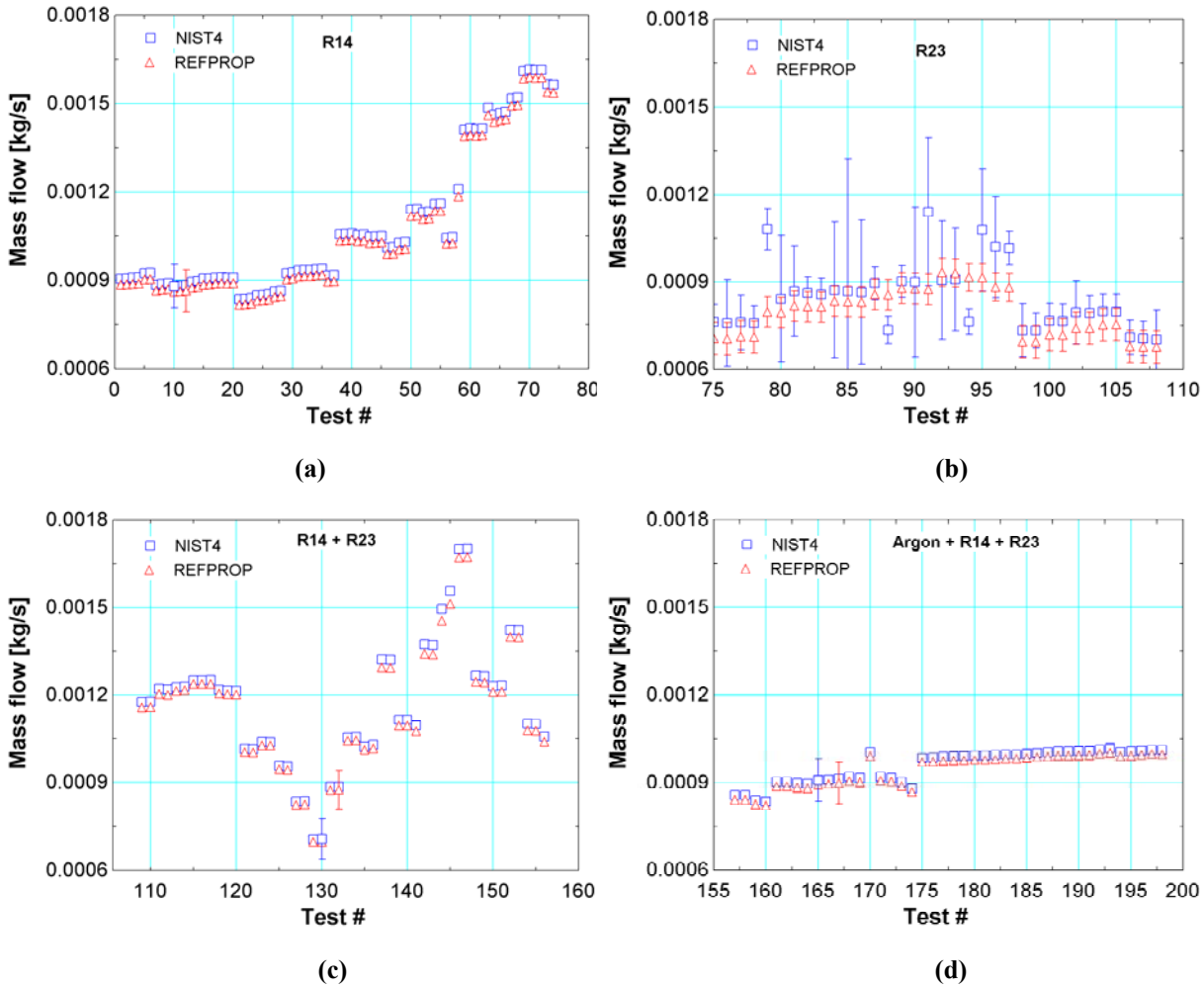

Figure 5-12: Mass flow measurements for the four sets of mixtures computed using the specific heat from the REFPROP and NIST4 databases. Data for (a) R14, (b) R23, (c) R14+R23, and (d) Argon+R14+R23 are shown with nominal error bars – note that the error bars for R23 varied significantly and so they were all plotted.

5.4.5 Recuperator pinch point violation using NIST4

As previously discussed in Section 5.4.3, the differing predictions for the bounds of the vapor dome obtained using NIST4 and REFPROP result in significantly different predictions of JT effect on the bubble line. The vapor dome location also affects the mixture heat capacity computed in the recuperator and can significantly affect the computed hot stream temperature profile. In fact, the poor prediction of the vapor dome by NIST4 often results in computation of

non-physical recuperator temperature profiles where the hot stream is predicted to be at a lower temperature than the cold stream (i.e. a pinch point violation), as shown in Figure 5-13. Figure 5-11 shows that NIST4 predicts the high pressure dewpoint at a few degrees higher than REFPROP (~5K), so that the heat capacity will be higher for NIST4 in the region between the two dewpoint line predictions. The hot stream location (Figure 5-13(b)) temperatures are computed using an energy balance on each of the sections, beginning with section 5 (using the directly measured temperature values in the cold stream at location 5 and 6, and the hot stream at location 6); this energy balance process is progressed towards the warm end of the recuperator to progressively compute each of the remaining hot stream temperatures at locations 4 to 0. Section 0 operates on the edge of the vapor dome, so the higher heat capacity predicted by NIST4 results in a lower temperature change, and subsequently causes a pinch point violation. This was a common result of the tests, and was the 2nd result underlying the decision to use REFPROP to compute the heat exchanger conductances and other cycle performance metrics.

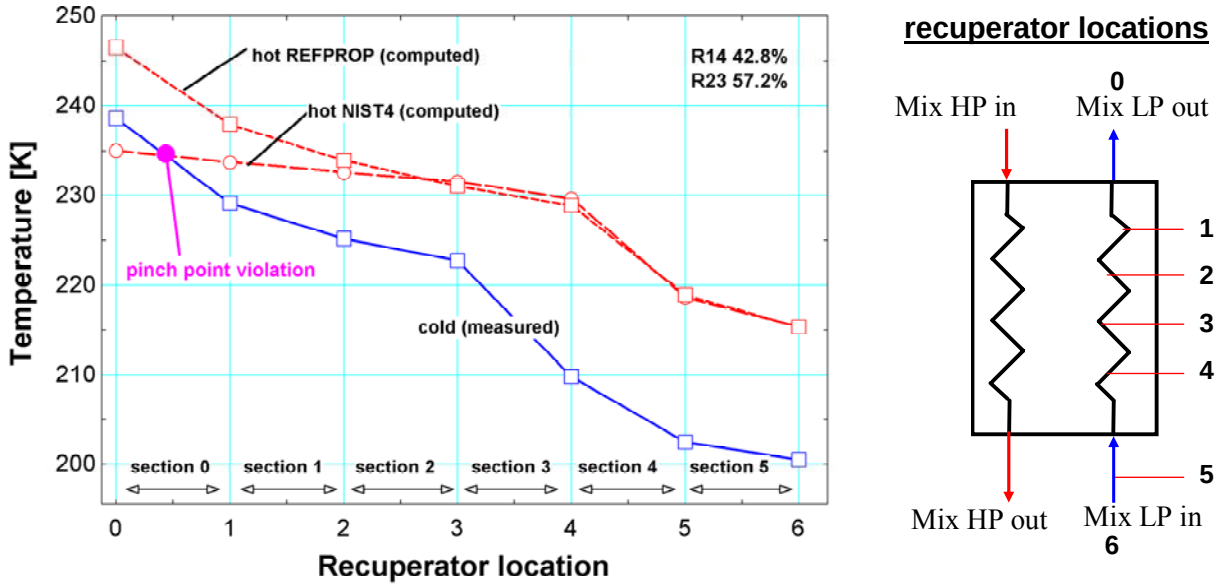

(a) **(b)**

Figure 5-13: (a) Measured and computed recuperator temperature profile as a function of recuperator location shown in (b). The hot stream temperature profiles are computed using the NSIT4 and REFRPOP databases, and the NIST4 values exhibit a pinch point violation.

5.4.6 Parasitic heating

The relatively small refrigeration effect associated with the JT cycle makes the measurements in the coldest components particularly sensitive to parasitic thermal loads. The test facility was carefully designed to minimize the parasitic heat input as discussed in Section 4.3.7. The effectiveness of this thermal isolation can be evaluated by computing the parasitic heat input between the high pressure exit and low pressure inlet of the recuperator. The parasitic heat leak is computed using an energy balance that debits the cryoprobe thermal load ($\dot{Q}_{load}$) from the enthalpy difference between states 7 and 5:

$$\dot{Q}_p = \dot{m}_{2^{nd}} \left(h_7 - h_5 \right) - \dot{Q}_{load} \tag{5.6}$$

Figure 5-14 shows the parasitic heat leak computed as a function of cryoprobe tip temperature. The data show significant scatter, however when reduced to values computed with

less than 1.5 W of uncertainty the values group very close to 0 W (with the exception of a few data points). The scattered data filtered by the uncertainty criteria were primarily from tests with mixtures, often in a two phase state; the enthalpies (and therefore the value of $\dot{Q}_p$), computed using the REFPROP mixture database were very sensitive to the temperature and pressure uncertainties. Conversely, the single component tests were carried out mostly in the vapor regime so that the property values were well defined and minimally sensitive to instrument error. As such, these data can be used with confidence to demonstrate that there was minimal parasitic heat leak into the system over a range of temperatures. Note that some of the data points with low uncertainty are associated with a *negative* parasitic load; this is likely caused by errors in property data prediction near the edge of the vapor dome.

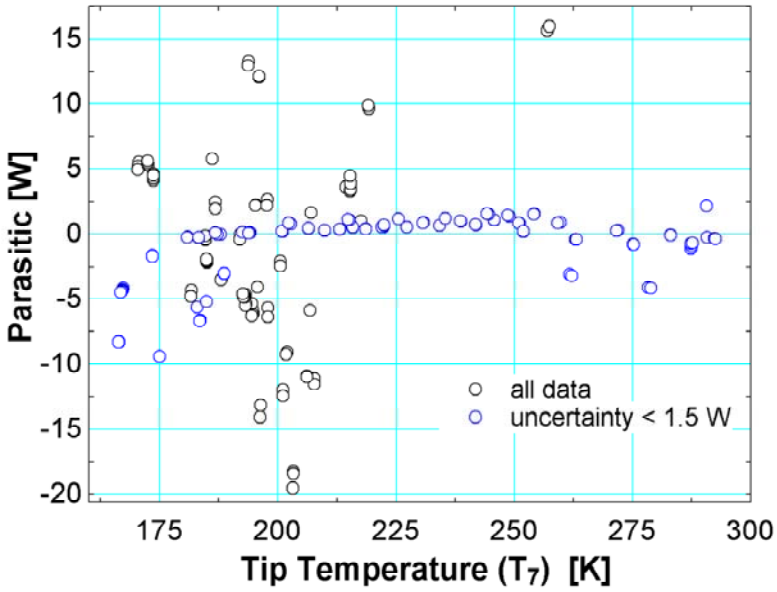

Figure 5-14: Parasitic heat leak into the 2nd stage cycle between state 5 and 7 as a function of tip temperature.

5.4.7 Pressure drop

The pressure drop in the recuperator is computed directly in the cold stream using measurements at state 7 and 1. Hot side pressure drop is computed using the measurement at

state 5 and the estimated pressure at state 4 (the average between 3 and 5, as discussed in Section 5.3.1). A rigorous presentation of the two-phase pressure drop should include a detailed model that considers the local pressure drop governed by liquid/vapor densities, superficial velocities and viscosities (see the Muller-Steinhagen & Heck correlation, for example). However, most of the most of the pressure drop will occur in the warmer sections of the heat exchanger where density is low and velocities are high (so the frictional losses are large). Therefore, the first order approximation made here is to assume that the pressure drop is governed entirely by the typically vapor phase flow at the warm end (or flow with thermodynamic quality near one, which by volume, is mostly vapor). Existing single phase pressure drop correlations for tubes typically follow the form:

$$\Delta P = f\left(Re, e, D\right)\frac{\rho v^2}{2}\frac{L}{D} \tag{5.7}$$

where ΔP is the pressure drop, f is the friction factor (which is a function of Reynolds number, Re, tube roughness, e, and diameter, D), ρ is the density, v is the velocity, and L is the flow passage length. The geometry is fixed so e, D and L are constant, and the Reynolds number does not vary significantly in these experiments. Subsequently, the pressure drop in the recuperator can be approximately correlated to just the $1/2\,\rho v^2$ value computed at the warm stream inlet and cold stream outlet. Figure 5-15 shows a fairly linear relationship exists for the pressure drop as a function of the $1/2\,\rho v^2$ values in both the warm and cold streams.

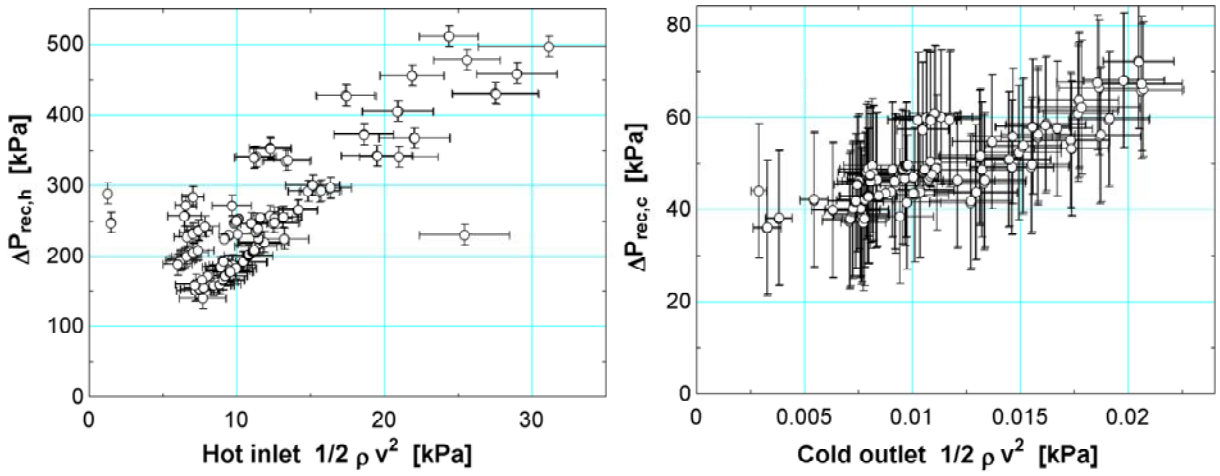

(a) **(b)**

Figure 5-15: Recuperator pressure drop for the (a) hot, and (b) cold, recuperator streams.

5.4.8 Recuperator conductance

The mechanisms underlying single and two-phase heat transfer are significantly different, so the conductance measurements were divided by flow phase to observe trends.

Vapor phase conductance

Figure 5-16 shows the conductance values in each of the six sections defined in Figure 5-6(a) as a function of cold stream Reynolds number (computed using the average properties for the section and the shell side frontal area listed as $A_{ff,rec,c,tube}$ in Table 4-6). The cold stream Reynolds number is chosen for this investigation because the cold side heat transfer coefficient is likely the limiting thermal resistance in the recuperator (as discussed in Section 5.2.1). However, the trends do not significantly change when plotted with the hot stream Reynolds number. The data filtered for uncertainty <40% have significantly reduced scatter as shown in Figure 5-16(b).

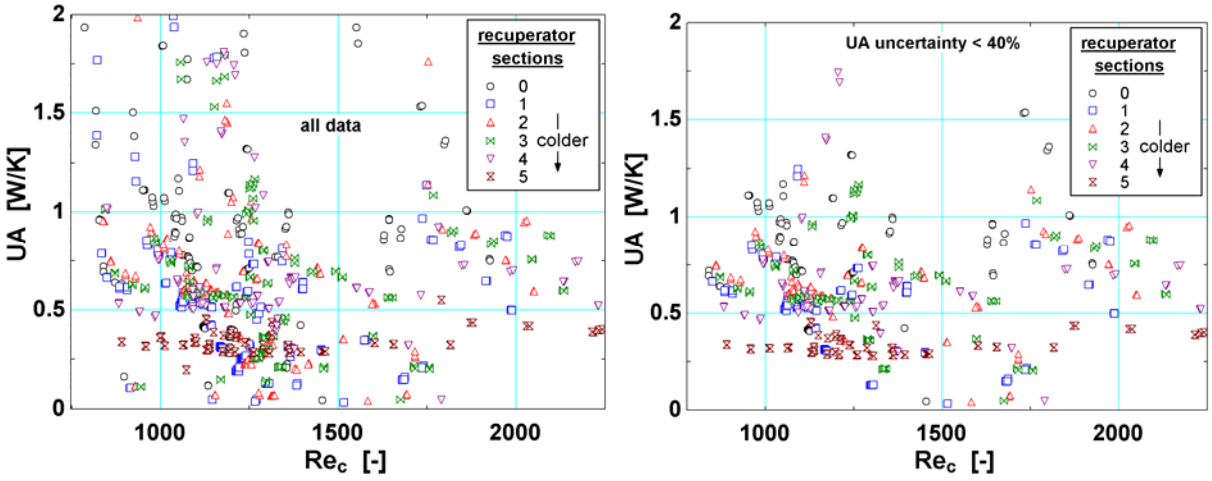

Figure 5-16: Vapor phase conductance measurements in the six recuperator sections where (a) all data are shown, and (b) data with 40% or less uncertainty are shown.

Further refinement of the vapor UA data considers the type and lengths of tube in each section, as summarized in Table 5-3. Section 5 is significantly different from the other tube sections in that it consists of a relatively short length (22.86 mm or 0.9 in.) of smooth tube (see Figure 4-18, Figure 4-25) between PRT7 and PRTi5. Furthermore this section intercepts any radiation parasitic incident on the relatively large conflat at the cold end of the cryoprobe sheath (see Figure 4-9). Section 0 is at the proximal end of the recuperator (see Figure 4-20 and Figure 4-23) and consists of 17.78 cm (7.0 in.) of finned tubing, 6.93 cm (2.73 in.) of smooth tubing ($L_{rec,d,s}$ and $L_{rec,d,w}$ in Table 4-6), and the space between the precooler shell and the outer SS sheath (shown in Figure 4-18) before the low pressure exit at state 1. Sections 1-3 are uniform with 25.65 cm (10.1 in.) of finned tubing each, and section 4 includes 22.10 cm (8.7 in.) of finned tubing and 2.46 cm (0.97 in.) of smooth tubing at the distal end of the recuperator ($L_{rec,p,s}$ and $L_{rec,p,w}$ in Table 4-6). The majority of the heat transfer occurs in the finned tubing, so it is useful to normalize the conductances by the lengths of finned tube in each section. These values could then be extended to designs where the finned tube length is varied. Figure 5-17 shows the

conductance data from Figure 5-16 normalized by length of finned tube (note that section 5 is omitted as it contains no finned tubing). Data with less than 40% experimental error are shown in Figure 5-16 and the sections somewhat collapse to a UA/L value of about 3 W/K-m.

Table 5-3: Lengths of finned and smooth sections of tube in each recuperator section between the PRT centerlines.

Section	Begin PRTs	End PRTs	axial length of finned tube [in]	length of finned tube [in]	length of smooth tube [in]
0	1	i1, i6	0.45	7.0	2.73
1	i1,i6	i2,i7	0.65	10.1	--
2	i2,i7	i3,i8	0.65	10.1	--
3	i3,i8	i4,i9	0.65	10.1	--
4	i4,i9	i5	0.56	8.7	0.97
5	i5	PRT 7	--	--	0.9

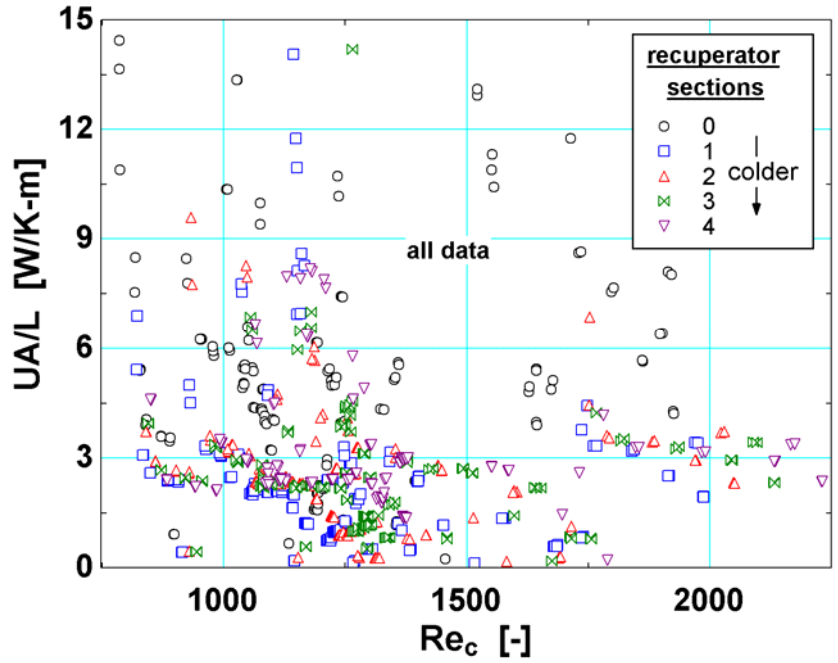

(a)

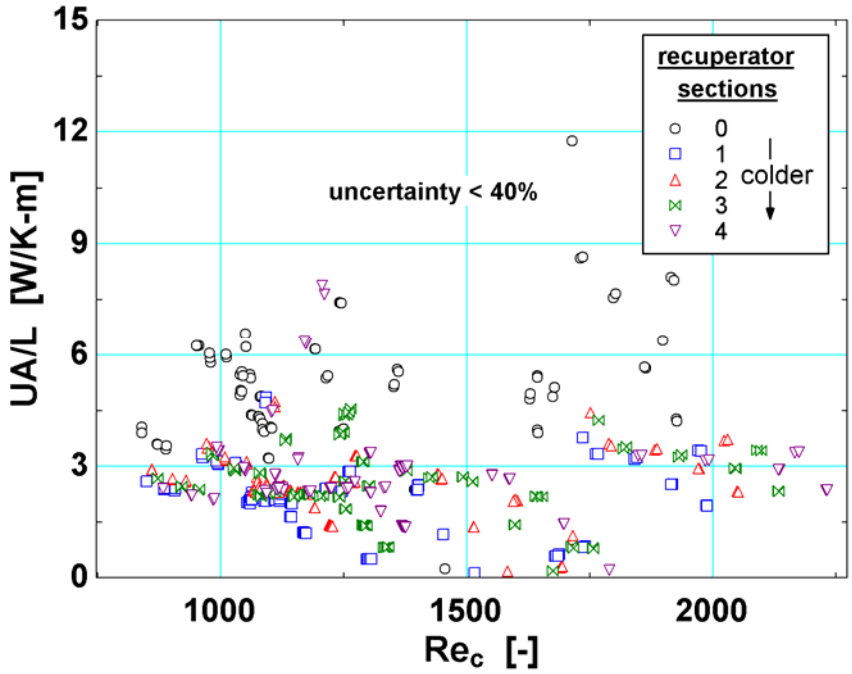

(b)

Figure 5-17: **Vapor phase conductance measurements normalized by length of finned tube in recuperator sections 0-5 where (a) all data are shown, and (b) data with 40% or less uncertainty are shown.**

These conductance data can be made even more broadly applicable by normalizing the conductance by the cold stream average thermal conductivity (similar to a Nusselt number) in each section. Figure 5-18 presents the conductance data normalized in this fashion; unfortunately, no significant collapse of data is observed using this normalization.

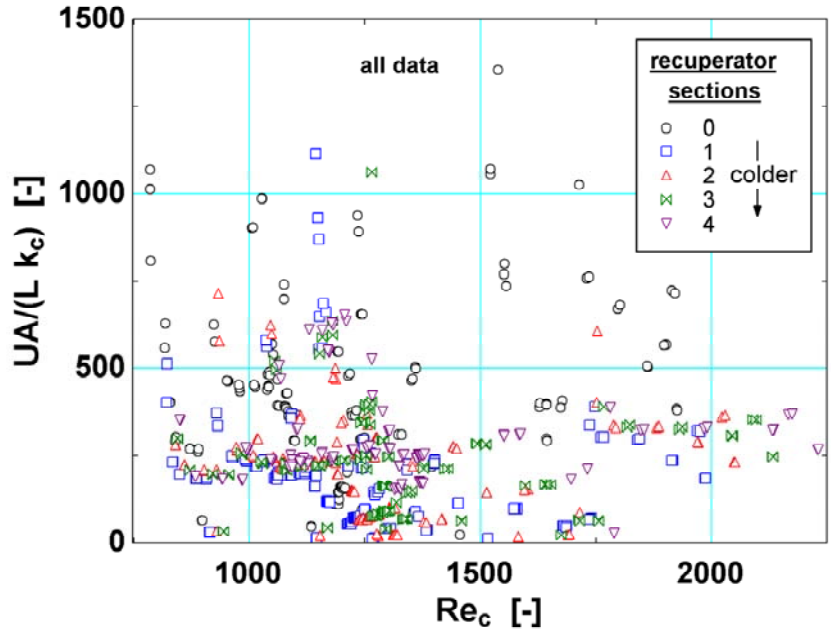

(a)

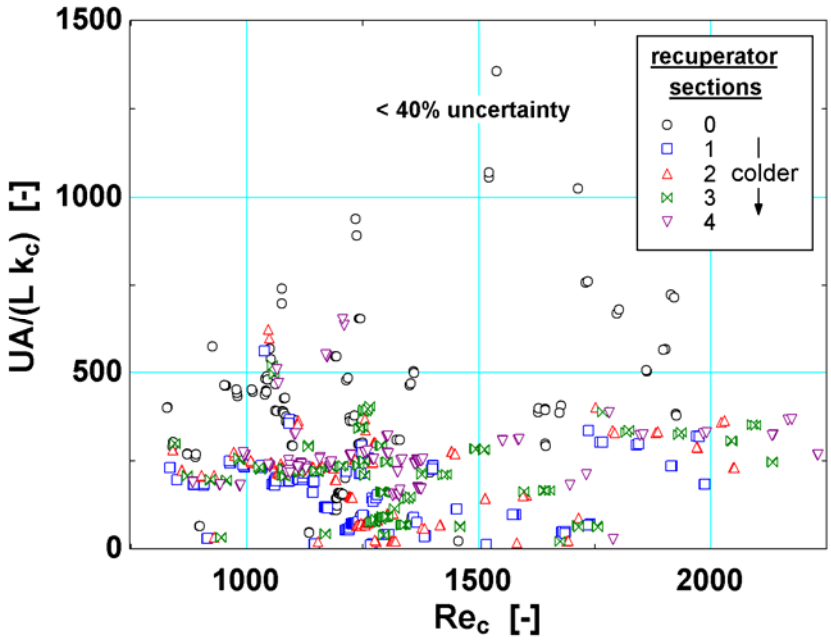

(b)

Figure 5-18: **Vapor phase conductance measurements normalized by length of finned tube and cold stream thermal conductivity for recuperator sections 0-5 where (a) all data are shown, and (b) data with 40% or less uncertainty are shown.**

Two-phase conductance

Separation of conductance data by phase was motivated by previous research project at UW-Madison where local heat transfer coefficients for mixtures at cryogenic temperature in small tubes were measured across the entire range of thermodynamic quality (Hughes 2004, Nellis 2005). Some of the test data from this work are displayed in Figure 5-19 and show that the two-phase heat transfer coefficients are much larger (4-6x) than their single-phase counterparts. Additionally, the data show that thermodynamic quality is an excellent correlating variable for the heat transfer coefficient in the vapor dome.

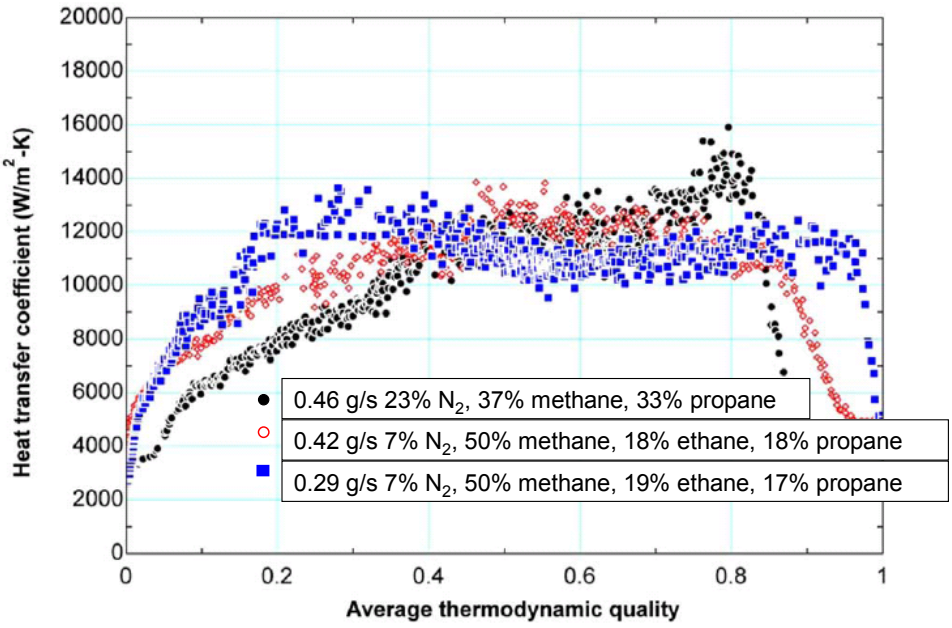

Figure 5-19: Measured two-phase mixture heat transfer coefficients for small tubes as a function of quality as reported in another study (Nellis,2005, Hughes 2004).

The recuperator conductance for the cryoprobe exhibits a similar increase in heat transfer coefficient within the vapor dome. Figure 5-20 shows the sectional variance in recuperator conductance; the section and overall conductance increases by as much as an order of magnitude when the refrigerant is in a two-phase, rather than vapor state.

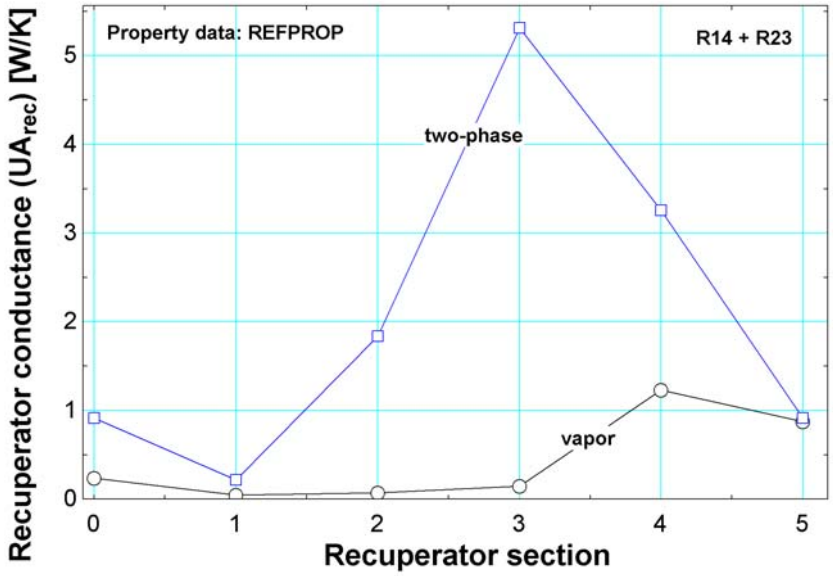

Figure 5-20: Conductance distribution in the recuperator as function of section (defined in Figure 5-13)

The thermal resistance network in the recuperator includes convection in the hot stream, conduction through the finned tube wall, and convection in the cold stream. Condensation and evaporation heat transfer coefficients are both relatively large so it is not clear which will represent the dominant resistance. However, some studies (discussed in Section 5.3.2) suggest that the low density and velocity in the low pressure side cause the shell side convection to limit the heat transfer. Furthermore, for the mixtures presented here, the low pressure stream generally crosses the dewpoint line into the vapor regime at lower temperatures and therefore will represent the dominant thermal resistance near the dewpoint line. Therefore, the conductance was plotted as function of the low pressure stream quality in order to better capture the restricted heat transfer near the dewpoint. Figure 5-21 shows the two-phase conductance normalized by finned tube length for each of the recuperator sections. Trends similar to those observed by Hughes (2004) and Nellis (2005) are observed. The heat transfer for a liquid and vapor are relatively small and the enhanced heat transfer in the vapor dome peaks at a vapor quality of 0.75.

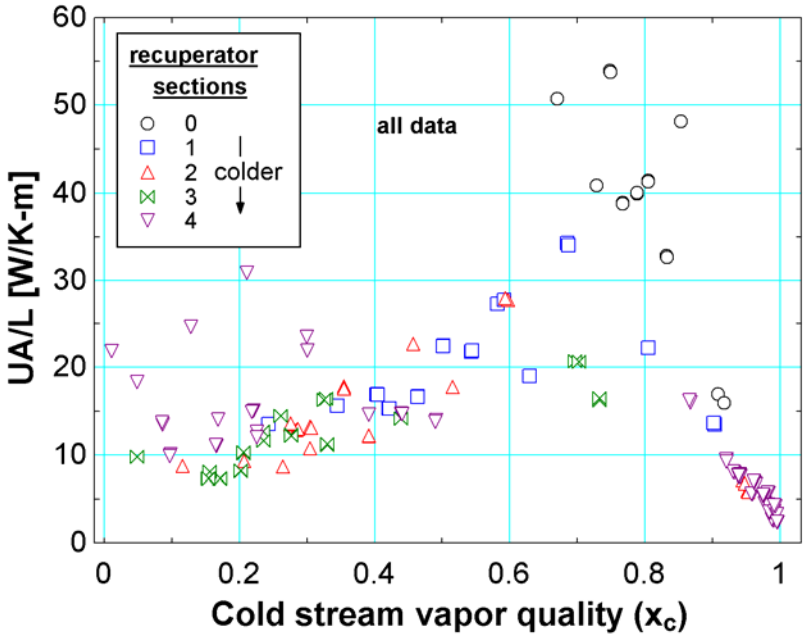

(a)

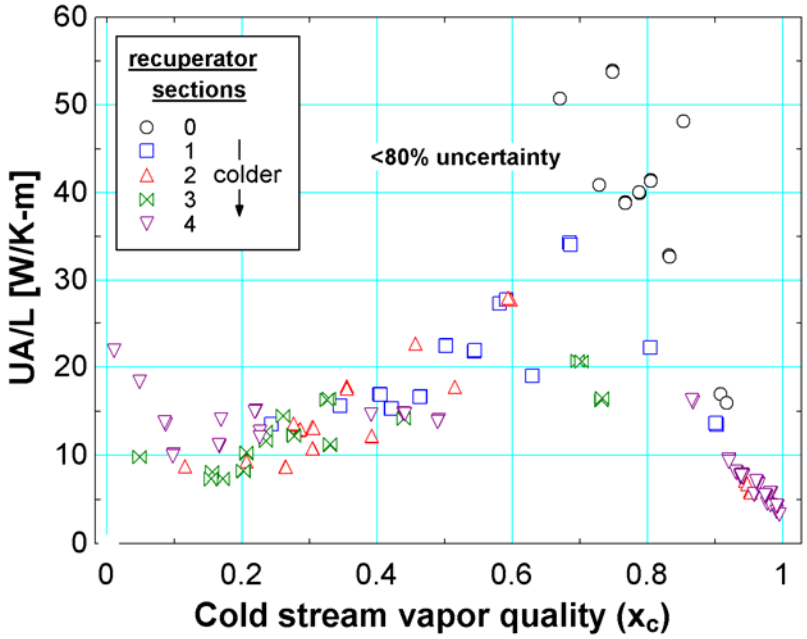

(b)

Figure 5-21: Section conductance normalized by finned tube length plotted against the cold stream vapor quality for (a) all data, and (b) less than 80% uncertainty.

Two-phase conductance normalized by mass flow

As discussed in Section 5.2.1, observing the change in two-phase heat transfer behavior under varied mass flux conditions can help to determine whether the heat transfer is dominated by nucleate boiling or convection. Figure 5-22 compares the conductance values normalized by length (b) with those normalized by length and mass flux (a) on the low pressure side of the recuperator (using the $A_{ff,rec,c,tube}$ value listed in Table 4-6). Mass flux varies by a factor of two within the data, from 13.4 to 27.3 kg/s-m^2; the trend does not significantly change between the two normalizations and therefore indicates that nucleate boiling dominates the heat transfer in the low pressure stream. This observation could be used in future work to help tune the empirical correlation of the conductance data, or to select a purely physics-based model to predict the two-phase heat transfer without the detailed measurements presented here.

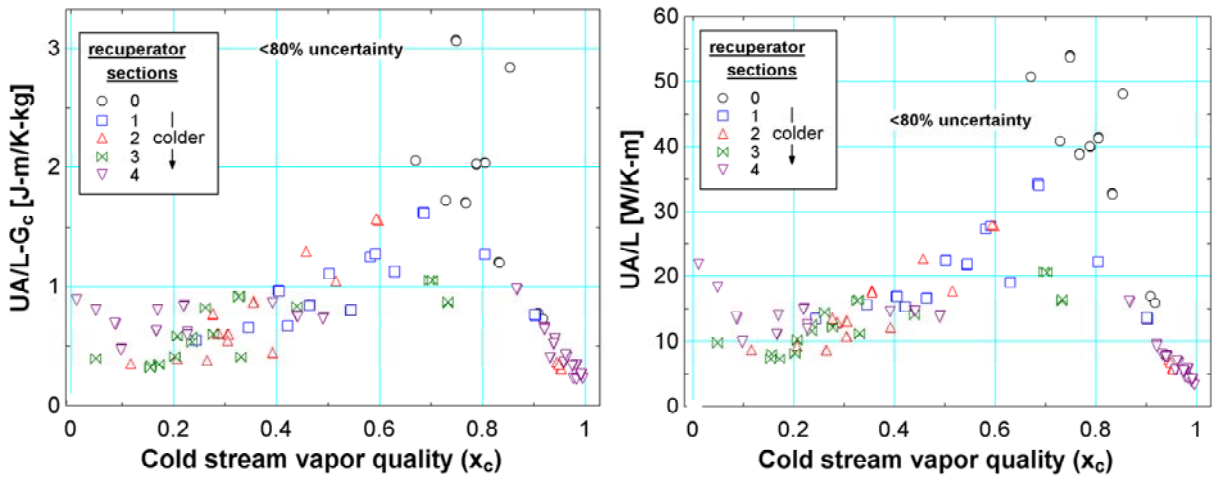

(a) (b)

Figure 5-22: Two phase recuperator conductance as a function of cold stream vapor quality. The data are normalized by (a) finned tube length and cold stream mass flux and (b) finned tube length.

5.4.9 Precooler conductance

The flow conditions of the R410a evaporating in the precooler (referred to as the "cold stream") did not significantly change for the tests presented here. Therefore, the heat transfer

characteristics of the high pressure 2nd stage working fluid (hot stream) were used to correlate the precooling conductance data. The 2nd stage fluid existed in both a vapor and a two phase state so, similar to the recuperator data, the conductance data are compared with the hot stream Reynolds number and the local thermodynamic quality. These data are not as resolved as the recuperator conductance measurements because only the cold stream exit temperature and pressure, and hot stream inlet temperature and pressure are directly measured. Assumptions about pressure drop through the precooler/recuperator tubes and an energy balance on the recuperator are used to compute the hot exit temperature (as discussed in Section 5.2), and the pressure drop of the R410a on the shell side of the precooler is neglected. These measurements represent a total heat transfer over the whole length of the precooler and therefore the results are normalized by the length of the finned tube (21.7 in), which has the same ID (0.041") and OD (0.056") as the recuperator tube.

The 2nd stage gas mix exits the precooler as a vapor for most of the data sets, so the conductance is correlated to the Reynolds number. Two different presentations of the vapor data were considered and are displayed in Figure 5-23 (a) and (b). The simpler correlation, shown in Figure (a), relates the vapor conductance normalized by the precooler tube length to the Reynolds number at the 2nd stage cycle precooler inlet (i.e., state 3). A second correlation, shown in Figure (b), compares the vapor conductance normalized by length and the average thermal conductivity as a function of the average Reynolds number, where the property data are averaged between the hot stream inlet and outlet values. An uncertainty filter is applied to the data at 50% and 20% levels; these filters do not significantly reduce the scatter. The data

roughly follow a linear trend and a first order fit is applied for the empirical recuperator model as presented in Chapter 6.

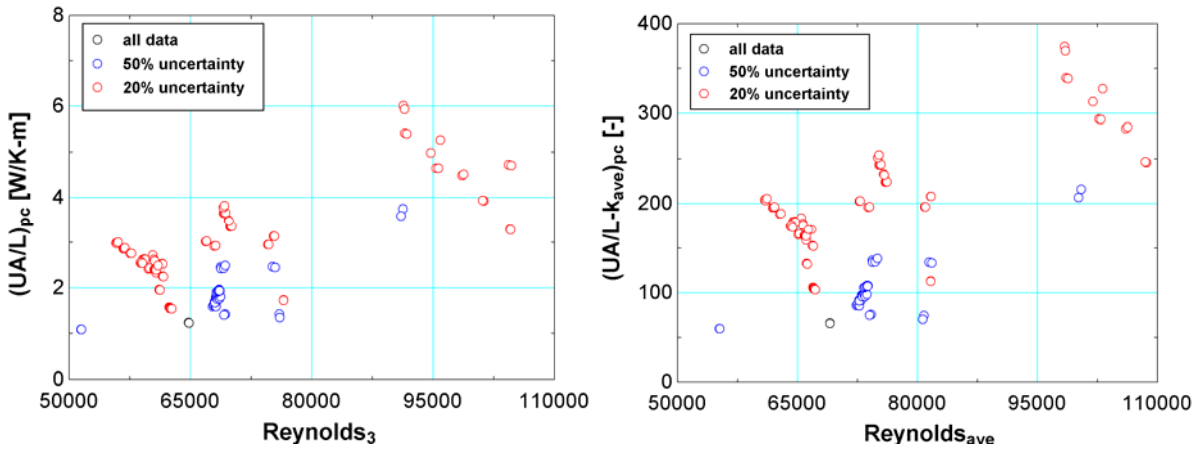

Figure 5-23: Precooler conductance data where the 2nd stage refrigerant exits as a vapor. (a) Conductance normalized by tube length and plotted against hot stream Reynolds number at state 3. (b) Conductance data normalized by tube length and average thermal conductivity as a function of average hot stream Reynolds number.

The overall precooler conductance significantly increased when the 2nd stage refrigerant exited in a two-phase state, as shown in Figure 5-24. The enhanced heat transfer is attributed to condensation and increases the overall conductance; this observation confirms the assumption presented in Section 5.2.1 about the 2nd stage vapor convection dominating the thermal resistance in the precooler. The length-normalized conductance as a function of local thermodynamic quality cannot be computed directly using only the precooler inlet/outlet measurements because the tube location of the transition between vapor and two-phase states is not known (in contrast with the recuperator where the transition can be located using the sensors at intermediate heat exchanger locations). However, the vapor conductance model developed in Section 6.4 can be used to determine the length of tube required to cool the high pressure 2nd stage fluid to the dewpoint line and this length can be debited from the overall length in order to

compute the length containing two-phase flow. The two-phase conductance as a function of quality is subsequently presented in Section 6.4

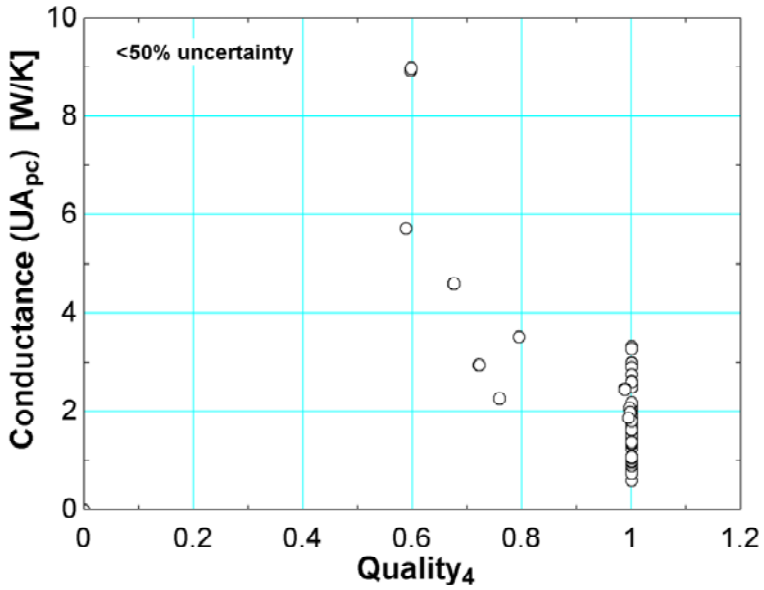

Figure 5-24: Overall precooler conductance normalized by length as a function of the quality at the 2nd stage exit (state 4).

5.5 References

Ely, J. F.; Huber, M. L. NIST Thermophysical Properties of Hydrocarbon Mixtures Database (SUPERTRAPP). 1992, 3.2.

Fredrikson, K. 2004. Optimization of Cryosurgical Probes for Cancer Treatment. M.S. thesis. Madison, WI USA: University of Wisconsin - Madison, Mechanical Engineering Dept.

Fredrikson, K.; Nellis, G.; Klein, S. A. "A Design Method for Cryosurgical Probes". *International Journal of Refrigeration* 2006, vol. 29, 700-715.

Hughes, C. B., G. F. Nellis and J. M. Pfotenhauer. 2004. "Measurement of heat transfer coefficients for non-azeotropic hydrocarbon mixtures at cryogenic temperatures". In 2004 ASME International Mechanical Engineering Congress and Exposition, IMECE, pp. 415-422.

Hughes, C. B. 2004. Experimental Measurement of Heat Transfer Coefficients for Mixed Gas Working Fluids in Joule-Thomson Systems M.S. thesis. Madison, WI USA: University of Wisconsin - Madison, Mechanical Engineering Dept.

Incropera, F. P.; DeWitt, D. P. *Fundamentals of Heat and Mass Transfer, Fourth Edition;* John Wiley & Sons: New York, 2002

Kandlikar, S. G., M. Shoji and V. K. Dhir, eds. 1999. *Handbook of Phase Change: Boiling and Condensation.*

Kuehn, T. H.; Ramsey, J. W.; Threlkeld, J. L. *Thermal Environmental Engineering;* Prentice Hall: 1998; pp 740.

Lemmon, E. W.; Huber, M. L.; McLinden, M. O. NIST Reference Fluid Thermodynamic and Transport Properties - REFPROP. 2007*, 8.0*. More information available at http://www.nist.gov/srd/nist23.cfm

Nellis, G., C. Hughes and J. Pfotenhauer. 2005. "Heat transfer coefficient measurements for mixed gas working fluids at cryogenic temperatures". *Cryogenics* 45(8): 546-556.

Skye, H.M., Klein, S.A., Nellis, G.F., "Modeling and Optimization of a Two-stage Mixed Gas Joule-Thomson Cryoprobe System (RP-1472)", ASHRAE Transactions Paper TRNS-00196-2008, 2008

Timmerhaus, K. D. and T. M. Flynn. 1989. *Cryogenic Process Engineering.*

Timmerhaus, K. D. and R. J. Schoenhals. 1974. "Design and Selection of Cryogenic Heat Exchangers". *Advances in Cryogenic Engineering* 1, pp 445-462.

Wambsganss, M. W., D. M. France, J. A. Jendrzejczyk and T. N. Tran. 1993. "Boiling heat transfer in a horizontal small-diameter tube". *Transactions of the ASME. Journal of Heat Transfer* 115(4): pp. 963-972.

6 Empirical Model Development

The precooled MGJT cryoprobe is a complex system that represents a significant design challenge; a full optimization must carefully consider the mixture composition, the performance of each hardware component, and the operating parameters of the system. Mass flow and pressure drop in the system are determined by the balance of the compressor pumping power (i.e. volumetric flow and pressure ratio relationship governed by the compressor performance curve) with the flow restrictions in the system including the precooler/recuperator tubing, jewel orifice (2^{nd} stage), and capillary tube (1^{st} stage). The cycle mass flows and pressure are further sensitive to the charge pressure, as observed in the experimental tests. Increasing the charge pressure tends to raise the cycle high and low pressures, as well as the mass flow in the system; this increases capacity at higher temperatures, but reduces the refrigeration capacity at lower temperatures and raises the lowest temperature attainable with the cycle. The precooling pressures determine the saturation temperature of the pure refrigerant in the precooling evaporator, and therefore partially determine the optimal mixture composition for the 2^{nd} stage cycle (see Section 1.3). Heat transfer performance in the recuperator determines the ability of the system recover the cooling exergy available in the 2^{nd} stage working fluid returning from the load. The JT effect across the jewel orifice determines the lowest temperature achieved in the cycle and is partially governed by the orifice diameter. As discussed in detail in Chapter 3, the cycle performance is very sensitive to the choice of working fluid for the 1^{st} and 2^{nd} stages. The choice of working fluid performance is further complicated by the composition shift exhibited by the mixtures as discussed in Section 5.4.2

The model developed for this project captures a significant portion of the physical phenomena and operating parameters listed above. The thermodynamic and flow parameters for components that are not included in the model are drawn from the experimental data and used as inputs to the model. Recuperator and precooler heat transfer and pressure drop performance are modeled, as well as the temperature drop across the JT orifice (given up/down stream pressures and upstream temperature, as shown in Section 5.4.3). The compressors and flow restrictions are not modeled, and the effect of charge pressure is not considered directly; instead, the mass flow and compressor suction/discharge pressures are inputs to the model. Furthermore, the cycle model requires as an input the circulating composition rather than the charge composition. The selection of the proper composition/pressure required to achieve a desired circulating composition is addressed elsewhere (Reddy 2010). Finally, the evaporation temperature of the R410a (1^{st} stage working fluid) in the precooler is considered as a model input that can be readily tuned in hardware by adjusting the capillary tube geometry. The sections that follow (Sections 6.1 through 6.4) address the empirical tuning of the precooler and recuperator models.

6.1 Recuperator/precooler pressure drop model

Figure 6-1 shows the measured cold and hot side pressure drop data presented in the previous chapter, with a linear curve fits overlaid on the data. It is expected that the velocity and pressure drop terms would go to zero together, however the linear fit yields an offset of 34 kPa and 106 kPa respectively for the cold and hot streams. Nevertheless, the curve fits track the data adequately for the results presented here. The curve fit parameters and correlation statistics are summarized in Table 6-1. Note that as, discussed in Section 5.3.1, the pressure at state 4 is assumed to be halfway between states 3 and 5, so in this case the pressure drop on the 2^{nd} stage

side of the precooler (state 3 to 4) is equivalent to the pressure drop on the hot side of the recuperator (state 4 to 5):

$$\Delta P_{pc,2nd} = \Delta P_{rec,h} \tag{6.1}$$

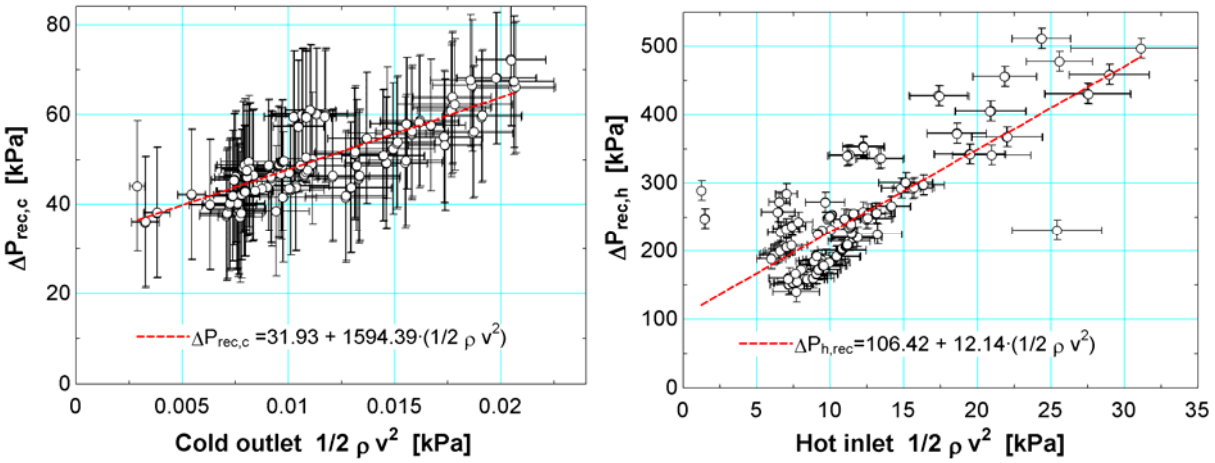

(a) (b)

Figure 6-1: Recuperator pressure drop empirical correlations for the (a) cold, and (b) hot streams of the recuperator.

Table 6-1: Recuperator pressure drop correlation coefficients and curve fit statistics.

Correlation form	a_0 [kPa]	a_1 [-]	RMS error [kPa]	R^2	N_{points}
$\Delta P_{rec,c} = a_0 + a_1 \left(1/2\, \rho_{rec,c,out}\, v^2_{rec,c,out}\right)$	31.93	1594.39	4.78	0.62	198
$\Delta P_{rec,h} = a_0 + a_1 \left(1/2\, \rho_{rec,h,in}\, v^2_{rec,h,in}\right)$	106.42	12.14	50.0	0.61	198

6.2 Recuperator conductance model

Conductance data for each of the recuperator sections were presented in Section 5.4.8 and examined by flow regime. In order to make these data more general, the division between sections is eliminated and all the data are assumed to represent heat transfer performance (per length) for the same heat exchanger geometry: a counterflow annular heat exchanger formed by

the helically wound finned tube between the mandrel and the G10 sheath (see Figure 4-18). Note that the lengths of unfinned tube in sections 0, 4, and 5 (Table 5-3) are ignored.

Vapor phase conductance

Figure 6-2 shows the recuperator conductance data normalized by (a) length, and (b) length and cold stream thermal conductivity. The data are filtered by uncertainty, where the red circles represent the tightest uncertainty constraint (20%), the blue circles are the additional data included with a 40% uncertainty level, and the black circles are the remaining data with even higher uncertainty. The uncertainty filter significantly reduces the scatter in the data, and the figure shows an example of the one and two coefficient curve fits used to try and correlate the data. The statistics for the fits are presented in Table 6-2, where each conductance normalization was fit using both a constant and linear correlation, for varied uncertainty level filters (20%, 40%, and 60%). Both sets of normalization data showed an insignificant change in the RMS error between the linear and constant curve fits. Furthermore, the normalization including thermal conductivity actually slightly reduced the quality of the fit (RMS error increases by a few percent). Subsequently, a constant fit where the conductance is normalized by length only is used to simplify the correlation. The 40% data highlighted in the table were selected to balance the RMS error with a more encompassing number of data points, and results in a (UA/L) value of 2.99 W/K-m.

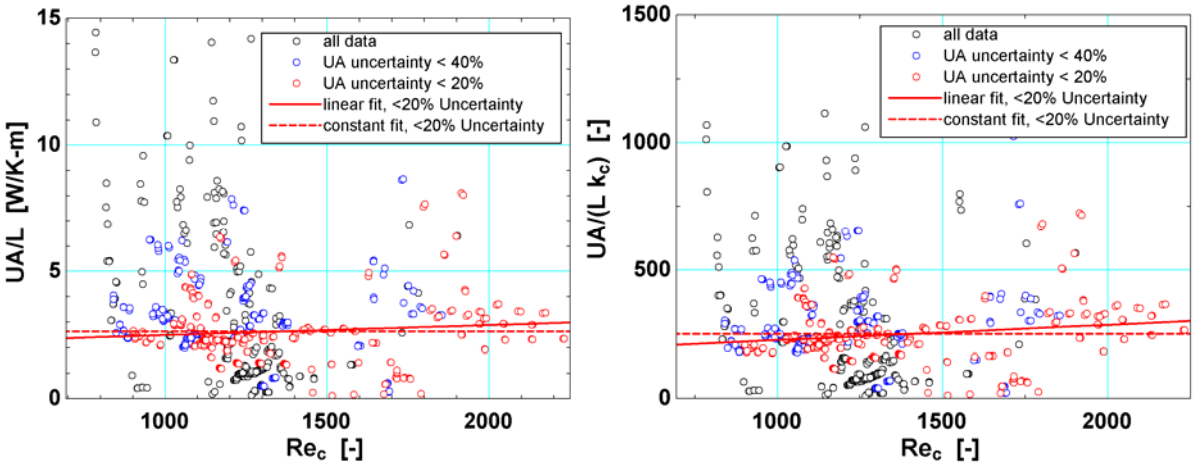

(a) (b)

Figure 6-2: **Recuperator vapor phase conductance data as a function of Reynolds number used to create the curve fit. Conductance data are normalized by (a) tube length, and (b) tube length and cold stream thermal conductivity.**

Table 6-2: **Recuperator vapor phase conductance correlation coefficients and fit statistics.**

***UA/L* correlation**							
Correlation form	**Uncertainty Criteria**	a_0 **[W/K-m]**	a_1 **[W/K-m]**	**RMS error [W/K-m]**	**RMS error**	R^2	N_{points}
$UA/L = a_0$	$UA/L < 20\%$	2.643	--	1.35	45%	--	235
	$UA/L < 40\%$	2.993	--	1.579	53%	--	415
	$UA/L < 60\%$	2.741	--	1.735	58%	--	533
$UA/L = a_0 + a_1 Re_c$	$UA/L < 20\%$	2.094	0.000393	1.343	45%	0	235
	$UA/L < 40\%$	3.066	-0.000055	1.579	53%	0	415
	$UA/L < 60\%$	2.882	-0.000108	1.735	58%	0	533

***UA/L-k* correlation**							
Correlation form	**Uncertainty Criteria**	a_0 **[-]**	a_1 **[-]**	**RMS error [-]**	**RMS error**	R^2	N_{points}
$UA/k_cL = a_0$	$UA/(L\,k_c) < 20\%$	250.7	--	118	48%	--	235
	$UA/(L\,k_c) < 40\%$	267.8	--	131.8	53%	--	415
	$UA/(L\,k_c) < 60\%$	240.5	--	147.6	59%	--	533
$UA/k_cL = a_0 + a_1 Re_c$	$UA/(L\,k_c) < 20\%$	167.7	0.0592	116.2	47%	0.03	235
	$UA/(L\,k_c) < 40\%$	207.1	0.0465	131.4	53%	0.006	415
	$UA/(L\,k_c) < 60\%$	196.3	0.0337	147.3	59%	0.004	533

Two-phase conductance

Figure 6-3 (a) shows the conductance data normalized by length for sections 1-4 as a function of vapor quality. Note that section 0 has been removed as a significant outlier (see Figure 5-21) – this section contains a significant length of unfinned tube and includes the space between the precooler shell and the outer SS sheath, as shown in Figure 4-18, which introduces an unknown heating/cooling effect on the stream. Section 5 has also been excluded as it represents a section of unfinned tube only. A 3rd order curve fit (rather than a 2nd order) is used to capture the asymmetry in the parabolic-like trend. This asymmetry is in agreement with the data presented in Figure 5-19 (Nellis 2005, Hughes 2004) which features a sharp increase in heat transfer between a quality of 1 and 0.8, and a slow progression downward from a quality of 0.3 to 0. The curve fit is forced to pass through the constant vapor (UA/L) value (2.99 W/K-m) at a quality of 1 so that the conductance-quality relationship (shown in Table 6-5) is continuous on the dewpoint line. Note that the two-phase data with quality of 0.95-1 trend downward very close to this point so the enforcement of the vapor value does not cause a noticeable distortion in the 3rd order fit. The curve fit is applied to data with varying levels of uncertainty and the fit statistics are presented in Table 6-3; the trend does not change significantly between the 40%, 80% and all data selections. Therefore, the 80% data were selected to include a larger set of data and yet eliminate a few of the significant outliers.

Note that the 3rd order fit exhibits an inflection upward in the low quality regions, which disagrees with the downward trend observed in Figure 5-19 (the liquid heat transfer coefficients are relatively low and nearly match the vapor values). The heat transfer measurements from the (Hughes 2004, Nellis 2005) study are much more controlled and precise than the measurements presented here, so the correlation is forced to follow the downward trend in the 0 to 0.3 vapor

quality region. The downward slope in Figure 5-19 follows a roughly linear trend, so a linear projection was drawn from the 3rd order fit before the inflection point. This projection takes the form:

$$\left(UA/L\right)_{lin} = b_0 + b_1 x_c \tag{6.2}$$

where $(UA/L)_{lin}$ is the linear fit to the conductance in the 0 to 0.3 quality region, x_c is the cold stream quality, and b_0 and b_1 are the fitting coefficients. The projection is carried out by enforcing equal slopes for the linear and 3rd order fits at a quality of 0.3:

$$b_1 = \left.\frac{d\left(UA/L\right)_{3rd}}{dx_c}\right|_{x_c=0.3} \tag{6.3}$$

where $(UA/L)_{3rd}$ is the 3rd order curve fit. The b_0 coefficient is computed by further equating the values of the fits at a quality of 0.3:

$$\left(UA/L\right)_{lin}\Big|_{x_c=0.3} = \left(UA/L\right)_{3rd}\Big|_{x_c=0.3} \tag{6.4}$$

Substituting (6.2) into (6.4) yields:

$$b_0 = \left(UA/L\right)_{3rd}\Big|_{x_c=0.3} - b_1\left(0.3\right) \tag{6.5}$$

The values of the b_0 and b_1 coefficients are listed in Table 6-4.

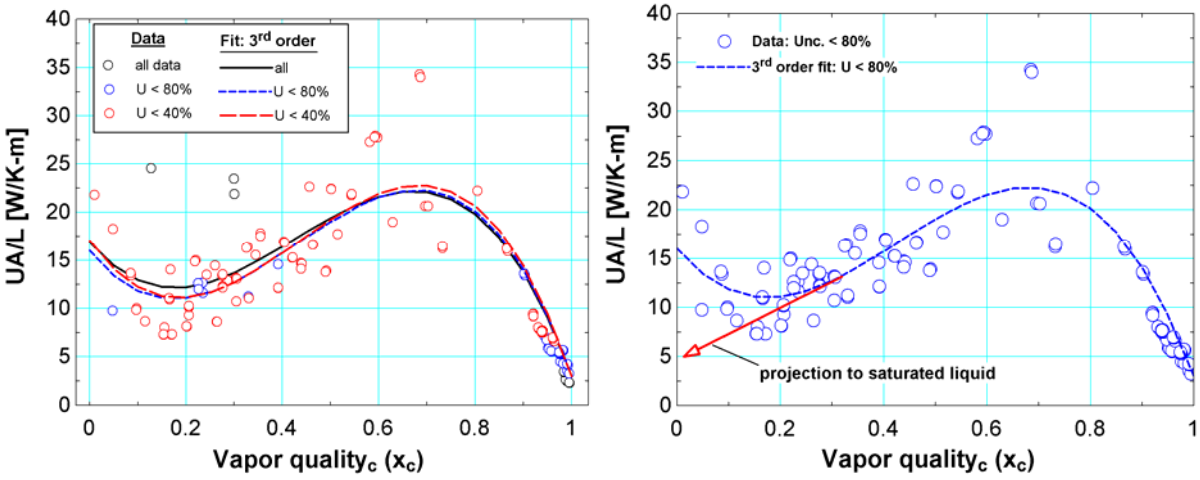

Figure 6-3: **Recuperator conductance normalized by tube length as a function of cold stream vapor quality. (a) shows the variation in curve fit between the various uncertainty filters, and (b) shows the 80% data with a projection toward saturated liquid from a quality of about 0.3.**

Table 6-3: **3rd order fit correlation for the recuperator conductance in the 0.3 to 1 cold stream quality region.**

Correlation form	Saturated Vapor Constraint
$(UA/L)_{3rd} = a_0 + a_1 x_c^2 + a_2 x_c^2 + a_3 x_c^3$	$(UA/L)_{3rd}\big\|_{x_c=1} = 2.99\ [W/K \bullet m]$

Uncertainty Criteria	a_0 [W/K-m]	a_1 [W/K-m]	a_2 [W/K-m]	a_3 [W/K-m]	RMS error (absolute)	R^2	N_{points}
UA < 40%	17.05	-70.95	244	-187.1	3.449	0.6847	95
UA < 80%	15.99	-62.49-	224.6	-175.1	3.143	0.7481	123
none	16.86	-58.96	211	-165.9	3.815	0.6847	134

Table 6-4: **Linear fit correlation for the recuperator conductance data in the 0 to 0.3 cold stream quality regions.**

Correlation form	b_0 [W/K-m]	b_1 [W/K-m]
$(UA/L)_{lin} = b_0 + b_1 x_c$	5.238	25.0

Few data were collected in the liquid regime, so a rigorous correlation for the liquid conductance is not presented here. Rather, the observation of the nominally constant conductance for the vapor regime is extended to the liquid regime, and a constant value equal to

b_0 (5.238 W/K-m) is assumed. Inaccuracies introduced by this assumption will not significantly impact the model verification here, as the validation data include very few points where the mixture enters the cold side of the recuperator as a liquid.

Table 6-5 summarizes the continuous conductance correlation that includes this liquid value, as well as the correlations for the two-phase and vapor regimes; this correlation is plotted in Figure 6-4.

Table 6-5: Recuperator conductance correlation over the entire range of cold stream quality.

Quality range	(UA_{rec}/L_{rec}) Correlation [W/K-m]
$x_c < 0$ (liquid)	5.238
$0 \le x_c < 0.3$	$5.238 + 25.0\, x_c$
$0.3 \le x_c \le 1$	$15.99 - 62.49\, x_c + 224.6\, x_c^2 - 175.1\, x_c^3$
$x_c > 1$ (vapor)	2.99

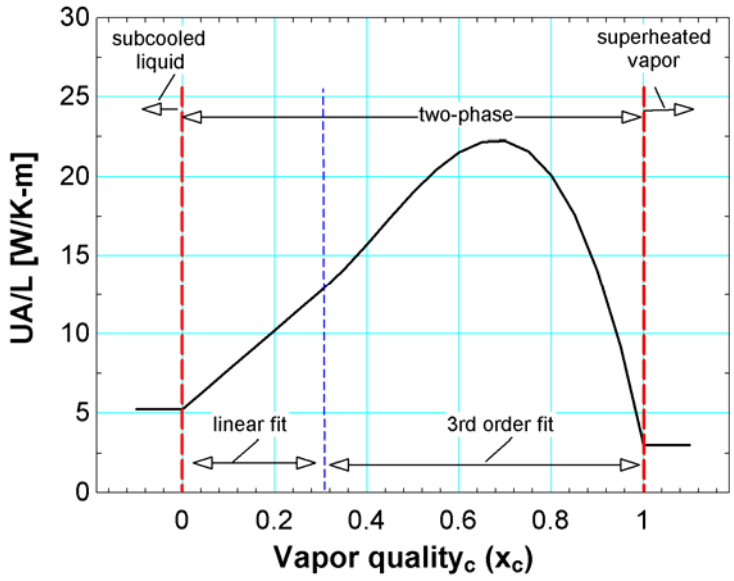

Figure 6-4: Recuperator conductance correlation over the liquid, two-phase, and vapor regimes. The linear and 3rd order fits in the two-phase region are delineated.

6.3 Recuperator model verification

The recuperator conductance model was verified by applying the correlation presented in Table 6-5 to the experimental data used to create the model. Ideally, this model would be validated against a different set of data covering different pressure ratios, flow rates, and mixture constituents to verify the broad applicability for the model. A validation of this nature is beyond the scope of this thesis; rather, the model is compared with the data that used to form the correlations. Nevertheless, this comparison serves as a first estimate of the accuracy of the model and could be confidently applied to select mixtures and operating conditions within the ranges presented in the test data. Recommendations for future work include extending the validation over a new set of data.

The accuracy of the recuperator model is evaluated by comparing the measured and predicted heat exchanger effectiveness, which is defined as:

$$\varepsilon = \frac{h_4 - h_5}{h_4 - h(P_4, T_7)} \tag{6.6}$$

where h_4 and h_5 are the enthalpies at states 4 and 5 (Figure 5-2), and $h(P_4,T_7)$ represents minimum possible enthalpy for the hot stream if the pinch point is assumed to occur at the cold end. Note that the uncertainty in the related to the indirect measurement of state 4 (the pressure is roughly estimated to lie halfway between state 3 and 5 and the temperature is computed using an energy balance on the recuperator - see Section 5.3.1) results in some experimental effectiveness values greater than one.

The predicted effectiveness values were computed using the inlet temperatures (T_7 and T_4) as well as two different sets of pressure measurements. The effectiveness values were first computed using all the available recuperator pressure measurements (P_5, P_7, P_1, and the estimation for P_4) and are shown as black squares in Figure 6-5. Next, the pressure drop model (Section 6.1) was incorporated into the recuperator model so effectiveness values were predicted using only the estimated pressure at state 4 and the measured pressure at state 7. These effectiveness values shown as blue circles in Figure 6-5 do not differ substantially from the first values. Figure 6-5 (a) shows all the data, and Figure 6-5 (b) shows the results filtered for <10% uncertainty; here the filter removes a few outliers but does not significantly change the results. The figure shows the exact predicted/measured match, as well as bands for 10% and 20% error – the results generally agree to within 10-15%. Note that the recuperator effectiveness spans a relatively small range from 0.7 to 1, regardless of the hot or cold stream quality. This relatively constant effectiveness is an interesting behavior of the recuperator that can be explained by the proportionate scaling of stream heat transfer coefficients and thermal capacity across the phase

regimes: the vapor stream exhibits low capacity and low heat transfer, whereas the two-phase stream has enhanced heat transfer and increased capacity related to the phase change.

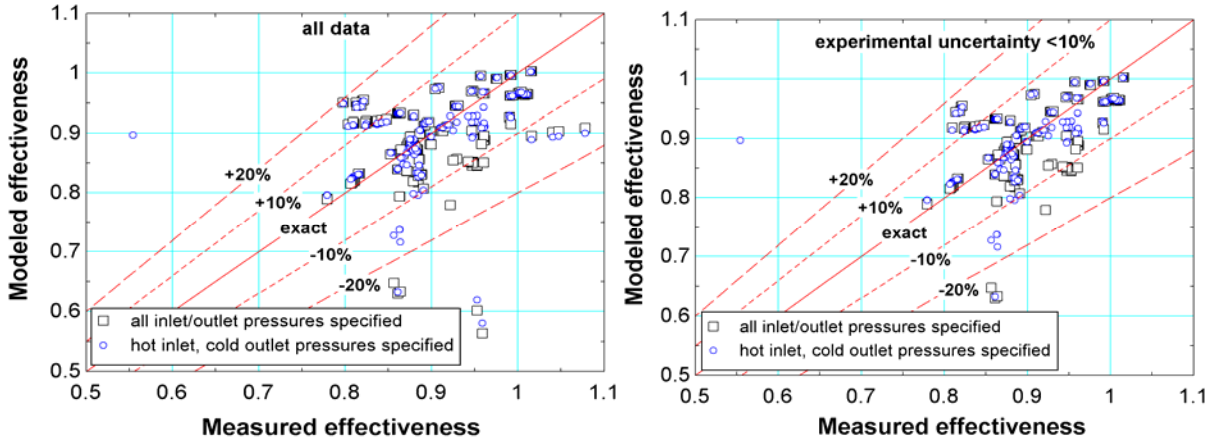

(a) **(b)**

Figure 6-5: Measured vs. predicted recuperator effectiveness for (a) all data and (b) data with less than 10% uncertainty. Predictions are made using both the measured pressure values described in Section 5.3.1, as well as using just the hot inlet and cold outlet pressures with the pressure drop models described in Section 6.1.

6.4 Precooler model

Vapor-phase conductance

A linear best fit was applied to correlate the precooler vapor conductance data (where the 2nd stage refrigerant in the precooler remained in a vapor state throughout the heat exchanger) to the Reynolds number of the 2nd stage fluid in the precooler. Three different uncertainty criteria for computing UA_{pc} from the data were applied including <20%, <50% and <70% uncertainty filters. A linear best curve fit was applied to the data for each level of uncertainty, and the final curve fit was selected to encompass as many points as possible while reducing the scatter. A summary of the fit statistics is presented in Table 6-6 for both the: (1) conductance normalized by length vs. hot stream inlet Reynolds number ($Reynolds_3$), and (2) conductance normalized by length and average thermal conductivity vs. average Reynolds number. Averaged properties

were computed as the average between the values evaluated at the 2nd stage precooler inlet and outlet.

The data with 50% or less uncertainty balanced the RMS error with number of included points well. Figure 6-6 presents the curves for the <50% uncertainty data, where (a) shows the conductance normalized by length and (b) is normalized for length and thermal conductivity. No significant improvement to the statistical fit was achieved using the more complex normalization involving averaged properties, so the simpler $(UA/L)_{pc}$ vs. $Reynolds_3$ was chosen for the vapor conductance model.

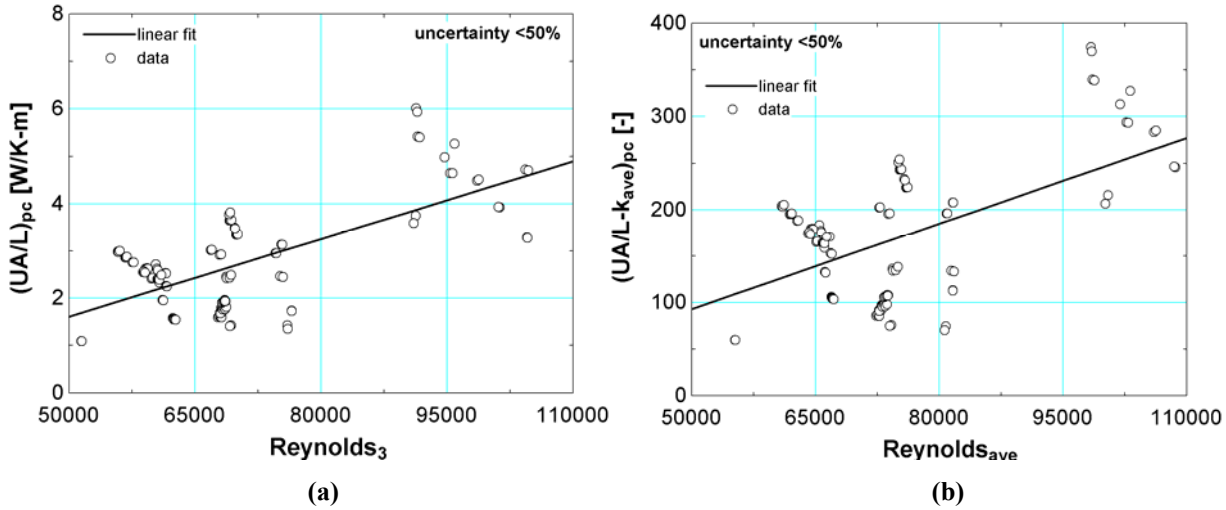

Figure 6-6: Precooler vapor conductance linear best fit for the <50% uncertainty data. (a) Conductance normalized by finned tube length vs. Reynolds at the hot stream inlet. (b) Conductance normalized by finned tube length and average thermal conductivity vs. average Reynolds number in the hot stream.

Table 6-6: Precooler vapor conductance linear fit and correlation statistics.

$\left(\frac{UA_{pc}}{L_{pc}}\right)_{vap}$ **vs. *Reynolds*$_3$ correlation**							
Correlation form	**Uncertainty Criteria**	a_0 **[W/K-m]**	a_1 **[W/K-m]**	**RMS error [W/K-m]**	**RMS error**	R^2	N_{points}
$\left(\frac{UA_{pc}}{L_{pc}}\right)_{vap} = a_0 + a_1 Re_3$	UA/L < 20% all points	-0.53371	5.14E-05	0.7055	19%	0.55	72
	UA/L < 50% all points	-1.13072	5.48E-05	0.8133	22%	0.44	104
	UA/L < 70% all points	-1.21125	5.56E-05	0.8142	22%	0.44	108

$\left(\frac{UA_{pc}}{L_{pc}\,k_{ave}}\right)_{vap}$ **vs. *Reynolds*$_{ave}$ correlation**							
Correlation form	**Uncertainty Criteria**	a_0 **[-]**	a_1 **[-]**	**RMS error [-]**	**RMS error**	R^2	N_{points}
$\left(\frac{UA_{pc}}{L_{pc}\,k_{ave}}\right)_{vap} = a_0 + a_1 Re_{ave}$	UA/L < 20% all points	-7.677	0.002771	44.4	22%	0.50	72
	UA/L < 50% all points	-60.84	0.003073	58.15	29%	0.36	104
	UA/L < 70% all points	-66.76	0.00313	58.73	29%	0.36	108

Table 6-7: Linear fit correlation for the precooler vapor conductance data.

Correlation form	a_0 **[W/K-m]**	a_1 **[W/K-m]**
$\left(UA_{pc}/L_{pc}\right)_{vap} = a_0 + a_1 Re_3$	-1.13	5.48E-05

Two-phase conductance

The vapor conductance model described in Table 6-7 is used with the numerical precooler model in order to determine the length of tube experiencing two-phase flow. There are relatively few data where the 2nd stage refrigerant exited the precooler in a two-phase state so the results represent a limited range of thermodynamic quality. Furthermore, the tube length

required to cool the 2nd stage refrigerant to the dewpoint line, as predicted using the vapor conductance model, exceeded the actual precooler tube length for some of the data. The length-normalized conductance for these data could not be inferred. Computing the tube lengths begins with computing the conductances ($UA_{pc,i}$) in each of the discrete heat exchanger sections using the effectiveness-NTU model as described in Section 5.3.2 The finned tube length associated with each section in the vapor state is computed using the length-normalized conductance presented in Table 6-7:

$$L_{tube,f,pc,i} = \frac{UA_{pc,i}}{\frac{UA_{pc}}{L_{pc}}\left(Re_3\right)} \tag{6.7}$$

where $\frac{UA_{pc}}{L_{pc}}\left(Re_3\right)$ is the normalized conductance evaluated with the hot inlet Reynolds number according to the correlation in Table 6-7. The tube lengths are computed using this method for the sections containing all vapor and also for the single section where the flow transitions to two-phase. The tube length assigned to the vapor phase in the transition section is computed based on the fraction of the heat transferred in the section to reach the saturation temperature at the section average pressure. Therefore the tube length containing two phase flow is computed as:

$$L_{tube,f,pc,2\phi} = L_{pc,f} - \left(\sum_{i=1}^{\#\text{sections}_{vapor}} \frac{UA_{pc,i}}{\frac{UA_{pc}}{L_{pc}}\left(Re_3\right)} + f_{trans,vap} \left. \frac{UA_{pc,i}}{\frac{UA_{pc}}{L_{pc}}\left(Re_3\right)} \right|_{trans} \right) \tag{6.8}$$

where:

$$f_{trans,vap} = \frac{h_{2nd,pc,i-1,trans} - enthalpy\left(\bar{y}_{2nd}, x_{2nd,pc} = 1, P = \left[P_{2nd,pc,i-1} - P_{2nd,pc,i}\right]/2\right)}{h_{2nd,pc,i-1,trans} - h_{2nd,pc,i,trans}} \tag{6.9}$$

where $h_{2nd,pc,i-1,trans}$, $h_{2nd,pc,i,trans}$, $P_{2nd,pc,i-1}$ and $P_{2nd,pc,i}$ are the enthalpies and pressures of the 2nd stage refrigerant at the beginning and end of the transition section, $L_{pc,w}$ is the total precooler finned tube length from Table 4-6, $x_{2nd,pc}$ is the thermodynamic quality of the 2nd stage refrigerant in the precooler, and $\left.\frac{UA_{pc,i}}{\frac{UA_{pc}}{L_{pc}}(Re_3)}\right|_{tran}$ is the computed tube length in the transition section. There is some error associated with using the $\frac{UA_{pc}}{L_{pc}}(Re_3)$ vapor conductance correlation to compute the length of the entire transition section with the two-phase section included in this calculation; however, the heat transfer at high quality will involve mist flow which has a relatively low heat transfer coefficient and therefore will behave in a manner that is similar to the vapor flow (as shown in the high quality regions of Figure 5-19). The method used to compute the two-phase conductance is analogous to the tube length calculation from Eq. (6.8) :

$$UA_{pc,2\phi} = UA_{pc} - \left(\sum_{i=1}^{\#sections_{vapor}} UA_{pc,i} + f_{trans,vap} UA_{pc,i}\Big|_{tran} \right) \tag{6.10}$$

where $UA_{pc,i}\Big|_{tran}$ is the conductance in the transition section and UA_{pc} is the total precooler conductance, computed as:

$$UA_{pc} = \sum_{i=1}^{N_{pc}} UA_{pc,i} \tag{6.11}$$

The length-normalized conductance for the two-phase section is subsequently computed as:

$$\left.\frac{UA_{pc}}{L_{pc}}\right)_{2\phi} = \frac{UA_{pc,2\phi}}{L_{tube,f,pc,2\phi}} \tag{6.12}$$

The quality averaged between the transition section (saturated vapor, $x_{2nd,pc}$ = 1) and the precooler hot exit is subsequently used to correlate the normalized conductance as shown in Figure 6-7(a). Note that the vapor values are also shown with a quality of 1.001 in order to allow comparison; these values are much lower that the two phase values.

A highly resolved curve fit is not possible for the limited precooler two-phase data (six points), so the fit is accomplished using a few assumptions that are based on observations from the recuperator conductance data. A second order polynomial described in Table 6-8 (also, the "two-phase correlation" term in Eq.(6.13)) is used to accommodate a peak with respect to quality. The saturated vapor value for the two-phase correlation is specified as 3.5 W/K-m to roughly intersect the average vapor values from Figure 6-6, and the saturated liquid value (quality = 0) is specified somewhat higher at 5 W/K-m. The liquid value does not reflect a physical phenomenon but rather is chosen to be about 50% higher than the vapor value; this approach is similar to the one taken for the recuperator two-phase region.

Table 6-8: Quadratic fit correlation for the precooler two-phase conductance data

Correlation form	b_0 [W/K-m]	b_1 [W/K-m]	b_2 [W/K-m]
$\left(UA_{pc}/L_{pc}\right)_{2\phi} = b_0 + b_1 x_{2nd,pc} + b_2 x_{2nd,pc}^2$	5	290.1	-291.6

The vapor conductance is a function of Reynolds number, so the transition between vapor and two-phase is more involved than with the recuperator (the recuperator vapor conductance is assumed to be constant so the two-phase conductance simply had to equal the vapor conductance value at a quality of 1). A precooler conductance correlation that includes both the linear vapor correlation and the quadratic two-phase correlation is used to enforce a continuous function between the regimes. An exponentially decaying term is applied to transition between the two-phase and vapor terms between a quality of 0.96 and 1 as shown in Figure 6-7 (a); the exponential term is shown as a function of quality in Figure 6-7 (b). The precooler conductance correlation is:

$$UA_{pc}/L_{pc} = Eterm\ \underbrace{\left(a_0 + a_1 Re_3\right)}_{vapor\ correlation} + \left(1 - Eterm\right)\underbrace{\left(b_0 + b_1 x_{2nd,pc} + b_2 x_{2nd,pc}^2\right)}_{two-phase\ correlation} \tag{6.13}$$

where:

$$Eterm = \exp\left(-100\left(1.001 - x_{2nd,pc}\right)\right) \tag{6.14}$$

where a_0 and a_1 are the vapor conductance curve fit terms from Table 6-7, Re_3 is the Reynolds number at the 2nd stage high pressure inlet of the precooler (state 3), b_0, b_1, and b_2 are the curve fit terms for the two-phase precooler conductance correlation, $x_{2nd,pc}$ is the quality of the 2nd stage fluid in the precooler. The b_0, b_1, and b_2 coefficients for the two-phase quadratic expression were subsequently fit by minimizing the RMS error between the data and the

correlation presented in Eq.(6.13); the coefficients are listed in Table 6-8 and the curve fit is plotted in Figure 6-7(a) and Figure 6-8. For clarity, the final precooler conductance model across the three phase regimes is summarized in Table 6-9.

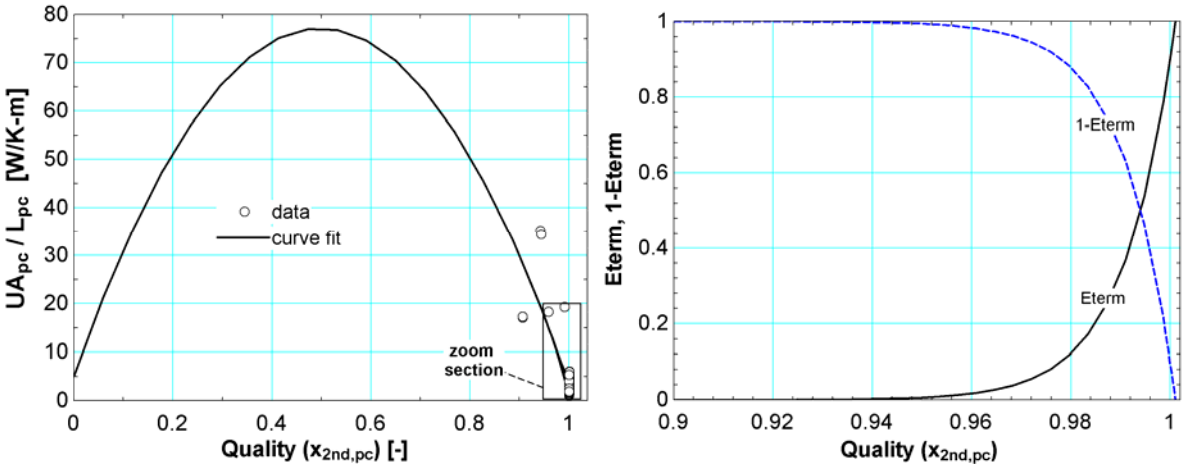

(a) (b)

Figure 6-7: **(a) Length-normalized two-phase precooler conductance data as a function of the local thermodynamic quality. The data points and curve fit are shown. Note that the vapor values are also shown with a quality of 1.001 for comparison. (b) Exponential term applied in conductance correlation.**

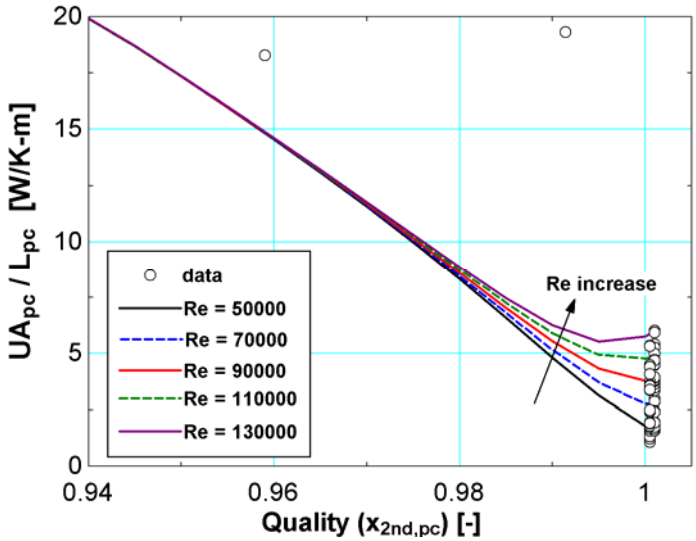

Figure 6-8: **Zoomed view of Figure 6-7(a) showing the precooler conductance data and curve fit as a function of Reynolds number (at state 3) and the local quality.**

Table 6-9: Final precooler conductance correlation extending through the liquid, two-phase, and vapor regimes.

Correlation form				
$UA_{pc} / L_{pc} = Eterm\left(a_0 + a_1 Re_3\right) + \left(1 - Eterm\right)\left(b_0 + b_1\, x_{2nd,pc} + b_2 x_{2nd,pc}^2\right)$				
$Eterm = \exp\left(-100\left(1.001 - x_{2nd,pc}\right)\right)$				
Coefficients				
a_0 **[W/K-m]**	a_1 **[W/K-m]**	b_0 **[W/K-m]**	b_1 **[W/K-m]**	b_2 **[W/K-m]**
-1.13	5.48E-05	5	290.1	-291.6

It should be noted that this correlation is applied with limited confidence in the two-phase region and represents an area for significant improvement that could be addresseed in future work on this project. Nevertheless, the 2nd stage fluid exits the precooler as a vapor for many of the experimental tests so the correlation will provide an adequate prediction for these data, and, the first-approximation two-phase model captures an important heat transfer enhancement related to condensation. Errors associated with the limited characterization of the precooler two-phase heat transfer (as well as the vapor conductance characterization, which is based on data with a large amount of scatter – see Figure 6-6) can result in a poor prediction of overall refrigeration performance; this result is discussed later in Section 6.6.1 and Figure 6-11(c).

6.5 Precooler model verification

The precooler conductance model presented in Section 6.4 was validated using a similar method described for the recuperator in Section 6.3. The temperature and pressure measurements for the R410a evaporating in the precooler are not sufficient to define the enthalpy change for the evaporating refrigerant. Therefore, the effectiveness is defined using the enthalpy change in the 2nd stage stream:

$$\varepsilon_{pc} = \frac{h_3 - h_4}{h_3 - h(P_3, T_8)} \tag{6.15}$$

where h_3 and h_4 are the 2nd stage inlet/outlet stream enthalpies, and $h(P_3,T_8)$ represents the minimum possible hot stream exit enthalpy where mixture exits at the evaporation temperature of the R410a (T_8). Figure 6-9 compares the measured effectiveness values compared with those computed using the conductance model developed in Section 6.4. Two different methods for computing the pressure at state 4 were used to investigate the sensitivity of the effectiveness calculation to the pressure drop model. The first method estimates the pressure as the average between the measurements at states 3 and 5 as discussed in Section 5.3.15.3.1, and the 2nd method uses the value determined using the pressure drop model. Note that the value computed between using the pressure drop model also lies halfway between states 3 and 5, but the pressure at state 5 is computed using the pressure drop model rather than the direct measurement (the pressure drop on the hot sides of the precooler and recuperator are assumed to be equal and are both computed using the ($\frac{1}{2}\rho v^2$) value at state 4 as discussed in Section 6.1). Lines enveloping the regions of 10% and 20% agreement are shown, and most of the data lie within the 20% region. A 50% uncertainty filter applied to the recuperator conductance measurement (UA_{pc}) eliminates several of the outliers, although it also excludes many of the points in the 0.4 to 0.6 effectiveness range.

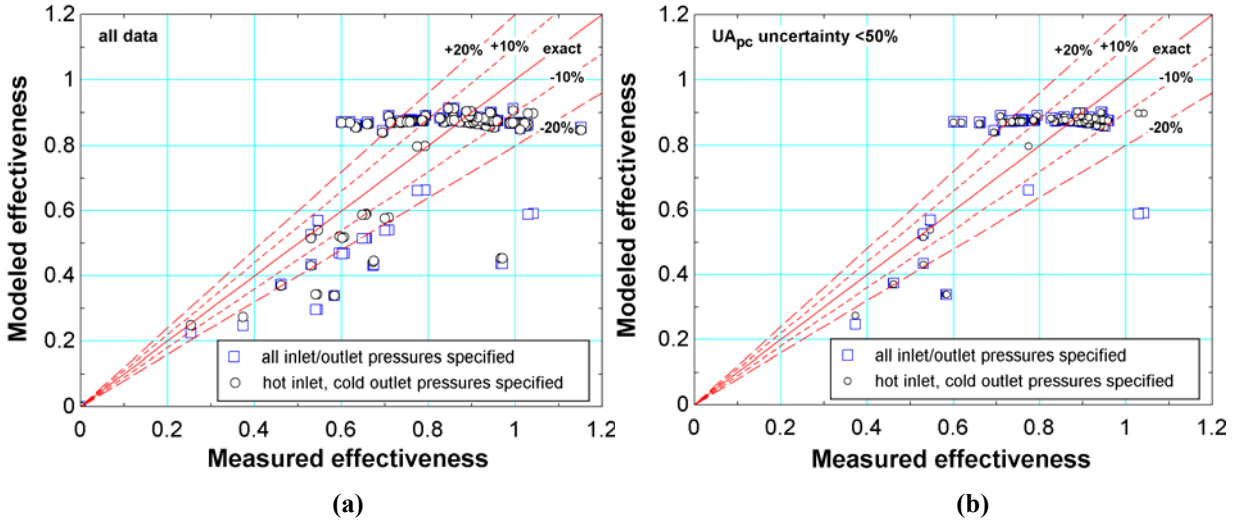

Figure 6-9: Comparison of the measured and modeled precooler effectiveness including values computed using all the available pressure measurements or using limited pressure measurements with the pressure drop model. (a) Shows all collected data and (b) shows the data where the conductance is measured with less than 50% uncertainty.

6.6 System model verification

6.6.1 Empirically tuned model

The correlations for conductance and pressure drop in the precooler/recuperator were integrated with the system-level model to evaluate the ability of the model to predict refrigeration power at a specified load temperature (T_7). The prediction is compared with the precisely controlled experimental thermal load applied between states 6 and 7 (the heat input is measured with ±0.00001 W uncertainty), where T_7 nominally represents temperature applied to the tissue for surgery. The model inputs are selected to be relatively basic in order to simulate a design environment where very few measurements are available for the system. Note that the 2nd stage mass flow and pressure are both given as inputs so the compressor performance map is not considered. Recommendations for future work include using experimental data to create a compressor model that can predict mass flow given a suction and discharge pressure. Inputs to the model from experimental data include the:

1. 2nd stage circulating mixture composition

2. 2nd stage mass flow
3. 2nd stage compressor suction and discharge pressures (P_1 and P_3),
4. 2nd stage load temperature (T_7),
5. 2nd stage high pressure inlet temperature (T_3, which is nominally ambient temperature)
6. 1st stage evaporator (precooler) saturation temperature ($T_8 = T_{11}$)

Given this information the model can compute the cycle performance including all the thermodynamic state points in the 2nd stage, the precooler and recuperator conductances and pressure drops, and the refrigeration load. Discrete heat exchanger models (very similar to the method as presented in Chapter 3) divide the energy exchange equally between very small sections (60 for the recuperator, 15 for the precooler) over which the temperature change and specific heat capacity variation for the mixture are small. The technique of dividing the heat exchangers enables the effectiveness-NTU relation to be applied for mixtures with highly temperature-variant specific heat. The iteration scheme also closely represents the one presented in Chapter 3, where the temperature difference at one end of each heat exchanger adjusted to achieve convergence. The criteria used for convergence is a match between computed and actual lengths of finned tube length in the precooler and recuperator; these criteria better represent the physical constraints of the system compared to the pinch point temperatures specified in the Chapter 3 model. Iteration is carried out in the recuperator by adjusting the hot end temperature difference ($\Delta T_{rec,hot}$) to achieve the actual recuperator finned tube length (46.1 in), note that the lengths of unfinned tube in recuperator sections 0, 4, and 5 (defined in Figure 5-6) are ignored. During each iteration, the finned tube length represented by each section is computed by dividing the conductance of each section (UA_i, computed using the energy balance and heat exchanger analysis presented in Chapter 3) by the empirical normalized

conductance correlation (UA_{rec}/L_{rec}) evaluated at the flow conditions present in the section. The total length of the recuperator tube recuperator is therefore computed as:

$$L_{tube,f,rec} = \sum_{i=1}^{N_{rec}} \frac{UA_{rec,i}}{\frac{UA_{rec}}{L_{rec}}\left(x_{c,i}\right)} \tag{6.16}$$

where N_{rec} is the number of discrete recuperator sections (60), $UA_{rec,i}$ is the section conductance, and $\frac{UA_{rec}}{L_{rec}}\left(x_{c,i}\right)$ is the normalized conductance evaluated at the low pressure stream quality using the correlation presented in Table 6-5.

The precooler finned tube length is enforced using a similar method where the cold end temperature difference ($\Delta T_{pc,pc}$) is adjusted until the computed finned tube length matches the actual measurement (21.7 in). Each iteration computes the precooler tube length as:

$$L_{tube,f,pc} = \sum_{i=1}^{N_{pc}} \frac{UA_{pc,i}}{\frac{UA_{pc}}{L_{pc}}\left(Re_3, x_{2nd,pc}\right)} \tag{6.17}$$

where N_{rec} is the number of discrete precooler sections (15), $UA_{pc,i}$ is the conductance computed for each section of equal energy exchange, and $\frac{UA_{pc}}{L_{pc}}\left(Re_3, x_{2nd,pc}\right)$ is the normalized conductance evaluated at the hot inlet Reynolds number and local thermodynamic quality according to the correlation in Eq. (6.13) and Table 6-9.

Figure 6-10 compares the refrigeration power measured during the tests with the values predicted using the empirical model with the five inputs from the experimental data listed in the beginning of this section. The prediction for tests where the experimental heat input is less than

15 W is excellent – these include the tests with the pure refrigerants, and a number of tests with mixtures. As the heat input increases, the agreement tends to become worse; these points unfortunately include many of the tests that outperformed the original mixture as shown in Figure 5-1.

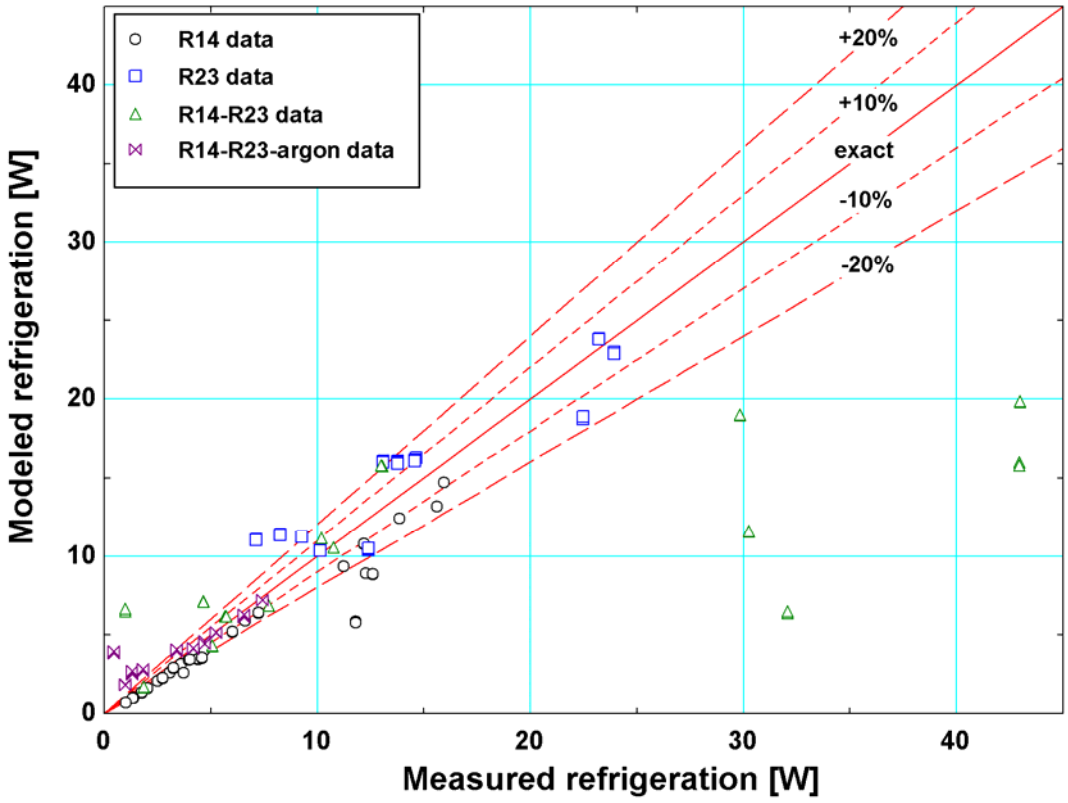

Figure 6-10: Measured refrigeration power compared to refrigeration predicted using the empirically tuned model.

Differences between the experimentally measured and predicted refrigeration values can be attributed to component level modeling errors in the recuperator, precooler, and the jewel orifice. Figure 6-11 compares the measured and predicted 2nd stage cycle operation on a P-h diagram for several different test cases. A test case where the measured and predicted refrigeration values (represented by the enthalpy difference between states 6 and 7 – note that state 7 is nearly identical for the modeled and measured performance) agree well is shown in

Figure 6-11(a); the refrigeration predictions coincide despite a difference in the measured and predicted pressure drop in the (high pressure side) of the precooler and recuperator. Figure 6-11(b) highlights a test case where the recuperator effectiveness is under predicted, and so the heat transfer from the fluid between states 4 and 5 (and, equally from 7 to 1) is lower in the model. This subsequently causes the enthalpy at state 6 to be *higher* that the enthalpy at state 7 so the predicted refrigeration power is negative, as opposed to the small heat input measured in the experiment. The difference in effectiveness may be caused by errors in the recuperator UA/L correlation in the low quality region (0-0.2), where the linear fit correlation region somewhat under predicts the measured conductance values as shown in Figure 6-3(b). The effect of a precooler effectiveness under prediction is shown in Figure 6-11(c): the enthalpy at state 4 predicted by the model is higher than the experimental measurement. This discrepancy propagates through to state 5 and 6, subsequently causing an under prediction in refrigeration power. Finally, Figure 6-11(d) shows a case where the experimental isenthalpic expansion process across the jewel orifice does not lie along a line of constant enthalpy predicted for the mixture by the REFPROP database. This deviation causes disagreement in the enthalpy value of state 6 and subsequently the refrigeration power.

The majority of the under prediction in the refrigeration capacity observed in Figure 6-10 for the larger loads (>15 W) can be attributed to an overly-conservative estimate of the precooler effectiveness. The next largest source of error is related to the under prediction of recuperator effectiveness at low temperatures; this occurs when less heat is applied to the cycle so the recuperator spans across most of the vapor dome as shown in Figure 6-11 (d). Refrigeration prediction errors that are caused only by inaccurate property data, as quantified by

deviations in the isenthalpic expansion process from state 5 to 6, are the smallest at about 20-30% deviation. Current and future work for this project involves developing a more sophisticated pressure drop model for the precooler and recuperator; this model can be used form a better estimate of the pressure and temperature at state 4 and subsequently improve the accuracy of the precooler conductance correlation. Furthermore, additional data where the 2nd stage refrigerant exits the precooler in a two-phase state can be used to refine the precooler two-phase conductance model.

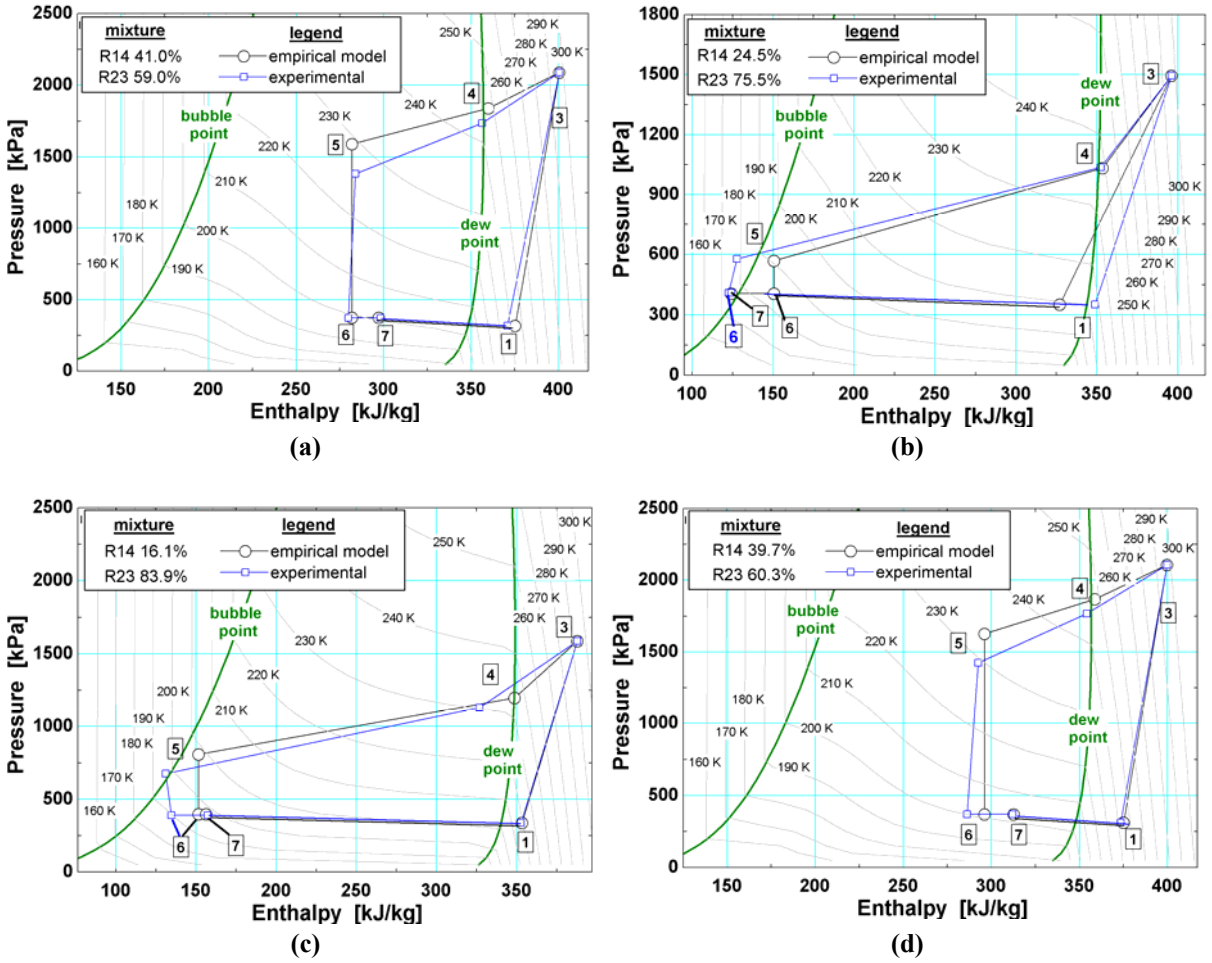

Figure 6-11: Pressure-enthalpy diagrams for the 2nd stage cycle comparing the measured performance to that predicted using the empirically tuned model. The individual graphs show tests where:

- **(a) the model predicts the performance including refrigeration power very well,**
- **(b) the recuperator effectiveness is under predicted,**
- **(c) the precooler effectiveness is under predicted, and**
- **(d) the experimental isenthalpic expansion process does not lie along a line of constant enthalpy predicted by the REFPROP database for the mixture.**

6.6.2 Comparing empirically tuned model with minimum isothermal enthalpy difference (Δh_{JT}) and pinch point models

The refrigeration performance for the cycle was also computed using two simpler models to demonstrate the advantage of using the new empirical model as a design tool. These models simulate a design environment restricted to modeling techniques described in the current MGJT

literature, which do not account for transport phenomena (i.e. heat transfer and pressure drop) in the heat exchangers.

The first model includes evaluating the minimum isothermal enthalpy difference over the operating temperature span of the recuperator as described in Section 1.3. Pressure drop in the heat exchangers is not considered so the compressor suction and discharge pressures represent the high and low cycle pressures (similar to $P_{high,2nd}$ and $P_{low,2nd}$ in Sections 1.2 and 1.3). The refrigeration effect is computed using the same method presented in Section 1.3:

$$\dot{Q}_{load} = \dot{m}_{2^{nd}} \min\left(\left[h\left(P_{low,2^{nd}}, T, \overline{y}_{2^{nd}}\right) - h\left(P_{high,2^{nd}}, T, \overline{y}_{2^{nd}}\right)\right] \text{for } T = T_4 \text{ to } T_7\right) \tag{6.18}$$

where $\dot{m}_{2^{nd}}$ is the 2nd stage mass flow, T is the temperature, $\overline{y}_{2nd}$ is the 2nd stage mixture composition and T_4 and T_7 respectively are the temperatures at the hot and cold inlets of the recuperator. The temperature at state 4 is computed by assuming a precooler cold end temperature difference ($\Delta T_{pc,cold}$). The inputs to the model from the experimental data therefore include:

1. 2nd stage circulating mixture composition
2. 2nd stage mass flow
3. 2nd stage compressor suction and discharge pressures (P_1 and P_3), which are assumed to represent the high and low pressures in the cycle
4. 2nd stage high pressure inlet temperature (T_3)
5. 2nd stage load temperature (T_7),
6. 1st stage evaporator saturation temperature ($T_8 = T_{11}$)

Furthermore, the precooler cold end temperature difference ($\Delta T_{pc,cold}$) is specified as 2 K; this does not reflect the value computed using the experimental data or any physical phenomena, but

rather is based on the general observation that the computed cold end temperature difference is typically about 1-2 K.

The second model used to compare the results of the empirical model includes the pinch point model presented in Chapter 3. Again, the pressure drop in the heat exchangers is neglected so all the 2nd stage cycle pressures before the orifice are specified at the compressor discharge pressure ($P_{high,2nd}$), and pressures after the orifice are specified at the suction pressure ($P_{low,2nd}$). Again, the precooler cold end temperature difference ($\Delta T_{pc,cold}$) was specified somewhat arbitrarily as 2K. The recuperator heat transfer performance is specified by selecting a pinch point temperature difference ($\Delta T_{pp,rec}$); this value is necessarily a guess in this design environment where the detailed heat transfer performance of the heat exchanger is not known. Specifying heat exchanger performance using the pinch point temperatures is a significant weakness of the pinch point model as this does not represent any physical parameters related to the working fluid or heat exchanger geometry. The sensitivity of the overall refrigeration performance to the pinch point temperature is shown in Figure 6-15(a); as the pinch point changes the refrigeration power changes but interestingly the optimal mixture remains the same. In addition to the thermodynamic state points, the pinch point model also computes the heat exchanger conductances (UA_{rec} and UA_{pc}), which can be used as a metric to minimize the cryoprobe size (by maximizing $\dot{Q}_{load} / UA_{total}$ as described in Section 3.1.4). The inputs to this model from the experimental data include:

1. 2nd stage circulating mixture composition
2. 2nd stage mass flow
3. 2nd stage compressor suction and discharge pressures (P_1 and P_3), which are assumed to represent the high and low pressures in the cycle

4. 2nd stage high pressure inlet temperature (T_3)
5. 2nd stage load temperature (T_7)
6. 1st stage evaporator saturation temperature ($T_8 = T_{11}$)

Figure 6-12 compares the cryoprobe tip refrigeration measured in the experiment with the values predicted by each of the three models presented in Sections 6.6.1 and 6.6.2. The general trend observed in the comparison is that the pinch point and Δh_{JT} models (referred to as the "simpler models") tend to over predict the refrigeration, where the Δh_{JT} model provides a somewhat higher prediction. Comparatively, the empirically tuned model provides a more realistic but sometimes over-conservative estimate.

The single component 2nd stage working fluid tests (not distinguished between mixture tests in Figure 6-12) had relatively low heat input power, about 15 W or less. For these tests the pinch point and Δh_{JT} models over predict the refrigeration by 30-40%. Conversely, the empirically tuned model provided a prediction within 10-20% for the same data. In the same 0-15 W experimental heat input range, the simpler models grossly over predict the refrigeration capacity for several mixtures, whereas the empirically tuned model appropriately penalizes these mixtures for poor heat transfer performance. The data points with higher refrigeration values (20-50 W) exclusively used mixtures in the 2nd stage, and advantage of the empirically tuned model is somewhat diminished. The simpler models provide over-optimistic refrigeration predictions, but here the empirical model tends to under predict the refrigeration effect (caused by the errors in the component performance observed in Figure 6-11), albeit to a lesser degree than the deviations with the simpler models. Ongoing efforts to improve the model with additional recuperator and precooler conductance data, and a physics-based pressure drop model

for the high pressure tubes in the 2nd stage are expected to improve the predictive capabilities of the empirically tuned model.

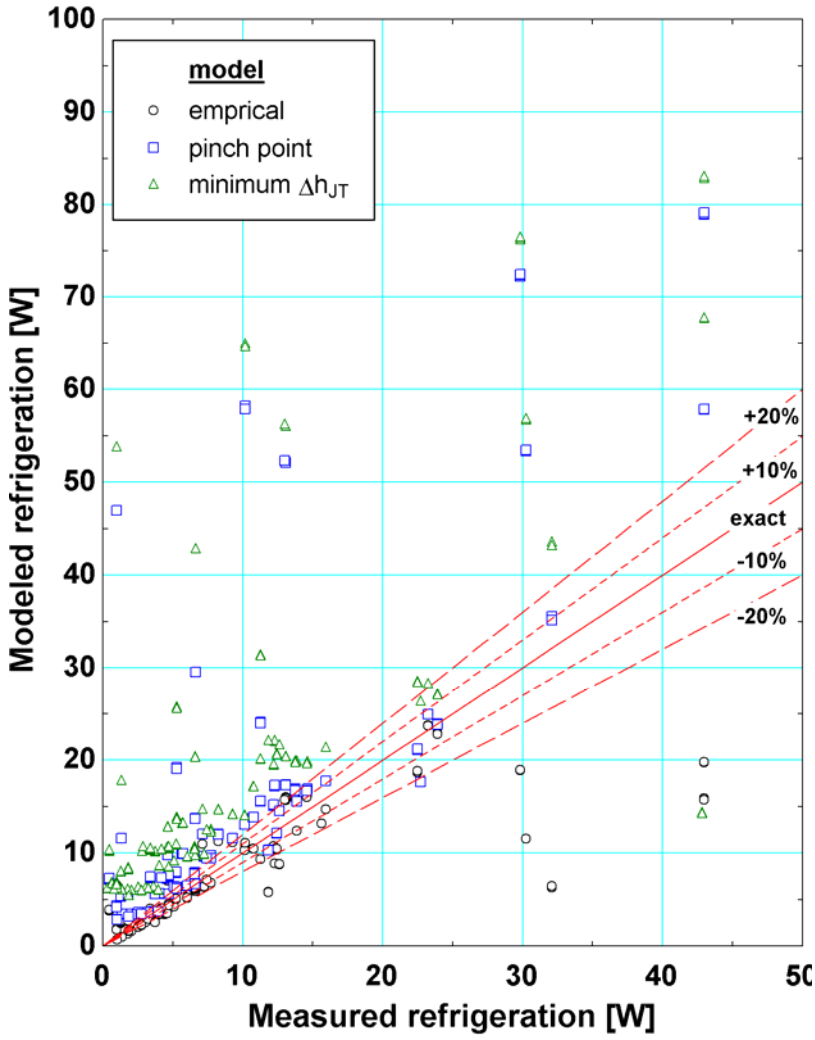

Figure 6-12: Measured and predicted refrigeration power for the empirical model, the pinch point model, and the isothermal enthalpy difference model.

6.7 Using the model as a mixture selection tool

Experience with the cryoprobe manufacturer has shown that the iceball size is the ultimate standard used to judge the medical effectiveness of the instrument. Developing a model to select gas mixtures that optimize the refrigeration performance of the MGJT cycle at a given load temperature is a major component of the design process to maximize the iceball size

produced by the cryosurgical probe. However, this model does not represent a complete design tool as the optimal tip temperature must still be determined. The mixture optimization model must be combined with a heat transfer analysis of the cryolesion (iceball) formation that considers: (1) the geometry of the active portion of the cryoprobe tip in contact with the tissue, (2) the thermal storage, phase change and heat transport properties of the tissue, and (3) the heat transfer from biological processes related to metabolic generation and blood perfusion (Fredrikson 2006). This heat transfer analysis establishes important design benchmarks including the optimal cryoprobe tip temperature, and the refrigeration capacity required to achieve a certain cryolesion size.

Sections 6.7.1 and 6.7.2 address these design issues through two different examples that optimize a binary mixture of R14 and R23; note that these methods could be readily extended to include mixtures with more than two constituents by utilizing the optimization algorithm described in Section 3.1.8 rather than the parametric study presented here. Adding additional components to the mixture could greatly increase the probe capacity (Maytal 2006), and the model requires additional refinement to achieve the level of accuracy required to apply the optimization with confidence. Therefore, the analyses described in Sections 6.7.1 and 6.7.2 are meant to provide an illustrative example rather than final design charts or specific mixtures to applied in the design of the cryosurgical probe.

The first design problem considers selecting an optimal mixture for a given cryoprobe system where the heat exchanger, compressor, and cryoprobe tip sizes have already been specified. The second design relaxes the heat exchanger geometry constraint and enables a mixture optimization that produces a tip temperature and refrigeration power required to achieve

a specified cryolesion size while using a minimal combined recuperator/precooler tube length. Minimizing the tube length reduces the required length and width of the heat exchanger assembly (see Figure 1-7) and therefore achieves the compact design critical for ergonomic use during surgery.

6.7.1 Mixture optimization for a fixed geometry

Optimized mixture for a given load temperature

A binary mixture of R14 and R23 is optimized for the cryoprobe studied in this project for a given 2nd stage mass flow, suction and discharge pressures, and 1st stage evaporator temperature specified in Table 6-10. Future work involving modeling compressor performance and pressure drop in the heat exchanger tubing and jewel orifice will allow for optimization of the suction/discharge pressures and the 2nd stage mass flow. A study similar to the one presented in Section 3.2 would be used to select the proper precooling temperature that maximizes refrigeration but does not result in an impractical precooler compressor size.

Table 6-10: Specified system operating conditions for the optimal binary mixture selection for the fixed geometry cryoprobe.

Parameter	Value
Load temperature (T_7)	170-210 K
2nd stage compressor discharge pressure (P_3)	289.5 psig
2nd stage compressor suction pressure (P_1)	31.7 psig
2nd stage mass flow ($\dot{m}_{2^{nd}}$)	0.0012 kg/s
1st stage evaporation temperature (T_8)	241.5 K
Mixture constituents	R14 & R23

The load temperature is varied between 170 and 210 K and ultimately must be selected to achieve the largest iceball as described below in Figure 6-16. The first step in the design

process is to generate load curves as a function of mixture composition for a specified cryoprobe tip temperature. Figure 6-13 shows the variation in refrigeration power predicted by the empirically tuned model, as well as the simpler minimum isothermal enthalpy difference (Δh_{JT}) model. As shown before in Figure 6-12, the Δh_{JT} model over-predicts the refrigeration capacity and so a design using this model would result in an underpowered probe. Additionally, the optimal mixture composition between the two models differs from 5% to 30% depending on the load temperature. Therefore, a design procedure that uses the Δh_{JT} model to select the mixture composition and then adjusts the length until the desired refrigeration effect is achieved will not achieve a compact design. This observation along with the over prediction of capacity highlights the importance of incorporating the heat transfer and pressure drop behavior in the mixture optimization model. Note that Table 6-11 summarizes the optimal compositions selected by these two models as well as the variations of the pinch point model described in the proceeding paragraphs.

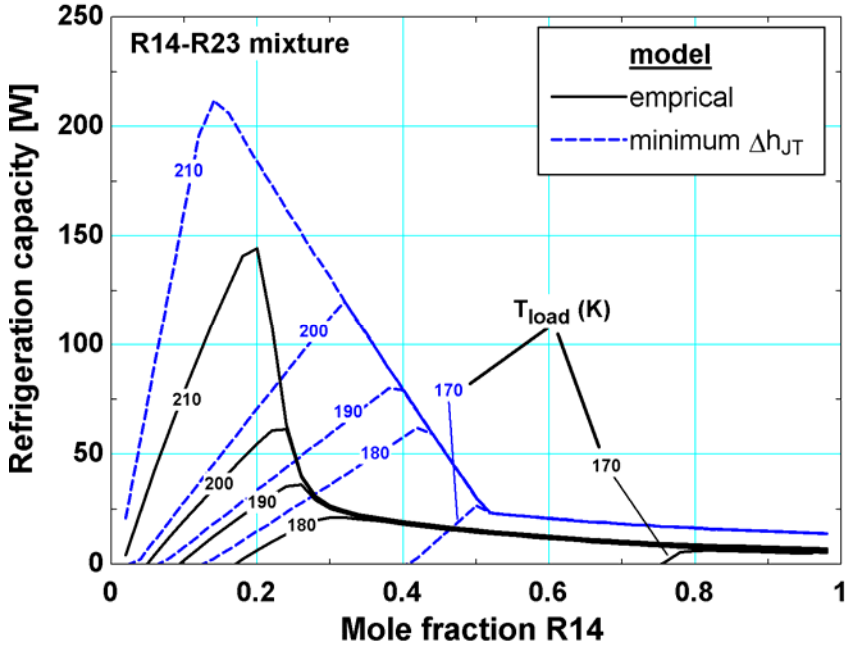

Figure 6-13: Cryoprobe refrigeration as a function of mole fraction R14 for the binary mixture. Results predicted using the empirical model and the minimum Δh_{JT} model are compared.

The load curves from the empirical model were also compared with the load curves from the pinch point model developed in Chapter 3. Mixture selection using the pinch point model is carried out by maximizing the cryoprobe compactness target ($\dot{Q}_{load}/UA_{total}$) rather than the refrigeration capacity as the UA_{total} is not known a priori with the pinch point model. The precooler and recuperator performances are defined by pinch point temperatures, respectively specified as 2 K and 5 K. Specifying the pinch point temperatures actually defines the lengths of the heat exchangers differently than the physical tube lengths measured in the experimental probe that that are specified as inputs to the empirical model. The comparison between these models is therefore not strictly equitable; however, comparing these methods is still useful for illustrating the differences in optimal mixtures selected by the two models. Figure 6-14 compares the refrigeration capacity predicted using the empirical model, and the $\dot{Q}_{load}/UA_{total}$ predicted by the pinch point model as a function of R14 fraction. The pinch point model

predicts the optimal mixture will have less R14 for the 170 K and 210 K tip temperatures, whereas the empirical model predicts the optimal mixture will have less R14 for the 180 K, 190 K and 200 K load curves.

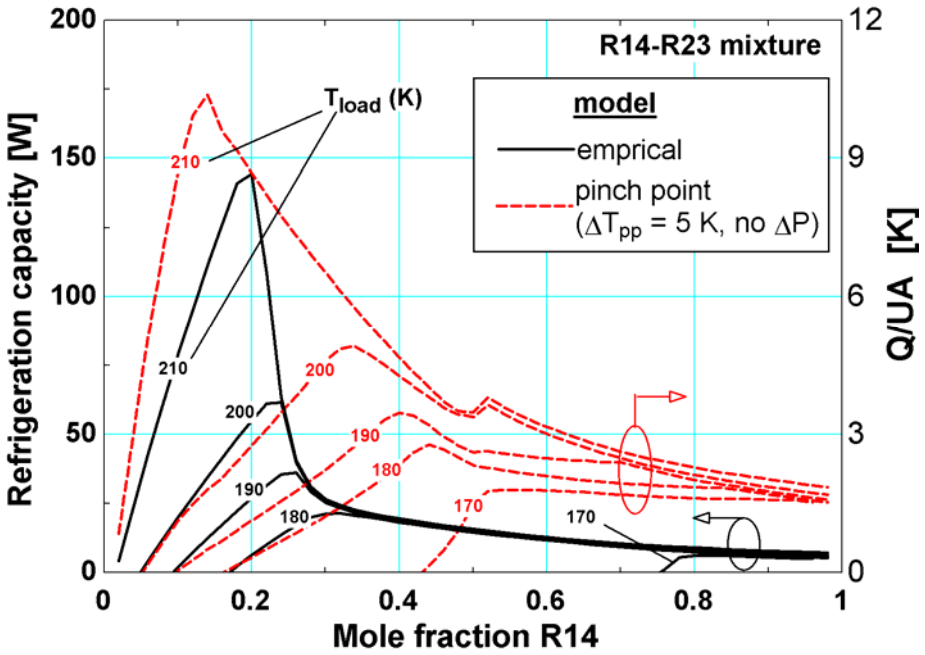

Figure 6-14: Refrigeration capacity predicted by the empirical model for varied R14 mole fraction at different load temperatures. The variation of Q/UA predicted by the pinch point model is also shown on the right scale.

Changes in optimal mixture composition selected by the pinch point model when the recuperator pinch point temperature is varied and the pressure drop model is included were also studied. These studies helped to discern the reasons underlying the difference in optimal mixtures selected by the empirical and pinch point models. Figure 6-15(a) shows that the refrigeration power changes with pinch point temperature, but the optimal composition does not. Figure 6-15(b) shows that the optimal composition is somewhat sensitive to pressure drop, especially for the 170 K and 210 K load curves, where the pressure drops were determined using the model described in Section 6.1. As shown in Table 6-11, the optimal compositions

predicted for the 170 K and 210 K load curves when the pressure drop model is used is much closer to the empirical model predictions.

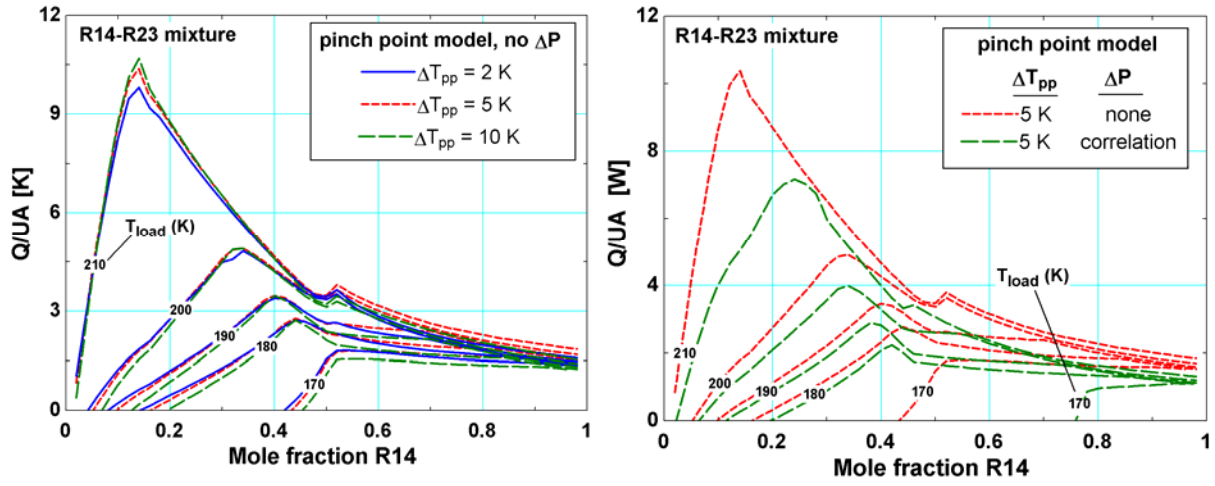

Figure 6-15: Q/UA vs. mole fraction R14 load curves for the pinch point model with (a) varied recuperator pinch point temperature and (b) precooler and recuperator pressure drop included.

It should be noted that using the pinch point model and the *Q*/*UA* design metric are *not* currently recommended for selecting optimal mixtures for the cryoprobe. The overall *Q*/*UA* metric assumes a distribution of tube length and conductance in the precooler and recuperator that are different from the actual tubes and will result in incorrect performance estimates. The logical design method in the absence of local heat transfer data would include adjusting the cryoprobe tube lengths in direct proportion to the *UA,* but this method would result in performance that differs from the pinch point model because of the variations in conductance with local thermodynamic quality and Reynolds number observed in Section 5.4.8. No single adjustment presented here aligned the pinch point model performance with the empirical model, and the deviation between the models is expected to increase as additional components are added to the mixture. Therefore, the equations presented in Chapter 3 must be modified by the pressure drop and conductance correlations in the design of an optimized cryoprobe.

It is worth considering whether the pinch point model could be used to approximately locate optimal mixtures. The experiments used here to measure pressure drop and conductance require significant time and investment, so it would be a considerable advantage to use the simpler pinch point model identify a family of mixtures that at a minimum, produce high refrigeration and a recuperator temperature profile that is favorable for compact heat exchange (Keppler 2004). Table 6-11 shows that for many of the tip temperatures, the empirical model selects optimal mixtures with more R23 that will result in more two-phase flow in the recuperator, indicating that the pinch model is under predicting the performance penalty related to vapor heat exchange (the lower boiling point for R14 causes vapor to occupy a large section of the recuperator, resulting in poor heat transfer). So, perhaps the pinch point model could be used to initially identify optimal mixtures, and then the mixture could be corrected to include a higher concentration of the higher-boiling components that would be in a two-phase state throughout the recuperator. Further work is required, especially with mixtures with three or more components, to determine if this is a valid design method.

Table 6-11: Optimal R14 compositions selected by the various models for the fixed geometry cryoprobe.

	Cryoprobe system model				
Load temperature (T_{load})	**Empirical**	**Minimum Δh_{JT}**	**Pinch point ΔTpp=5 K, no ΔP**	**Pinch point ΔTpp=2 K, no ΔP**	**Pinch point ΔTpp=10 K, no ΔP**
170 K	82%	50%	50%	50%	52%
180 K	32%	42%	44%	44%	44%
190 K	28%	38%	40%	40%	40%
200 K	24%	32%	32%	32%	32%
210 K	20%	14%	14%	14%	14%

	Cryoprobe system model
Load temperature (T_{load})	**Pinch point ΔTpp=5 K, ΔP from correlation**
170 K	78%
180 K	40%
190 K	38%
200 K	32%
210 K	22%

Optimizing the load temperature

The maximum refrigeration available for a given set of mixture constituents and load temperature has been identified using the empirically tuned model as shown in Figure 6-13. However, selection of the proper tip temperature remains and is not obvious. Probes optimized for tip temperature or refrigeration capacity along will be poorly matched with the probe conductance and therefore will yield small iceballs. The refrigeration capacity of the probe decreases as the tip temperature is reduced, so the design must balance the ultimate tip

temperature achieved with the capacity (Fredrikson 2006). A colder tip has the *potential* to create an iceball that penetrates further into the tissue, but, the refrigeration capacity must be sufficient to intercept the heat input (conduction through tissue, convection via blood perfusion) that increases as the surface area of the iceball grows. Consideration of the iceball formation characteristics enables proper balancing of the tip temperature and refrigeration power; this process has been exhaustively studied by Fredrikson et al. (2004, 2006) and is briefly illustrated here.

The optimum refrigeration capacities at each tip temperature are combined to form the load curve for the probe that is referred to as the "best mixture locus" in Figure 6-16. The best mixture locus is compared to the steady state iceball formation load curve also shown in Figure 6-16, which determines the refrigeration capacity required to maintain the probe at a given steady state tip temperature in the tissue (i.e. to balance the temperature difference between the cold probe and the warm tissue). The iceball radius corresponding to the steady state iceball load curve is also shown on the right axis. Fredrikson et al. (2004, 2006) found that the intersection of the best mixture locus and the iceball load curve represents the best operating point for the cryoprobe, so the intersection tip temperature is used to select the optimal mixture from the design chart in Figure 6-13. Note that the iceball load curve and iceball radius line are fictitious representations used here for illustration that are based on general trends observed by Fredrikson et al. (2004, 2006). A detailed heat transfer analysis quantifying the iceball growth and the conductance of the probe tip are needed to determine the actual values, but such an analysis is beyond the scope of this thesis.

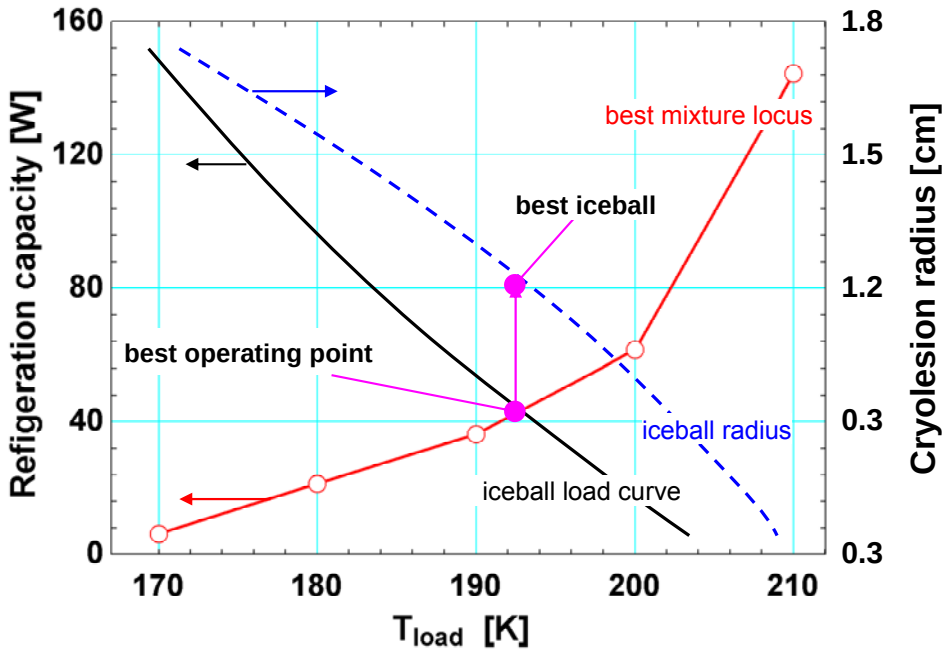

Figure 6-16: Optimal cryoprobe refrigeration load curve and the fictitious steady state iceball formation load curve. The steady state iceball radius as a function of tip temperature is also shown to illustrate the size of the optimal iceball.

6.7.2 Mixture optimization for new design of precooler and recuperator.

An ideal design procedure would begin by specifying the desired size and shape (i.e. length and radius) of the iceball, and then use a modeling tool to select the hardware, mixtures, and operating parameters that achieve the specification within the smallest cryoprobe and compressor cabinet footprint. This section describes a design process similar to the one in Section 6.7.1 (where mixture composition, and tip temperature are optimized for specified compressor suction and discharge pressures, mass flow, and precooler temperature), except that the refrigeration power and tip temperature are specified to yield a desired iceball size and the mixture is optimized to achieve this performance with minimal combined precooler/recuperator tube length.

Specifying the cryolesion size defines the shape and conductance of the cryoprobe tip, and subsequently the steady state iceball load curve and cryolesion radius curve as shown in Figure

6-16 (Fredrikson et al. 2004, 2006). The iceball refrigeration power and tip temperature corresponding to the required iceball radius represents the design operating point. The remaining task is to select the optimal mixture that will achieve the design tip temperature and refrigeration capacity using a minimal combined recuperator and precooler tube length. The mixture is again selected from the binary combination of R14 and R23, and the fixed system parameters specified in Table 6-10 are applied to the optimization.

The empirical model described in Section 6.6.1 is used to compute the overall heat exchanger (recuperator & precooler) tube length required to achieve an arbitrarily chosen 40 W refrigeration load at various load temperatures ranging from 170 K to 210 K as shown in Figure 6-17(c). Note that the 40 W does not equal the optimum design point identified in Figure 6-16. The actual refrigeration power and load temperature would be specified using the iceball refrigeration load curve as described in the preceding paragraph. The pinch point temperature in the recuperator is also parametrically varied and has an optimal value in the design. Specifically, the pinch point temperature is specified as 2 K, 5 K and 10 K, where the 5 K value achieves the shortest tube length for all load temperatures. Increasing the pinch point temperature reduces the exergetic efficiency of the heat exchange in the recuperator and penalizes the capacity in the cycle. However, the increased temperature differential in the recuperator enables more heat transfer per length of tube. The optimal pinch point balances these two design considerations to reach the refrigeration target with the minimal tube length. The best mixture for the probe at the design tip temperatures is identified at the valley of the appropriate tube length curves as shown in Figure 6-17.

The analysis used to generate Figure 6-17 is not strictly correct and is primarily meant to illustrate the design process. The pressure drop model is applied based on the correlation developed in Section 6.1 for the fixed tube lengths (recuperator 1.17 m /46.1 in. and precooler 0.55 m / 21.7 in.) in the tested cryoprobe system. The tube lengths clearly vary in the calculations presented here, so there will be error related to the pressure drop as the overall length changes significantly from 1.72 m. Furthermore the overall tube length was computed according to:

$$L_{tube,total} = 40W\left(\frac{1}{\dot{Q}/\dot{m}}\right)\Bigg|_o \left(\frac{L_{tube}}{\dot{m}}\right)\Bigg|_o \tag{6.19}$$

where $\dot{Q}/\dot{m}\big|_o$ is the refrigeration per mass flow and $L/\dot{m}\big|_o$ is the overall tube length per mass flow required to achieve a given pinch point temperature, where the values are computed at the fixed mass flow of 0.0012 kg/s from Table 6-10. The variations of these two parameters with mixture composition are respectively shown in Figure 6-17(a) and (b), and illustrate the tradeoff between refrigeration capacity and tube length as the pinch point temperature is varied. This computation assumes that refrigeration and tube length scale linearly with mass flow, which does not account for the non-linear variance of heat transfer and pressure drop with mass flow. The heat transfer is dependent on the Reynolds number and temperature profile (which is affected by the pressure drop) and the pressure drop is dependent on the precooler hot exit dynamic pressure that varies with the flow rate in a non-linear fashion. The mass flows used for computing the performance in Figure 6-17 can differ significantly from the fixed value so the error may be significant. Future modeling work should not make these linearized assumptions in the development of the system design model.

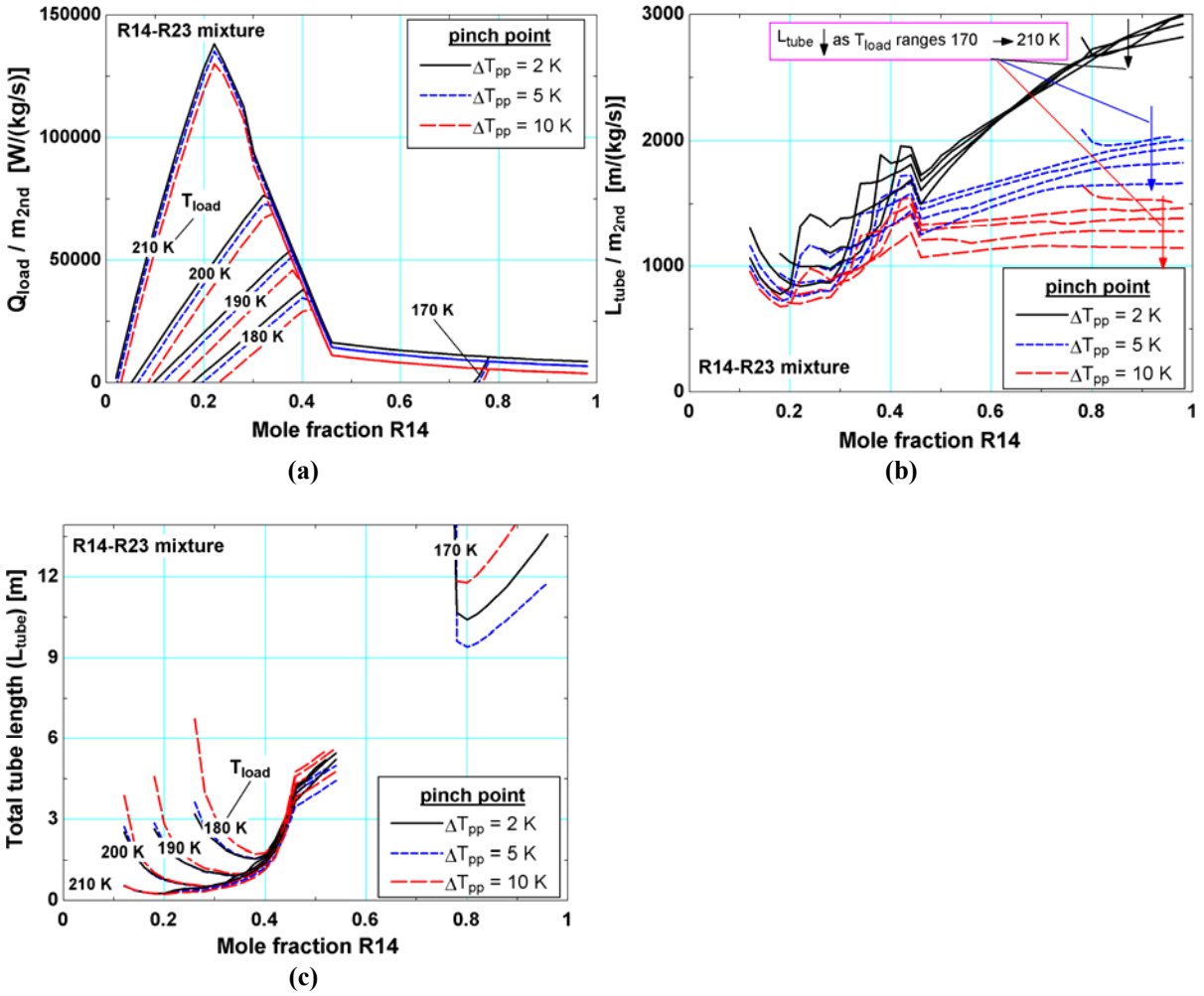

Figure 6-17: Cryoprobe tube length and mixture design charts showing performance with various compositions of R14 and R23. Performance parameters include (a) refrigeration per mass flow, (b) tube length per mass flow, and (c) tube length required to achieve 40 W of refrigeration at a specified tip temperature.

6.8 References

Fredrikson, K. 2004. Optimization of Cryosurgical Probes for Cancer Treatment. M.S. thesis. Madison, WI USA: University of Wisconsin - Madison, Mechanical Engineering Dept.

Fredrikson, K.; Nellis, G.; Klein, S. A. "A Design Method for Cryosurgical Probes". *International Journal of Refrigeration* 2006, vol. 29, 700-715.

Hughes, C. B., G. F. Nellis and J. M. Pfotenhauer. 2004. "Measurement of heat transfer coefficients for non-azeotropic hydrocarbon mixtures at cryogenic temperatures". In 2004 ASME International Mechanical Engineering Congress and Exposition, IMECE, pp. 415-422.

Hughes, C. B. 2004. Experimental Measurement of Heat Transfer Coefficients for Mixed Gas Working Fluids in Joule-Thomson Systems M.S. thesis. Madison, WI USA: University of Wisconsin - Madison, Mechanical Engineering Dept.

Keppler, F.; Nellis, G.; Klein, S. A. “Optimization of the Composition of a Gas Mixture in a Joule-Thomson cycle”. *HVAC&R Research* 2004, vol. 10, 213-230.

Maytal, B., Nellis, G. F., Klein, S. A., Pfotenhauer, J. M.; “Elevated-pressure mixed-coolants Joule–Thomson cryocooling”. *Cryogenics* 2006, 46, 55-67.

Nellis, G., C. Hughes and J. Pfotenhauer. 2005. “Heat transfer coefficient measurements for mixed gas working fluids at cryogenic temperatures”. *Cryogenics* 45(8): 546-556.

Rajesh Reddy, K., Srinivasa Murthy, S., Venkatarathnam, G. (2010). "Relationship between the Cooldown Characteristics of J–T Refrigerators and Mixture Composition." *Cryogenics,* 50(6-7), 421-425.

7 Conclusions and Recommendations for Future Work

7.1 Summary/conclusions

Each thesis section identifies several significant design aspects and discoveries related to MGJT cycle cryoprobes that have been made throughout this project. Many of the important points are collected and highlighted here for emphasis.

Chapter 1 discussed the evolution of cryosurgerical systems from the topical application of liquid cryogens to modern systems that integrate the powerful and compact MGJT cycles with a cryoprobe to create an inexpensive yet extremely effective surgical instrument. Chapter 2 outlined the history of MGJT cycles and their application to cryosurgery. The limited availability of detailed MGJT models and experiments motivated the work carried out for this thesis involving the development of an empirically tuned component level model of the system that could be used to select optimal gas mixtures.

Chapter 3 presented the detailed thermodynamic and heat transfer equations that are used to compute the precooled cryoprobe system performance. The model optimizes the refrigerant mixture for the 2nd stage according to the cryoprobe compactness target, $\dot{Q}_{load}/UA_{total}$. Subsequent experimental tests discussed in Chapters 5 and 6 showed that the exclusion of pressure drop and local heat transfer coefficient from this model significantly degrades the models ability predict system performance. Optimal binary R14/R23 compositions selected using the $\dot{Q}_{load}/UA_{total}$ metric differed by 6-32% from the empirically tuned model; this observation suggests that caution should be used when the unmodified version of the model from Chapter 3 is used to select optimal mixtures. It is possible that correcting mixtures selected by the Chapter 3 model to include more high boiling components could be used a

design method in the absence of detailed pressure drop and heat transfer data; however, further investigation of this method is required. Until this method can be validated, it is recommended that the Chapter 3 equations be corrected to include the empirical pressure drop and heat transfer correlations.

Despite the deficiencies of the Chapter 3 model, it was a useful tool for investigating cycle design issues related to proper selection of precooling temperature and mixture compositions. Specifically, a design tradeoff was identified between the cryoprobe compactness and the size and power requirements of the compressors and condensors. Furthermore, methodologies applied to the Chapter 3 model related to genetic optimization, freezing point calculation, and discrete heat exchanger modeling are also applicable to the empirically corrected model.

The experimental construction detailed in Chapter 4 highlighted some of the iterative system design issues that are related to oil and moisture management, as well as leak control. Flow path obstruction problems related to oil and water migration to the cold components of the system caused significant delays in this research project; the final solution to contamination control is presented as reference for the future design of a similar experimental apparatus. Creating the high quality leak-tight joints that are required for a vacuum test facility, most notably those required for the PRT wire feedthroughs and the cryoprobe sheath, proved to be difficult because of material embrittlement and differential contraction at low temperatures. The flexible and reliable PRT measurement system presented integrated the thermometer directly into the flowstream via a VCR tee, and provided hundreds of hours of leak-free operation.

Chapter 4 presents further details regarding the geometry of the PRTs that are integrated into the cryoprobe sheath to measure recuperator temperature profiles. The measurements are

provided with enough details that the PRT measurements could be placed in relation to specific locations along the recuperator tube. These measurements are unique in the MGJT cycle literature, and the local temperature and conductance measurements represent a significant advance in understanding the behavior of mixtures at cryogenic temperatures in the compact helically wound finned tube heat exchanger.

Chapter 5 shows the trends that are observed in circulating gas composition shift followed the same behavior recorded by other researchers (Gong 2002, 2007); it is imperitive that this shift be quantified using a Gas Chromatograph so that accurate property data are used to compute component and cycle performance metrics. Property data evaluation showed that the REFPROP database provided somewhat better predictions of the Joule-Thomson effect temperature change than the NIST4 database. Furthermore, the NIST4 database prediction of the dewpoint line temperature often caused the predicted temperature profile in the recuperator to violate the pinch point restriction. As a result, the REFPROP database was selected for processing the experimental data in the empirically tuned model.

Component performance measurements presented in Chapter 5 heavily relied on an uncertainty analysis to filter out scatter in the data in order to develop correlative heat transfer and pressure drop relations, and for test facility verification. The measurements where the cycle operated near the vapor dome were particulariliy sensitive to sharp variations in thermal capacity caused by variations in the prediction of the dew point and bubble point lines. The heat transfer data notably followed trends measured in a different experimental test facility that is dedicated solely to measuring heat transfer coefficients of mixtures at cryogenic temperatures (Hughes 2004, Nellis 2005). The pressure drop and heat transfer measurements that meet

specified uncertainty criteria are correlated for the precooler and recuperator across the liquid, two-phase, and vapor regimes, and eventually fit to models in Chapter 6.

In Chapter 6, the correlations for precooler/recuperator pressure drop and heat transfer are applied to the thermodynamic model developed in Chapter 3. The empirically tuned model shows greatly improved refrigeration prediction capabilities for a cycle operating in a vapor phase and eliminates mixtures that other, simpler models do not properly discount because of large pressure drop or poor heat transfer. The empirical model predictive capability is reduced for the 2nd stage cycle operating within the vapor dome, including several important experimental operating points where the mixture outperformed the manufacturers' original mixture. However, the modeling errors have been identified and are largely related to an underprediction in the precooler effectiveness when the mixture exits the precooler in a two-phase state. The next largest source of error is caused by an underprediction of recuperator conductance in the low quality (0-0.2) region. Future work including carrying out more tests where the mixture is in a two-phase state in the precooler or closer to the bubble line in the recuperator will help refine the heat exchanger conductance models and therefore the overall refrigeration prediction.

Finally, Chapter 6 presents a design process for selecting the optimal mixture and tip temperature to: (1) maximize cryolesion size for a given cryoprobe heat exchanger geometry and (2) achieve a specified iceball size with minimal heat exchanger size in a more flexible design environment where the precooler and recuperator tube lengths can be adjusted.

7.2 Future Work

Recommendations for future work can be broadly divided into those related to modeling and experimental work.

Recommendations for modeling

The recuperator/precooler pressure drop model presented in Chapter 6 is relatively basic and should be expanded to include a more rigorous, physics-based characterization that spans all phase regimes. This new model could also eliminate the assumption made in Chapter 5, which is that pressure drop in the high pressure circuit of the 2nd stage is equally divided between the recuperator and the precooler.

As shown in Section 6.7, the optimization model still requires fixed mass flow and compressor pressure inputs. The model's flexibility and usefulness for system-wide optimization could be greatly improved by integrating a model of the relationship between the pressures and mass flows in the JT cycle; this would require modeling the compressor and the jewel orifce.

The performance of the system with mixtures is extremely sensitive to charge pressure. This observation was not explicitly stated in the experimental data presented here, but the charge pressure was varied substantially to achieve the range of operating conditions observed in Chapters 5 and 6. In general, increasing the charge pressure increases the mass flow and refrigeration available at higher temperatures, but decreases the low-temperature refrigeration and ultimate temperature in the cycle. As the total charge is increased, both the suction and discharge pressures tend to increase, and the net effect is a smaller temperature change across the jewel orifice which results in higher overall cycle temperatures. A modeling study to

account for the distribution of the refrigerant (and subsequently, pressure) in the cycle governed by the pumping power of the compressor, the total system volume, and the various flow restrictions in the system could be useful for optimizing the charge pressure for each mixture.

The heat transfer and pressure drop models presented in Chapter 6 require some refinement to better capture component performance. In addition to further testing and the development of models with greater physical basis, additional refinement may be made by considering some of the secondary flow passages and parasitic heat transfer paths that are not included in the model presented here. For example, the model neglects the unfinned portions of recuperator and precooler tubing (these lengths are listed in Table 4-6 and Table 5-3). The model also neglects heat transferred to the 2nd stage low pressure stream as it flows between the annulus created by the SS sheath and the precooler outer shell (see Figure 4-18). Axial conduction in the SS sheath is small because the tube is thin-walled (0.020"); this heat transfer is neglected in the model but the ineffectiveness introduced may play a significant role in cases where the recuperator effectiveness approaches unity (Nellis and Klein, 2009, Sec 8.7).

Normalizing the conductance values by the thermal conductivity to form a term analogous to a Nusselt number did not help to reduce the scatter in the data in Chapter 5. Applying the correlations to geometries and flow conditions other than those presented in this thesis requires a grouping of the heat transfer results into non-dimensional quantities; further effort is required to produce strongly correlated non-dimensional groups.

The circulating mixture reaches a steady and uniform composition throughout the cycle after thermodynamic equilibrium is achieved relative to the temperatures/pressures in the system and adsorption into the compressor oil. As stated before, the circulating composition represents

the mixture that is actually the working fluid for the cycle and this composition must be used to calculate the thermodynamic performance of the system. However, two-phase transport processes are sensitive to the "local" composition in each component which can significantly differ from the circulating composition. The "local" composition here refers the composition that includes both circulating and non-circulating mixture collected within a component; for example, refrigerant that has condensed out of circulation in the recuperator will play an important role in the heat transfer (i.e, nucleate boiling) and pressure drop. Fitting the two-phase transport processes to a phenomenological model (i.e. one that can provide the conductance values without the extensive experimental testing described here) therefore will require tracking the local composition using thermodymamic equilibria calculations and consideration of contained volume.

Recommendations for experiments

Tests using mixtures within a binary family are useful for evaluating the performance of the system. The property computations execute quickly and can be applied with high accuracy as the number of species and mixing paremeters, which each introduce uncertainty into the property data, are relatively small. Complete parametric studies varying the ratio of the components can be carried out in a timely fashion yet provide valuable insights into the cycle operation.

Further tests using the R23-R14 mixture should be used to fill out the 0-0.2 and 0.5-0.8 quality regions of the two-phase recuperator conductance data from Figure 5-21. The 0.5-0.8 quality region contains significant scatter and should be refined. Further data in the 0 to 0.2 quality region is required to help assess the validity of the "linear" portion of the conductance fit

(see Figure 6-3(b) and Figure 6-4). An additional binary mixture family of refrigerants should be tested so that the results can be added to the existing database and/or compared with the R14-R23 data in order to evaluate the general applicability of the heat transfer and pressure drop correlations.

The next set of mixture constituents that should be used for testing should include a low-boiler (e.g. R14), a mid-boiler (e.g. R23), and a high boiler (e.g. R410a or R134a). For the R14-R23 tests presented in Chapter 5, the recuperator operated with at least one section having vapor flow that significantly restricted heat transfer. Note that this problem was exacerbated with the addition of argon in the argon-R14-R23 mixture tests. Adding a high boiler can eliminate the low vapor-heat-transfer restriction, and would allow for more R14 in the mixture to increase the refrigeration capacity at lower temperatures. This behavior can be explained by evaluating the superimposed effects of the individual components operating in the cycle; this is not strictly correct as the component molecules interact in each other in such a way that the mixture exhibits behavior that differs somewhat from the superposition (as governed by the mixture equations of state), but this analysis is nevertheless useful as a heuristic tool. The R14 provides the refrigeration effect at low temperatures (the R23 expands from a liquid to a liquid or a low quality mixture at low temperature and produces little refrigeration effect); however, heat transfer considerations limited the amount of R14 in the best mixtures because the R14 is in a vapor state over most of the recuperator temperature distribution. High concentrations (80% or greater) of R23 were required to achieve the desired two-phase flow for efficient heat exchange. The combined percentage of R23 and the high boiler required to carry the same heat transfer burden will likely be less, so additional R14 could be added. Note that there is a limit to the

benefit that can be achieved by adding the high-boiler as it will produce even less refrigeration effect at low temperatures (but still must be cooled by the R14 expanding across the jewel orifice).

Adding a high boiler will also extend the thermodynamic qualities of the 2nd stage refrigerant at the exit of the precooler. The two-phase data were very limited (six points) and so the confidence in the corresponding fit is low. Characterizing the two-phase heat transfer in the precooler is very important; as discussed in the summary, errors in the two-phase precooler conductance account for the poor refrigeration prediction for some of the mixtures that actually perform the best.

The final recommendations are related to developing a better cryoprobe rather than a better modeling tool. The precooling temperature in the cycle can, and should be, reduced below the ~240 K level encountered during typical operation. At 240 K, the precool cycle capacity greatly exceeds the amount of heat that can be extracted from the 2nd stage stream from ambient temperature to 240 K. In fact, a dedicated 10" fin-fan heat exchanger had to be installed in the flowstream to vaporize the 1st stage refrigerant (R410a) exiting the precooler in order to protect the mass flow meter from the cold temperatures. The precooling temperature could be lowered, for example, by increasing the restriction of the capillary tube to lower the compressor suction pressure and subsequently the evaporator saturation pressure. The accompanying reduction in mass flow rate and capacity of the precooling state will limit the reduction in precooling temperature. Note that the same effect could be achieved, perhaps with greater efficiency, using an alternate refrigerant in the precooling cycle. The second design recommendation includes enhancing the recuperator tube and fins with a surface treatment to promote nucleate boiling.

As shown in Section 5.4.8, the conductance data indicate nucleate boiling dominates the heat transfer and therefore the heat exchange could be greatly improved with various porous- or micro-structures that are widely available in industry.

7.3 References

Gong, M.Q.; Wu, J.F.; Qi, Y.F.; Hu, G.; and Zhou, Y. "Research on the Change of Mixture Compositions in Mixed-Refrigerant Joule-Thomson Cryocoolers". Advances in Cryogenic Engineering, Vol 47, 2002

Gong, M.; Zhou, W.; and Wu, J. "Composition Shift due to Different Solubility in Lubricant Oil for Multicomponent Mixtures", Cryocoolers 14, 2007

Gong, M.; Deng, Z.; Wu, J.; "Composition Shift of a Mixed-Gas Joule-Thomson Refrigerator Driven by an Oil-Free Compressor", Cryocoolers 14, 2007

Hughes, C. B. 2004. Experimental Measurement of Heat Transfer Coefficients for Mixed Gas Working Fluids in Joule-Thomson Systems M.S. thesis. Madison, WI USA: University of Wisconsin - Madison, Mechanical Engineering Dept.

Nellis, G., C. Hughes and J. Pfotenhauer. 2005. "Heat transfer coefficient measurements for mixed gas working fluids at cryogenic temperatures". *Cryogenics* 45(8): 546-556.

Nellis, G. and Klein, S., *Heat Transfer*, Cambridge University Press, 2009 ISBN 9780521881074